

MODELLING THE MICROSTRUCTURE AND MECHANICAL
PROPERTIES OF AUSTEMPERED DUCTILE IRONS

By

Miguel Angel Yescas-González

Darwin College, Cambridge

University of Cambridge

Department of Materials Science and Metallurgy

Pembroke Street, Cambridge CB2 3QZ

*A dissertation submitted for the
degree of Doctor of Philosophy
at the University of Cambridge*

November 2001

This Thesis is dedicated
to my parents

Ma de los Angeles
and
Francisco

ZE ILLNAMIKIZ NIN EZKAYO

**IKA TLEN NI YAZKI
AMITLA NI TENYO TILLIUH
TLAKUITLAPAN TLALLIPAN
KEH NI KICHUA NOYOLOHZIN
AZEH MOTOPALLI TIUALLA
NEMILLIZ IN KUEPONIZ
TLALLIPAN
TI NEZKAYOTOTIUH XOCHIMEH
TI NEZKAYOTOTIUH KUIKAMEH**

NEZAHUALCOYOTL
1403-1473

UN RECUERDO QUE DEJO

**CON QUE HE DE IRME ?
NADA DEJARE EN POS DE MI
SOBRE LA TIERRA ?
COMO HA DE ACTUAR MI CORAZON ?
A CASO EN VANO VENIMOS A VIVIR ?
A BROTAR SOBRE LA TIERRA ?
DEJEMOS AL MENOS FLORES
DEJEMOS AL MENOS CANTOS.**

I LEAVE A MEMORY

**WHAT AM I TO TAKE WITH ME ?
WILL I LEAVE NO LEGACY ON THIS EARTH ?
HOW IS MY HEART TO FEEL ?
DO WE LIVE OUR LIVES IN VAIN ?
TO ROOT ON THIS EARTH ?
LET US AT LEAST LEAVE FLOWERS
LET US AT LEAST LEAVE SONGS**

PREFACE

This dissertation is submitted for the degree of Doctor of Philosophy at the University of Cambridge. The research described herein was conducted under the supervision of Professor H. K. D. H. Bhadeshia in the Department of Materials Science and Metallurgy, University of Cambridge, between October 1998 and October 2001.

This work is to the best of my knowledge original, except where acknowledgements and references are made to previous work. Neither this, nor any substantially similar dissertation has been or is being submitted for any other degree, diploma or other qualification at any other university. This dissertation contains less than 60,000 words.

Part of this work has been presented in the following publications:

M. A. Yescas, H. K. D. H. Bhadeshia and D. J. MacKay, *Estimation of the amount of retained austenite in austempered ductile irons using neural networks*. Materials Science and Engineering A311 (2001) 162-173.

M. A. Yescas and H. K. D. H. Bhadeshia, *Model for the maximum fraction of retained austenite in austempered ductile cast iron*. Materials Science and Engineering (2001) in press.

M. A. Yescas, *Prediction of the Vickers hardness in austempered ductile irons using neural networks*, International Journal of Cast Metals Research, in press.

Miguel Angel Yescas-Gonzalez

November 2001

ACKNOWLEDGEMENTS

I would like to thank Professors D. J. Fray and A. H. Windle for the provision of the laboratory facilities in the Department of Materials Science and Metallurgy at the University of Cambridge. I am extremely grateful to my supervisor Professor H. K. D. H. Bhadeshia for his endless support, enthusiasm, knowledge and friendship.

I am indebted to The National Council of Science and Technology (CONACYT) of Mexico, for a scholarship to come to Cambridge University.

I would also like to thank the past and present members of the Phase Transformations and Complex Properties Research Group for their help and friendship, in particular to Harsha Lalam, Thomas Sourmail, Marimuthu Muruganath, Shingo Yamasaki, Gareth Hopkin, Francisca Caballero, Hiroshi Matsuda, Carlos Capdevila, Pedro Rivera, Toshihiro Tsuchiyama, Franck Tancret, Carlos Garcia, Dominique Carrouge, Pascal Jaques, and Nick Tyas. It was an enormous pleasure to find such a nice fellows.

Thanks also to my friends and to the people I met both at Darwin College and other Colleges during my time in Cambridge.

Finally, I take this opportunity to express my gratitude to my family for their love, unfailing encouragement and support. Special thanks to my parents Francisco and Ma de los Angeles, I cannot find appropriate words to convey my sense of gratitude for their support throughout my life.

ABSTRACT

Austempered ductile irons (ADI) are distinguished by their microstructure which consists of spheroidal graphite in a matrix of bainitic ferrite, carbon-enriched retained austenite and martensite. This microstructure is generated by the isothermal transformation of austenite to bainite at a temperature somewhere between the bainite-start and martensite-start temperatures. ADI has been recognised as a potential engineering material since its discovery in the early 1960's. This is because it has a good combination of mechanical properties, good castability and because it is cheaper to produce than forged steels. Its major use has been in the automotive industry, particularly for gears and camshafts. However, it has not been exploited to its full potential. One of the reasons is that it is a complex material. So, there is a need for a better and quantitative understanding of the metallurgical phenomena associated with ADI.

This thesis is about the development of models which predict aspects of the microstructure as well as mechanical properties as a function of chemical composition and heat treatment conditions. The models have been created using phase transformation theory and neural networks analysis. It has been proved that the T_0 concept which is based on thermodynamics, successfully reveals key and useful features of the microstructure. In the same way, kinetic theory has been used to model the precipitation of cementite from austenite. The uncontrolled precipitation of carbides can result in a deterioration in the mechanical properties.

The neural network technique within a Bayesian frame work has been used to create a suit of models which allow the selection of appropriate chemical composition and optimum procedure for the austempering heat treatment of existing and new ductile irons. This is helpful to meet required level of mechanical properties for specific applications.

A correlation between the model which predicts elongation, and the one for Charpy toughness was found. This is in general not common in wrought metals or weld metal and strongly suggests that results from un-notched samples, as commonly used in ADI, do not give a real measure of toughness, but a measure of ductility.

This work also includes a novel ultra-low temperature austempering treatment for ADI. This heat treatment which was defined from the T_0 concept, have proved to produce high volume fractions of ultra fine bainitic ferrite and very thin films of retained austenite. This microstructure has already been obtained in steels giving rise to strength levels up to 2.5 GPa. In ADI, however, the presence of second phase particles induce cleavage fracture under tensile strength, but in compression tests, strength levels over 2.3 GPa are observed. Reduction of the second phase particles volume fraction should be considered in future experiments. This would improve the mechanical properties of this ultra-low austempering process.

Contents

1	Introduction	1
1.1	Introduction to Austempered ductile irons	1
1.2	Cast irons	2
1.3	Austempered Ductile Iron	6
1.3.1	Typical chemical composition	7
1.3.2	The heat treatment	7
1.3.3	Cooling rate during quenching	8
1.4	Microstructure of ADI	9
1.4.1	Upper bainite	9
1.4.2	Lower bainite	9
1.4.3	Austenite	9
1.4.4	Martensite	10
1.4.5	Carbides	10
1.5	The processing window	10
1.5.1	Segregation	11
1.6	Mechanical properties	12
1.7	Applications of ADI	14
2	Experimental Procedures	16
2.1	Introduction	16
2.2	Material	17
2.3	Heat treatments	17
2.3.1	Furnace heat treatments	17
2.3.2	Thermomechanical simulator heat treatments	17
2.4	Hardness measurements	21
2.5	Optical microscopy	21
2.5.1	Heat tinting	21
2.6	Scanning Electron Microscopy	21
2.7	Transmission electron microscopy	22
2.7.1	Thin foil preparation	22

2.7.2	Extraction replica preparation	22
2.7.3	Camera constant	23
2.8	X-ray diffraction	25
3	Characterisation of ADI	28
3.1	Introduction	28
3.1.1	Microanalysis	28
3.2	Chemical segregation	28
3.3	Austempering of samples	29
3.4	Optical microstructure	33
3.5	Hardness	38
3.6	X-ray Diffraction	38
3.7	Transmission electron microscopy	43
3.7.1	Thin foils	43
3.7.2	Carbon extraction replicas	43
3.8	Dilatometry	48
3.9	Discussion of results	48
3.10	Summary	52
4	Neural Network Modelling	53
4.1	Introduction	53
4.2	Neural Networks	53
4.3	Error Estimation	55
4.4	Overfitting	57
4.5	Model Development Procedure	58
4.6	Interpretation	58
5	Neural Network Model of Retained Austenite	60
5.1	Introduction	60
5.2	The variables	61
5.3	Analysis	65
5.4	Application of the model	65
5.4.1	Carbon	67
5.4.2	Silicon	69
5.4.3	Manganese	69
5.4.4	Molybdenum, copper and nickel	70
5.4.5	Austenitising conditions	72
5.4.6	Austempering conditions	73
5.4.7	Segregation effects	73

5.4.8	Contour plots	74
5.5	Conclusions	74
6	Physical Model for Retained Austenite	76
6.1	Introduction	76
6.2	The T_0 concept	76
6.3	Carbon in lower bainite	80
6.4	Predictions of $V_{\gamma_r}^{\max}$ using the model	81
6.5	Discussion	83
6.6	Summary	84
7	Physical Model of Carbide Precipitation	85
7.1	Introduction	85
7.2	Nucleation and Growth Transformation	85
7.3	Classical Theory of Nucleation in Solids	85
7.4	Free energy change during nucleation	87
7.4.1	Heterogeneous Nucleation	89
7.5	Overall Transformation Kinetics	89
7.6	The Model	91
7.6.1	Nucleation of cementite	91
7.6.2	Overall Transformation Kinetics	94
7.7	Predictions	95
7.7.1	Effect of Manganese	96
7.7.2	Effect of Silicon	96
7.8	Summary	98
8	Neural Network Models for Mechanical Properties	99
8.1	Introduction	99
8.2	Vickers Hardness Model	99
8.2.1	The variables	100
8.2.2	Characteristics of the model	101
8.2.3	Application of the model	102
8.3	Ultimate Tensile Strength, Yield Strength and Elongation Models	106
8.3.1	Predictions using the model	106
8.3.2	Contour plots	108
8.4	Charpy Toughness Model	113
8.5	The processing window	119
8.6	Summary	122

9 Ultra Low Temperature ADI	123
9.1 Introduction	123
9.2 Previous work	123
9.3 Experiments	124
9.4 Vickers hardness	125
9.5 Microscopy	126
9.6 X-ray diffraction	127
9.7 TEM	128
9.8 Tensile test	128
9.9 Summary	134
10 Summary and Future Work	135

NOMENCLATURE AND ABBREVIATIONS

a	Lattice parameter
c	Speed of light in vacuo
d	Interatomic spacing along a specific crystallographic orientation
e^{-2m}	Temperature factor
eV	Electron volt
h	Hidden unit
h	Planck's constant
k	Boltzmann constant
k_A	Avrami parameter
m	Electron mass
n	Time exponent in Avrami equation
p	multiplicity factor
r	Radius
r^*	Critical radius for a viable nucleus
t	Time
t_1	End of stage I in the austempering process
t_2	Beginning of stage II in the austempering process
t_{min}	Minimum time in the processing window
t_{max}	Maximum time in the processing window
t_A	Austempering time
t_γ	Austenitising time
v	Volume of unit cell
v_τ	Volume of a particle nucleated at time τ
x	independent variable or input
\bar{x}	carbon concentration of a cast iron
x_γ	Carbon concentration of austenite
x_N	Normalised value of the variable in database
$x^{\gamma\theta}$	carbon concentration in γ in equilibrium with θ
$x^{\theta\gamma}$	carbon concentration in θ in equilibrium with γ
x_{T_0}	Carbon concentration given by the T_0 curve
y	Dependent variable or output
w	weights or coefficients of the function y
Ae_1	Temperature separating the α and $\alpha+\gamma$ phase fields for a specific alloy
Ae_3	Temperature separating the $\alpha+\gamma$ and γ phase fields for a specific alloy
B_S	Bainite start temperature
D	Carbon diffusion coefficient in γ

F	Structure factor
G	Free energy
G^*	Free energy barrier to nucleation
G_γ	Free energy for γ
G_θ	Free energy for θ
ΔG	Free energy change
ΔG_n	Driving force for nucleation per mole
ΔG_v	Chemical driving force for nucleation per unit volume of nucleus
E_D	Error between predicted and measured values
I	Nucleation rate per unit volume
$I_{\alpha(hkl)}$	Integrated intensity from a given (hkl) of ferrite
$I_{\gamma(hkl)}$	Integrated intensity from a given (hkl) from the γ phase
L	Camera length
L	Individual model in models committee
L_p	Lorentz-polarization factor
M_S	Martensite start temperature
N_0	Initial number density of sites
Q	Activation energy (for diffusion or nucleation)
R	Distance between transmitted and diffracted electron beams
R	Molar gas constant
T	Temperature
T_0	Temperature at which γ and α of the same composition have the same free energy.
T_γ	Austenitising temperature
T_A	Austempering temperature
V	Volume fraction
V^θ	Volume fraction of θ
V_e^θ	Extended volume fraction of θ
V_{α_b}	Volume fraction of bainitic ferrite
V_γ	Volume fraction of residual austenite
V_{γ_r}	Volume fraction of retained austenite
V_m	Molar volume
α	Ferrite
α'	Martensite
γ	austenite
ϵ	Epsilon carbide
λ	Electron wavelength
σ	Error bar calculated using Bayesian statistics
σ	Interfacial energy per unit area
σ_ν	Inferred noise level in predictions
σ_w	Perceived significance of an input parameter

σ_{UTS}	Ultimate tensile strength
σ_y	Yield strength
θ	Bragg angle
θ	Cementite
θ	Additional constant
τ	Tau carbide
τ	Incubation time
ν	Rate at which post critical nuclei can form
χ	3-dimensional parabolic growth constant
ξ	Normalised volume fraction
ζ	Fraction of transformation of a phase
ADI	Austempered Ductile Iron
ASTM	American Society for Testing and Materials
BCIRA	British Cast Iron Research Association
EDS	Energy Dispersive Electron X-ray Spectroscopy
CE	Carbon Equivalent value
HB	Brinell Hardness
HV	Vickers Hardness
LDP	Log predictive error
MTDATA	Metallurgical and Thermodynamic Data Service
N	$\sqrt{h^2 + k^2 + l^2}$ where h , k and l are plane indices
SEM	Scanning Electron Microscopy
SGTE	Scientific Group Thermodata Europe
SPEED	Selective Etching Electrolytic Dissolution
TEM	Transmission Electron Microscopy
UTS	Ultimate Tensile Strength
Y	Yield strength
ZAF	Atomic number, absorption and fluorescence correction factors in microanalysis

Chapter 1

Introduction

The aim of this chapter is to provide a brief background to austempered ductile irons and the characteristics of this material which are important in understanding the subject.

1.1 Introduction to Austempered ductile irons

Austempered ductile iron (ADI) has a microstructure containing spheroidal graphite embedded in a matrix which is in general a mixture of phases. Of these, bainitic ferrite and austenite are the most desirable phases, but in many cases small amounts of martensite and/or carbides may also be present in the microstructure. The bainitic ferrite is generated during isothermal transformation of austenite at temperatures below the bainite-start (B_S) temperature; this heat treatment is known as “austempering”. An optimum combination of high-carbon austenite and bainitic ferrite confers excellent mechanical properties to such cast irons. The proportions of phases change with the chemical composition and heat treatment, making it possible to produce a family of ADIs. This in turn allows a wide range of applications with ADI competing favourably against steel forgings and aluminium alloys in terms of mechanical properties, manufacturing cost, physical properties, and weight saving [1]. However, much of the development work on ADI has been empirical with the testing of a large number of samples. It is therefore not clear whether the best procedures are currently in place.

The large concentration of silicon typically present in graphitic cast irons has a key role in the development of the microstructure of austempered irons. The silicon hinders the precipitation of carbides during the bainite transformation [2]. The austempering time must ensure that the formation of bainitic ferrite adequately enriches the residual austenite with carbon, allowing much of it to be retained to room temperature. Unfortunately, prolonged austempering causes the decomposition of the residual austenite into a mixture of carbides and ferrite [3]. This has a detrimental effect on the mechanical properties.

Although ADI was developed during the early 1960's, it could, to some extent still be considered as a new material. This is because despite the huge number of papers

and research dedicated to ADI, many of them deal with the routine characterisation of microstructure and mechanical properties with a view to optimising processing. Others consider the role of chemical segregation, and the effect of specific alloying elements. However, a lot less are committed to the application or development of basic theory of phase transformations, for the benefit of ADI. In addition, little attention has been dedicated to developing physical or empirical models which allow a quantitative estimation of the microstructure and mechanical properties.

Since ADI is a complex material, it is not easy for industry to exploit the potential market in different areas, and only specialised parts have been developed using the trial and error method. Models can be of great help since they reduce the exhausting number of trial and error experiments and can be useful in the design of new products for brand new applications.

The purpose of this research was to develop quantitative models which allow the estimation of the microstructure and mechanical properties of austempered ductile irons as a function of their chemical composition and heat treatment conditions.

1.2 Cast irons

Although the focus of the work in this thesis is on austempered ductile iron, a brief introduction to cast irons in general is useful since ADI emerged as a new member of the family during the 1960's. The list of cast irons is big and this section describes only the most important ones.

Cast iron is an Fe-C-Si alloy that often contains other alloying elements and is used in the as-cast condition or after heat treatment. Cast irons offer a virtually unique combination of low cost and engineering versatility. The low cost, together with castability, strength, machinability, hardness, wear resistance, corrosion resistance, thermal conductivity, and damping makes them excel even amongst casting alloys [4]. The different types vary from grey iron, which is machinable, to white iron which is not easily machinable. The white irons of suitable composition can be annealed to give malleable cast iron to improve ductility. A simple classification of cast irons is shown in Fig. 1.1. This is based on the form of graphite and the type of matrix structure in which it is embedded [5].

Two factors determine the microstructure (white, ferritic gray, pearlitic gray, etc.) a cast iron will have on solidification. These factors are chemical composition and cooling rate. Fig. 1.2 is a schematic diagram of the effect of carbon and silicon concentrations, and of cooling rate on the microstructure of cast irons [6]. Fig. 1.2 shows that an increase in cooling rate decreases the tendency to form graphite. An increase in the carbon or silicon concentration on the other hand, promotes graphitisation. These observations lead to the definition of a carbon-equivalent value (CE) which is an index that indicates the combined effect of elements such as silicon and phosphorus in terms of the influence of

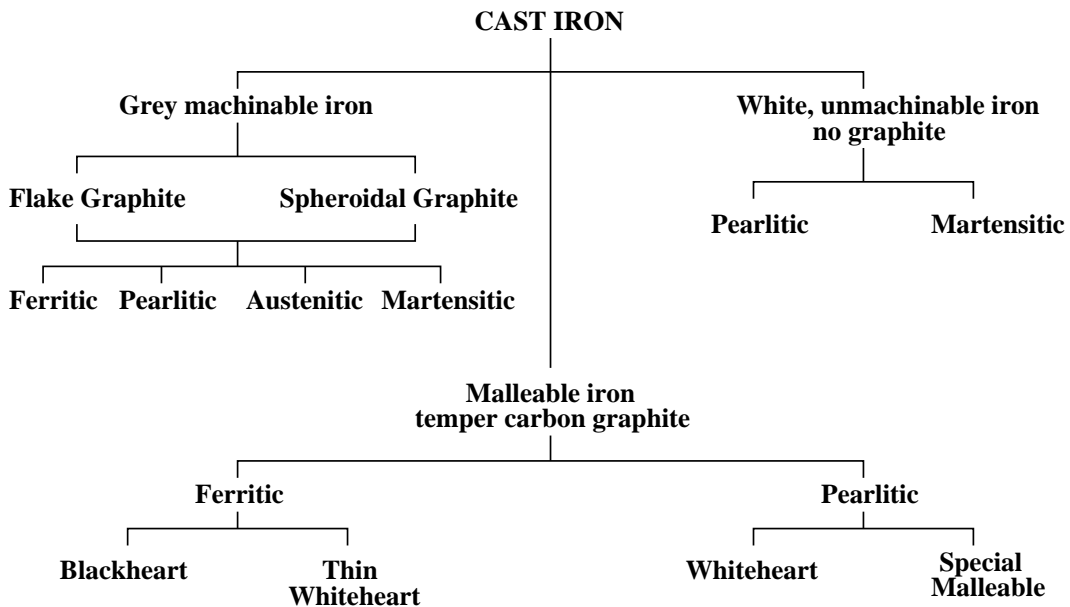


Figure 1.1: Classification of Cast iron [5]

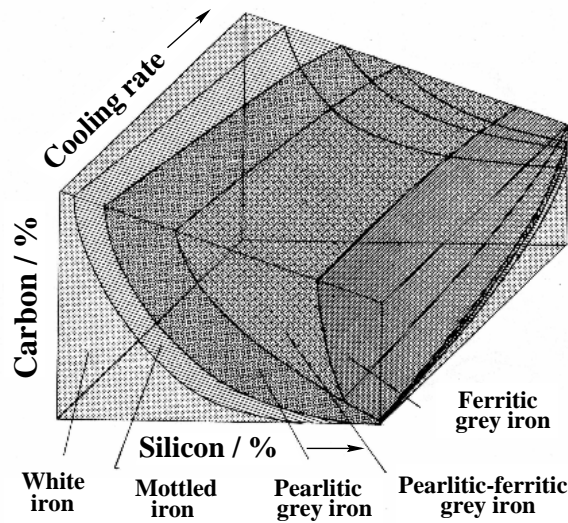


Figure 1.2: The effect of cooling rate and chemical composition on the microstructure of cast iron. Mottled cast irons is a mixture of the white and the gray cast iron microstructures [6]

carbon. [5] (Fig. 1.3). As the carbon content or CE is reduced below 4.3 wt%, there is a progressive decrease in the amount of graphite, until a mottled or white iron is reached:

$$CE(\text{wt}\%) = C + \frac{(Si + P)}{3} \quad (1.1)$$

For a given cooling rate, the carbon equivalent value (CE) determines how close a given

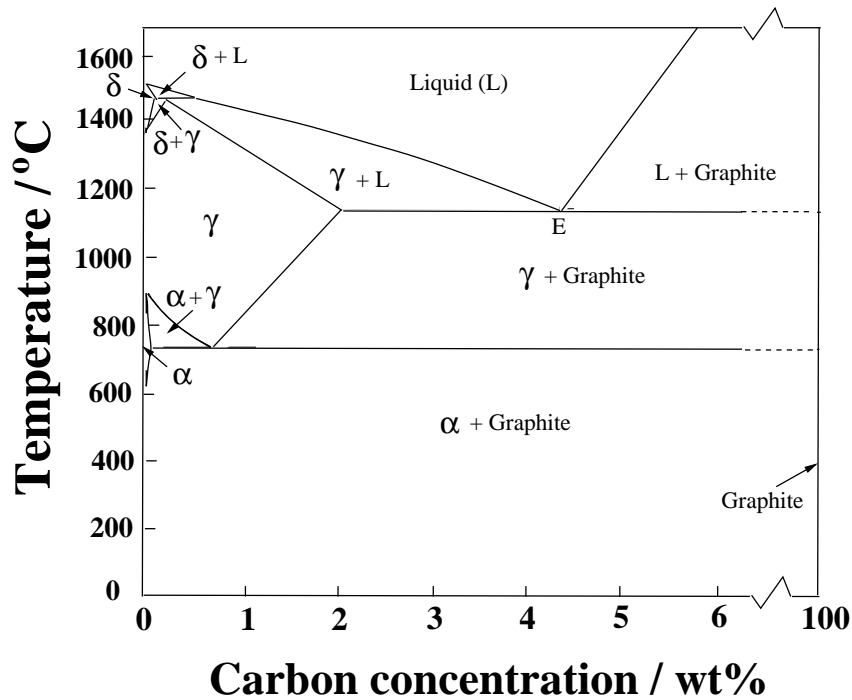


Figure 1.3: The iron-carbon phase diagram. The eutectic point, labelled as “E”, corresponds to a carbon content of 4.3 wt%

composition of iron is to the eutectic in the Fe-C phase diagram ($CE=4.3$) and therefore how much free graphite is likely to be present.

Thus, if the cast iron has a CE sufficiently below the eutectic value, possibly because of a low silicon content, appreciable quantities of carbide-stabilising elements, or if the cooling rate is sufficiently rapid, graphite is suppressed. The microstructure then consists of primary dendrites of pearlite with interdendritic areas of transformed ledeburite, which is a eutectic mixture of iron carbide and pearlite known as white cast-iron [7] Fig. 1.4a. The cementite in white cast irons can be induced to decompose into graphite by prolonged annealing at high temperatures. The final microstructure following heat treatment consists of graphite distributed in a matrix of ferrite or pearlite. The resulting alloy is called malleable cast iron [6] which for many applications has better mechanical properties than white cast irons which are brittle and hard Fig. 1.4b.

The most common type of cast iron with more than 34 million tons produced in 1999 [8] is grey cast iron. Flakes of graphite form during solidification and the austenite undergoes a eutectoid decomposition into pearlite [6] Fig. 1.5a.

The shape of the graphite precipitated during solidification can be modified markedly. The addition of minute quantities of magnesium or cerium poisons preferred growth di-

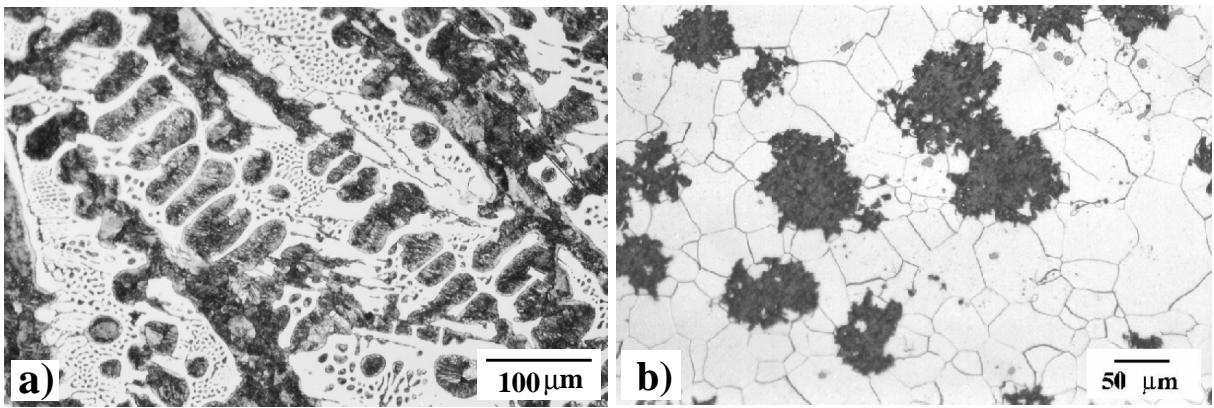


Figure 1.4: Microstructure of a) white cast iron, Fe-3.6C-0.1Si wt%, dendrites of pearlite (from pro-eutectoid austenite) surrounded by areas of pearlite and Fe_3C , b) malleable cast iron produced by heating white cast iron at 900-950°C for many days before cooling slowly. This results in a microstructure containing irregular though equiaxed nodules of graphite in a ferritic matrix. Etchant: 2% nital.

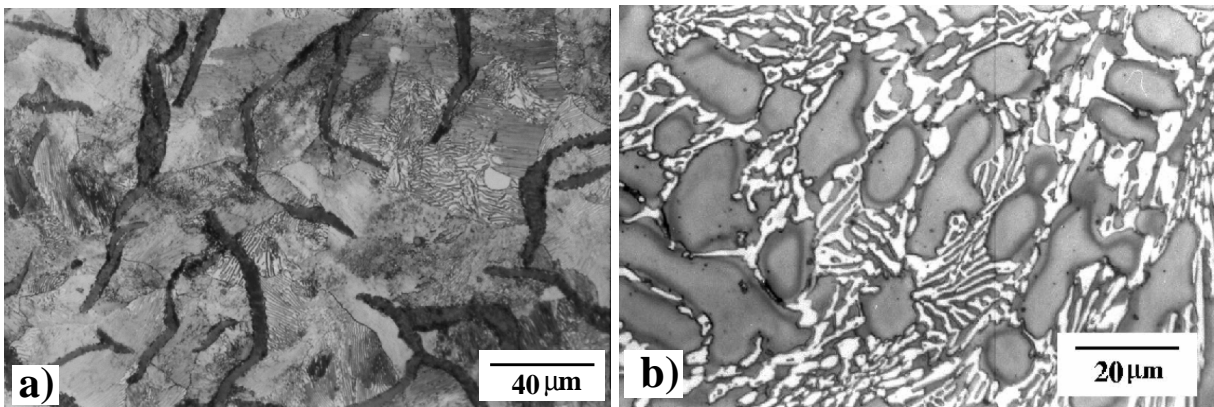


Figure 1.5: Microstructure of grey cast iron, Fe-3.2C-1.1Si wt%, containing graphite flakes in a matrix which is pearlitic. Etchant: Nital 2%, b) wear-resistant high-chromium cast iron, Fe-2.6C-17Cr-2Mo-2Ni wt%. The white phase is a chromium-rich known as M_7C_3 . The matrix consists of dendrites of austenite [9]. Etchant: Villela's reagent.

rections and leads to isotropic growth resulting in spheroids of graphite. This change in graphite shape gives an increase in ductility 5 to 20 times greater than grey cast iron [10]. In addition, as established by Flinn and Kraft [10], the mechanical properties of spheroidal graphite cast irons are determined largely by the matrix, which may be ferritic, pearlitic or a mixture of both as shown in Fig. 1.6a.

Spheroidal graphite cast irons usually have a pearlitic matrix Fig. 1.6b or a mixture of ferrite and pearlite. However, annealing causes the carbon in the pearlite to precipitate on the existing graphite or to form further small graphite particles, leaving behind a ferritic matrix that gives the iron even greater ductility (Fig. 1.7a).

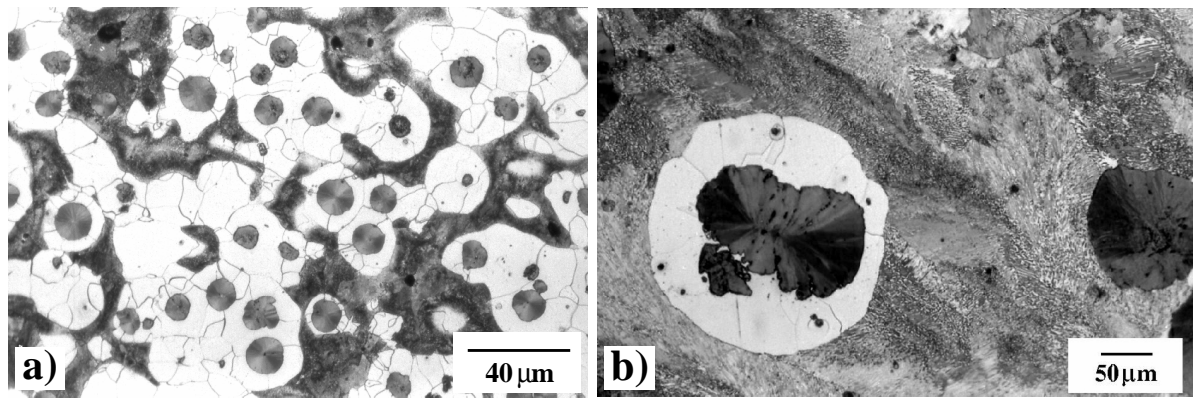


Figure 1.6: Microstructure of a) spheroidal graphite cast iron as-cast, Fe-3.5C-2.5Si-0.5Mn-0.15Mo-0.31Cu-0.042Mg wt%. Nodules of graphite, pearlite (dark islands) and ferrite (light background), b) spheroidal graphite cast iron as-cast, Fe-3.2C-2.5Si-0.05Mg wt% containing graphite nodules in a matrix which is pearlitic. One of the nodules is surrounded by ferrite, simply because the region around the nodule is decarburised as carbon deposits on the graphite. Etchant: Nital 2 wt%.

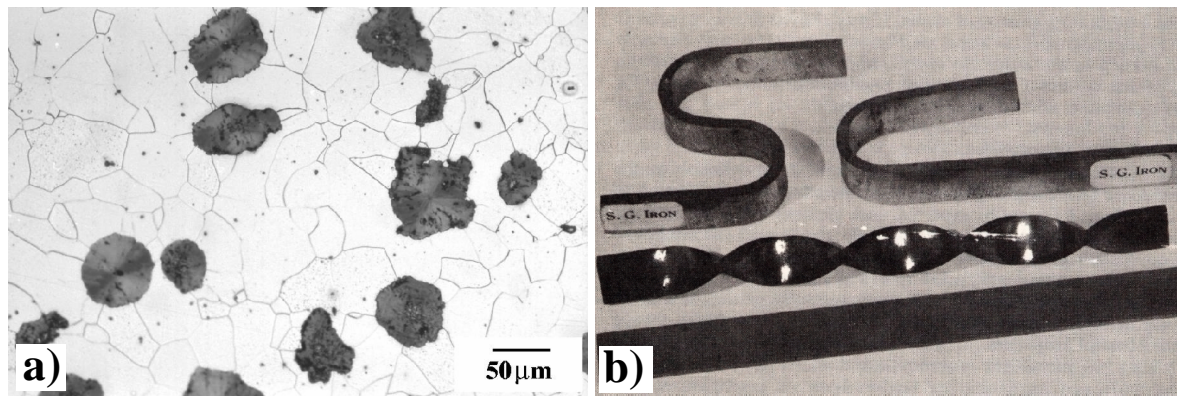


Figure 1.7: Microstructure of a) the same as Fig. 1.6b but annealed. Graphite nodules in a ferritic matrix. Etchant: Nital 2 wt%, b) an illustration of the ductility of spheroidal graphite cast iron [11].

1.3 Austempered Ductile Iron

Since the mechanical properties of spheroidal graphite cast iron depend essentially on the matrix, further enhancements might be achieved by improving the matrix microstructure. The austempering process is an isothermal heat-treatment in the bainitic transformation range, usually 250-450°C. This results in austempered ductile cast iron, with twice the strength of spheroidal graphite cast irons at the same level of toughness and ductility [12]. ADI also has advantages over other materials such as cast or forged steels. This is because ADI has good castability, lower processing cost, higher damping capacity, and a 10% lower density. These characteristics, along with the wide range of mechanical properties that can be achieved via the austempering process, makes ADI competitive for many applications where wrought steels have dominated in the past.

1.3.1 Typical chemical composition

ADI nominally has the chemical composition Fe-3.6C-2.50Si-0.5Mn-0.05Mg wt.%, but a variety of other additions may be made. It is common to see additions of elements such as Mo, Ni and Cu. One reason for alloying is to suppress the pearlite reaction so that the austenite can transform into bainite. Other elements such as chromium and vanadium may be added also to improve hardenability [13]; However, this is not common since these are strong carbide-forming elements.

Manganese is a strong promoter of hardenability and its addition is useful to prevent pearlite formation in thick cast-sections. However, manganese strongly segregates in the intercellular areas between nodules of graphite, causing the precipitation of carbides [14]. It is therefore advisable to keep its average concentration in the range 0.25 to 0.5 wt% [15, 16].

Apart from carbon, molybdenum is the most potent hardenability enhancer in ADI (about 1.6 times more than Mn) [3]. However, like manganese, it segregates at cell boundaries during solidification to form carbides [17], so its concentration is usually limited to less than 0.3 wt% [16, 12, 14].

Nickel and copper do not segregate as much as Mn and Mo, and in any case, they partition preferentially into the solid phase [14]. They do not significantly affect the hardenability, but when combined with manganese or molybdenum, there is a useful increase in the maximum section size that can be austempered successfully [3]. Additions of nickel may vary from 0.5 to 3.5 wt%, whereas Cu varies from 0.5 to 1.0 wt%.

There are three important points to consider when selecting the chemical composition of ADI [18];

1. The iron should be sufficiently alloyed to avoid transformation to pearlite, but not over-alloyed to avoid the retardation of the bainite transformation.
2. The microstructure should be free from intercellular carbides and phosphides.
3. The tendency for chemical segregation should be minimised for the sake of uniformity in the cast component.

It has been claimed [3] that small additions of multiple alloying elements are more effective in promoting hardenability than large amounts of individual alloying elements.

1.3.2 The heat treatment

The austempering process consists of two stages:

1. Austenitisation. The cast component is heated to temperatures between 850 and 950°C for 15 min to 2 h. In contrast to steels, the austenitising temperature determines the matrix carbon content because the graphite nodules serve as a source

or sink for carbon and because the solubility of graphite in austenite increases with temperature.

2. Austempering. After austenitising, the cast component is quenched into a salt bath at a temperature in the range 450-250 °C, usually for 0.5 and 3 h, followed by cooling to room temperature.

The temperature of the isothermal transformation is lower than that associated with pearlite but greater than the martensite-start temperature. The heat-treatment produces different types of bainitic microstructures, depending on the temperature and time of treatment. An isothermal transformation diagram of the austempering heat treatment cycle is shown in Fig. 1.8

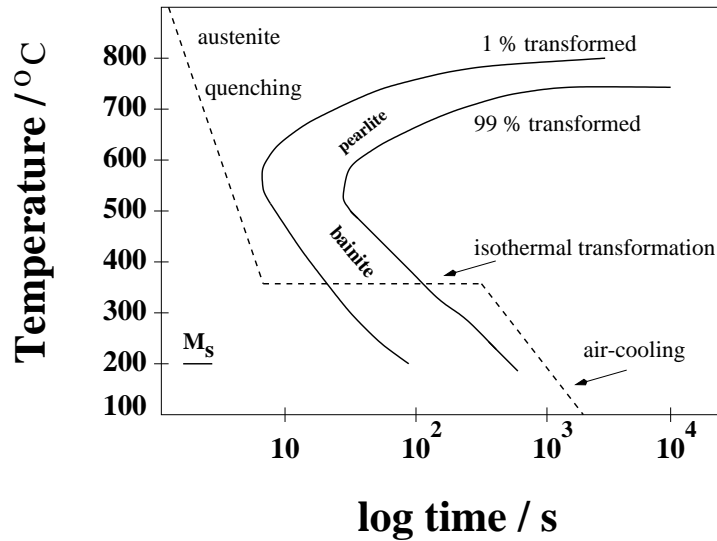


Figure 1.8: Isothermal transformation diagram for an unalloyed spheroidal iron Fe-3.5C-2.5Si-01Mn-0.045Mg wt% with superimposed temperature-time plot typical of an austempering treatment.

1.3.3 Cooling rate during quenching

The rapid reduction of temperature from the austenitising temperature to the austempering temperature is achieved when the component is placed in the austempering medium. The cooling rate during this stage is of importance since it determines the matrix microstructure of the ductile iron which is to be austempered. A slow quench will tend to produce pearlite; this might occur in large-section casting where the central sections experience lower cooling rates compared with the outer regions. Manganese is often added to reduce the rate of pearlite formation during cooling and hence to allow larger castings to be produced. The degree to which bainite can be obtained during the isothermal heat-

treatment whilst avoiding pearlite or martensite is known as the ‘bainitic-hardenedability’ of an alloy.

1.4 Microstructure of ADI

The austempered microstructure that optimises ductility is a mixture of bainitic ferrite and high-carbon retained-austenite. Other constituents include martensite, carbides and pearlite, all of which tend to reduce ductility. It is difficult during normal processing to avoid these constituents completely, since the composition of the component is rarely uniform.

1.4.1 Upper bainite

Upper bainite consists of fine ferrite plates, each of which is about $0.2 \mu\text{m}$ thick and about $10 \mu\text{m}$ long [19]. The plates grow in clusters called sheaves. Within each sheaf the plates are parallel and of identical crystallographic orientation, each with a well-defined crystallographic habit. The individual plates in a sheaf are often called the ‘sub-units’ of bainite. They are separated by low-misorientation boundaries or cementite particles in the context of conventional steels [19]. Cementite is not found in austempered ductile iron, or in high-silicon steels. It is replaced by films of carbon-enriched austenite with or without some metastable carbides such as ϵ or Hägg depending on the chemical composition and heat-treatment conditions [19, 20].

1.4.2 Lower bainite

Lower bainite is the predominant morphology in cast irons transformed below 330°C [21]. It has a microstructure and crystallographic features which are similar to those of upper bainite. The major distinction is that the transformation is at lower temperature so that carbides can also precipitate inside the plates of ferrite. There are, therefore, two kinds of carbides: those which may grow from the carbon-enriched austenite, and others which precipitate inside the supersaturated bainitic ferrite (Fig. 1.9). In conventional steels these carbides are cementite but in high-silicon steels and in ADI they could be ϵ or other transition carbides. The formation of this microstructure is substantially independent of austempering time and composition.

1.4.3 Austenite

Austenite is formed during the high temperature step of the heat treatment of ADI. The carbon content of this austenite changes as a function of the austenitising temperature. As a consequence of transformation to bainitic ferrite, the residual austenite becomes enriched with carbon. This reduces the driving force for further transformation [19]. The austenite

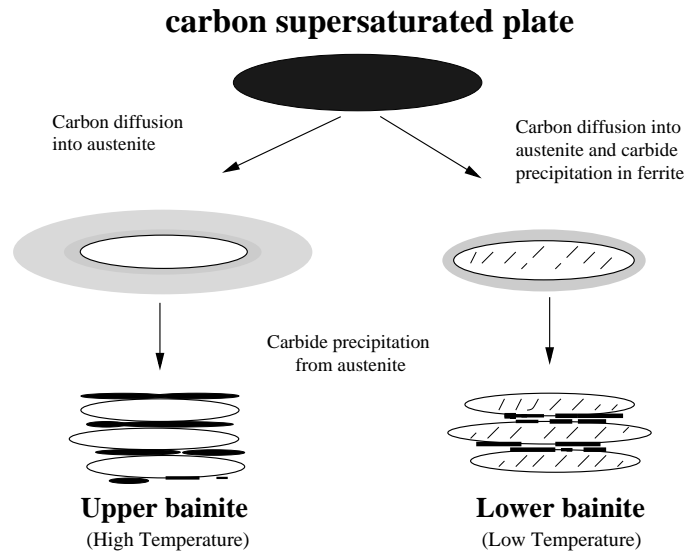


Figure 1.9: Mechanism of formation of lower and upper bainite [19].

that is left when the bainite transformation ceases is stabilised by the carbon enrichment and hence can be retained at room temperature. The volume fraction of retained austenite can be as high as 0.6 [22].

When discussing the microstructure, it is necessary to distinguish between *residual austenite*, which exists at the isothermal transformation temperature, and *retained austenite* which remains untransformed at ambient temperature.

1.4.4 Martensite

Some of the carbon-enriched residual austenite may transform into martensite on cooling to room temperature Fig. 1.10.

1.4.5 Carbides

It is silicon which hinders the precipitation of cementite in which it has a very low solubility [2]. Thus, transition carbides precipitate either in austenite or in bainitic ferrite depending on the chemical composition and heat treatment [23]. Prolonged austempering can cause the decomposition of the residual austenite into a mixture of carbides and ferrite [3]. This is detrimental to mechanical properties.

1.5 The processing window

The austempering process is conventionally defined in two stages [24]. The end of the first stage corresponds to the maximisation of the fraction of bainitic ferrite and the enrichment of the austenite, the second with the onset of carbide precipitation. The time interval be-

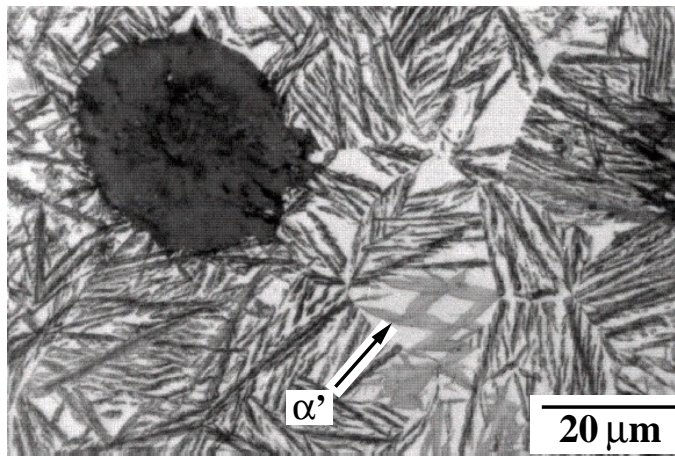


Figure 1.10: Microstructure of ADI showing graphite, and a mixture of upper bainitic ferrite (dark sheaves), retained austenite (light phase), and some martensite (α') inside retained austenite area.

tween these two stages is the heat treatment window (Fig. 1.11). During this interval, only minor changes in the morphology and composition of the ferrite and stabilised-austenite microstructure take place [3]. The extent of this heat-treatment window depends on many factors, including the chemical composition, segregation patterns, and the austempering and austenitising temperature [12]. Manganese has a strong effect and high contents of this element can effectively shrink or even eliminate the heat-treatment window due to overlap of stages I and II [25]. A closed processing window (Fig. 1.11) means that the optimum mechanical properties cannot be achieved due to the severity of the overlap. Martensite occurs in regions with less carbon-enrichment of austenite, and carbides in those regions where stage II has started prematurely because of chemical segregation.

1.5.1 Segregation

Most of the alloying elements segregate between the liquid and solid phases during solidification. This can strongly influence the processing window and, therefore, the mechanical properties. The distribution of alloying elements is related to the eutectic cell that forms around the nodules of graphite during solidification, and leads to a different response in transformation kinetics as a function of position. Three zones along the eutectic cell have been designated to illustrate the distribution of elements in ductile irons [26, 27] Fig. 1.12.

1. Zone I is located along the graphite. In this zone the silicon, nickel and copper levels are high but the manganese is depleted.
2. Zone II represents the greater part of the matrix where the change in solute concentration is more gradual.

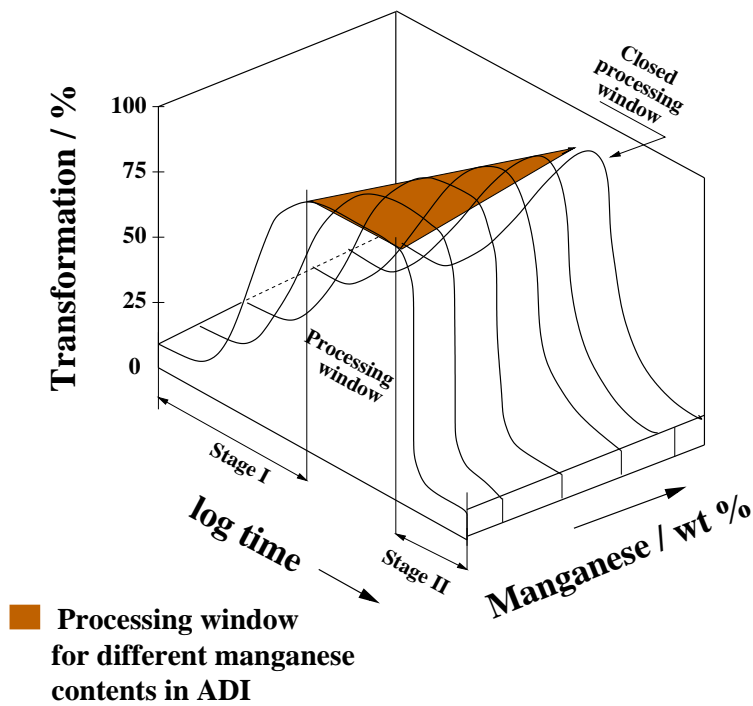


Figure 1.11: Schematic representation of the heat-treatment processing window and the influence of manganese.

3. Zone III is located at the solidification cell boundary. The silicon and copper levels are low but manganese, molybdenum, chromium and phosphorus are enriched.

1.6 Mechanical properties

Austempered ductile irons can have tensile strengths of up to 1700 MPa with about 1.7% elongation (Table 1.1) and high hardness, for applications in which wear resistance is of primary importance. Materials of lower hardness having tensile strengths between 900 to 1200 MPa and elongation of up to 16% can also be produced, for engineering applications where ductility is vital [15, 28]. For practical purposes, there are two types of ADI:

1. Class I: ductile irons transformed at low austempering temperatures exhibiting a lower bainite matrix. These irons have high hardness (≥ 400 HB) and strength, and are particularly desirable for gears and other applications requiring resistance to high contact stress.
2. Class II: ductile irons transformed at high austempering temperatures exhibiting upper bainite. These irons have hardnesses ranging from 260 to 350 HB. They combine high ductility and toughness with high fatigue strength and wear resistance. They are reasonably machinable and are commonly used in structural applications [29].

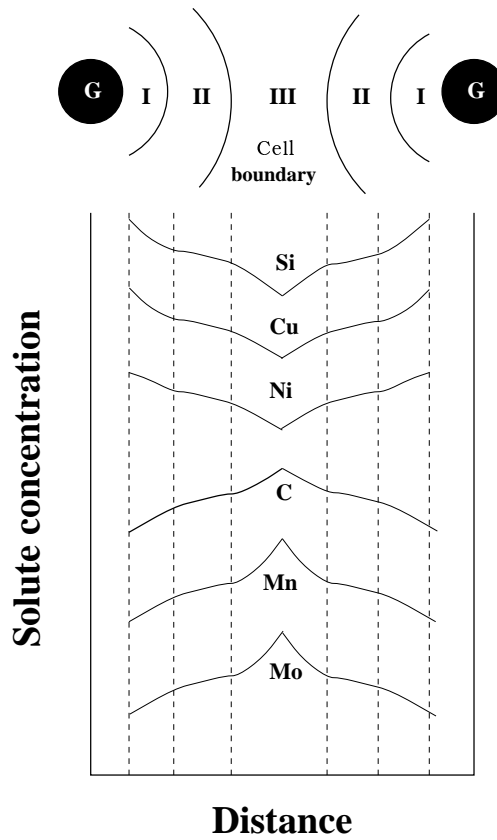


Figure 1.12: Solute segregation zones between adjacent graphite nodules.

It has been suggested that development of the unique combination of strength and ductility in ADI is a result of the presence of the relatively continuous high carbon austenite matrix [30].

Main elements wt. %	T_γ °C	t_γ min	T_A °C	t_A min	UTS MPa	Elongation %	Reference
3.6C-2.5Si-0.45Mn-0.75Ni-0.5Cu	871	90	260	90	1707	1.7	Kovacs, 1988
3.56C-2.63Si-0.15Mn-0.45Ni-0.44Cu	900	90	300	180	1602	1.7	Lin, 1996
3.44C-2.41Si-0.15Mn	898	120	302	120	1510	2.8	Putatunda, 1999
3.8C-2.6Si-0.25Mn-0.1Mo	897	60	297	60	1500	4	Takahashi, 1996
3.6C-2.7Si-0.2Mn-0.28Mo-0.6Ni-0.6Cu	970	60	343	60	1250	9	Stenfors, 1986
3.4C-2.95Si-4.83Ni	900	20	300	120	1352	10	Aoyama, 1996
3.56C-2.8Si-0.96Ni	900	30	375	30	1169	16.6	Varahraam, 1990

Table 1.1: Some examples of mechanical properties, UTS and elongation as a function of chemical composition and heat treatment conditions in ADI. T_γ = austenitising temperature, t_γ = austenitising time, T_A = austempering temperature, t_A = austempering time.

The British Standards specification (BS-EN-1564) for ADI is shown in Table 1.2 with minimum acceptable values. These values can be compared with data shown in Table 1.1.

Material identification	Number	Tensile strength MPa (min)	0.2% Proof stress MPa (min)	Elongation % (min)
EN-GJS-800-8	EN-JS1000	800	500	8
EN-GJS-1000-5	EN-JS11100	1000	700	5
EN-GJS-1200-1	EN-JS1120	1200	850	2
EN-GJS-1400-1	EN-JS1130	1400	1100	1

Table 1.2: British Standards specification for ADI BS-EN1564:1997

1.7 Applications of ADI

Before indicating some applications of ADI it is important to remember some physical characteristics, which combined with the mechanical properties of ADI, open the market for this material in many different industries, but particularly for automotive components.

1. Good castability and near net shape casting production of parts.
2. 10% lower density than steel.
3. Higher damping capacity than steel which makes the parts absorb energy 2-5 times more than steels, thereby reducing the level of noise to about 8-10 decibels in gear boxes [31, 32].

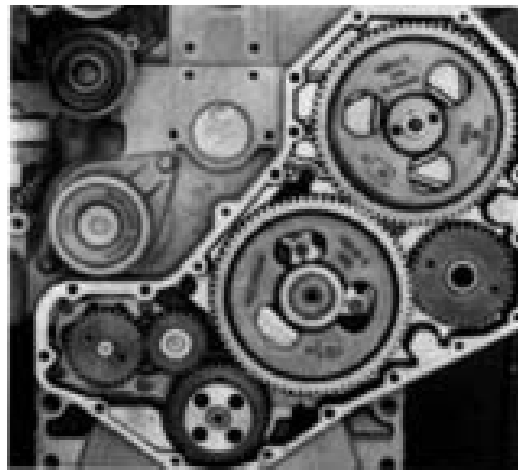


Figure 1.13: Timing gears for diesel engines. ADI has been chosen in preference to induction hardened AISI 4140 steel. These ADI gears were austempered at 238°C to give high hardness [33].

The combination of these characteristics with the austempering process creates a big family of ADIs which can compete with forging steels and even with aluminium parts [1], not only in the mechanical performance but also in the cost of production. Examples of applications are:

1. Automotive: crankshafts, camshafts, hypod pinion and ring gear pairs, and timing gears for diesel engines Fig. 1.13.
2. Heavy trucks: spring hangar brackets, “U”-bolt plates, pivot pins, clip plates, connecting-rods, engine mounts and gears.
3. Railroads: side bearing top caps, track plates, motor nose supports, pick-up arms, rail braces and suspension components.
4. Mining: sprockets, chains, chain guides, track trends, wear plates,
5. Pumps and compressors: impellers, valve bodies, compressor housings, gears and drilling heads.
6. Construction equipment: track guides, hydraulic cylinders, track shoes, adjustment cams, rock guards, pin covers, backhoe digger teeth, circle drive gears, bearing caps, and support arms

Since the potential of ADI is enormous, it is important to know all the mechanisms involved in the production of optimum ADI parts. This may give industry better tools to exploit the market which has for some time been reluctant to use ADI, partly due to the difficulties in controlling all the variables. The creation of physical and empirical models can contribute enormously in the improvement and design of new components.

Chapter 2

Experimental Procedures

2.1 Introduction

This chapter introduces the experimental procedures utilised to characterise austempered ductile irons studied. The experiments described were also used to validate models included in latter chapters. Fig. 2.1 is the general flow chart of experimental procedures.

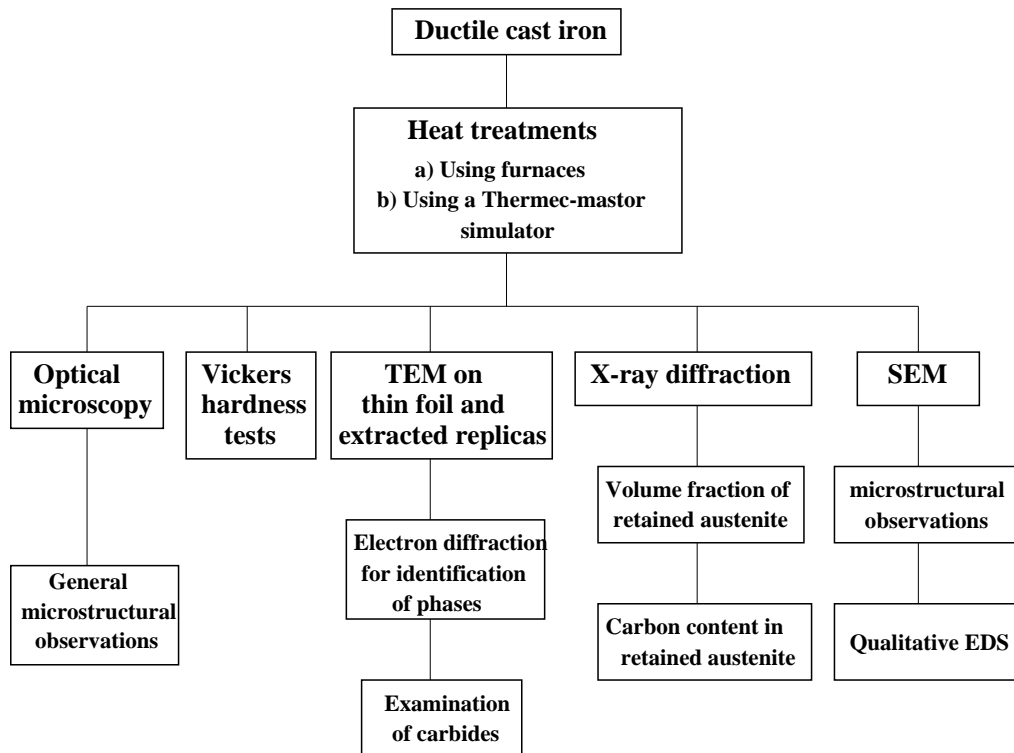


Figure 2.1: Flow chart illustrating the experimental programme for austempered samples. TEM: Transmission electron microscopy, SEM: Scanning electron microscopy, EDS: Energy dispersive X-ray Spectroscopy.

2.2 Material

A ductile cast iron produced in a commercial foundry using electric melting has been used for the experiments. Its chemical composition is Fe-3.55C-2.5Si-0.55Mn-0.15Mo-0.31Cu-0.042Mg wt%. Solid cylindrical specimens with dimensions 8 mm diameter and 12 mm length were machined from a keel block for heat treatment.

2.3 Heat treatments

2.3.1 Furnace heat treatments

All samples which required heat treatment in a furnace, either for homogenisation or for austempering, were sealed in quartz tubes under a partial pressure of argon to prevent oxidation. Homogenisation consisted of holding the samples at 1000°C for 3 days before quenching in water while breaking the quartz tubes. The calibration of furnaces used was verified before any heat treatment was performed to ensure accuracy in temperature measurements. This was done by placing a thermocouple in different points of the chamber, measuring the temperature with an external instrument, and comparing that temperature with the one of the furnace display. It was found that at the centre of the chamber, temperature was $\pm 2^\circ\text{C}$ different from the furnace display.

2.3.2 Thermomechanical simulator heat treatments

The “Thermecmastor Z” thermomechanical simulator, manufactured by Fuji Electronic Industrial Co. Ltd., is a laboratory machine capable of implementing specified thermal cycles on small samples, under accurate computer control. The temperature and diametrical dilatation of the specimen are measured and thus the progress of phase transformations within the material can be followed.

A solid cylindrical specimen with dimensions of 8 mm diameter and 12 mm length is placed vertically in the chamber (Fig. 2.2) between two silicon–nitride dies. The die holders are insulated from the dies by mica discs. The upper die can be raised and lowered using a hydraulic ram to hold the sample in position. A platinum / platinum–10% rhodium thermocouple is spot–welded to the specimen in a central position with the wires spaced approximately 1 mm apart. The accuracy of the temperature reading is $\pm 3^\circ\text{C}$ whilst the variation along the specimen length is no more than $\pm 10^\circ\text{C}$. The diametrical dilatation of the sample is monitored using a He-Ne laser beam, which moves and scans with the ram to ensure the same location on the sample is measured throughout the experiment. The beam is positioned at the same height as the thermocouple on the sample to ensure that the temperature and dilatation measurements are for the same location.

The accuracy of the dilatation reading is $\pm 1 \mu\text{m}$. The sealed chamber is then pumped

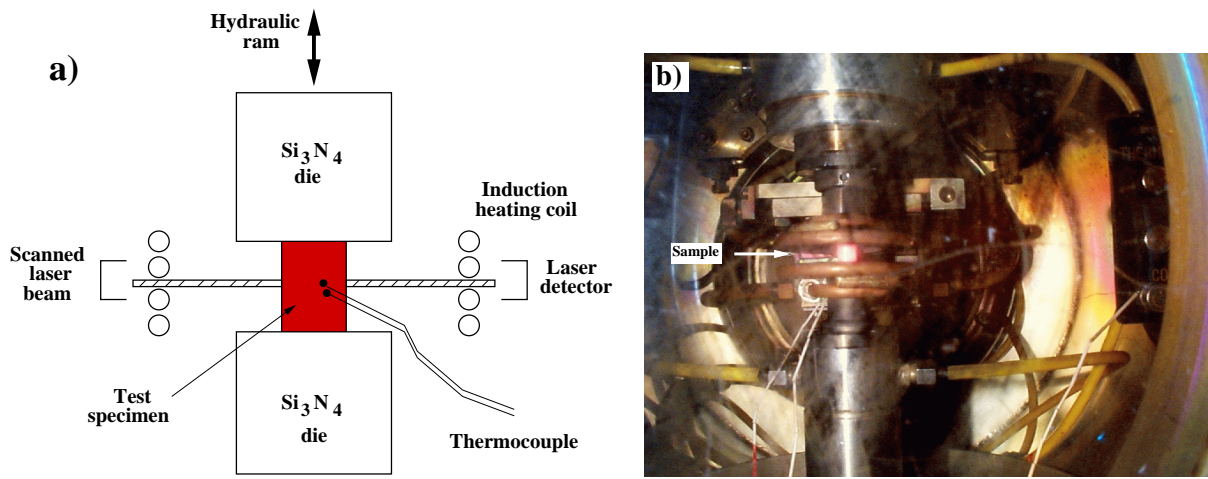


Figure 2.2: The arrangement of equipment within the *Thermecmator Z* thermomechanical simulator. The specimen is situated between Si_3N_4 dies, inside an induction coil. Temperature, dilatometric and load data can be simultaneously measured. (a) Drawing of the arrangement inside the chamber. (b) Photograph of the actual chamber.

out to a vacuum of $\approx 10^{-2}$ Pa to prevent oxidation of the specimen. An inert gas (argon) atmosphere can also be introduced if required. Heating is provided by a water-cooled, high frequency induction coil which surrounds the sample. Cooling can be controlled using gas (He or N_2) or water. Helium was used in all the experiments. Time, temperature and dilatation are recorded and can be stored on a computer for subsequent analysis.

The thermomechanical simulator was used to perform heat treatments at different austempering temperatures and times. The heat treatment cycle was as follows: The samples were heated at a rate of 10°C s^{-1} up to austenitising temperature of 950°C and held there for 15 min for homogenised samples, and for 30 min for non-homogenised samples. The cooling rate used from the austenitising temperature (950°C) to the austempering temperature was 100°C s^{-1} . Isothermal treatment range was $250\text{-}450^\circ\text{C}$ for different austempering times.

The presence of silicon in the range of 2-3 wt% which is common in ductile irons, significantly alters the Fe-C equilibrium diagram and its critical temperatures. It is then important to show that the austenitising temperature used in experiments falls within the austenite+graphite region for the present ductile iron. This is indicated in Fig. 2.3 with a spot in the γ +graphite field. Calculations using MTDATA (version 4.71) [34] for the present ductile iron were performed in order to show the thermodynamical values at austenitising temperature as obtained from MTDATA (Fig. 5.2). For these calculations the database *PLUS* for solutions was used, and the phases allowed at 950°C were graphite and austenite.

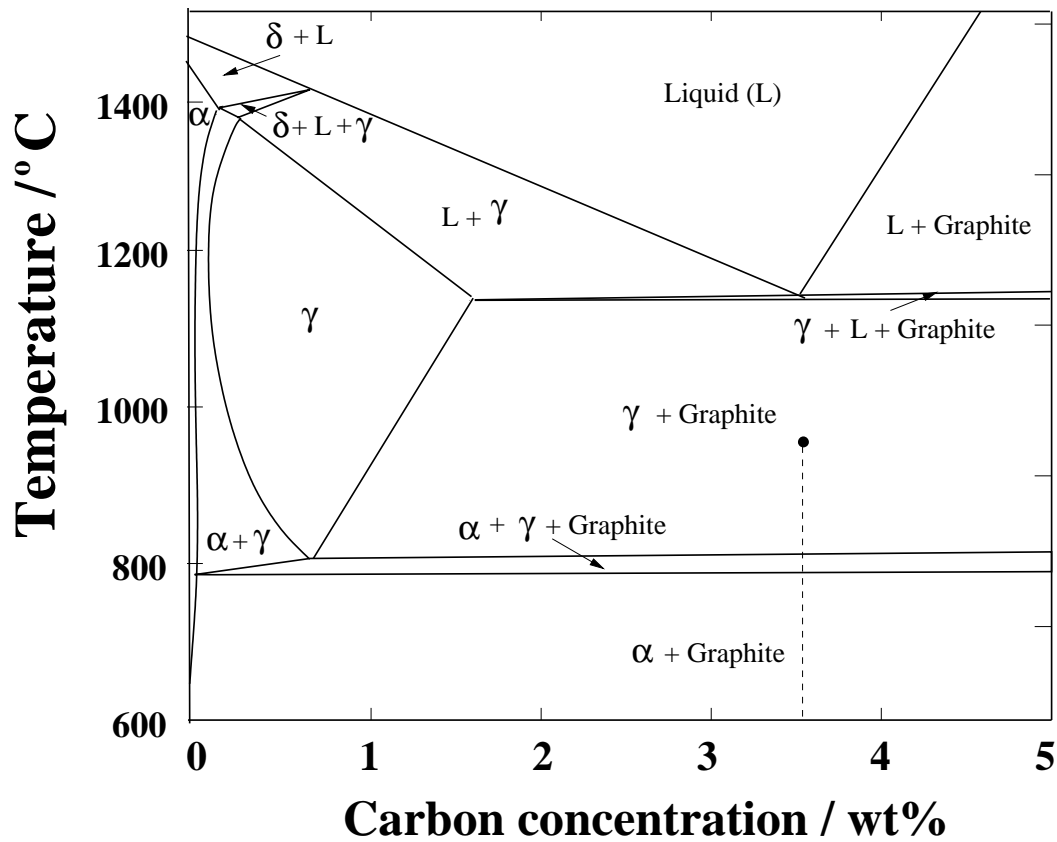


Figure 2.3: Phase diagram for Fe-C-2.5Si wt%. Calculated using MTDATA [34]. The spot in the $\gamma + \text{Graphite}$ field corresponds to the austenitising temperature for the ductile iron used in experiments. Note that this vertical section of the ternary phase diagram cannot be used to deduce equilibrium compositions since the tie lines do not necessarily lie in the plane of the diagram. The database used for these calculations was *PLUS* and the phases allowed were ferrite, austenite, liquid and graphite.

Temperature = 1223 K

Fixed pressure = 1.013250E+05 Pa, 1.00E+00 atm

	Amount mole	Mole fraction Notional activity
Phase GRAPHITE		
C<GRAPHITE>	2.1618E+00	1.000
Phase FCC_A1		
Fe:1 <FCC_A1>	1.6641E+03	0.4702013
C:2 <FCC_A1>	7.9379E+01	0.0224278
Si:1 <FCC_A1>	8.9013E+01	0.0251500
Mn:1 <FCC_A1>	1.0011E+01	0.0028286
Mo:1 <FCC_A1>	1.5634E+00	0.0004417
Cu:1 <FCC_A1>	4.8783E+00	0.0013783
Va:2 <FCC_A1>	1.6902E+03	0.4775722
Phase total is	3.5393E+03	1.0000000

Component	Chemical potential	Activity	Amount/mol	Mass/Kg
Fe	-6.005295E+04	2.723879E-03	1.6641E+03	9.294E+01
C	-1.862039E+04	1.602280E-01	2.9556E+02	3.550E+00
Si	-1.627601E+05	1.118538E-07	8.9013E+01	2.500E+00
Mn	-1.267985E+05	3.841853E-06	1.0011E+01	5.500E-01
Mo	-1.043985E+05	3.477162E-06	1.5634E+00	1.500E-01
Cu	-8.177524E+04	3.216969E-04	4.8783E+00	3.100E-01
Total			2.0652E+03	1.000E+02

Gibbs Energy = -1.2176247175E+08

Percentage distribution of components between phases

	Fe	Si	C
GRAPHITE	0.00	0.00	73.14
FCC_A1	100.00	100.00	26.85
	Mn	Mo	Cu
GRAPHITE	0.00	0.00	0.00
FCC_A1	100.00	100.00	100.00

Amount moles of component	Phase	Mole fraction of component within phase		
		Fe	Si	C
2.9556E+02	GRAPHITE	0.000000	0.000000	1.000000
2.9556E+02	FCC_A1	0.900031	0.048140	0.042929
		Mn	Mo	Cu
2.9556E+02	GRAPHITE	0.000000	0.000000	0.000000
2.9556E+02	FCC_A1	0.005414	0.000845	0.002638
Mass/ Kg	Phase	Mass fraction of component within phase		
		Fe	Si	C
2.9556E+02	GRAPHITE	0.000000	0.000000	1.000000
2.9556E+02	FCC_A1	0.954175	0.025666	0.009788
		Mn	Mo	Cu
2.9556E+02	GRAPHITE	0.000000	0.000000	0.000000
2.9556E+02	FCC_A1	0.005646	0.1540	0.003182

Figure 2.4: The output of MTDATA calculations for an Fe-2.5Si-0.55Mn-0.15Mo-0.31Cu wt% at 950 °C. Calculations were obtained by using the database *PLUS* for solutions allowing austenite and graphite phases.

2.4 Hardness measurements

A Vickers hardness testing machine with 10 kg load and $\frac{2}{3}$ " objective was used to measure the macro-hardness of the ductile iron as-cast, and of all austempered samples. The load was applied for 15 seconds during testing. Seven measurements were taken over the metallographic specimen area.

2.5 Optical microscopy

After heat treatment, the samples were prepared for metallographic analysis. From each specimen a slice of 6 mm length was cut and mounted in Bakelite. The newly formed surface was ground on SiC paper to 800 grit and polished with 1 μm cloth coated with diamond paste. The samples were etched using 2% nital (2% concentrated nitric acid in methanol solution).

2.5.1 Heat tinting

Since it is difficult even for the expert eye to identify the various phases in ADI on a black and white photomicrograph, a heat tinting technique [35] was used to reveal the manganese carbides. Heat tinting is an oxidation process to cause the various phases of ADI to appear in distinct colours. Unmounted ADI samples were prepared as for optical microscopy and etched with 2% nital. Then heated in an oven at about 260°C for 4h.

Optical micrographs were taken with a 35 mm camera attached to a *Leitz* microscope.

2.6 Scanning Electron Microscopy

A JEOL JSM-5800LV scanning electron microscope equipped with energy dispersive X-ray spectroscope (EDS) was used to get high magnification images, and to do chemical analysis on as-cast and heat treated specimens. Apart from fracture surface analysis on tensile samples which did not need any preparation, the other specimens were prepared in the same way as for metallographic observation. Samples were observed using secondary electrons at 15 kV. Light elements such as *B*, *C* and *O* were not included in the elemental quantification because elements with low atomic number are difficult to detect using EDS. This is because the outer surface of the EDS detector is normally protected by a window made of a polymer film to prevent contamination from condensing on the cold detector. The window absorbs low energy X-rays and so the signals from light elements cannot be detected by the EDS detector. Therefore, if any of these elements are present in the spectra, their values can only be used for comparison.

2.7 Transmission electron microscopy

Specimens for transmission electron microscopy (TEM) were prepared from selected samples using both ion-milling of thin foils and the carbon extraction replica technique.

2.7.1 Thin foil preparation

3 mm diameter discs 0.5 mm thick were mechanically polished using 800 grit silicon carbide paper to 100 μm thickness. A precision dimple grinder instrument was then used to reduce the thickness to about 30 μm at the centre of the discs. Finally, ion-milling with two argon ion guns was used for about 35 h, until a hole was observed. The angle between the ion beams and specimen was set to 10°. Ion milling was used instead of electro-polishing because of the extremely large difference in the electrochemical properties of graphite and the matrix. Transmission electron microscopy was conducted using a JEOL JEM-200CX electron microscope operated at 200 kV.

2.7.2 Extraction replica preparation

The extraction replica technique is very useful for the identification of carbide or precipitate phases in a metallic system. The main advantage of replicas over thin foil specimens is that they eliminate any effect due to the iron matrix and thus enable the chemical composition of the carbides to be determined more accurately. Working with a ferromagnetic specimen is also more difficult in the electron microscope because remanent or induced fields cause a deflection of the electron beam. The replica is very thin ≈ 10 nm, and has almost no self-structure.

Single-stage carbon extraction replicas were prepared using the method described by Brandon [36] from surfaces prepared as for optical microscopy but using the SPEED etching (selective etching by electrolytic dissolution) method to remove the matrix around the carbides [37]. The non-aqueous electrolyte solution used in the SPEED process consists of 10% acetyl acetone, 1% tetramethyl-ammonium chloride and methanol. A carbon coating of 20-30 nm (color blue-brown) was deposited in a vacuum of 10^{-5} torr on the etched specimens. The coated surfaces were then cut with a razor blade into 3 mm squares. The replicas were etched free from the specimens with a solution of 20% nitric acid in ethanol and were captured on 400 square mesh copper grids for examination in the TEM. Fig. 2.5 shows schematically the method for making carbon extraction replicas.

The extracted carbon replicas were examined using a JEOL JEM-200CX electron microscope operated at 200 kV.

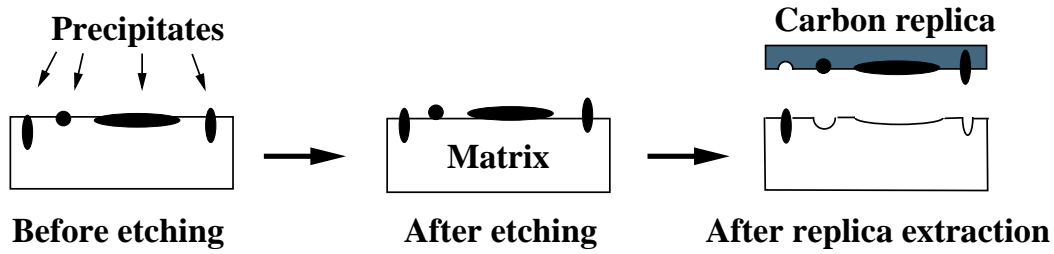


Figure 2.5: Schematic diagram illustrating the preparation of carbon extraction replicas

2.7.3 Camera constant

A TEM consists of electromagnetic lenses which amongst other things control the magnification of the diffraction patterns. The magnification of diffraction patterns is expressed as a camera length, as shown in Fig. 2.6

$$Rd_{hkl} = L\lambda = \text{Camera constant} \quad (2.1)$$

where R is the real distance between the transmitted spot and the diffracted spot, L is the camera length, d_{hkl} is the spacing of the $\{hkl\}$ crystallographic planes giving rise to the diffracted beam and λ the electron wavelength is calculated using following equation;

$$\lambda = \frac{h}{\sqrt{2meV(1 + \frac{eV}{2mc^2})}} \quad (\text{\AA}) \quad (2.2)$$

where h is Planck's constant, m and e are the electron mass and charge respectively, V is the accelerating voltage of the electrons and c is the speed of light in vacuum.

The camera constant was measured by examination of a diffraction pattern from gold sputtered on a copper grid, at 200 kV on the JEOL 200CX TEM. For a given electron beam direction a number of particles are oriented so as to satisfy the Bragg equation [38]. Hence each plane gives number of reflections lying on a cone of angle 4θ . The final diffraction pattern contains a number of concentric rings corresponding to the $\{hkl\}$ planes which are diffracting, as shown in Fig. 2.7.

To calculate the camera constant, the diameters of the rings in the diffraction pattern were measured, then the ratio between the squares of the radii of the outer rings to those of the first or second low-index ring were calculated. This enables the N values corresponding to each of the rings to be found using equation 2.3.

$$N^2 = h^2 + k^2 + l^2 \quad (2.3)$$

where h , k and l are the plane indices. Then d -spacings were calculated using equation 2.4 for cubic systems:

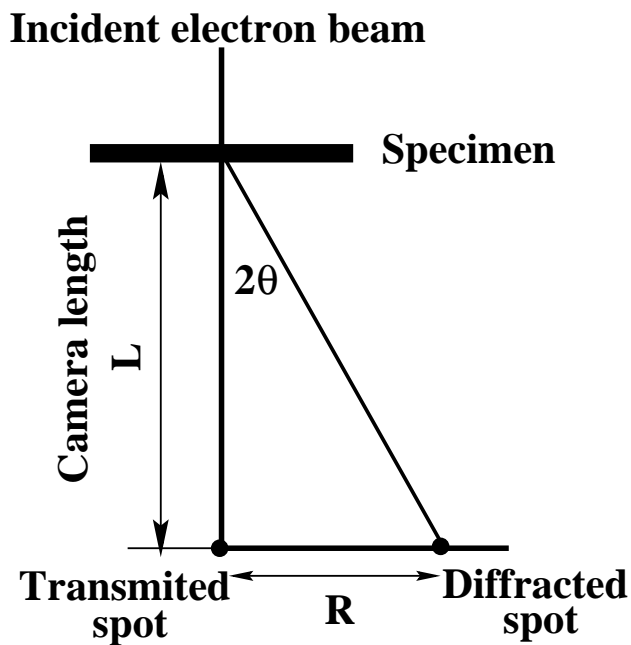


Figure 2.6: Schematic diagram showing the magnification of a diffraction pattern by electron microscopic lenses. The Bragg angle is denoted θ .

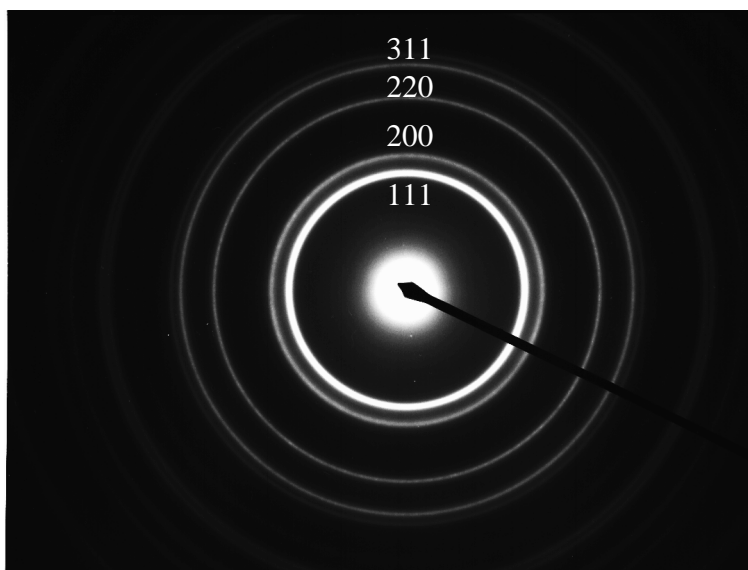


Figure 2.7: Diffraction pattern from the sputtered gold film used to determine the camera constant at 137 cm camera length (L) and 200 kV.

$$d = \frac{a}{\sqrt{N}} \quad (2.4)$$

The accurate lattice parameter (a) of gold is 4.0780 Å [39] and the calculated d -spacings are shown in Table 2.1. The calculated camera constants at different camera lengths at 200k kV are shown in Table 2.2.

Whenever possible, calibration of the camera length was made using the lattice parameter of ferrite.

$\sqrt{h^2 + k^2 + l^2}$	Lattice spacing (d) in Å
1	2.355
2	2.039
3	1.442
4	1.230
5	1.177
6	1.096
7	0.935
8	0.912
9	0.832

Table 2.1: The calculated d-spacing in gold.

Camera length / cm	Calculated camera constant / 10^{-12} m ²
82	2.00
137	3.36
205	5.18

Table 2.2: Calculated camera constants for a number of different camera lengths at an electron accelerating voltage of 200 kV.

2.8 X-ray diffraction

The carbon content of retained austenite (x_γ), and its volume fraction (V_γ) in the austempered specimens were measured using X-ray diffraction with Cu K_α radiation at 40 kV and 40 mA. A Phillips diffractometer was used in a step scan mode to cover the angular 2θ range from 47.0 to 103°. The 2θ step size was 0.03° with a dwell time of 30 s. The samples were ground and polished using the normal metallographic preparation procedure with at least two cycles of polishing and etching before the X-ray diffraction to remove any deformed layer caused by the grinding.

The volume fraction of retained austenite could be estimated from measurements of the integrated intensities of ferrite and austenite phases assuming they are the only phases present. The ratio of the intensities of diffraction peaks from two phases of a polycrystalline sample is given by Cullity [40]:

$$\frac{I_{\gamma(hkl)}}{I_{\alpha(hkl)}} = \frac{R_{\gamma(hkl)}}{R_{\alpha(hkl)}} \times \frac{V_\gamma}{V_\alpha} \quad (2.5)$$

where

$I_{\gamma(hkl)}$ = integrated intensity from a given (hkl) from the γ phase,

$I_{\alpha(hkl)}$ = integrated intensity from a given (hkl) of ferrite,

V_{γ} = volume fraction of γ ,

V_{α} = volume fraction of α ,

and $R_{\gamma(hkl)}$ and $R_{\alpha(hkl)}$ are given by the expression for a specific peak:

$$R = \frac{1}{v^2} [|F|^2(p)(L_p)] e^{-2m} \quad (2.6)$$

where

v = volume of unit cell,

F = structure factor,

p = multiplicity factor,

L_p = Lorentz-polarization factor,

e^{-2m} = temperature factor.

Considering that all materials in reality always exhibit a preferred orientation to some extent, the average integrated intensity used was from at least three specific reflections from austenite and three from ferrite (Table 2.3):

Phase <i>i</i>	Diffracting plane <i>hkl</i>
Ferrite 1	002
Ferrite 2	112
Ferrite 3	022
Austenite 1	002
Austenite 2	022
Austenite 3	113

Table 2.3: Diffraction hkl planes used for bainitic ferrite and austenite in ADI

$$\frac{I_{\gamma}}{R_{\gamma}} = \frac{1}{3} \sum_{i=1}^3 \frac{I_i^{\gamma}}{R_i^{\gamma}} \quad (2.7)$$

$$\frac{I_{\alpha}}{R_{\alpha}} = \frac{1}{3} \sum_{i=1}^3 \frac{I_i^{\alpha}}{R_i^{\alpha}} \quad (2.8)$$

The value of V_{γ}/V_{α} in equation 2.5 can be obtained from the measurement of I_{γ}/I_{α} and the calculation of R_{γ}/R_{α} . Once V_{γ}/V_{α} is found, the value of V_{γ} can be obtained from the additional relationship.

$$V_{\gamma} + V_{\alpha} = 1 \quad (2.9)$$

The carbon concentration was calculated from the measured lattice parameter of the retained austenite. The 2θ values for three austenite peaks were used to calculate the d spacings with Bragg's law and then the lattice parameters a . These values were plotted against $\sin^2\theta$. An accurate value of a_γ is found by extrapolation to $\sin^2\theta=1$ [40]. The carbon content was then computed using the relationship developed by Dyson and Holmes [41], in which the elements are given in wt% and a_γ is given in Å:

$$\begin{aligned}
 a_\gamma = & 3.578 + 0.033C + 0.00095Mn - 0.0002Ni + 0.0006Cr \\
 & + 0.0220N + 0.0056Al - 0.0004Co + 0.0015Cu + 0.0031Mo \\
 & + 0.0051Nb + 0.0039Ti + 0.0018V + 0.0018W
 \end{aligned} \tag{2.10}$$

Chapter 3

Characterisation of ADI

3.1 Introduction

The work presented in this chapter is a comparison of as-received cast-iron against samples which are homogenised before austempering. The purpose was to examine the effects of chemical segregation in the evolution of microstructure during austempering, whilst at the same time illustrating some general microstructural features of austempered ductile irons.

3.1.1 Microanalysis

Samples of cast iron in the as-cast and homogenised conditions (Fig. 3.1), were chemically analysed using a scanning electron microscope (SEM) equipped with energy dispersive X-ray spectroscope (EDS), to characterise the distribution of chemical elements between adjacent nodules of graphite. At least three analyses were performed in each sample, the results shown in Tables 3.1, and 3.2 indicate that manganese concentration in the cell boundary may be up to 1.73 ± 0.12 wt%, and about 0.57 ± 0.10 wt% close to a nodule of graphite in the as-cast condition. By contrast, the average manganese concentration is about 0.81 ± 0.23 wt% at the cell boundary, and 0.57 ± 0.11 wt% close to a graphite nodule in the homogenised sample.

3.2 Chemical segregation

As indicated in chapter 1, alloying elements tend to partition between the liquid and solid phases during solidification. Under nonequilibrium cooling conditions this leads to chemical segregation. Manganese, which is found in most ductile irons, is the most significant in this context because it strongly delays the bainite transformation at the cell boundaries (Fig. 3.3). This reduces the enrichment of carbon in the residual austenite so that it may transform to martensite on cooling to room temperature. In addition, there is a tendency for the precipitation of coarse $(\text{Fe, Mn})_3\text{C}$ carbides in the manganese-enriched region, as shown in Fig. 3.3b.

Element	Cell boundary			
	wt%	wt%	wt%	Average
Mn	2.03 ± 0.26	1.46 ± 0.22	1.70 ± 0.24	1.73
Si	1.72 ± 0.10	1.65 ± 0.10	1.85 ± 0.12	1.75
Mo	1.39 ± 0.18	0.78 ± 0.18	1.10 ± 0.18	1.09
Close to graphite				
Mn	0.60 ± 0.22	0.50 ± 0.22	0.62 ± 0.20	0.57
Si	2.47 ± 0.14	2.49 ± 0.14	2.40 ± 0.14	2.45
Mo	0.10 ± 0.18	0.03 ± 0.18	0.08 ± 0.18	0.07

Table 3.1: Results of microanalysis for as-cast ductile iron. Nominal chemical composition: Fe-3.55C-2.51Si-0.55Mn-0.15Mo-3.11Cu wt%. ZAF corrections have been made during EDS analyses.

Element	Cell boundary			
	wt%	wt%	wt%	Average
Mn	0.90 ± 0.24	0.83 ± 0.24	0.70 ± 0.22	0.81
Si	2.31 ± 0.16	2.23 ± 0.14	2.39 ± 0.14	2.31
Mo	0.12 ± 0.20	0.20 ± 0.20	0.18 ± 0.18	0.16
Close to graphite				
Mn	0.60 ± 0.22	0.65 ± 0.22	0.46 ± 0.24	0.57
Si	2.41 ± 0.14	2.58 ± 0.14	2.50 ± 0.14	2.49
Mo	0.24 ± 0.20	0.0 ± 0.0	0.19 ± 0.20	0.14

Table 3.2: Results of EDS analysis for homogenised ductile iron. Nominal chemical composition: Fe-3.55C-2.51Si-0.55Mn-0.15Mo-3.11Cu wt%. ZAF corrections have been made during EDS analyses.

3.3 Austempering of samples

Homogenised and as-cast samples were austempered at temperatures in the range of 250-450°C for a variety of time periods (Table 3.3). The time was chosen to be that consistent with the achievement of the maximum volume fraction of retained austenite using the neural network model described in chapter 5.

Samples were named according to the austempering temperature and austempering time. Thus, the sample austempered at 250°C for 50 min was named “25050”. Homogenised specimens were given an extra letter “h”. The sample austempered at 250°C for 50 min with homogenisation treatment is therefore designated “25050h”.

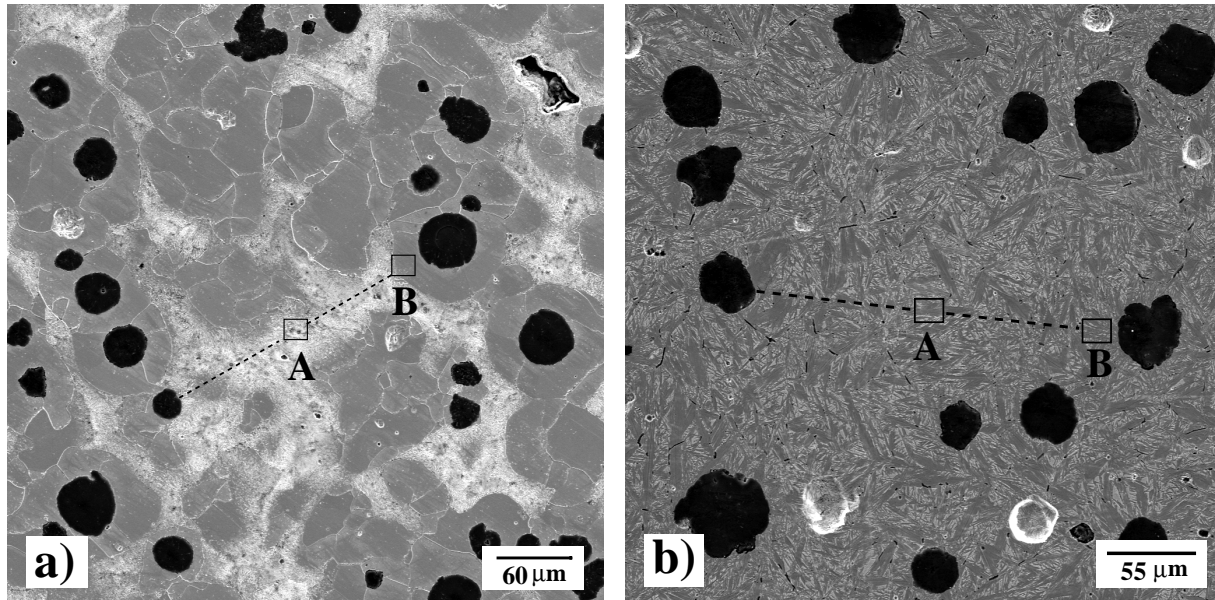


Figure 3.1: Micrographs of the ductile iron utilised in the analysis (a) As-cast, with nodules of graphite, pearlite (white islands) and ferrite (dark background), (b) Homogenised for 3 days at 1000°C, showing a more uniform microstructure consisting of graphite, martensite and retained austenite. Etchant: Nital 2%.

T_A °C	t_A min								
250	50	300	63	350	64	400	52	450	13
260	55	310	63	360	67	410	40		
270	60	320	63	370	70	420	31		
280	61	330	63	380	70	430	23		
290	63	340	63	390	63	440	17		

Table 3.3: Austempering temperature (T_A), and calculated austempering time (t_A) for maximisation of volume fraction of retained austenite.

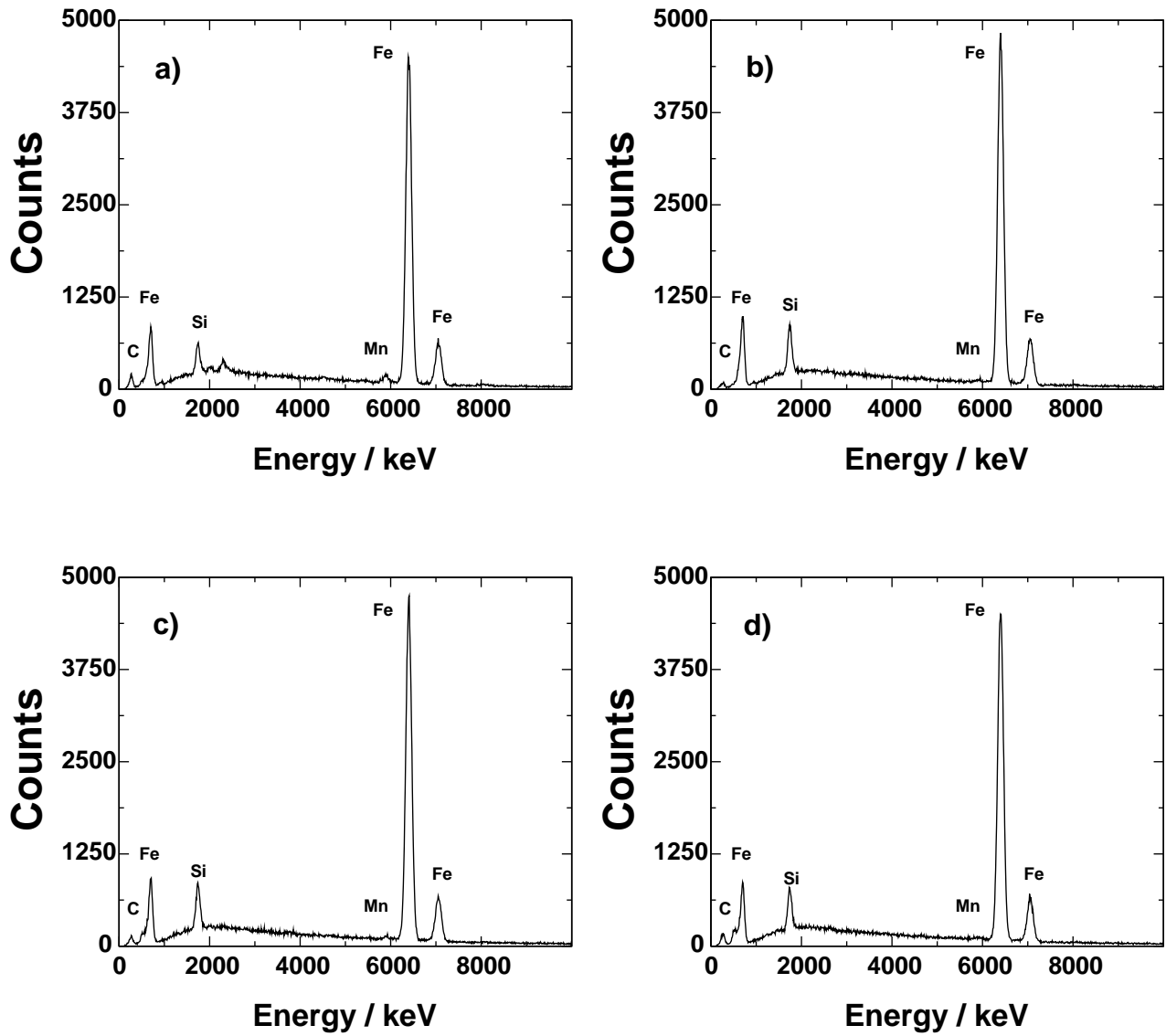


Figure 3.2: EDS Analysis of as-cast and homogenised samples, (a) Diffractogram of as-cast in zone “A”. (b) As-cast zone “B”. (c) Homogenised zone “A” and (d) homogenised zone “B” indicated in Fig. 3.1.

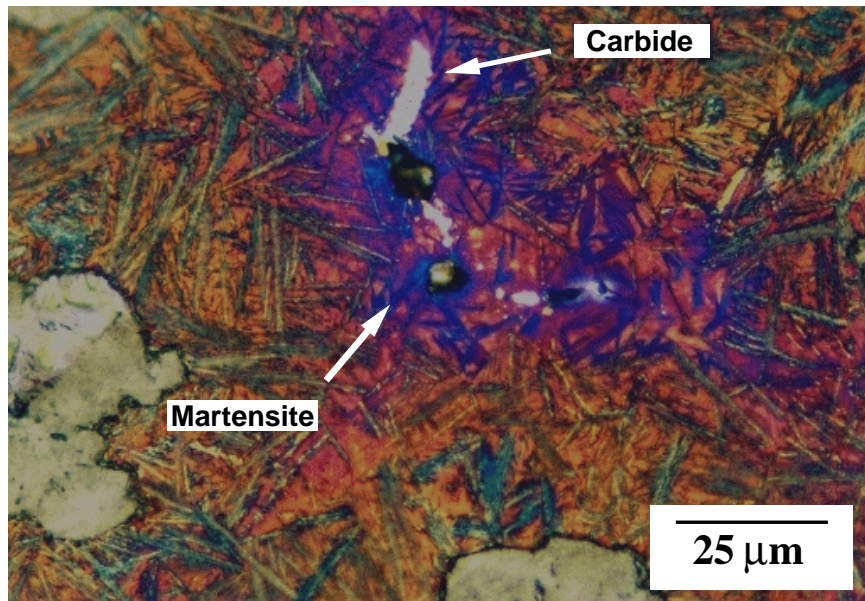
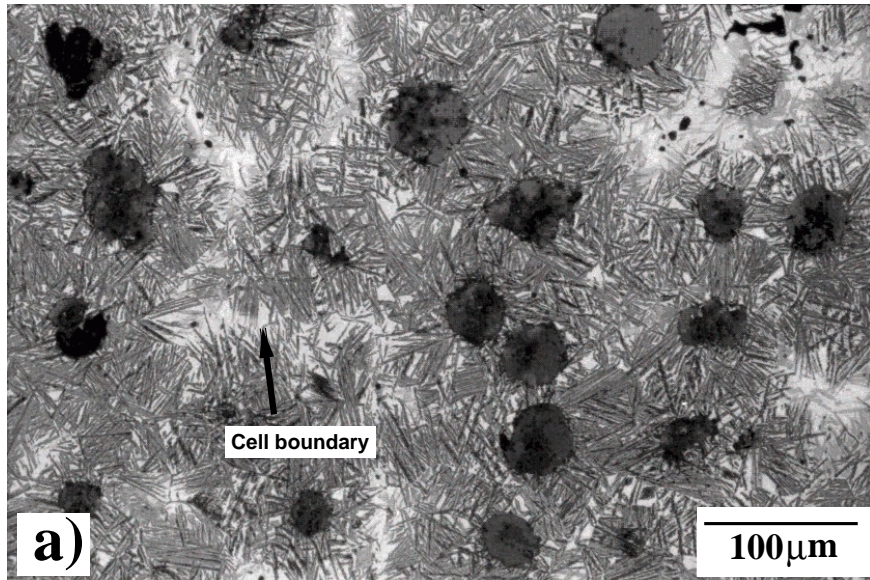


Figure 3.3: ADI sample (Table 3.1) austenitized at 950°C for 64 min. (a) The decrease in the amount of bainite at the cell boundaries which are manganese enriched. The microstructure is otherwise graphite in a matrix which is a mixture of bainitic ferrite, retained austenite and some martensite. Etched with nital 2%. (b) The same as (a) but heat-tinted to reveal manganese carbides (white or cream colour particles), and martensite (blue plates).

3.4 Optical microstructure

General features of the microstructure are illustrated in Figs. 3.4 to 3.7. They show how the morphology of bainitic ferrite changes with the austempering temperature. Both upper and lower bainite consist of aggregates of plates of ferrite. The aggregates of plates are called sheaves and the plates within each sheaf are the sub-units. At low austempering temperatures the sheaves of bainite are finer (Fig. 3.4) because the driving force for transformation is higher as is the strength of the austenite [42]. As the austempering temperature increases, the sheaves of bainite become thicker and so the sub-units are easier to resolve. Previous observations [43], including two-surface analysis experiments have shown that the shape of a sheaf is that of a wedge-shaped plate. The thicker end of the wedge begins at the nucleation site which is usually an austenite grain surface. This is clearly observed in Fig. 3.5f.

In all as-cast samples the most favoured site for bainitic ferrite nucleation appears to be close to the nodules of graphite in the eutectic cell. On the other hand, white areas devoid of bainite are seen at the cell boundaries where manganese content is greater [44, 3]. The lack of carbon partitioning from bainite makes the austenite less stable than martensite can be seen at the cell boundaries. In the case of sample 25050, the observation of martensite close to graphite nodules suggests that the austempering time was not enough to achieve the maximum amount of bainite.

It seems from the micrographs that more martensite is observed in as-cast samples, and blocky regions of austenite are smaller in the homogenised samples. Martensite can be seen easily at higher magnifications and is a relatively light-etching phase because it is not tempered (Fig. 3.4b and Fig. 3.5f).

Homogenised samples have a finer microstructure, the distribution of phases is more even and the microstructure contains less martensite. Coarse carbides were not observed in any homogenised sample by optical microscopy.

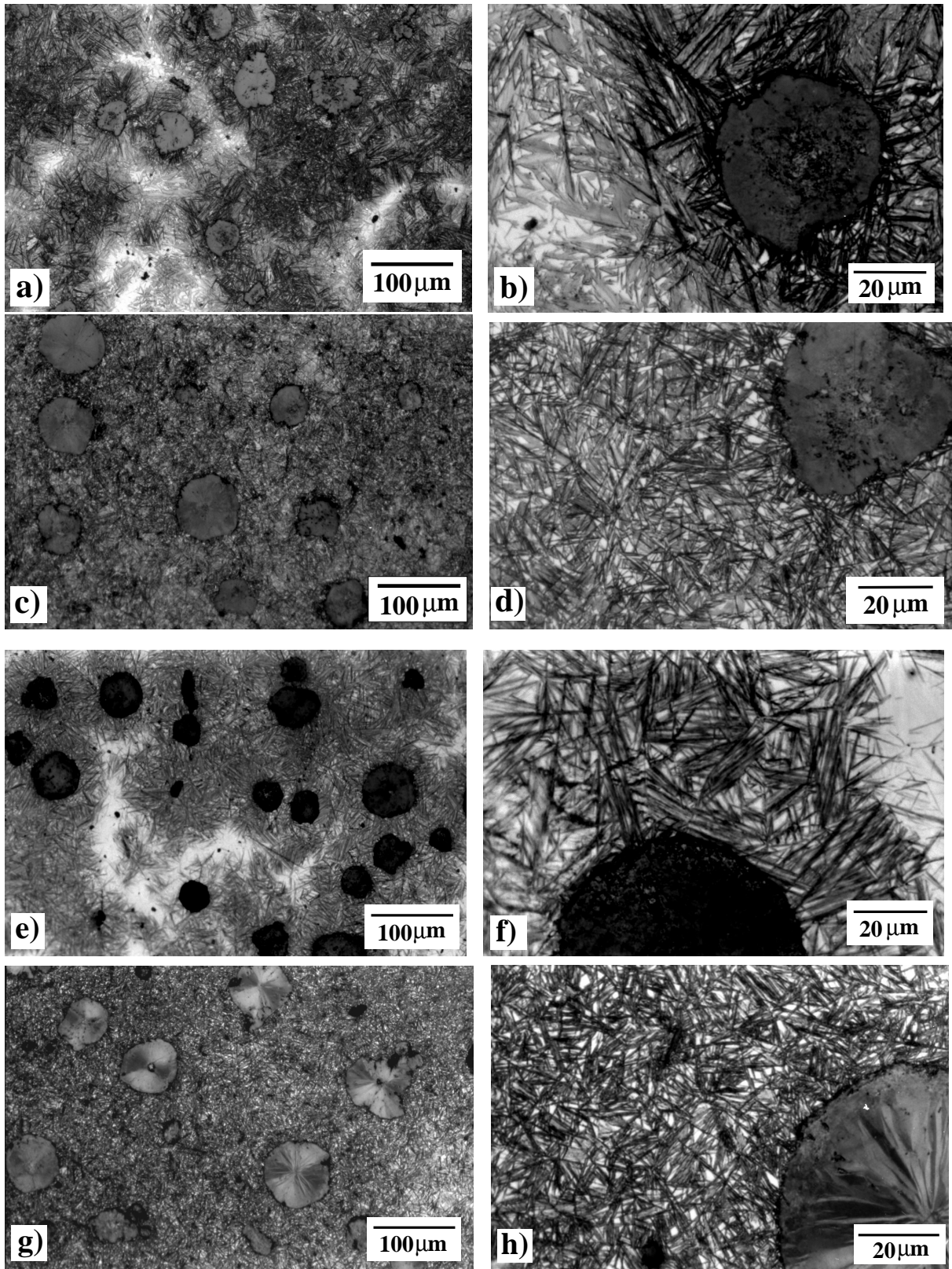


Figure 3.4: Optical micrographs illustrating the microstructure obtained in specimens (a) and (b) 25050, (c) and (d) 25050h, (e) and (f) 28061, and (g) and (h) 28061h.

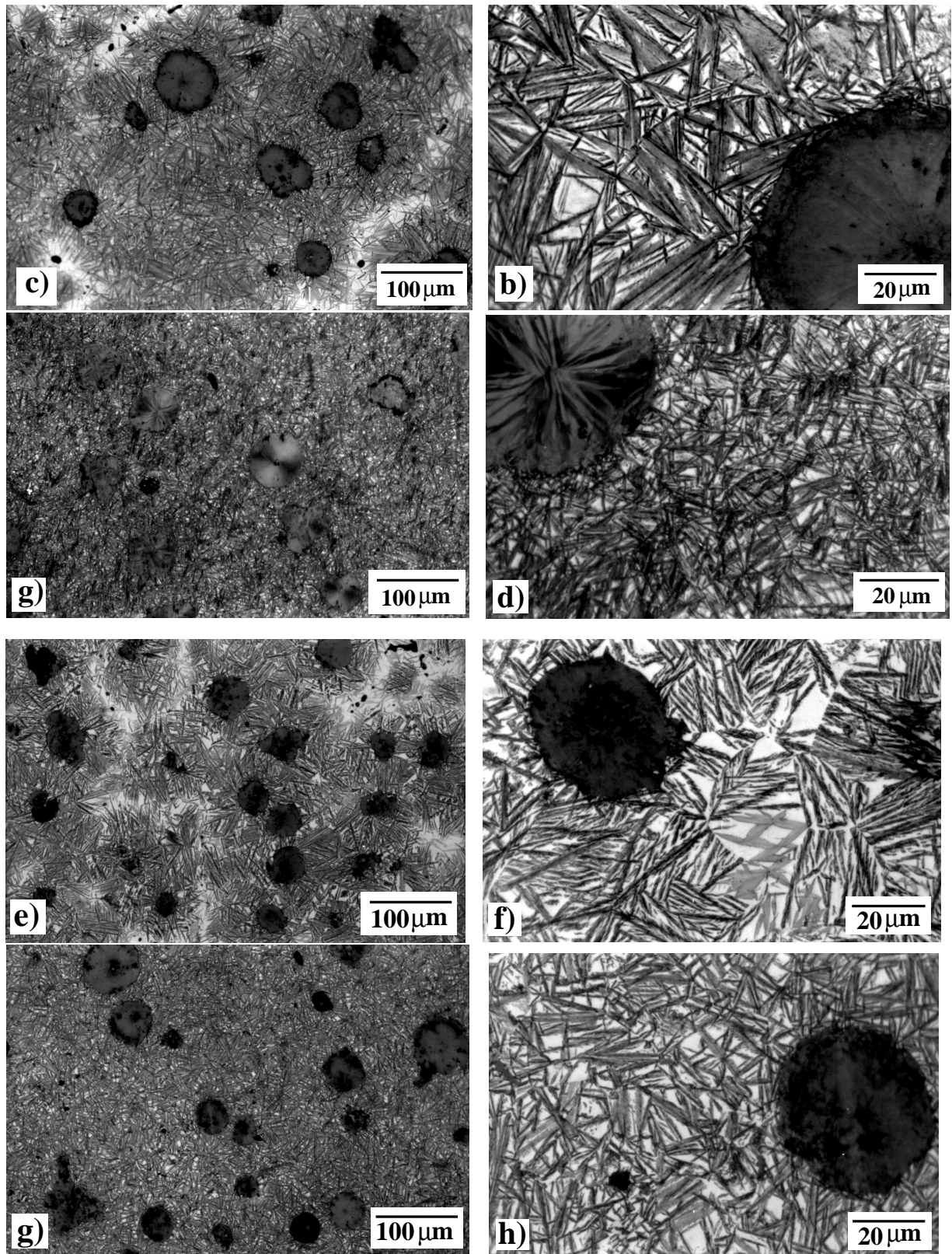


Figure 3.5: Optical micrographs illustrating the microstructure obtained in specimens (a) and (b) 30063, (c) and (d) 30063h, (e) and (f) 35064, and (g) and (h) 35064h.

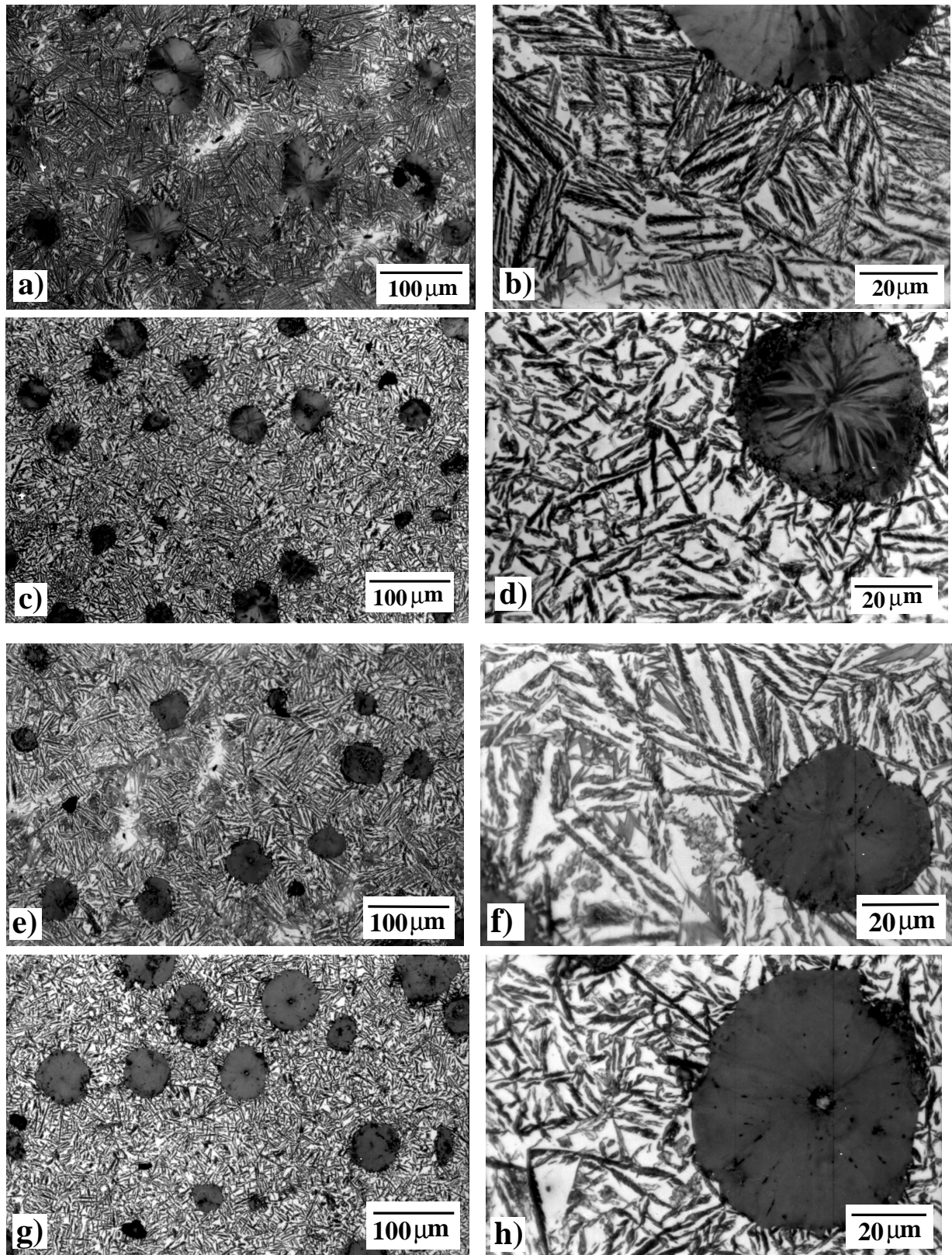


Figure 3.6: Optical micrographs illustrating the microstructure obtained in specimens (a) and (b) 38071, (c) and (d) 38071h, (e) and (f) 40052, and (g) and (h) 40052h.

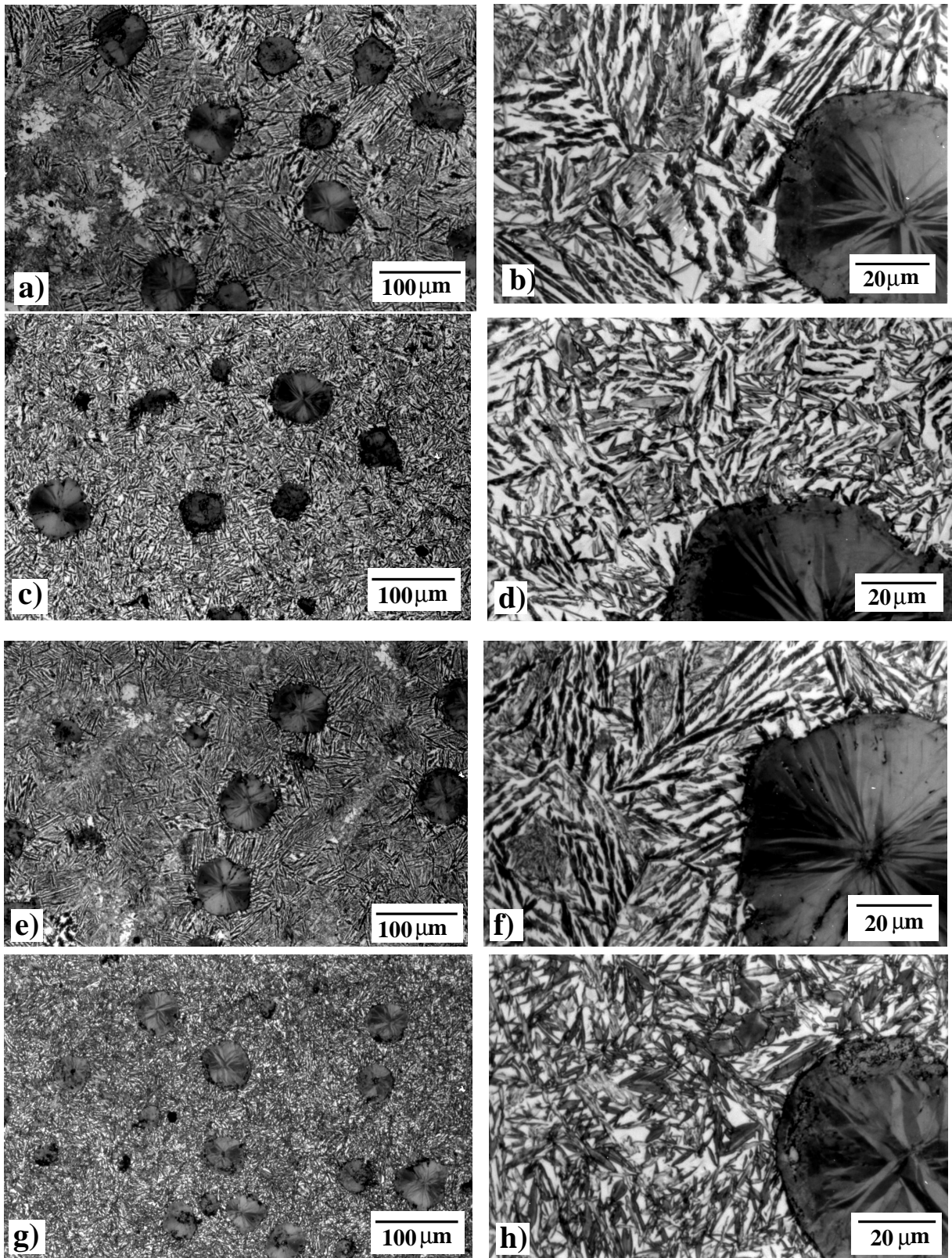


Figure 3.7: Optical micrographs illustrating the microstructure obtained in specimens (a) and (b) 43023, (c) and (d) 43023h, (e) and (f) 45013, and (g) and (h) 45013h.

3.5 Hardness

Fig. 3.8 shows that the hardness of the as-cast specimens is always larger, presumably because of the greater fraction of martensite in the manganese-rich regions. The second observation is that the scatter in hardness, as indicated by the plotted standard deviations is in general larger in the as-cast samples. This, of course, is expected since the microstructure is more uniform in the homogenised samples.

The hardness is seen to go through a minimum as a function of the transformation temperature. This is because at temperatures close to B_S , the amount of bainite that can form is so small, that martensite cannot be avoided on cooling to room temperature. At low temperatures the fraction of bainite is large, giving rise to hardening. These trends are of course reflected in the variation of soft retained austenite as illustrated in Fig. 3.9. The details of the mechanism of the trend illustrated in Fig. 3.9 are described in chapter 8.

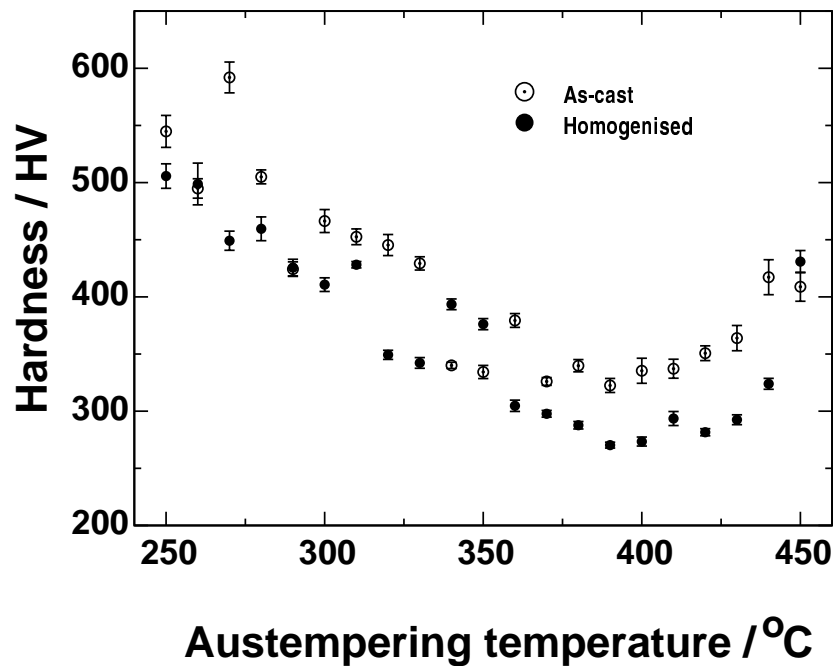


Figure 3.8: Average hardness as a function of austempering temperature for the samples listed in Table 3.3. The error bars represent the standard deviation determined on seven hardness measurements in each case.

3.6 X-ray Diffraction

The fact that more retained austenite is found in homogenised samples is because there is more bainite transformed in these samples. This phenomenon has already been reported for high-silicon steels [19].

The martensite content observed in samples austempered at low temperatures as well as in samples austempered at 450°C and close to this temperature caused a noticeable asymmetry and broadening of ferrite peaks. This is seen in Fig. 3.11 and Fig. 3.12. In most cases, the austenite peaks show higher intensities for the homogenised samples.

The carbon content of retained austenite is illustrated in Fig. 3.10, calculated from the measured austenite lattice parameter as described in previous chapter. It is important to indicate that these concentrations represent average values, since it is well known that the distribution of carbon in the residual austenite is not in general homogeneous after isothermal transformation to bainite [19]. Fig. 3.10 shows that the highest values were obtained from samples austempered at 300°C in both homogenised and as-cast samples. After this temperature there is a smooth decrease in carbon content. The majority of the retained austenite in homogenised samples has less carbon content than in the as-cast samples.

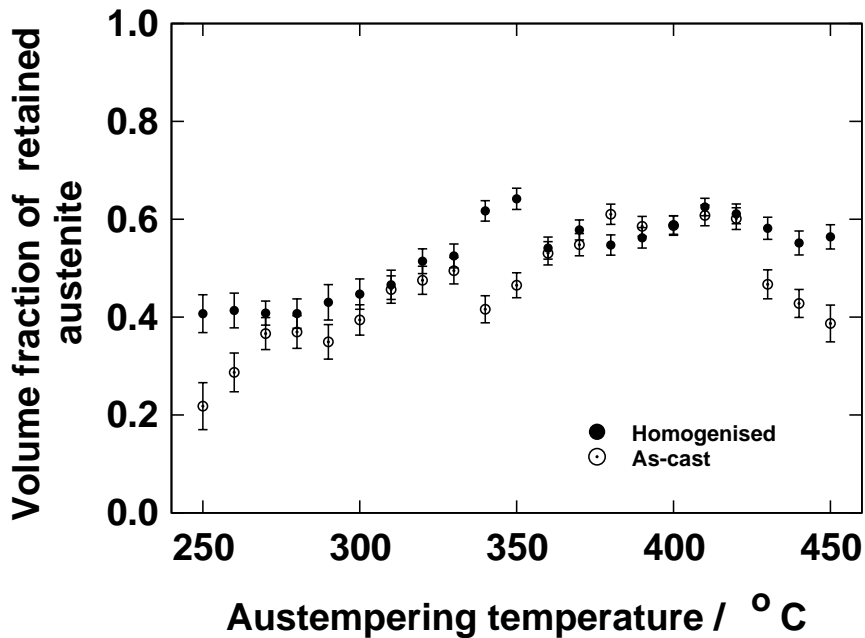


Figure 3.9: Volume fraction of retained austenite in as-cast and homogenised samples. The error bars were obtained from the austenite peak-intensities by dividing 1 over the square root of the intensity.

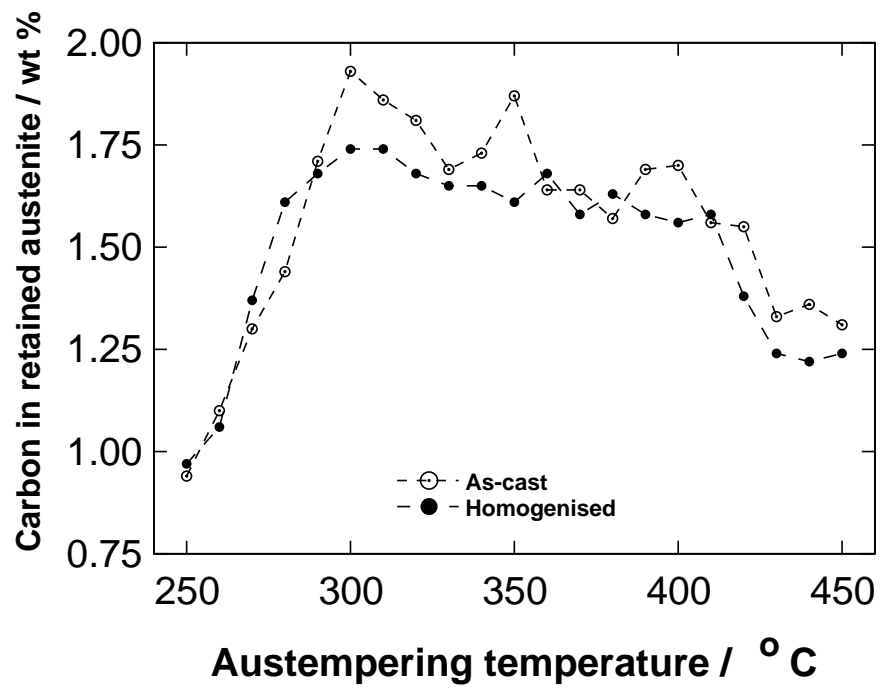


Figure 3.10: Carbon content in retained austenite of as-cast and homogenised samples.

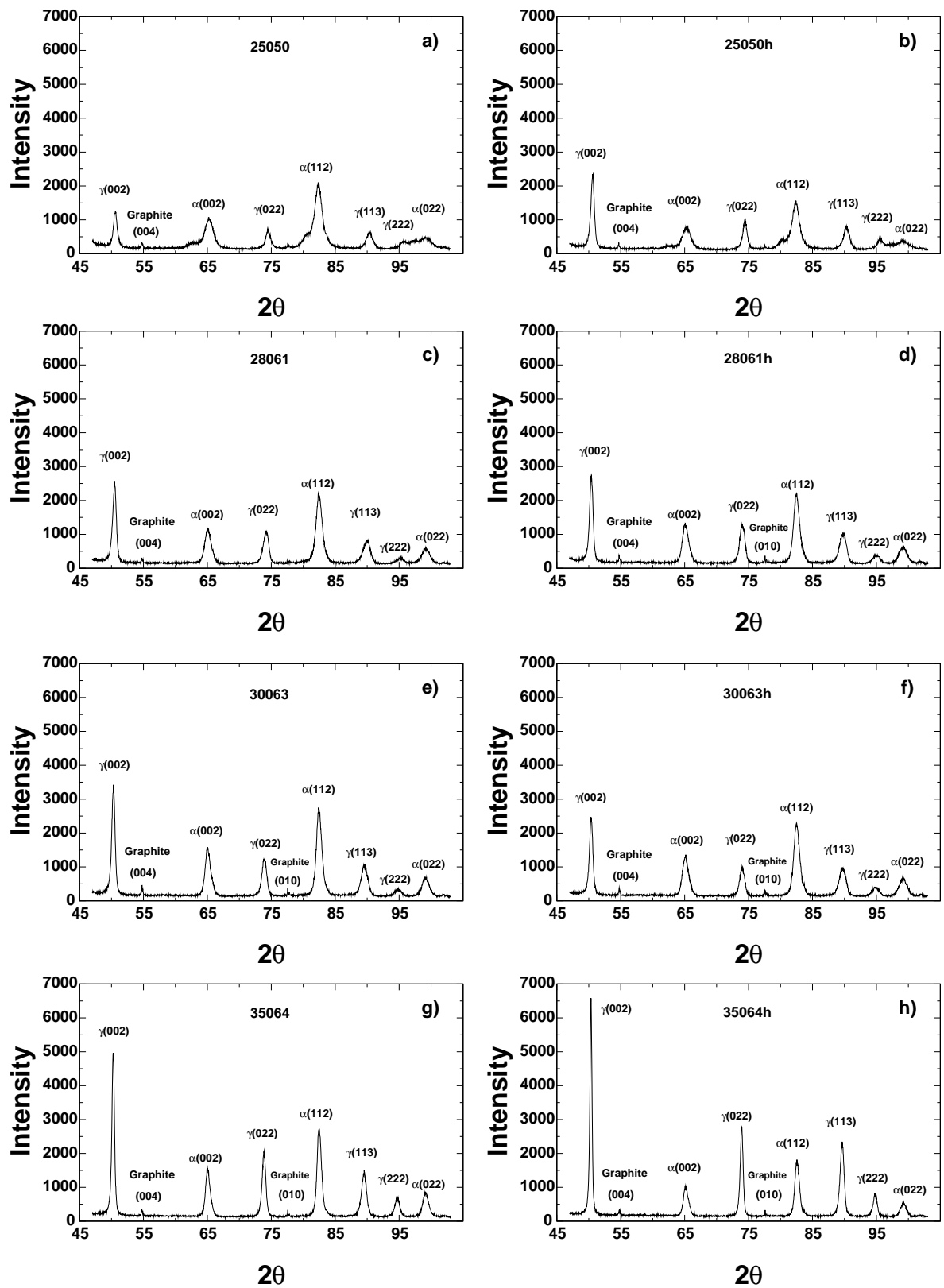


Figure 3.11: X-ray diffraction pattern of homogenised and as-cast samples. Note that the alpha peak labelled as (112) shows broadening due to the influence of martensite. Note also a decrease in this broadening due to the reduction of martensite in the diffractograms of the sample austempered at 350°C

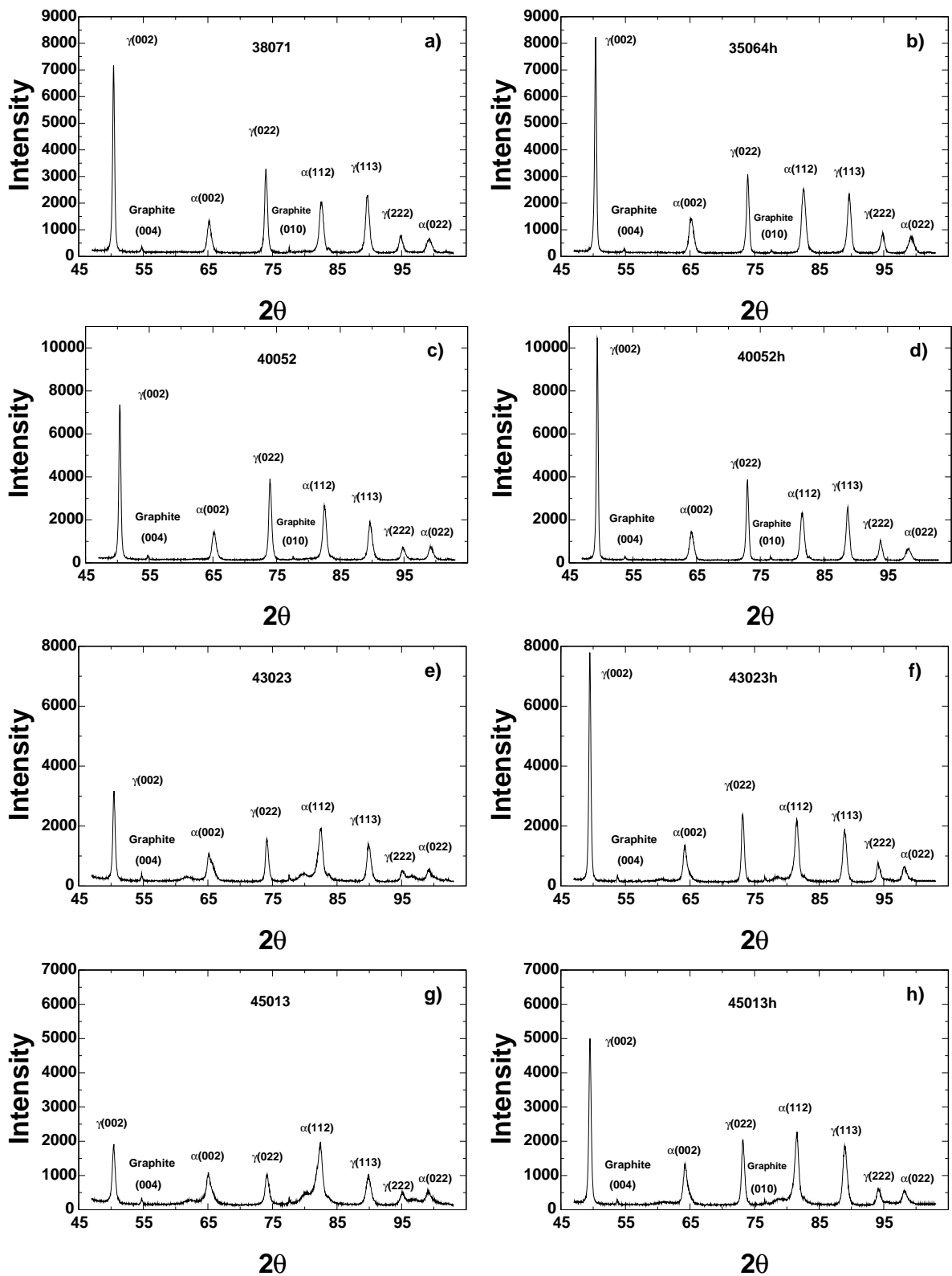


Figure 3.12: X-ray diffraction pattern of homogenised and as-cast samples. Note that the alpha peak labelled as (112) shows broadening due to the influence of martensite. Note also a decrease in this broadening due to the reduction of martensite in the diffractograms of the sample austempered at 350°C

3.7 Transmission electron microscopy

3.7.1 Thin foils

As-cast samples austempered at 250°C for 50 and 90 min were prepared as indicated in chapter 3 for transmission electron microscopy. The results showed that carbides were present within the bainitic ferrite. Fig. 3.13a shows a bright field image of carbides for which a diffraction pattern is shown in Fig. 3.13c. Ahmadabadi [45] found the same diffraction pattern though he did not index it. The pattern could not be indexed to other carbides of the kind associated with bainite [19] but was consistent with τ carbide, which is orthorhombic with lattice parameters $a = 14.8$, $b = 11.4$ and $c = 8.5$ Å as found by Schissler [23]. Fig. 3.13b shows another bright field image of carbides identified as silicon carbides of the type $(\text{Fe,Si})\text{C}_x$ [23]. This carbide is also orthorhombic with lattice parameters $a = 6.5$, $b = 7.7$ and $c = 10.4$ Å. Fig. 3.13d shows its selected area diffraction pattern.

Fig. 3.14 shows a sample austempered at 350 for 64 min in which sub-units of bainitic ferrite separated by thin films of retained austenite are clearly revealed. This sub-units form a sheaf of bainite. A selected area electron diffraction pattern of this area shows reflections of bainitic ferrite. No carbides were observed in this sample.

3.7.2 Carbon extraction replicas

Carbon replicas extracted from samples austempered at 350°C for 20 and 30 minutes were analysed on the TEM. The carbon replicas reveal the morphology of bainitic ferrite quite well. It is possible to see that bainite consists of fine plates of ferrite growing in clusters known as sheaves Fig. 3.15. The fine plates within a sheaf are known as sub-units. In addition it is known that within each sheaf, the plates are parallel and in identical crystallographic orientation (Fig. 3.14), each one with a well-defined crystallographic habit plane [19]. Some circular particles were observed both inside and outside the plates of bainite. However, it was not possible to obtain diffraction patterns from these particles because they are extremely small and even some of the largest did not produce any detectable reflections. No carbides were detected in these samples.

More carbon replicas were obtained from a sample austempered at 350°C for 67 min austempering time. Fig. 3.16 shows that many particles spheroidal and semi-spheroidal shape are present at this condition. The diffraction pattern indicates that these particles are epsilon carbides Fig. 3.16d.

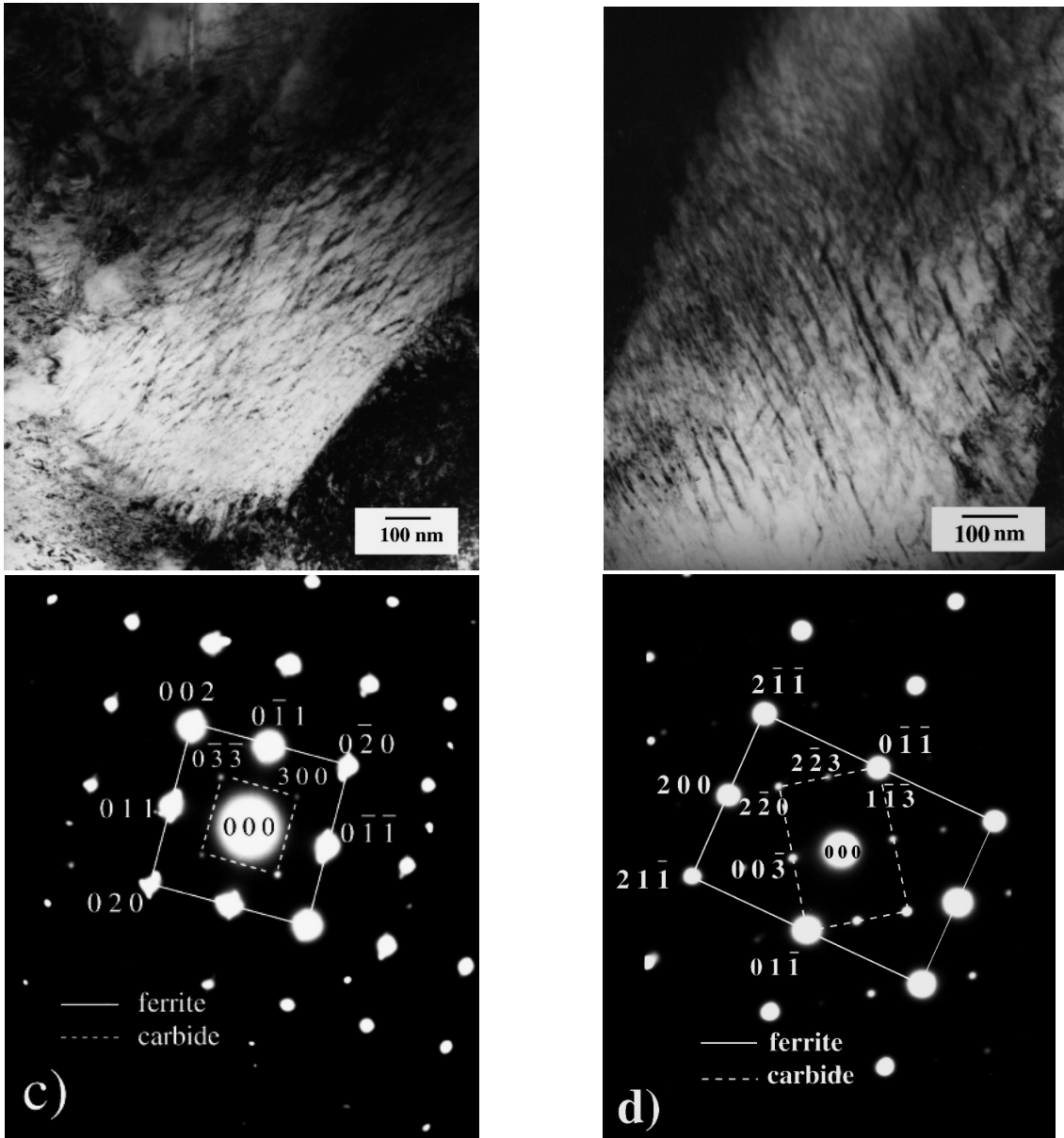


Figure 3.13: TEM micrographs showing bright field images of (a) τ carbides and (b) silicon-rich carbides of the type $(\text{Fe,Si})\text{C}_x$. Selected area electron diffraction patterns of (c) τ and (d) silicon-rich carbides.

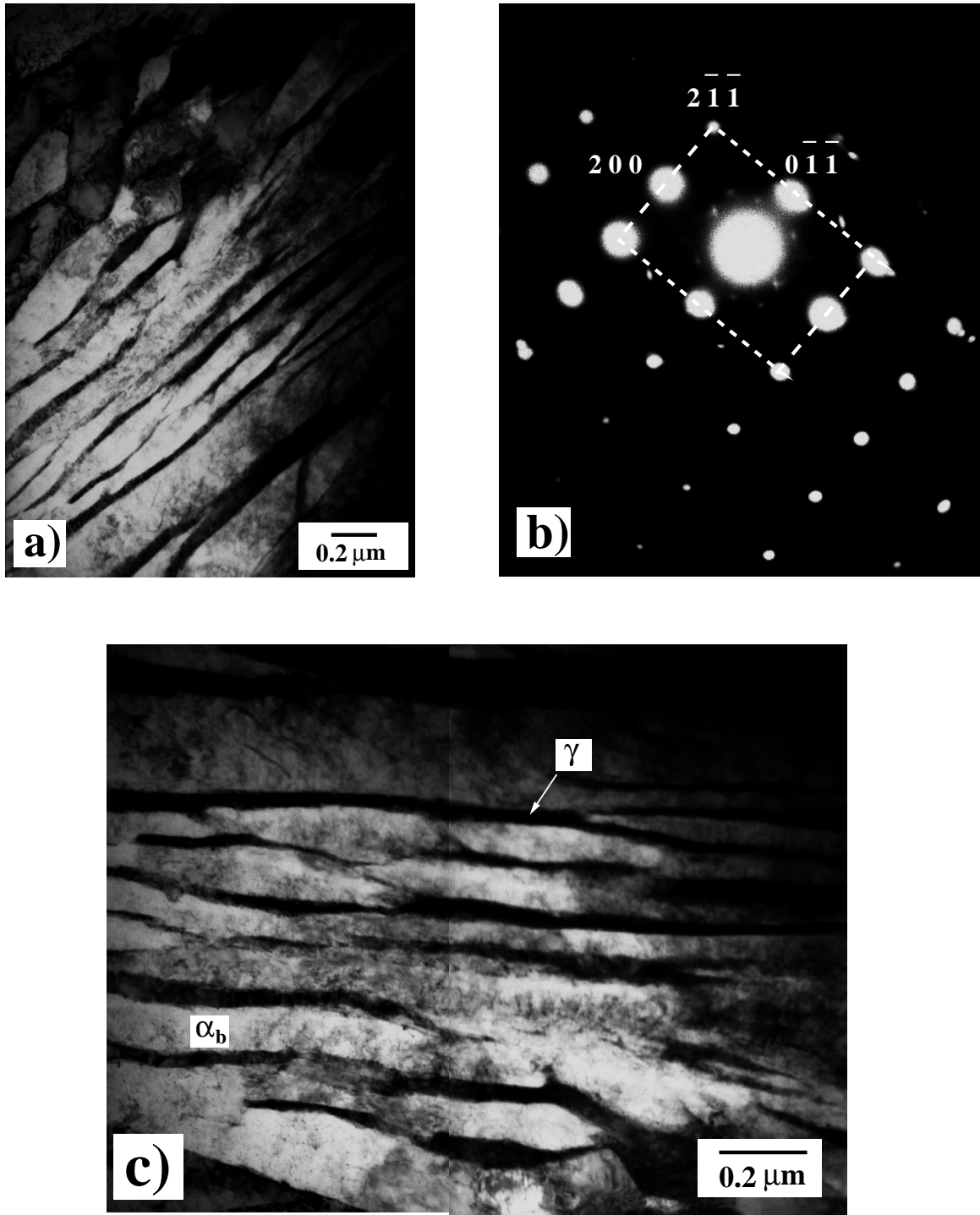


Figure 3.14: TEM micrographs of thin foil. Sample austenitised at 950°C for 30 min and austempered at 350°C for 64 min. (a) Bright field image showing sub-units of bainitic ferrite forming a sheaf of bainite. (b) Selected area electron diffraction pattern obtained from ferrite. (c) Higher magnification showing films of retained austenite between the bainitic ferrite platelets.

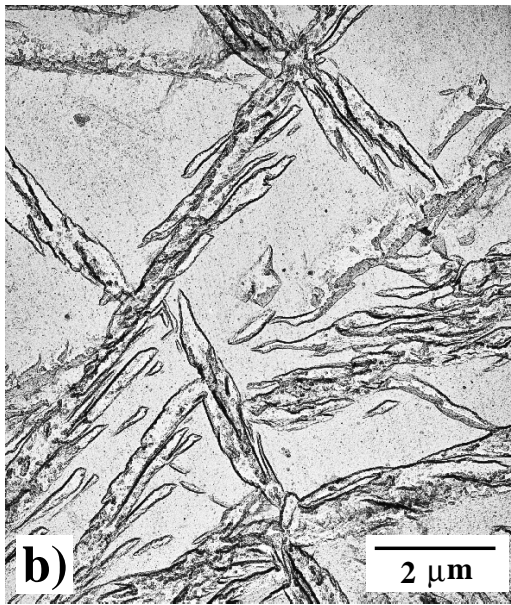
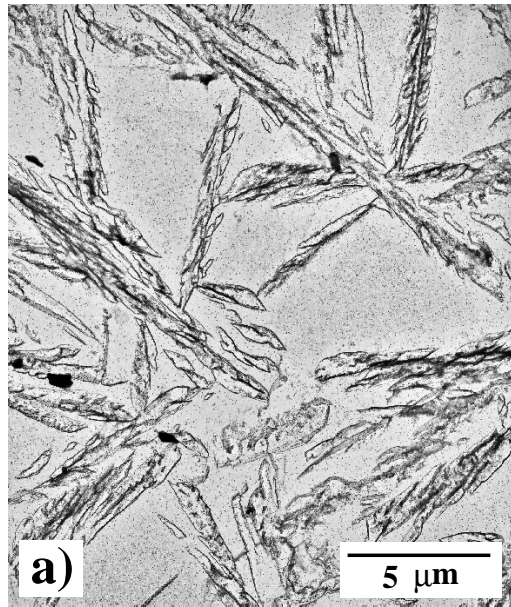


Figure 3.15: Carbon replicas taken from samples austenitised at 950°C for 15 min and austempered for at 350°C for (a) 20 min and (b) 30 min. These replicas reveal the bainitic ferrite boundaries.

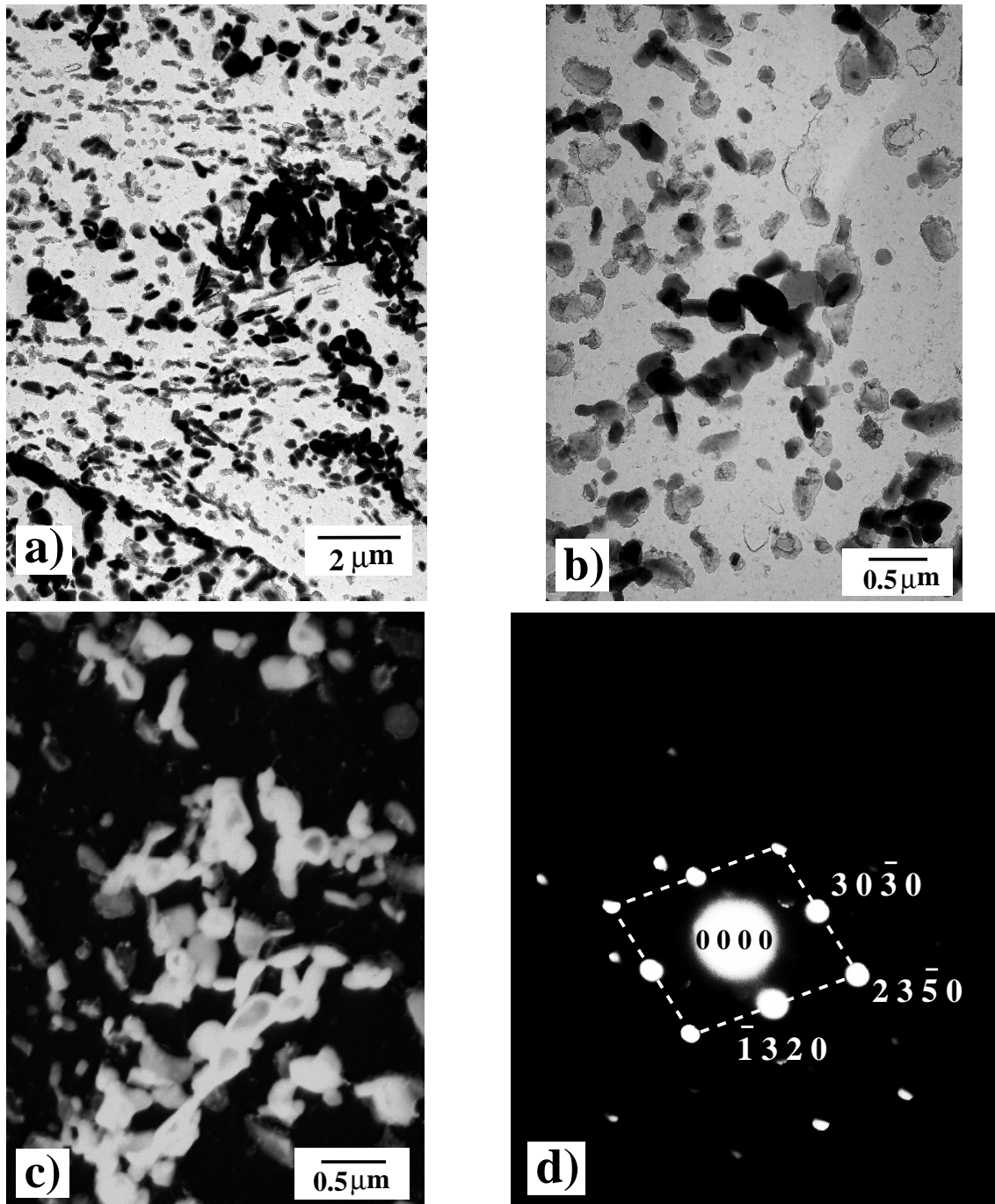


Figure 3.16: Carbon replicas taken from samples austenitised at 950°C for 15 min and austempered for at 350°C for 67 min. (a) and (b) reveal the presence of carbides. (c) shows a dark field image of carbides and (d) is a selected area diffraction pattern of carbides identified as epsilon type.

3.8 Dilatometry

As indicated in chapter 2, the dilatometric data can be utilised for further analysis. Dilatation measurements taken during transformation can be converted into fraction of bainitic ferrite [46]. In order to do this the thermal expansion coefficients of austenite and ferrite are required. For ferrite a sample was heated to 600 °C and held for 30 min. The sample was then cooled at a rate of 1 °C s⁻¹ and the change in dilatation measured. The effect of cementite was neglected in the analysis. The mean expansion coefficient in the range of 200 to 500 °C was found to be 1.40119 x 10⁻⁵ °C.

The austenite expansion coefficient was measured by heating a sample to 1000 °C and holding for 5 minutes to obtain fully austenitic microstructure, followed by cooling at a rate of 1°C s⁻¹ to 500°C and quenching to room temperature. The austenite expansion coefficient was found to be 2.56132 x 10⁻⁵ °C. Fig. 3.17 shows the dilatation measurements made during the cooling cycle.

The isothermal transformation kinetics of bainite obtained from dilatometry test show that more bainite is formed in samples with homogenisation heat treatment. In addition, the rate of bainite transformation in homogenised samples is faster. Plots of selected samples are shown in Figs 3.18 and 3.19.

3.9 Discussion of results

The energy dispersive X-ray spectroscopy (EDS) analysis showed that a homogenisation treatment consisting of austenitising at 1000 °C for 3 days, indeed reduces the segregation of elements such as manganese, molybdenum and silicon. At least three different areas were analysed as a function of distance between two nodules of graphite.

Metallography showed that the homogenised sample contained a more uniform microstructure. An important feature of these samples is that the sheaves of bainite are finer. This is because nucleation of bainite is more uniform in homogenised samples. This is consistent with the dilatometry results that indicate higher volume fraction of retained austenite in homogenised samples. Better distribution of bainite means that carbon enriched residual austenite is more homogeneous, as observed in Fig. 3.10.

It is important to bear in mind, however, that in general if more bainite is formed, less austenite is available for retention because bainite formation consumes austenite. This combination of mechanisms will be discussed in chapter 6.

The transmission electron microscopy of thin foils austempered at 250 °C showed that silicon and transition carbides do precipitate inside bainitic ferrite in the same way as they do in silicon steels as reported by different researchers [23, 47, 48]. The carbon replicas obtained from samples austempered for short time (20 and 30 min) at 350 °C did not show carbides, however, sample austempered at the same temperature, but longer time

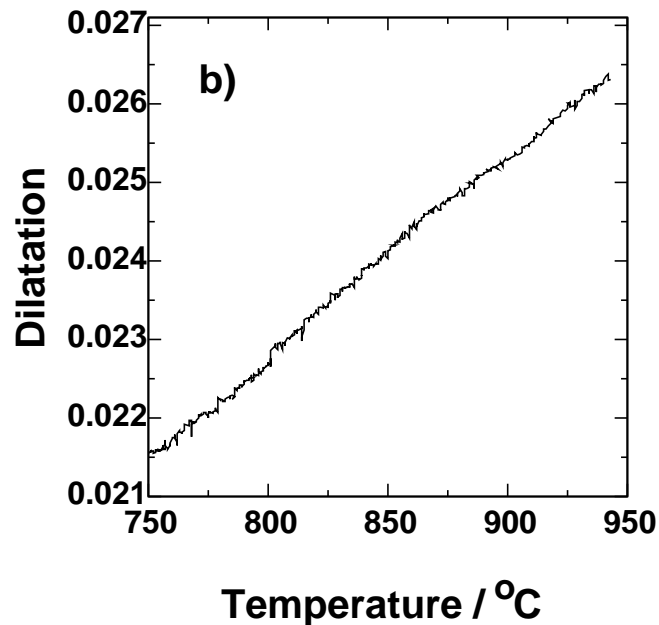
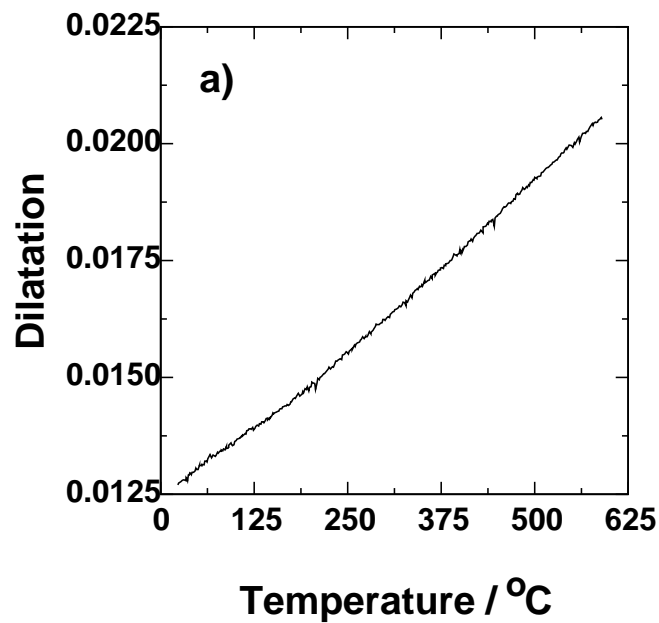


Figure 3.17: Dilatation measurements during cooling at $1\text{ }^{\circ}\text{C s}^{-1}$ of a cast iron of (a) Ferrite and (b) Austenite. The expansion coefficients are clearly not constant but are here assumed to be so.

revealed epsilon carbide. The effect of silicon is generally reconciled with the fact that its solubility in cementite is very small. It means that high-silicon iron alloys form a poor environment for the precipitation of cementite [19]. The need for silicon to diffuse away from the cementite/ferrite interface could explain the retardation of its growth [2]. During the tempering of martensite in high-silicon steels, the retardation of cementite growth allows transition carbides to persist for longer periods [19]. It was at one time

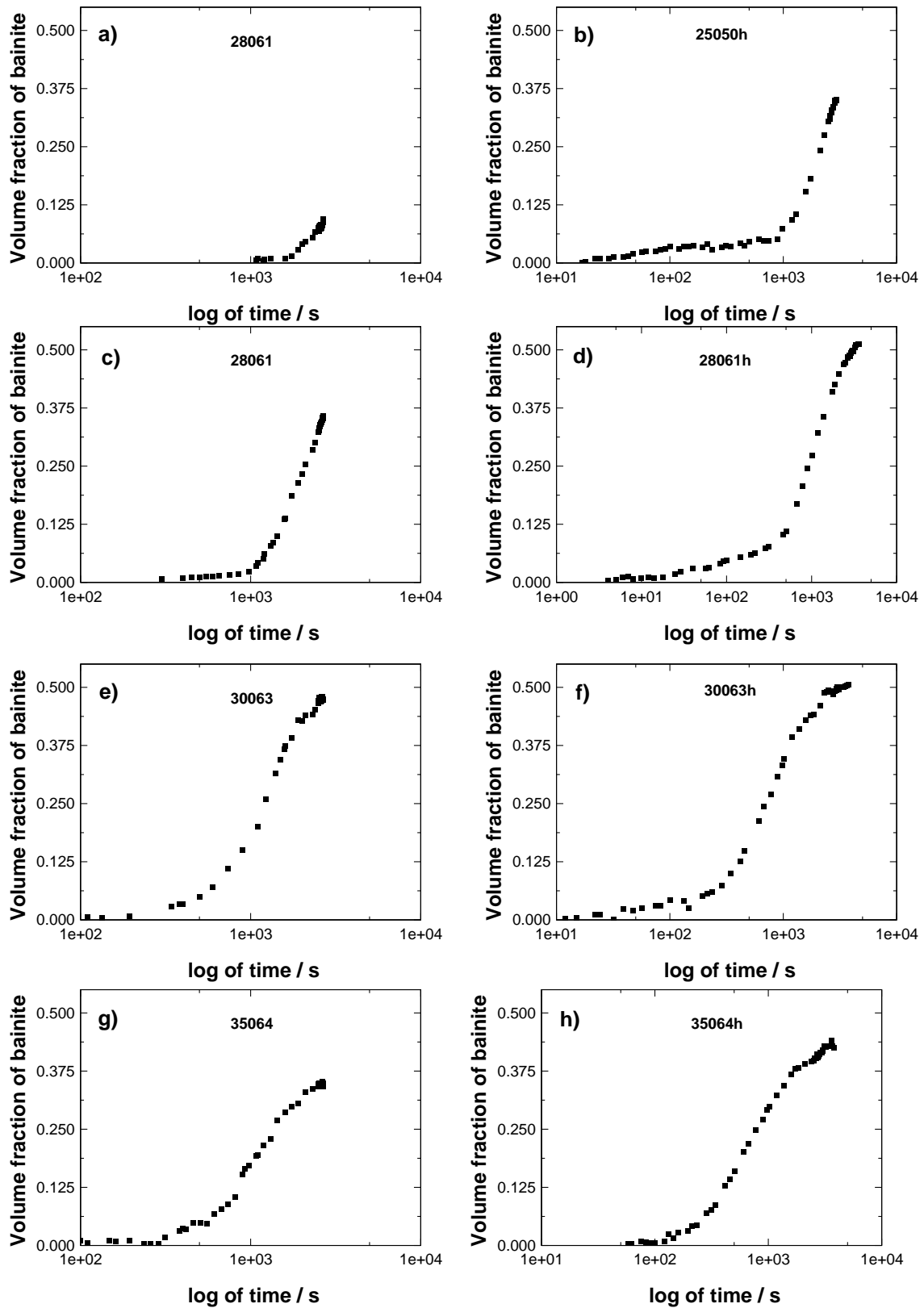


Figure 3.18: Plots of isothermal transformation kinetics of bainite for as-cast and homogenised samples.

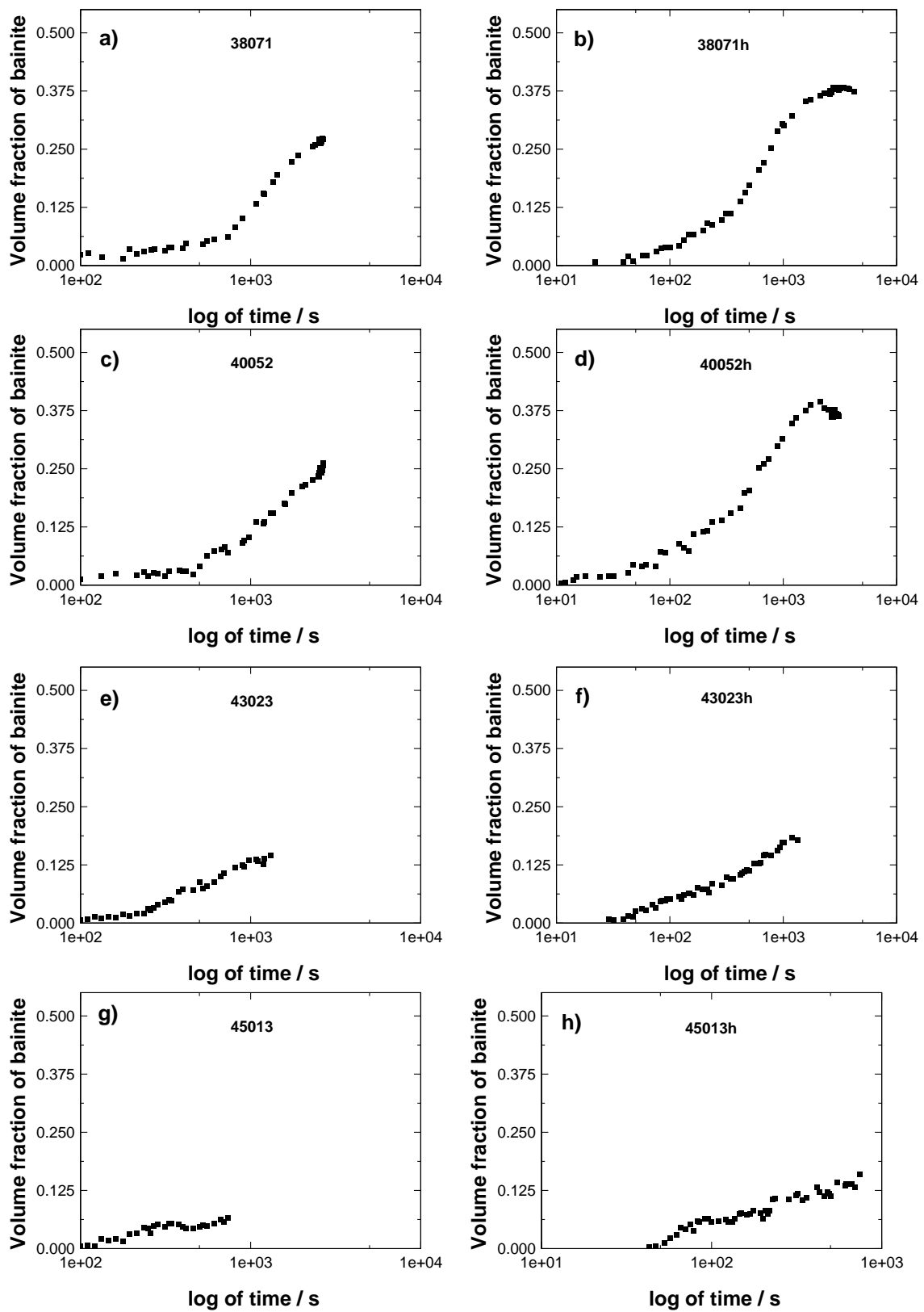


Figure 3.19: Plots of isothermal transformation kinetics of bainite for as-cast and homogenised samples.

thought that the effect was really due to the stabilisation of the transition carbides which have a high solubility for silicon, rather than the retardation of cementite growth [49]. This is confirmed with the carbides observed on the carbon replicas of samples austempered for 67 min which were indexed as epsilon carbide.

3.10 Summary

The experimental results show clearly the influence of chemical segregation in the microstructure of ADI. Manganese is the most prominent in this regard. Results also show how the austempering temperature affects the development of microstructure. This leads to a variety of austempered ductile irons with different mechanical properties as demonstrated here with the hardness tests. The microstructures and mechanical properties can therefore be changed according to need by altering the austempering time and austenitising conditions, as well as the chemical composition. The following chapters describe empirical as well as physical models created to predict the microstructure and mechanical properties of ADI as a function of these variables.

Chapter 4

Neural Network Modelling

4.1 Introduction

Modelling the microstructure and mechanical properties of ADI is not an easy task due to the many variables involved. Chemical composition and heat treatment conditions are the most important, but, the presence of inevitable solidification-induced chemical segregation makes the task even more difficult. Most scientists are familiar with regression analysis where experimental data are best-fitted to a specified relationship which is usually linear and chosen before the best-fit coefficients are derived. The general form of the equation developed using linear regression is a sum of the products of inputs x_i corresponding coefficients (or weights) w_i , possibly with an additional constant (θ). This gives an estimate of the output $y = \sum_j w_j x_j + \theta$. This linear equation may contain non-linear terms, forming a pseudo-linear equation. In regression models like these, the relationship between an input and output tends to be linear and applies across the entire range of the input space, which may not be a reasonable representation of reality. Neural networks form a general method of non-linear regression. Their flexibility enables them to discover more complex relationships in data than traditional statistical models. In this Chapter, the fundamentals of neural networks and the procedures followed to create models described later in the thesis are discussed.

4.2 Neural Networks

A neural network is a general method of regression analysis in which a flexible non-linear function is fitted to experimental data, Fig. 4.1 as in linear regression, the input variable x_i is multiplied by a weight w_i^1 , but the sum of all these products forms the argument of a another transfer function, which in the present work is a hyperbolic tangent (Eq. 4.2). The final output is defined as linear function of hidden nodes and a constant, Eq. 4.1. Thus, the dependent variable y is defined as;

$$y = \sum_i w_i^{(2)} h_i + \theta^{(2)}, \quad (4.1)$$

where h_i defined as;

$$h_i = \tanh \left(\sum_j w_{ij}^{(1)} x_j + \theta_i^{(1)} \right) \quad (4.2)$$

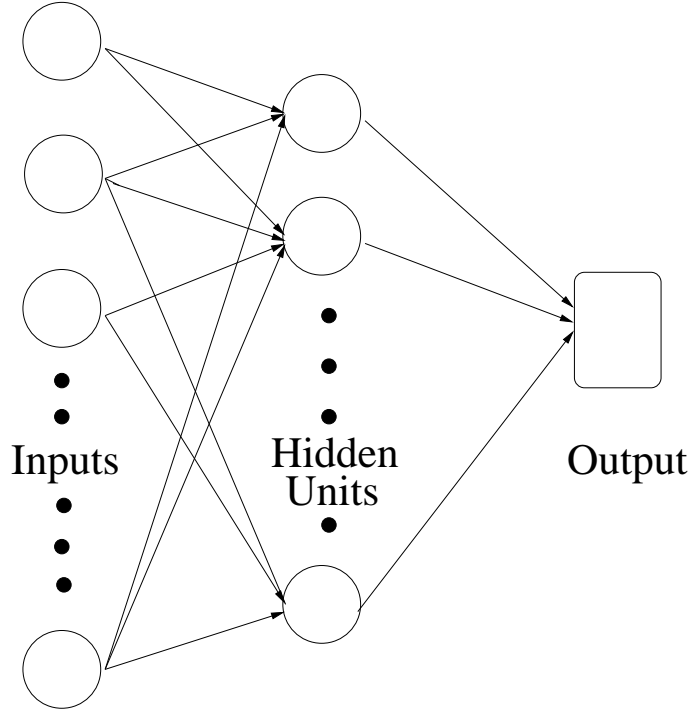


Figure 4.1: Schematic illustration of input, hidden and output layers of neural network model used in the present work.

where x_j are the j variables on which the output y depends, w_i are the weights and θ_i are the biases. Note that the hyperbolic tangent function has a range ± 1 , so a second linear function (e.g. Fig.4.1) enables the output to be arbitrarily small or large. The combination of Eq. 4.2 with a set of weights, biases, value of i and the minimum and maximum values of the input variables defines the network completely, Fig. 4.1. The availability of a sufficiently complex and flexible function means that the analysis is not as restricted as in linear regression where the form of the equation has to be specified before the analysis. The strength of the hyperbolic tangent transfer function is determined by the weights w_j ; the exact shape can be varied by altering the weights. A model with one hidden unit (Fig. 4.2a) may not be sufficiently flexible to capture the complexity of the information in the database. The flexibility of the transfer function can be increased by combining several of the hyperbolic tangents, as shown in Fig. 4.2b.

The neural network can capture interactions between the inputs because the hidden

units are nonlinear. The nature of these interactions is implicit in the values of the weights, but the weights may not always be easy to interpret. For example, there may exist more than just pairwise interactions, in which case the problem becomes difficult to visualise from an examination of the weights. A better method is to actually use the network to make predictions and to see how these depend on various combinations of inputs.

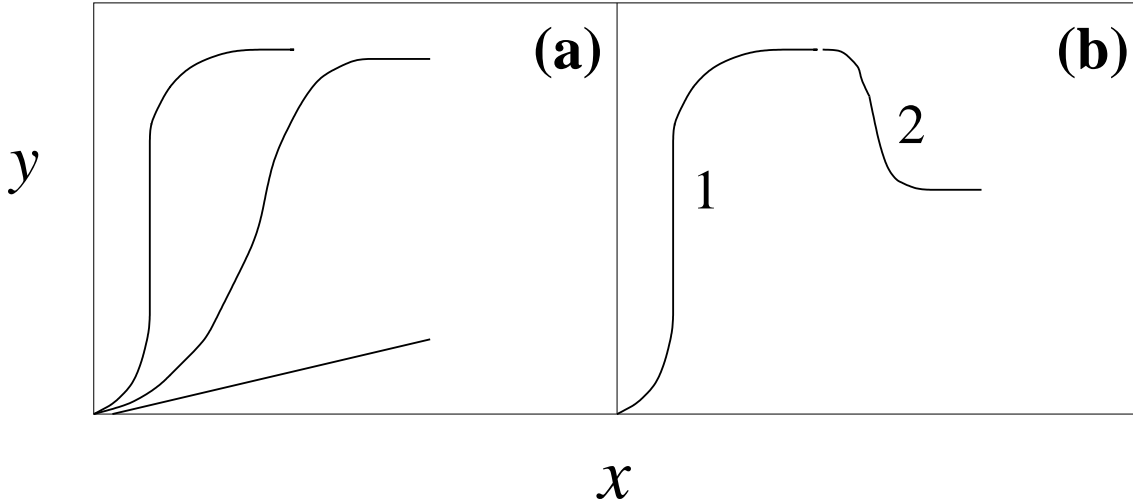


Figure 4.2: Hyperbolic tangent relation between input x and output y . (a) Single flexible hyperbolic tangent with varying weights. (b) Combination of two such tangents.

4.3 Error Estimation

The input parameters are generally assumed in the analysis to be precise and it is normal to calculate an overall error by comparing the predicted values y_j of the output against those measured t_j , for example,

$$E_D \propto \sum_j (t_j - y_j)^2 \quad (4.3)$$

E_D is expected to increase if important input variables have been excluded from the analysis. Whereas E_D gives an overall perceived level of noise in the output parameter, it is, on its own, an unsatisfying description of the uncertainties of prediction.

MacKay has developed a particularly useful treatment of neural networks in a Bayesian framework [50], which allows the calculation of error bars representing the uncertainty in the fitting parameters. The method recognises that there are many functions which can be fitted or extrapolated into uncertain regions of the input space, without unduly compromising the fit in adjacent regions which are rich in accurate data. Instead of calculating a unique set of weights, a probability distribution of sets of weights is used to

define the fitting uncertainty. The error bars therefore become large when data are sparse or locally noisy.

In this context, a very useful measure is the log predictive error because the penalty for making a wild prediction is reduced if that wild prediction is accompanied by appropriately large error bars [50]:

$$\text{LPE} = \sum_m \left[\frac{1}{2} \frac{(t^{(m)} - y^{(m)})^2}{\sigma_y^{(m)^2} + \log(\sqrt{2\pi\sigma_y^{(m)}})} \right] \quad (4.4)$$

where $\sigma^{(m)}$ is the error bar calculated using Bayesian statistics [50]. A larger value of the log predictive error implies a better model, Fig. 4.3b.

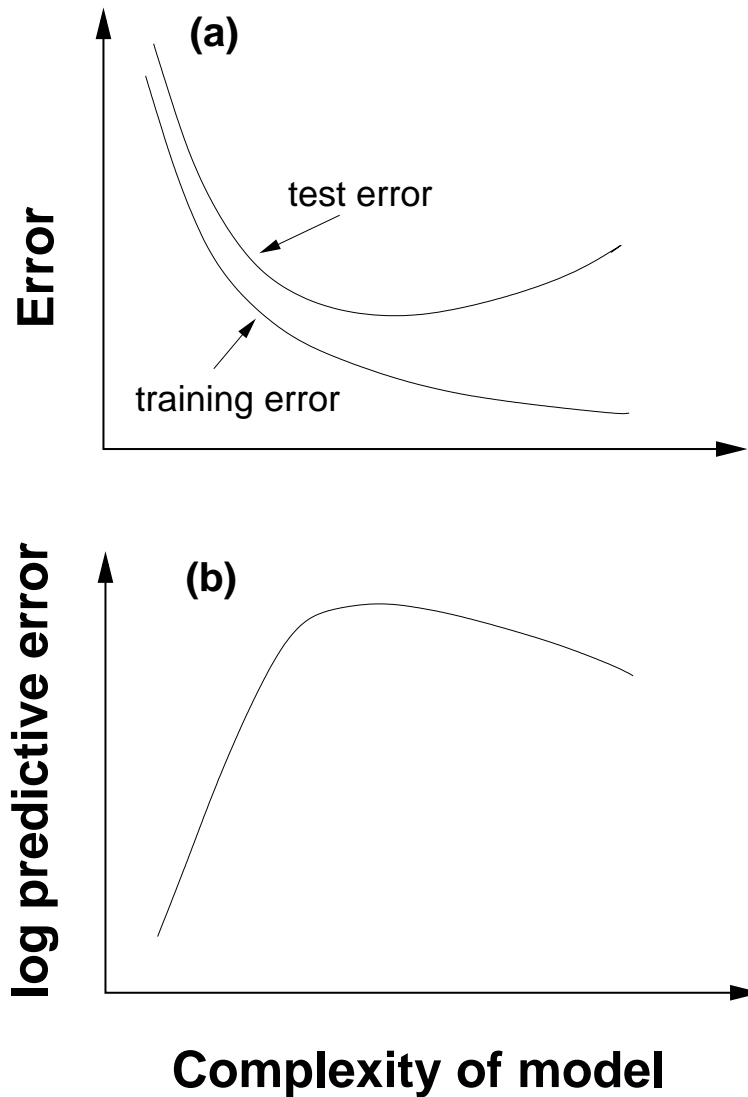


Figure 4.3: Ranking procedure of trained models with varying model complexity. (a) Variation in the test and training error. (b) log predictive error [50].

4.4 Overfitting

A potential difficulty with the use of powerful non-linear regression methods is the possibility of overfitting data. To avoid this, the experimental data can be divided into two sets, a *training* dataset and a *test* dataset. Fig. 4.4 illustrates different degrees of complexity in fitting the training dataset and the test data. A linear model is simple and does not capture the real information form the data Fig. 4.4a. An overcomplex model fits all the data in the training dataset, but generalises badly. The optimum model is one which captures the complexity in the data but does not model noise Fig. 4.4b.

The model is produced using only the training data. The test data are then used to check that the model behaves itself when presented with previously unseen data. The training error tends to decrease continuously as the model complexity increases, Fig. 4.3a. It is the highest log predictive error (Fig. 4.3b) which enables that model to be chosen which generalises best on unseen data [50].

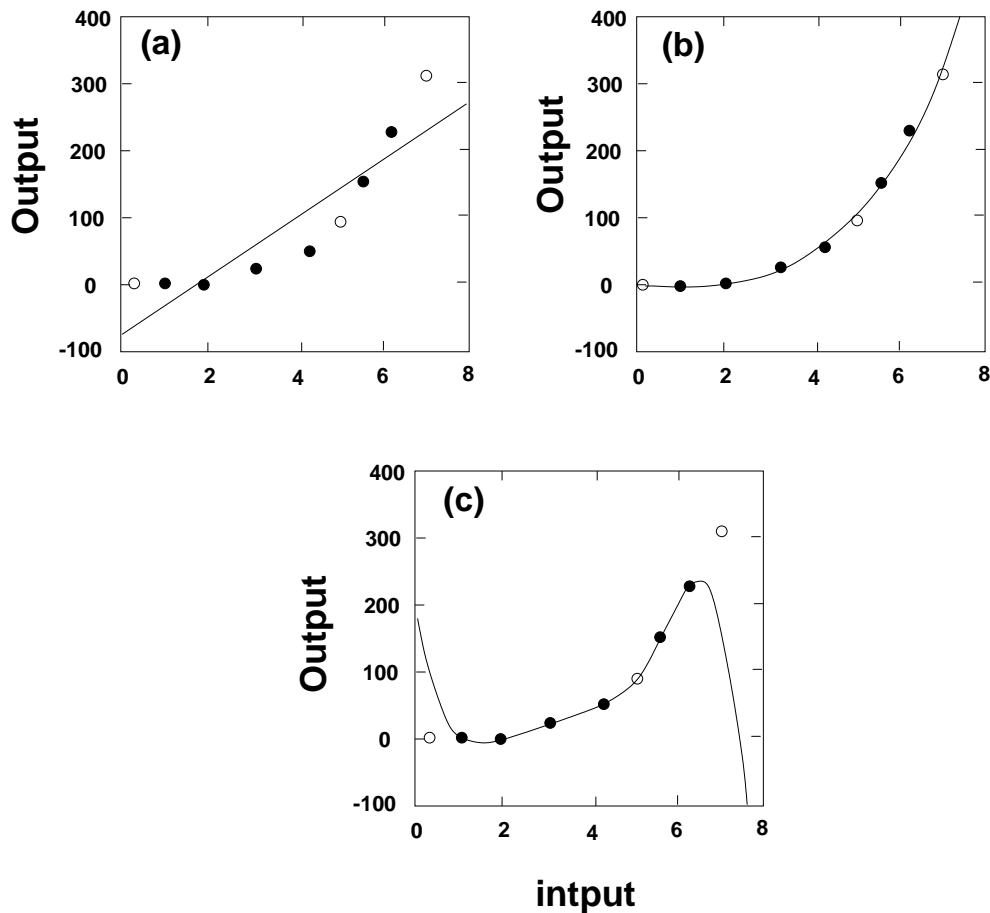


Figure 4.4: Different degrees of complexity of fitting inputs and output. The filled point were used to create a model (*i.e.* they represent training data) and the circles constitute the test data. (a) A linear function which is too simple. (b) A cubic polynomial with optimum representation of both the training and test data. (c) A fifth order polynomial which generalises poorly [51] .

The analysis uses normalised values of the variables in the range ± 0.5 as follows:

$$x_N = \frac{x - x_{min}}{x_{max} - x_{min}} - 0.5 \quad (4.5)$$

where x is the original value from the database, x_{max} and x_{min} are the respective maximum and minimum of each variable in the original data and x_N is the normalised value. This step is not essential to the running of the neural network but is a convenient way of comparing the effect of different variables on the output.

4.5 Model Development Procedure

The experimental data collected are stored in a particular format. These data are normalised using Eq. 4.5. Around 100 different neural network models are selected for training over chosen functions (Eq. 4.1 and 4.2). These models will differ in number of hidden units and seed to generate random starting weights. Before training, the experimental database is randomised in order to divide the information into test and training datasets in a fair manner. The first half of the randomised dataset is used for training and the remaining is for assessing how the trained models behave with unseen data.

The trained models are ranked in decreasing magnitude of log predictive error. It is possible that a committee of models can make more reliable predictions than an individual model [50]. Starting from the best model, the committee models are selected until the minimum test error is obtained. The committee prediction is the average value of individual model predictions. During predictions using the committee model containing ‘ L ’ individual models, the average output \bar{y} and the committee error bar σ are calculated using the following equations;

$$\bar{y} = \frac{1}{L} \sum_l y^{(l)} \quad (4.6)$$

$$\sigma^2 = \frac{1}{L} \sum_l \sigma_y^{(l)2} + \frac{1}{L} \sum_l (y^{(l)} - \bar{y})^2 \quad (4.7)$$

Without changing the complexity of individual models, the committee is retrained on the whole database. During the retraining the weights undergo relatively small adjustments to better fit the whole data base.

4.6 Interpretation

The neural network can capture interactions between the inputs because the hidden units are non-linear. The error bars, which are calculated using Bayesian inference [50] have special meaning. As shown in Fig. 4.5, the error bar is a measure of uncertainty in fitting

parameters in the noisy data region (A) or acts as a warning message when conducting calculations in the region of input space where the data are sparse (B). Thus, error bars calculated using Bayesian neural network represents both experimental noise and the uncertainty in prediction due to lack of knowledge.

A model developed using neural networks to predict the volume fraction of retained austenite is discussed in next chapter. Other properties are discussed in later chapters.

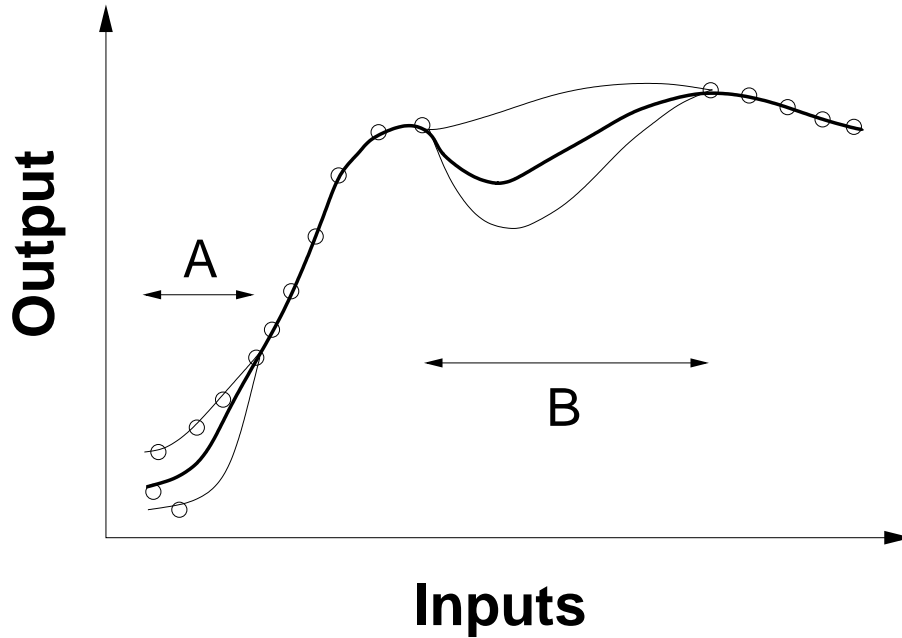


Figure 4.5: Schematic illustration of the uncertainty in defining a fitting function in regions where data are sparse (B) or where there is scatter (A). The thinner lines represent error bounds due to uncertainties in determining the weights.

Chapter 5

Neural Network Model of Retained Austenite

5.1 Introduction

Austempered ductile iron has a microstructure containing spheroidal graphite embedded in a matrix which is in general a mixture of bainitic ferrite, austenite and some martensite. The bainitic ferrite is generated by the isothermal transformation of austenite in the bainite transformation temperature range.

The large concentration of silicon typically present in graphitic cast irons has a key role in the development of the microstructure of austempered irons. The silicon hinders the precipitation of carbides during the bainite transformation [2]. The austempering time must ensure that the formation of bainitic ferrite adequately enriches the residual austenite with carbon, allowing much of it to be retained to room temperature. Unfortunately, prolonged austempering causes the decomposition of the residual austenite into a mixture of carbides and ferrite [3]. This is detrimental to the mechanical properties.

The austempering process is conventionally defined in two stages [52]. The end of the first stage corresponds to the maximisation of the fraction of bainitic ferrite and the enrichment of the austenite. The second stage corresponds to the onset of carbide precipitation. The time interval between these two stages is the heat treatment window (Fig. 5.1). The effect of austempering can be optimised within the confines of this window: too short an austempering time leads to an inadequate enrichment of the austenite and hence a lower retained austenite content. Austempering beyond the commencement of stage II causes carbide precipitation and once again, a reduction in the retained austenite content. The extent of the heat treatment window is reduced by the presence of inevitable solidification-induced chemical segregation, since the transformations occur at different times in different regions of the sample. It thus becomes difficult, if not impossible, to define an ideal austempering time for the whole of the cast iron component. Since the austenitising temperature and time defines the carbon concentration of austenite prior to the isothermal treatment, it is important to take account of it. Austempering tem-

perature on the other hand, defines the volume fraction of bainite to be transformed [19].

This chapter describes the development of a neural network model (Chapter 4) of the retained austenite content of ADI as a function of the chemical composition, and the austenitisation and austempering heat treatments.

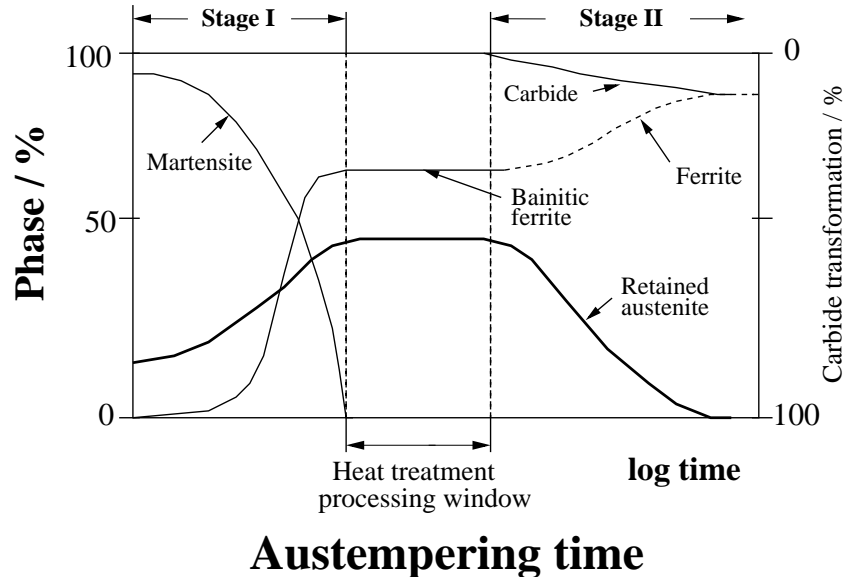


Figure 5.1: Schematic representation of the development of microstructure during austempering, together with an illustration of the “processing window”. Martensite is present only when the sample is cooled to room temperature before the austempering has been completed.

5.2 The variables

The analysis is based on published data and is therefore limited to quantities that are readily measured and frequently reported. For example, in order to predict the quantity of retained austenite it would be ideal to include the fraction of bainite as an input, but this is rarely measured in practice. Therefore, a pragmatic set of variables must be chosen which implicitly contain all the information needed to estimate the amount of retained austenite.

The set of inputs Table 8.1 therefore included the detailed chemical composition in wt%, the austenitisation temperature in °C and time in min (T_γ and t_γ respectively), and the austempering temperature and time (T_A and t_A respectively). This is almost all that is necessary to define the retained austenite volume fraction (V_{γ_r}). However, due to a lack of appropriate data, no explicit account can be taken of the incomplete dissolution of carbides during austenitisation. Failure to do this should reflect in a greater uncertainty in the predictions that are made using the trained neural networks. A total of 1910 experimental data were collected from published literature [12,16,17,20,27,28,52-83] and digitised.

Input element	Minimum	Maximum	Mean	Standard Deviation
Carbon / wt%	2.3	3.97	3.58	0.165
Silicon / wt%	1.57	3.78	2.57	0.21
Manganese / wt%	0.01	1.52	0.34	0.23
Molybdenum / wt%	0.0	0.74	0.16	0.17
Nickel / wt%	0.0	3.82	0.29	0.53
Copper / wt%	0.0	1.60	0.23	0.29
Austenitising temperature / °C	800	1050	900	34
Austenitising time / min	15	240	97	34
Austempering temperature / °C	230	455	350	39
Austempering time / min	0.5	60000	1039	5625
Austempering time $\log\{t_A/s\}$	1.477	6.556	3.659	0.948
$\log\{-\log\{V_{\gamma_r}\}\}$	-0.875	2.03	0.414	0.418

Table 5.1: The variables used to develop the neural network model. Molybdenum, nickel and copper were frequently not reported in publications since they were not deliberate additions, in which case their concentrations were set to zero.

One approach is to use the neural network with the austempering time as an input. However, this is not justified metallurgically since the fraction is not expected to vary linearly with time, but as the logarithm of time. The evolution of volume fraction with time in nucleation and growth reactions follows a sigmoidal behaviour. This is because the bainite reaction associated with the first stage of austempering, and indeed, the subsequent decomposition of the austenite in stage two, should both follow an Avrami type equation with

$$\zeta = 1 - \exp\{-k_A t^n\} \quad (5.1)$$

where ζ is the fraction of transformation. The detailed values of the Avrami parameter k_A and the time exponent n will depend on many different factors, as reviewed by Christian [84]. If ζ is the fraction of bainitic ferrite then $V_\gamma = 1 - \zeta$ during stage I, so it is expected that

$$\log\{-\log\{V_\gamma\}\} \propto \log\{t_A\} \quad (5.2)$$

Interestingly, since it is the residual austenite which undergoes transformation to carbides and ferrite during stage II, the relationship implied in Eq. 5.2 also applies there.

It follows that it is natural to use $\log\{-\log\{V_{\gamma_r}\}\}$ as the output parameter in the neural network analysis, rather than V_{γ_r} directly. The former is physically justified on the basis of the Avrami equation, but is additionally important because V_{γ_r} and its associated error calculations become bounded between 0 and 1 for all positive values of t , as they should be. This will become apparent later in the chapter.

On a similar rationale, the time parameter in the input set should be $\log\{t_A\}$ rather than t_A . This became obvious after the first attempt to create the present model. Fig. 5.2 shows that using only t_A as one of the inputs, is not enough to reproduce the evolution of retained austenite with time properly. However, it is conceivable that there might be some unknown process which varies directly with t_A so both the logarithmic time and the time were included as input variables. This has the advantage of avoiding bias in the inputs; the method used here has automatic relevance determination [50] and hence sets the weights associated with an irrelevant input to small or zero values should that be justified. It will be shown latter that by including the logarithmic time and the time, the change of retained austenite as a function of austempering time will be following proper trends.

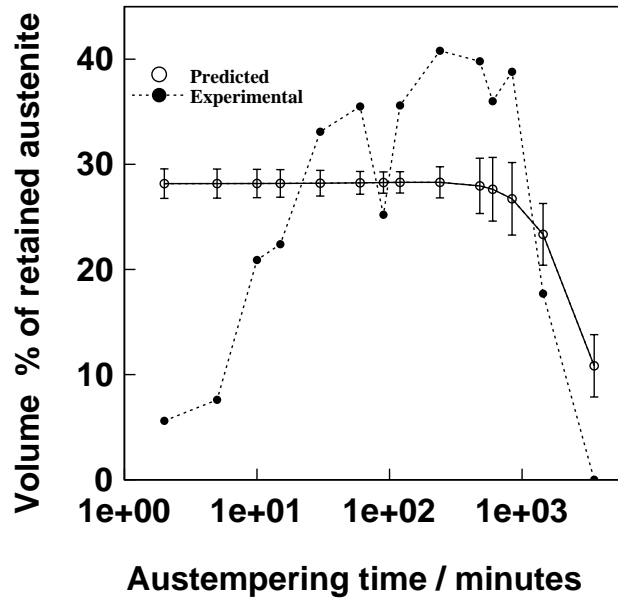


Figure 5.2: A first attempt to model the volume fraction of austenite as a function of chemical composition and heat-treatment conditions. This plot shows that a single variable of time t_A is not enough to reproduce actual trends in the retained austenite evolution. Experimental results from the published literature [16] correspond to a Fe-3.6C-2.4Si-0.3Mn-0.45Mo iron austempered at 927 °C for 2 h and austempered at 370 °C

It is emphasised that unlike linear regression analysis, the ranges stated in Table 8.1 cannot be used to define the range of applicability of the neural network model. As indicated in chapter 4, it is the Bayesian framework of this neural network analysis which makes possible the calculation of error bars whose magnitudes vary with the position in the input space, which define the range of useful applicability of the trained network. A visual impression of the spread of the data is shown in Fig. 5.3.

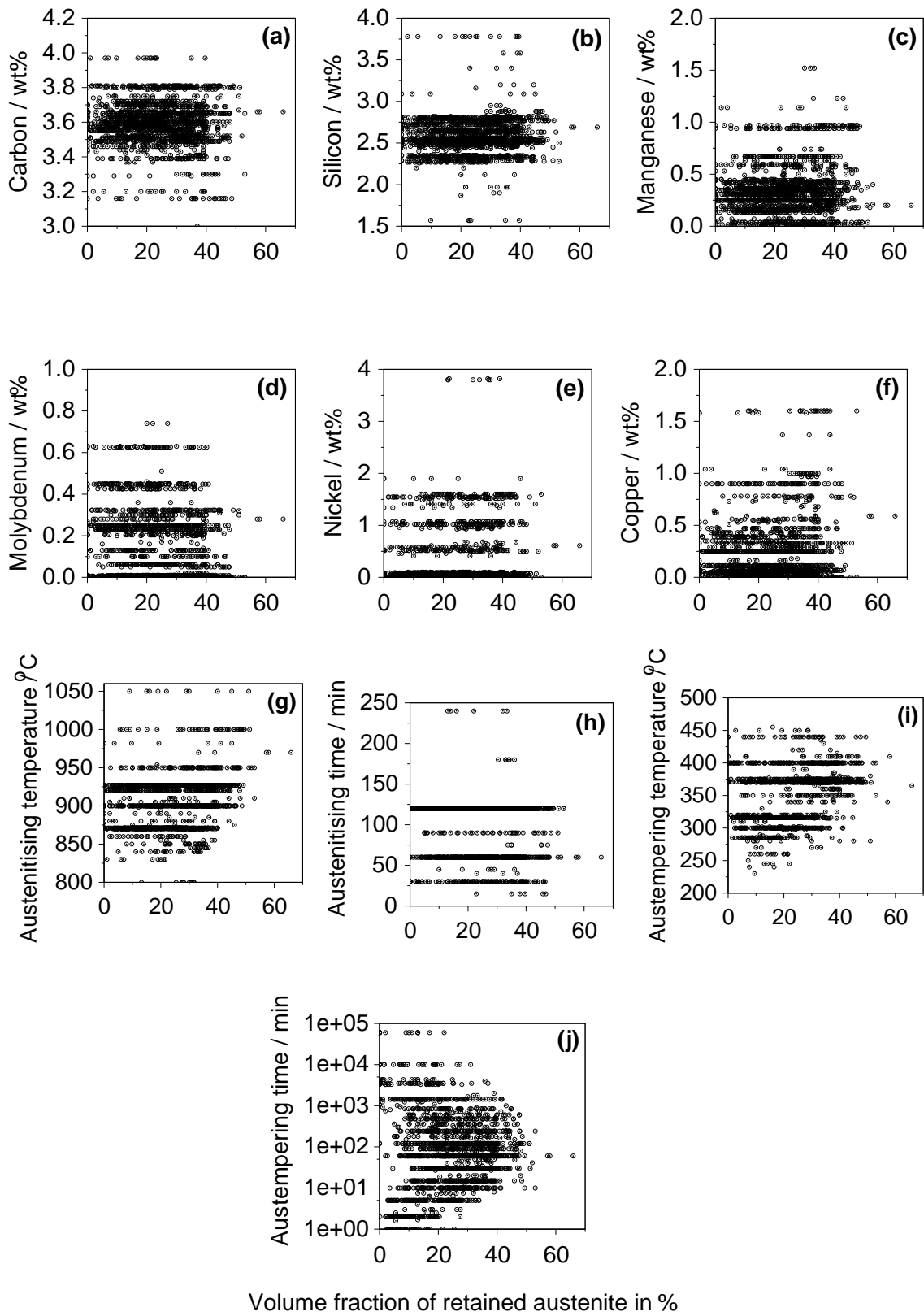


Figure 5.3: The database values of each variable versus the volume fraction in % of retained austenite.

5.3 Analysis

All the variables were normalised within a range of ± 0.5 . After this, the database was randomised and partitioned equally into test and training data sets. Training involves the derivation of the weights by the minimisation of the regularised sum of squared errors σ_ν . The complexity of the model is controlled by the number of hidden nodes, and the values of the regularisation constants [50], one associated with each input, one for biases and one for all weights connected to the output.

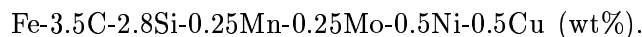
The inferred noise level σ_ν , as expected decreases as the number of hidden units (Fig. 5.4a). The number of hidden units was set by examining the performance of the model on unseen test data. The test set error tends to go through a minimum at an optimum complexity (Fig. 5.4b). After the best models are ranked using the values of the test errors, committees are then formed by combining the predictions of the best L models, where $L = 1, 2, \dots$; the size of the committee. A plot of the test error of the committee versus its size L gives a minimum which defines the optimum size of the committee as shown in Fig. 5.4c. The test error associated with the best single model is greater than that of any of the committees. However, the committee with sixteen models was found to have an optimum membership with the smallest test error (Fig. 5.4c). Once the optimum committee was chosen, it was retrained on the entire dataset without changing the complexity of each model, with the exception of the inevitable and relatively small adjustments to the weights.

Fig. 5.5 shows normalised predicted values versus experimental values for the best model in the training and test datasets. The predictions made using the optimum committee of models are illustrated in Fig. 5.5c.

Fig. 5.6 illustrates the significance of each of the input variables as perceived by the neural network in influencing the retained austenite content. The magnitude of the significance is a measure of the extent to which a particular input explains the variation in the retained austenite content. As expected, the austempering time and temperature, and the austenitisation temperature feature prominently.

5.4 Application of the model

The model can be used in extrapolation given that it indicates appropriately large uncertainties when knowledge is sparse. The basic cast iron chosen to study the variations has the chemical composition



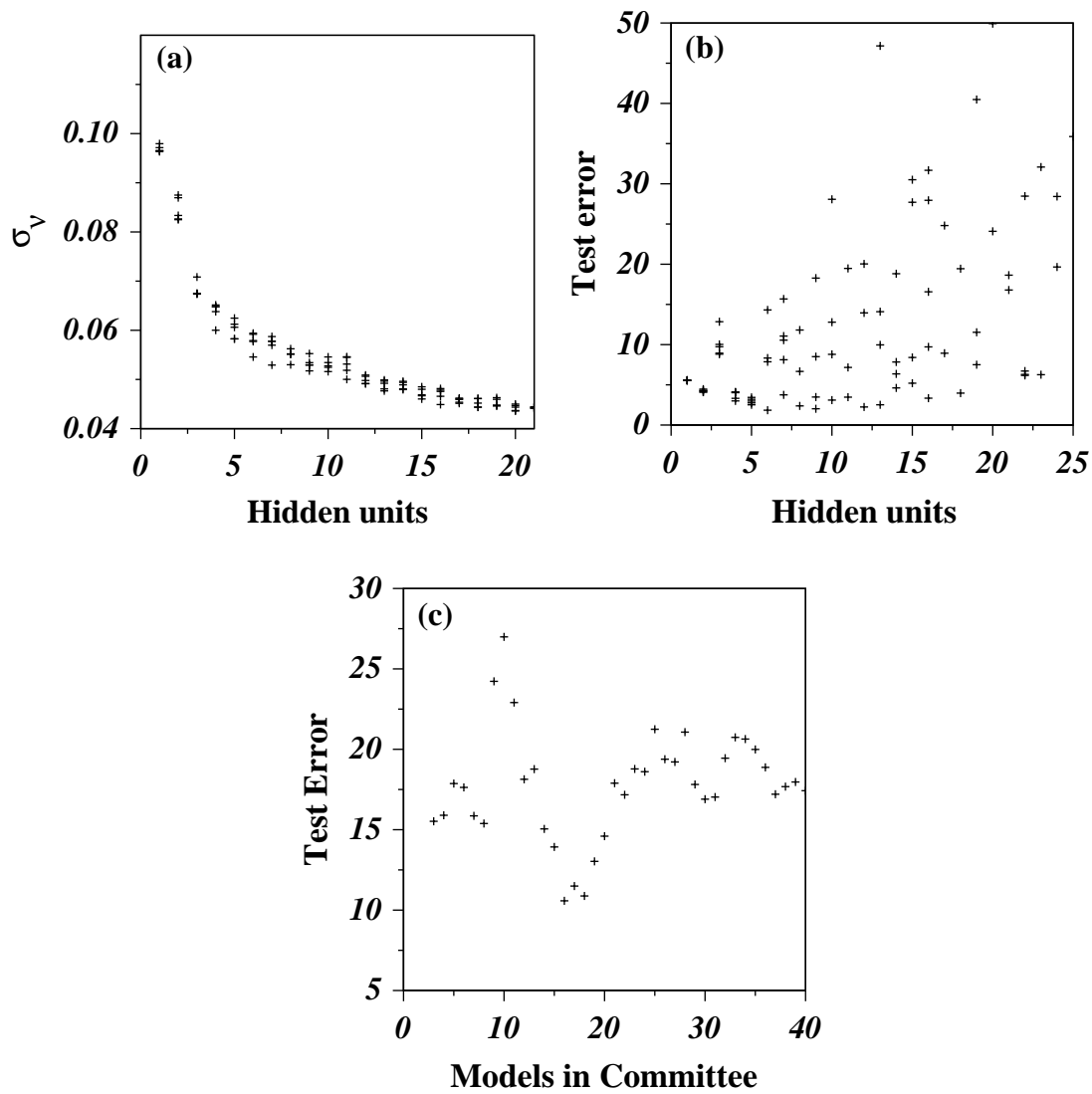


Figure 5.4: (a) σ_ν and (b) test error as a function of the number of hidden units; (c) the test error plotted as a function of the number of models in a committee of models.

According to the literature [14, 16, 85, 3] this should have a low tendency to form intercellular carbides; at the same time, chemical segregation should not be excessive. The austemperability is expected to be around 34.3 mm in diameter, calculated using a relationship due to Lee and Voigt [86]. Unless otherwise stated, the heat treatment parameters used in this chapter are: $T_\gamma = 900^\circ\text{C}$, $t_\gamma = 60$ min, $T_A = 370^\circ\text{C}$ and $t_A = 60$ min.

Fig. 5.7 illustrates the effect of two different austenitising temperatures on the calculated quantity of retained austenite. Consistent with the first stage reaction, V_{γ_r} at first increases, but then starts to decrease with the onset of stage II which is connected with carbide precipitation. Calculations like these can easily be used to define the heat treatment window, which is marked on each of the plots.

Although the influence of T_γ will be discussed in more detail later, Fig. 5.7a shows

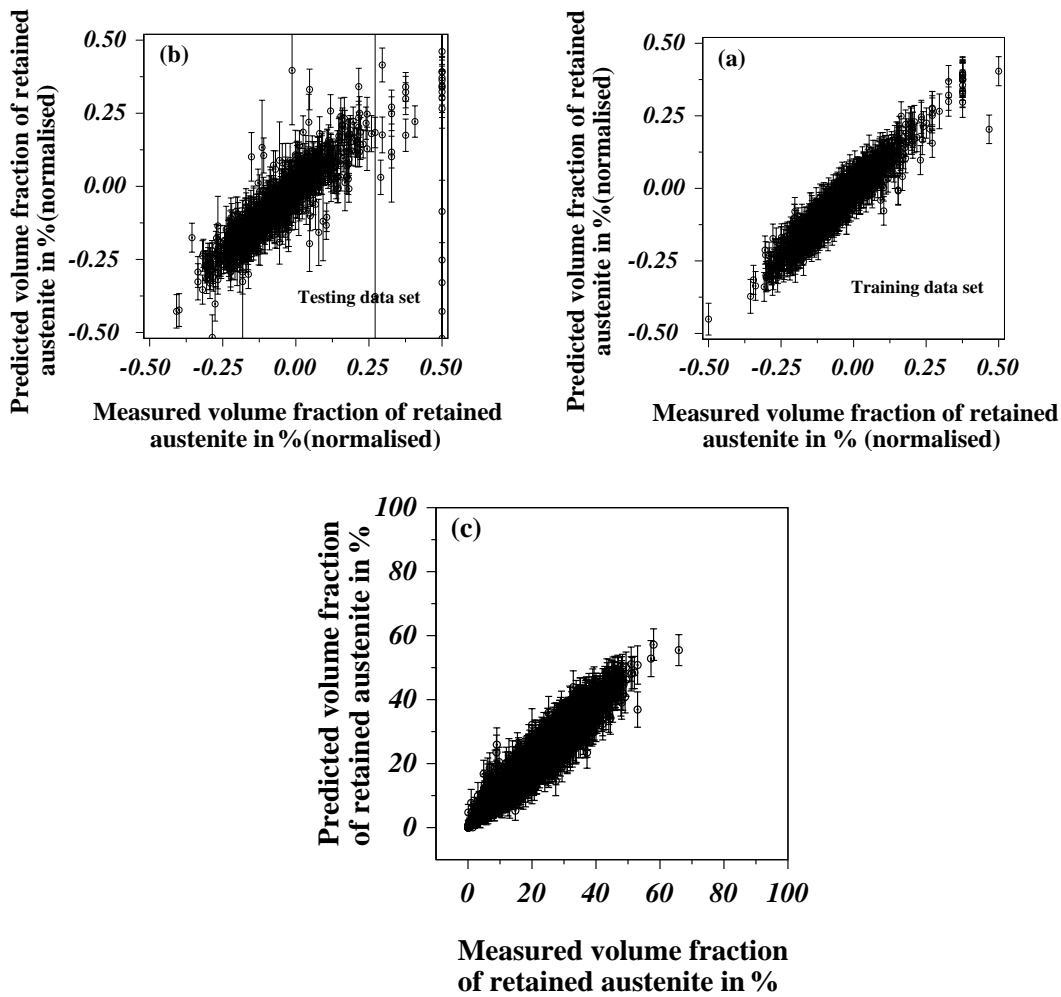


Figure 5.5: Predictions made using the best model, selected as the one having the smallest test error. (a) Training data set. (b) Test data set. (c) Predictions made on the entire dataset using the optimum committee.

that for an austenitising temperature of 900 °C, the end of stage I reaction occurs after approximately 30 min whilst for $T_\gamma = 950$ °C (Fig. 5.7b) it happens after some 50 min. This behaviour has been explained by several researchers [60, 68]. A decrease in T_γ accelerates the bainite reaction kinetics because it leads to a reduction in the equilibrium carbon concentration of the austenite. Consequently, the amount of austenite that is retained is reduced, as predicted by the model.

5.4.1 Carbon

Fig. 5.8a shows that V_{γ_r} hardly changes as the carbon concentration of the cast iron (\bar{x}) is increased from 3.1 to 3.7 wt%. In an ideal Fe–C binary cast iron, there should be no change in the equilibrium carbon concentration of the austenite (x_γ) as the average concentration \bar{x} is increased, although there would be an increase in the fraction of graphite. However, the cast iron studied is not a binary alloy but contains many other elements

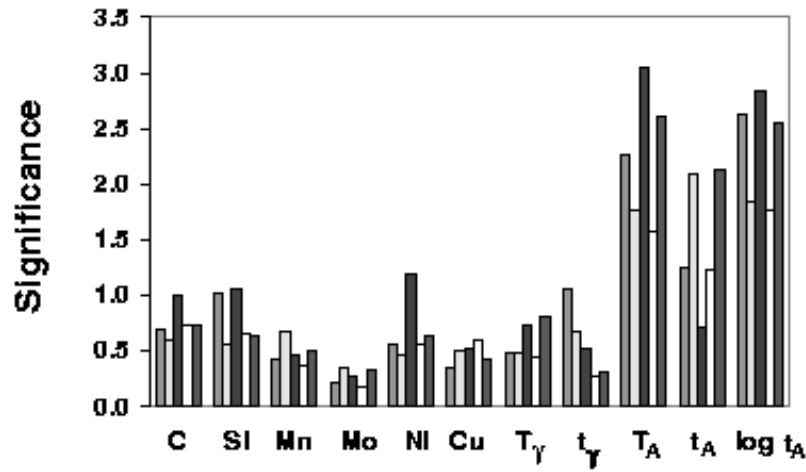


Figure 5.6: Model perceived significance of input parameters in the best five models from the committee trained on the volume fraction of retained austenite. σ_w values are presented for each variable.

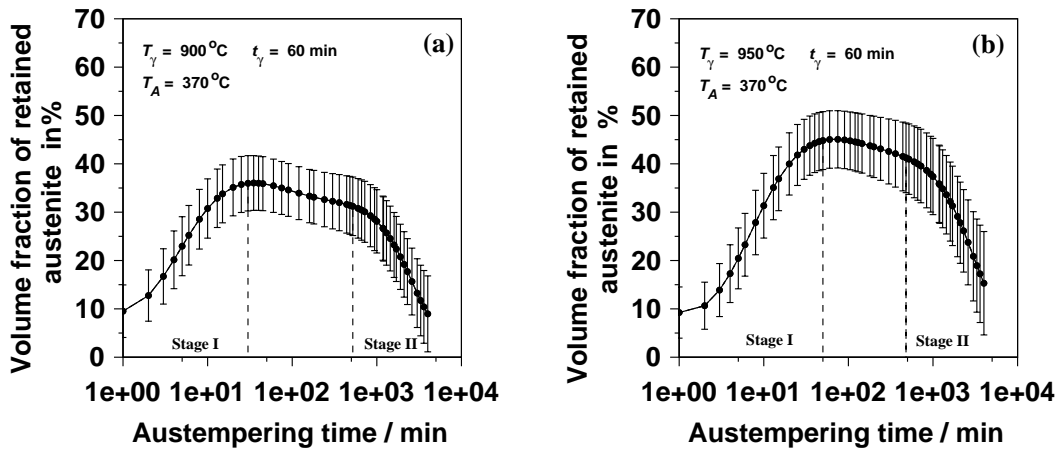


Figure 5.7: Predictions of volume fraction of retained austenite in % as a functions of austempering time for an alloy Fe-3.5C-2.8Si-0.25Mn-0.25Mo-0.5Ni-0.5Cu (wt%), a) at $T_\gamma = 900$ °C and b) at $T_\gamma = 950$ °C.

which give the material additional degrees of freedom according to the phase rule. In such a multicomponent system, a change in \bar{x} may in fact alter x_γ .

C (wt%)	3.1	3.2	3.3	3.4	3.5	3.6	3.7	3.8	3.9	4.0
x_γ (wt%)	0.7830	0.7826	0.7822	0.7818	0.7813	0.7809	0.7805	0.7801	0.7797	0.7793

Table 5.2: Carbon content of austenite (x_γ) at 900 °C calculated using MTDATA with SGTE database, for an iron of composition Fe-C-2.8Si-0.25Mn-0.25Mo-0.5Ni-0.5Cu (wt%).

Such effects can be studied using MTDATA which is a computer program that in

combination with the SGTE database [34] permits the calculation of phase diagrams in multicomponent, multiphase systems. Table 5.2 shows the results of those MTDATA calculations in our cast iron allowing for just two phases (ferrite and free graphite) at the austenitising temperature. The results do reveal that the equilibrium value of x_γ at 900 °C remains almost constant, but there is a slight decrease as \bar{x} is increased.

The same figure (Fig. 5.8a) shows that there is a significant rise in retained austenite beyond 3.6 wt%. Although there is little information to support this behaviour, a possible answer would be that it takes longer for equilibrium to be reached when \bar{x} is large.

5.4.2 Silicon

Silicon levels in excess of 2 wt% are generally recommended for ductile irons; the silicon promotes graphite formation but equally importantly, it is essential to delay the precipitation of cementite. This leads to the development of the mixed bainitic ferrite and carbon-enriched austenite microstructure which is so beneficial to the mechanical properties of ADI [4]. An increase in the Si concentration from 2.5 to 3.1 wt% has been shown to delay the onset of the stage II reaction from 70 min to 4.5 h [3]. This might allow for more bainitic transformation and consequently more austenite carbon enrichment without precipitation of carbide. Therefore, an increase in retained austenite is expected as is observed in Fig. 5.8b. However, beyond 3.2 wt% Si, which seems to be the optimum silicon content, there is a drop in retained austenite. This might be caused by the formation of islands of pro-eutectoid ferrite in the bainite structure as found by Gagne [87] in his experiments for an ADI with 3.7 wt% Si austenitised at the same temperature as in Fig. 5.8b (900 °C). The eutectoid temperature for this alloy is around 858 °C [87], assuming a homogeneous alloy. However, in practice there will be some regions where the silicon concentration could be higher than 3.7 wt% and eutectoid temperature near 900 °C [87].

5.4.3 Manganese

Manganese is added to ductile iron primarily to improve its hardenability, but it has a pronounced tendency to segregate during solidification, thereby causing the precipitation of complex Fe–Mn carbides at solidification–cell boundaries [64, 3, 88].

Fig. 5.8c shows that beyond about 0.7 wt%, manganese leads to a reduction in the quantity of retained austenite. This is easily understood because it greatly retards both the kinetics of the bainite reaction and the maximum amount of bainite that can form at any temperature [19], thereby reducing the extent to which austenite can be enriched with carbon. This, of course, reduces the stability of the residual austenite to martensitic transformation, causing the decline in V_{γ_r} .

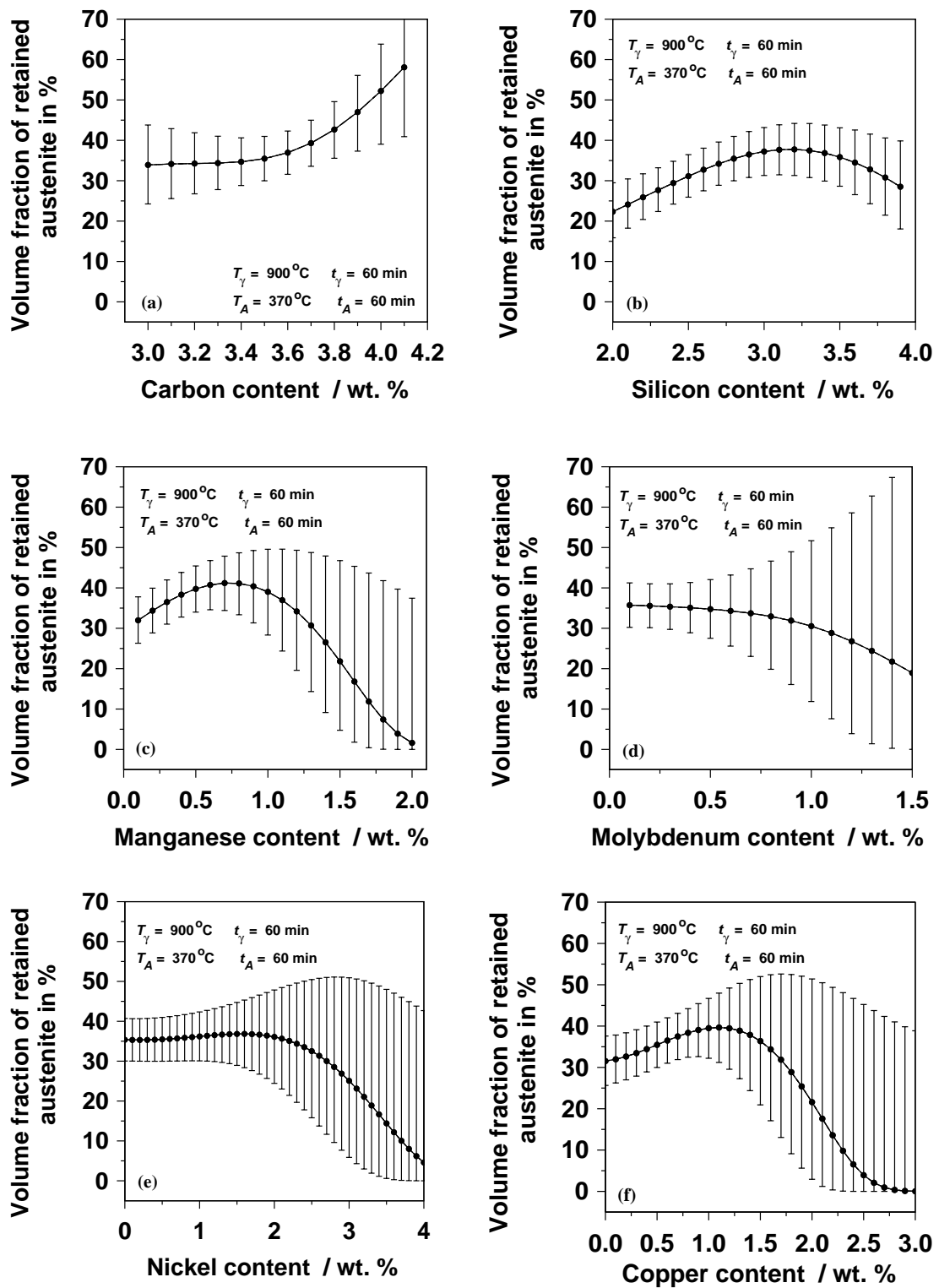


Figure 5.8: Predictions of volume fraction of retained austenite in % as a function of chemical composition (basic cast iron: Fe-3.5C-2.8Si-0.25Mn-0.25Mo-0.5Ni-0.5Cu wt%).

5.4.4 Molybdenum, copper and nickel

Molybdenum has a powerful influence on the hardenability of ductile irons and so is an essential alloying element for the production of large components. However, like man-

ganese, it segregates at cell boundaries during solidification to form carbides. The use of molybdenum should thus be limited. The molybdenum carbides are very stable and hardly dissolve during austenitisation.

Consistent with experimental data [89], Fig. 5.8d shows that for concentrations less than 0.5 wt%, molybdenum has hardly any effect on the retained austenite content; the predictions are too uncertain for larger concentrations.

It has been argued [16, 85] that the net effect of molybdenum is to delay the stage II although there are contradictory reports from BCIRA [15]. The present model can be used to clarify this. Fig. 5.9 shows with considerable certainty that there is no major difference between irons containing different molybdenum concentrations except for very long austempering times, where the alloy richest in molybdenum is more resistant to stage II decomposition.

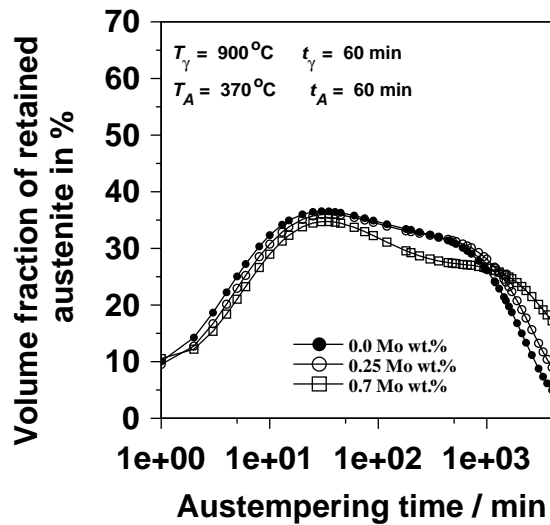


Figure 5.9: Influence of molybdenum on the retained austenite content for an iron Fe-3.5C-2.8Si-0.25Mn-Mo-0.5Ni-0.5Cu (wt%).

There are contradictory claims about the influence of copper on the retained austenite content [4, 19]. The present model, which is based on the analysis of a very large database, shows that copper does indeed stabilise austenite and hence leads to a greater fraction of retained austenite at concentrations less than 1 wt%. Naturally, any element which increases the hardenability (e.g. Mn, Ni, Cu) will retard the bainite reaction so that excessive alloying must eventually lead to a smaller V_{γ_r} , as is apparent in Fig. 5.8f.

Nickel is usually added to improve hardenability since copper alone does not provide sufficient hardenability to successfully austemper thick castings. However, as shown in Fig. 5.8e nickel concentrations less than 2 wt% does not seem to have any influence on retained austenite as copper does seem to have. More experiments are needed for nickel

concentrations higher than 2 wt%. This is inferred from the large error bars.

5.4.5 Austenitising conditions

The austenitising temperature and time determines the carbon concentration x_γ of austenite which is in equilibrium with the graphite at T_γ . Austenitisation must therefore greatly influence the stability of the austenite, as is evident from Fig. 5.10a. A higher T_γ corresponds to a larger x_γ . The effect of austenitisation time is less significant for $t_\gamma < 200$ min and the large error bars associated with longer times indicate a need for experiments. The effect of t_γ is small, presumably because equilibrium is established fairly quickly at these temperatures.

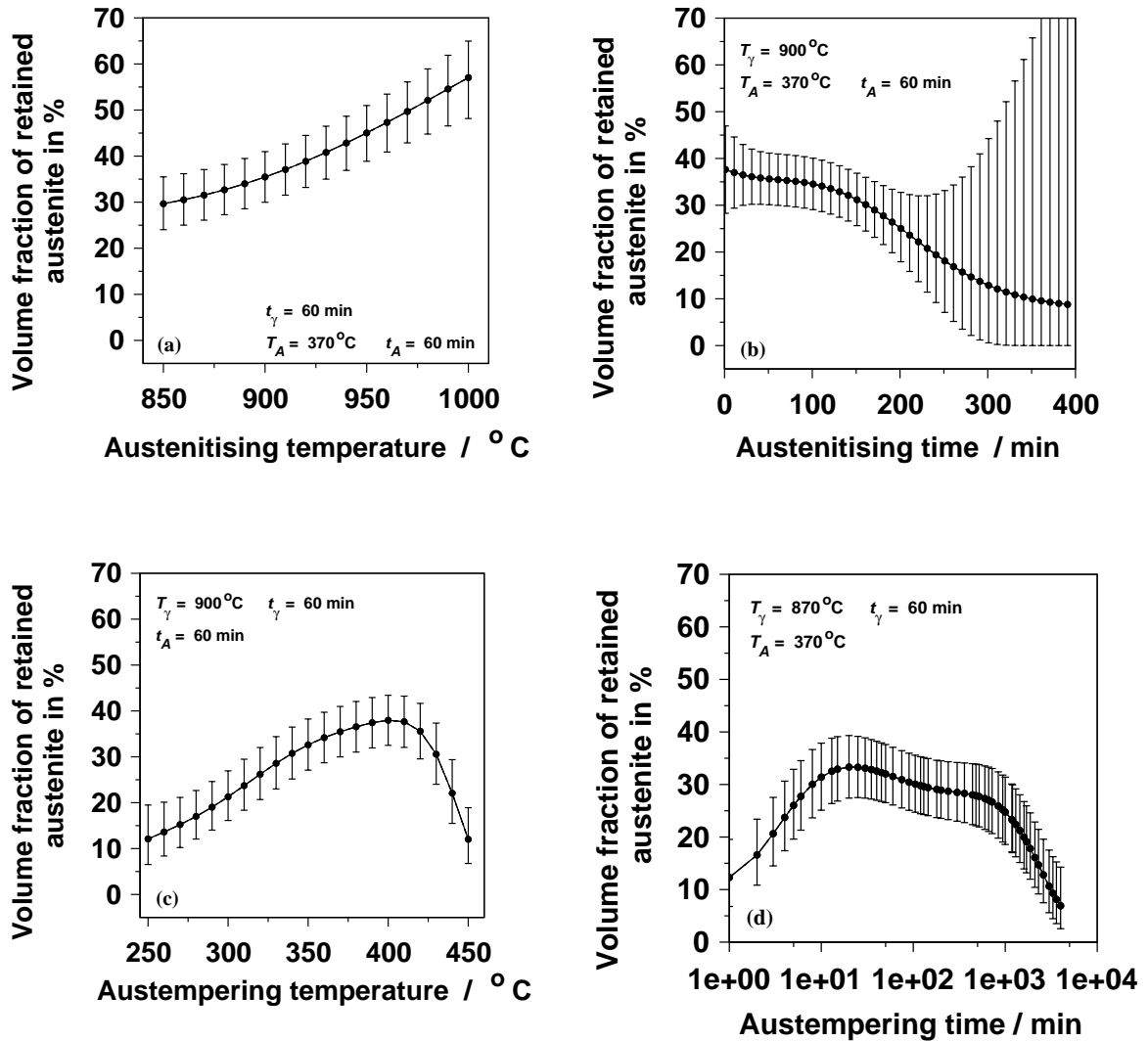


Figure 5.10: Predictions of volume fraction of retained austenite in % as a function of the heat treatment conditions (basic cast iron: Fe-3.5C-2.8Si-0.25Mn-0.25Mo-0.5Ni-0.5Cu wt%).

5.4.6 Austempering conditions

There are clearly major effects of T_A and t_A on the fraction of austenite that is retained at ambient temperature (Fig. 5.10). The predicted effects are precisely those expected.

Considering first the effect of austempering temperature, the fraction of bainite that can form is smallest at temperatures close to the bainite–start temperature B_S [88]. Consequently, the retained austenite content is close to zero at high temperatures. It increases as more bainite is able to form with increasing undercooling below B_S . The maximum arises because of two competitive effects: whereas an increase in the fraction of bainite raises x_γ , the bainite also consumes austenite so that less remains to be retained. Thus, at the lower temperatures, the latter effect dominates leading to a fall in the amount of retained austenite.

The effect of the austempering time is straightforward, that there are the stage I and stage II phenomena which lead to the behaviour illustrated in Fig. 5.10d.

5.4.7 Segregation effects

The effect of chemical segregation is illustrated in Fig. 5.11, by conducting calculations for typical matrix compositions in the vicinity of a graphite nodule and along the midpoint between adjacent nodules.

Notice that the curve which describes the intercellular region has less stable austenite than that for the vicinity of the nodules of graphite (Fig. 5.11). This is expected since the silicon concentration is the lowest in the intercellular region and manganese is the highest.

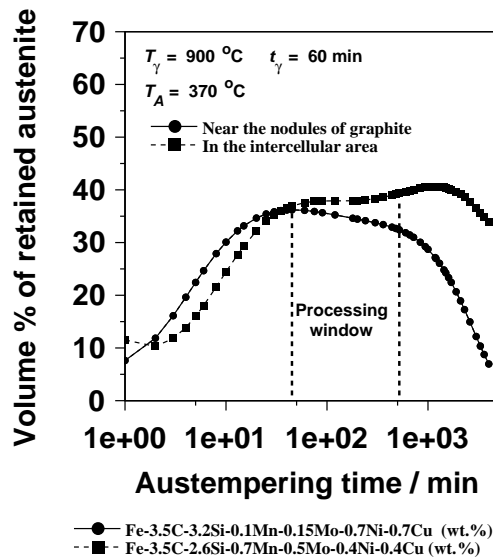


Figure 5.11: Predictions of volume fraction of retained austenite in % for the alloy described at the beginning of this section taking into account segregation of alloying elements towards nodules of graphite and intercellular area.

5.4.8 Contour plots

Fig. 5.12 shows some contour plots, many of which enable the selection of conditions for the optimisation of the fraction of retained austenite by visual inspection. The effect of manganese is remarkable since as manganese increases the field of maximum retained austenite is reduced dramatically as well as shifted towards longer times, consistent with the previous discussion about its effect on hardenability.

5.5 Conclusions

A neural network model has been developed to enable the estimation of the fraction of retained austenite in austempered ductile cast irons as a function of their chemical composition (C, Mn, Si, Ni, Mo, Cu), and the austenitisation and austempering parameters. The model successfully reproduces many experimentally observed trends. It can be exploited in two ways, first in the design of cast irons and their heat treatments, but also to identify whether experiments are needed in the future. If the model prediction is associated with a large uncertainty, then new experiments can be considered to be novel and useful.

The computer program associated with this work can be obtained freely from the *Materials Algorithms Project Library* on: <http://www.msm.cam.ac.uk/map/mapmain.html>

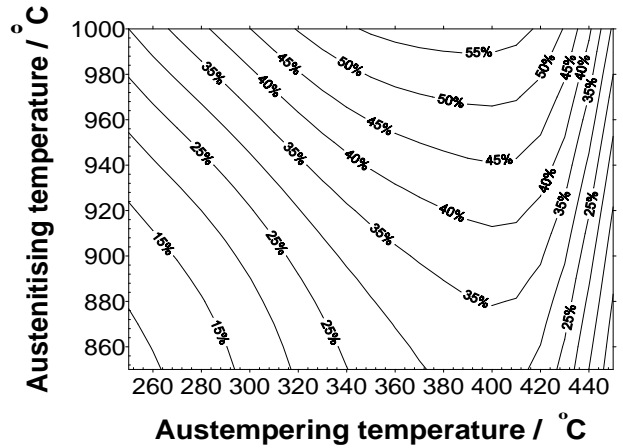
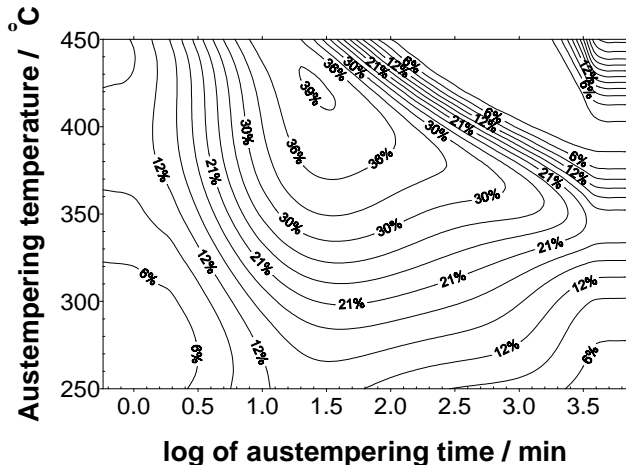
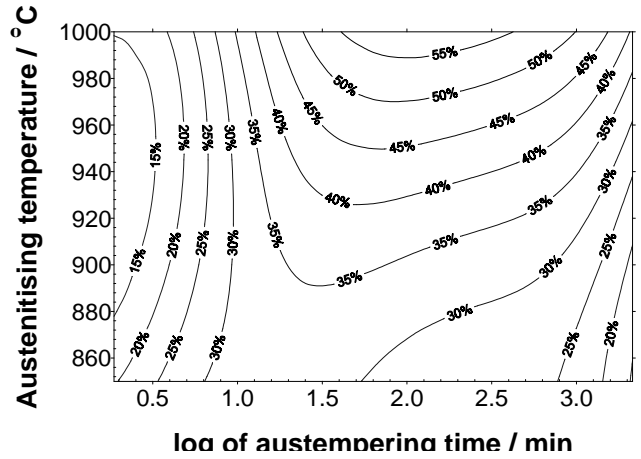
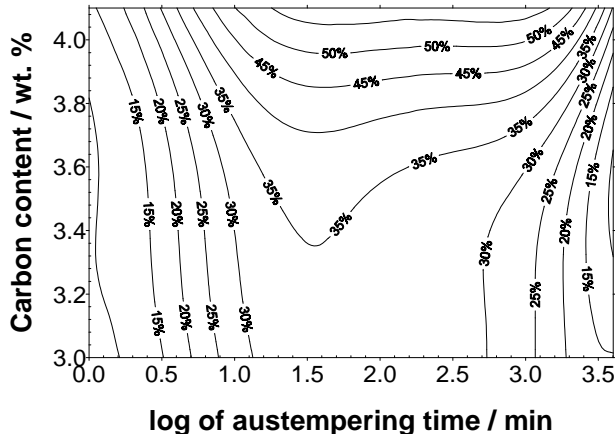
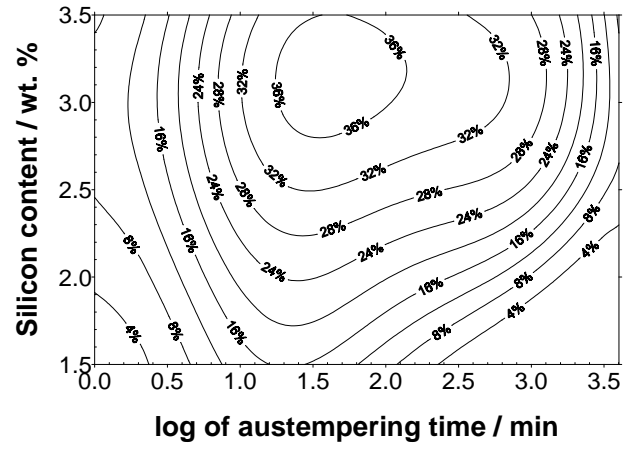
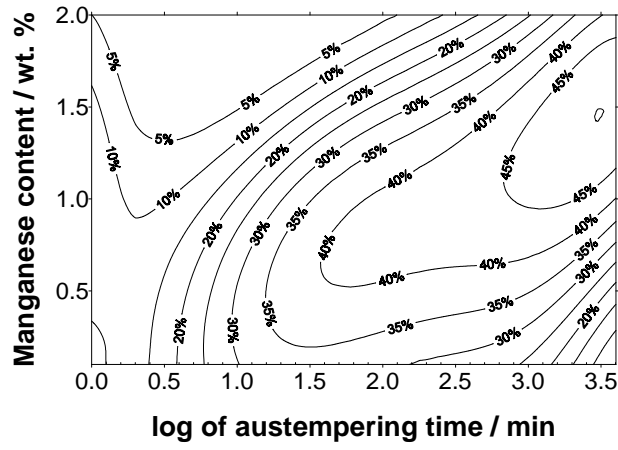


Figure 5.12: Contour plots of the volume fraction of retained austenite in % for (Fe-3.5C-2.8Si-0.25Mn-0.25Mo-0.5Ni-0.5Cu wt%) using $T_\gamma = 900\text{ }^\circ\text{C}$, $t_\gamma = 60\text{ min}$, $T_A = 350\text{ }^\circ\text{C}$, $t_A = 60\text{ min}$. The error bars associated with these predictions have been omitted for the sake of clarity.

Chapter 6

Physical Model for Retained Austenite

6.1 Introduction

The previous chapter described a model which predicts the volume fraction of retained austenite using an empirical analysis and experimental results published in the literature. The model seemed to capture the complexity of ADIs and can easily be used to find the austempering conditions needed to optimise the retained austenite content. A mechanism based model is presented here, for the estimation of the maximum fraction of retained austenite, as a function of the chemical composition and heat treatment.

6.2 The T_0 concept

Diffusionless growth requires that transformation occurs at a temperature below T_0 , when the free energy of bainite becomes less than that of austenite of the same composition. A locus of the T_0 temperature of the function of the carbon concentration is called the T_0 curve [90, 91], an example of which is plotted on the Fe–C phase diagram in Fig. 6.1. Growth without diffusion can only occur if the carbon concentration of the austenite lies to the left of the T_0 curve.

Suppose that the plate of bainite forms without diffusion, but that any excess carbon is soon afterwards rejected into the residual austenite. The next plate of bainite then has to grow from carbon enriched austenite (Fig. 6.2a). This process must cease when the austenite carbon concentration reaches the T_0 curve. The reaction is said to be incomplete [92, 93], since the austenite has not achieved its equilibrium composition (given by the Ae_3 curve) at the point the reaction stops. If on the other hand, the ferrite grows with equilibrium carbon concentration then the transformation should cease when the austenite carbon concentration reaches the Ae_3 curve.

It is found experimentally in the case of steels that the transformation to bainite does indeed stop at the T_0 boundary (Fig. 6.2b) The balance of the evidence is that

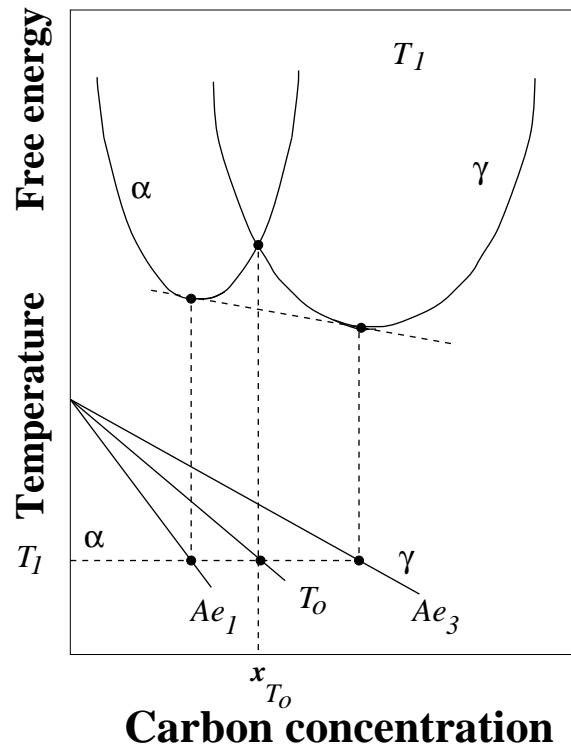


Figure 6.1: Schematic illustration of the origin of the T_0 curve on a Fe-C phase diagram. Austenite with a carbon concentration to the left of the T_0 boundary can in principle transform without any diffusion. Diffusionless transformation is thermodynamically impossible if the carbon concentration of the austenite exceeds the T_0 curve.

the growth of bainite below the B_S temperature involves the successive nucleation and martensitic growth of sub-units, followed in upper bainite by the diffusion of carbon into the surrounding austenite [94].

As discussed in chapter 1, the isothermal transformation of cast iron to generate bainite is known as “austempering”, a process which has two stages [52]. The end of the first stage corresponds to the maximisation of the fraction of bainitic ferrite and the enrichment of the austenite, the second with the onset of carbide precipitation. The time interval between these two stages is the heat treatment window [52, 25] (Fig. 8.16). The effect of austempering can be optimised within the confines of this window: too short an austempering time leads to an inadequate enrichment of the austenite and hence a low retained austenite content. Austempering beyond the commencement of stage II causes carbide precipitation and hence a reduction in the retained austenite content Fig. 8.16b.

It is known that the extent of transformation to bainite in ductile irons, as in steels, decreases ultimately to zero when increasing the isothermal transformation temperature towards the bainite-start temperature [93]. This is because the austenite can only transform to bainite if its carbon concentration is less than a value x_{T_0} given by the T_0 curve defined earlier. It follows [95] that the distribution of carbon at the point where the bainite

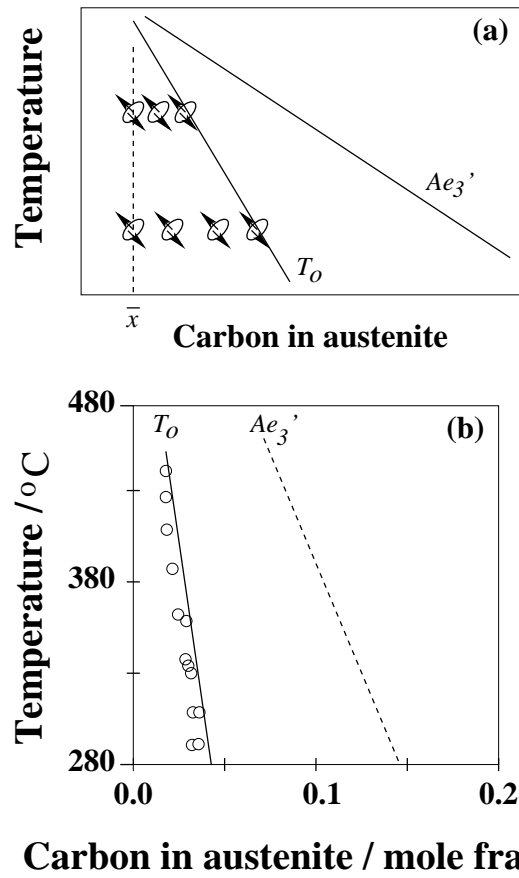


Figure 6.2: (a) Illustration of the incomplete reaction phenomenon. During isothermal transformation, a plate of bainite grows without diffusion, then partitions its excess carbon into the residual austenite. The next plate therefore has to grow from carbon-enriched austenite. This process continues until diffusionless transformation becomes impossible when the austenite composition eventually reaches the T_0 boundary. (b) Experimental data showing that the growth of bainite stops when the austenite carbon concentration reaches the T_0 curve (Fe-0.43C-3Mn-2.12Si wt% alloy) [94].

reaction stops is given ideally by

$$\bar{x} = V_{\alpha_b} x_{\alpha_b} + V_{\gamma} x_{T_0} \quad (6.1)$$

where \bar{x} is the average carbon concentration of the austenite prior to transformation, V_{α_b} and V_{γ} are the volume fractions of bainitic ferrite and residual austenite respectively, at the point where the reaction stops. x_{α_b} is the carbon concentration of the bainitic ferrite. Given that in silicon-rich alloys, such as the cast irons considered here, $V_{\gamma} = 1 - V_{\alpha_b}$, the maximum fraction of bainitic ferrite is given approximately by

$$V_{\alpha_b}^{\max} = \frac{x_{T_0} - \bar{x}}{x_{T_0} - x_{\alpha_b}} \quad (6.2)$$

Since x_{T_0} is the carbon concentration of the residual austenite, its value can be used to calculate the martensite-start temperature (M_S) of that austenite. If M_S falls below

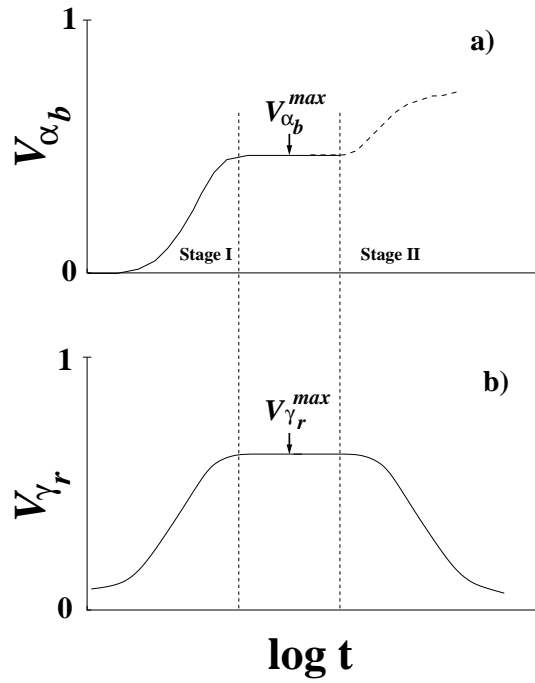


Figure 6.3: Schematic representation of (a) bainitic ferrite, and (b) retained austenite, as a function of time. V_{α_b} and V_{γ_r} represent the volume fractions of bainitic ferrite and retained austenite respectively.

room temperature, the austenite is retained completely. The maximum volume fraction of retained austenite $V_{\gamma_r}^{\max}$ will then equal $1 - V_{\alpha_b}^{\max}$ which is calculated using Eq. 6.2. On the other hand, if M_S exceeds room temperature $V_{\gamma_r}^{\max}$ can be calculated using the relationship first introduced by Koistinen and Marburger [96], which describes the progress of athermal martensitic transformation in a sample which is initially fully austenitic:

$$1 - V_{\alpha'} = \exp(-C_1[M_S - T]) \quad (6.3)$$

where $V_{\alpha'}$ is the volume fraction of martensite and C_1 is a constant obtained originally by fitting to experimental data. For the present purposes where we wish to determine the austenite retained, T is set to 20 °C.

For a specimen which is initially fully austenitic, the term $(1 - V_{\alpha'})$ in Eq. 6.3 is equal to $V_{\gamma_r}^{\max}$ because it represents the volume fraction of austenite which does not transform to martensite.

An alternative relationship due to Khan and Bhadeshia [95], based on the effect of autocatalytic nucleation is given by

$$-\ln(1 - V_{\alpha'})/V_{\alpha'} = 1 + C_2[M_S - T] \quad (6.4)$$

where $C_2 = 0.0029$ is another fitting constant and the temperatures are expressed in °C or Kelvin.

It has been pointed out in previous work [90, 97] and as shown in Fig. 6.4, that the concentration of carbon in the austenite may not be limited exactly by the T_0 line when the distribution of carbon in the austenite is not uniform. Indeed, studies specific to cast iron using X-ray diffraction, by Niesawaah and Hijhof [98], Ahmadabadi *et al.* [99], and Chang [100] have shown that the average carbon concentration in the retained austenite tends to be slightly higher than indicated by the T_0 curve. A part of the reason is that in a heterogeneous sample, X-ray diffraction tends to over-estimate the carbon concentration since it is only the high-carbon regions of austenite that are retained [101].

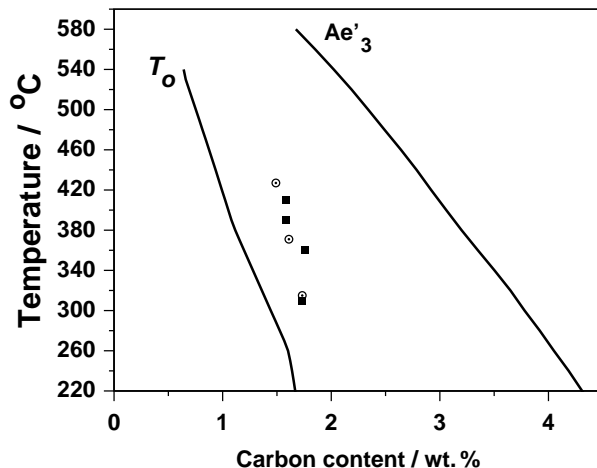


Figure 6.4: The calculated [91] T_0 and paraequilibrium Ae'_3 curves for Fe-3.5C-2.5Si-0.55Mn-0.15Mo-0.31Cu (wt%). Experimental values of x_γ are also shown. Squares correspond to the iron used for T_0 and Ae'_3 lines, whereas the open circles are for a similar iron studied by Rundman *et al.* [22] (Fe-3.5C-2.1Si-0.5Mn-0.71Mo wt%).

It is necessary to take account of the transition from upper to lower bainite in cast irons [21]. It is assumed here that the transition temperature is about 350 °C [102, 103]. The carbon content of upper bainitic ferrite was considered to be 0.03 (wt%) [91]. For lower bainite, the carbon locked in the ferrite as carbides must increase as the transformation temperature is reduced; this is discussed in the next section.

6.3 Carbon in lower bainite

Epsilon (ϵ) and other transition carbides often occur in lower bainite in high-carbon high-silicon steels [104, 105], as well as in ADI [14, 20, 106]. The detection of these carbides in lower bainite is important in that it demonstrates that a part of the carbon is not available for partitioning into the residual austenite. The presence of transition carbides may also imply the retention of a high carbon concentration in solution in the ferrite. Thus, Roberts *et al.* [107] reported dissolved carbon to a concentration of about 0.25 (wt%) during the precipitation of ϵ carbide. Kang *et al.* [108] made *in situ* observations using hot-stage

transmission electron microscopy of the precipitation of carbides within lower bainite and reported a supersaturation of the order of 0.3 (wt%) for a high-silicon steel transformed to bainite at 310°C.

In chapter 3, it was demonstrated that carbides can be found within bainitic ferrite for austempered ductile iron Fe-3.5C-2.5Si-0.55Mn-0.15Mo-0.31Cu (wt%) austenitised at 950 °C and austempered at 250 °C for 50 and 90 min. There is good evidence that the amount of carbon that is precipitated from supersaturated ferrite during the bainite transformation, in the form of carbides, increases as the transformation temperature is reduced [59]. Indeed, this constitutes the mechanism for the transition from upper to lower bainite as the transformation temperature is reduced. A profile illustrated in Fig. 6.5 was therefore determined by optimising the fit between the measured retained austenite content (Fig. 3.9) for transformation temperatures less than 350 °C, and that calculated using Eqs. 6.2, and 6.4.

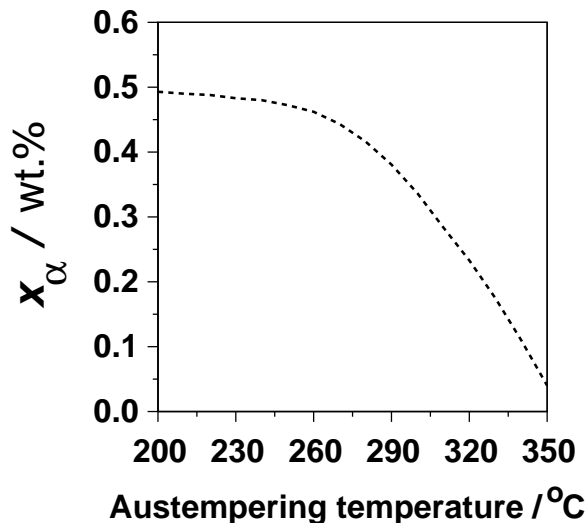


Figure 6.5: Assumed concentration of carbon trapped in lower bainitic ferrite, in the form of carbides and in solution, as a function of temperature.

6.4 Predictions of $V_{\gamma_r}^{\max}$ using the model

Eq. 6.2 for the calculation of the maximum volume fraction of bainite, and Eq. 6.4 which is due to Khan and Bhadeshia, were used in conjunction with the curve illustrated in Fig. 6.5, to estimate $V_{\gamma_r}^{\max}$ for ADI as a function of chemical composition and heat treatment. Predictions using Eq. 6.3 showed no significant difference with those using Eq. 6.4. The relevant computer program for doing these calculations was linked dynamically to MTDATA [34] which is a commercially available phase diagram calculation software. The database *PLUS* for solutions was used and the phases allowed at austenitising temper-

ature were graphite and austenite. The role of MTDATA in the present work was to enable the estimation of the carbon concentration in the austenite which is in equilibrium with graphite at the austenitisation temperature, *i.e.* \bar{x} , for any chemical composition and austenitising temperature. MTDATA was also used to calculate the M_S temperature of the retained austenite according to the method described by Cool [109]. The method requires thermodynamical calculations to obtain the free energy change for the austenite→ferrite transformation over a temperature range.

Predictions using the model are shown in Fig. 6.6, where experimental results were also plotted for comparison. These experimental results correspond to volume fraction of retained austenite in homogenised samples (Fig. 3.9). Full details of these results were given in chapter 3.

Fig. 6.6 also shows with a dashed line the predictions of the volume fraction of retained austenite taking into account that no carbon is trapped within lower bainite (Fig. 6.5). It can be seen that without making any correction for carbon trapped in lower bainite, the model greatly overestimates $V_{\gamma_r}^{\max}$.

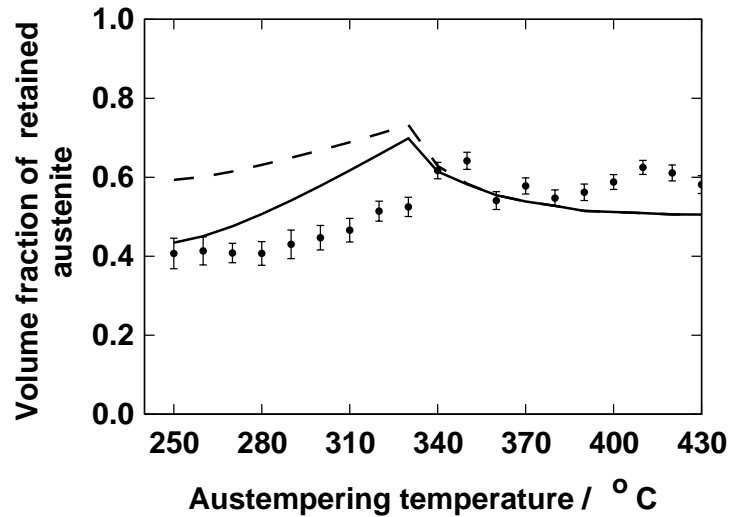


Figure 6.6: Model (solid line) compared with experiments. The dashed line shows the predicted trend assuming that carbon is not trapped within lower bainite. Iron composition is Fe-3.55C-2.5Si-0.55Mn-0.15Mo-0.31Cu (wt.%) Austenitising temperature $T_\gamma = 950$ °C.

There are two competing effects which explain the shape of the curve in Fig. 6.6. The maximum fraction of bainite that can form increases as the transformation temperature is reduced, simply because of the slope of the T_0 curve (Fig. 6.7). This in turn means that the carbon concentration x_{T_0} of the residual austenite is larger at lower temperatures. Carbon stabilises austenite and therefore, more of it would tend to be retained on cooling to ambient temperature.

The second, counteracting effect, is that the formation of bainite consumes austenite; less austenite is therefore available for retention as $V_{\alpha_b}^{\max}$ increases. This effect domi-

nates once $(1 - V_{\alpha_b}^{\max})$ approaches $V_{\gamma_r}^{\max}$, *i.e.* at the lowest of transformation temperatures (Fig. 6.7). This is the reason for the peak occurring at the point where there is a change in the factor controlling the retention of austenite.

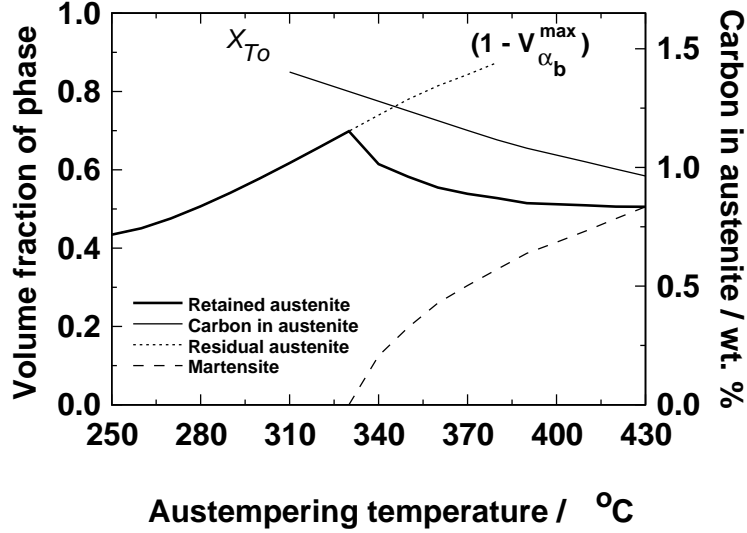


Figure 6.7: Variation of the calculated volume fraction of retained austenite as a function of the austempering temperature (Fe-3.5C-2.5Si-0.55Mn-0.15Mo-0.31Cu wt%). Austenitising temperature $T_{\gamma} = 950^{\circ}\text{C}$.

6.5 Discussion

The predicted retained austenite content is found to be in reasonable agreement with that observed in chapter 3. As stated previously, the maximum volume fraction of retained austenite depends on two competing effects: whereas an increase in the fraction of bainite raises the carbon concentration in the austenite, bainite also consumes austenite and hence less remains to be retained. At low temperatures, it is the latter effect which dominates leading to a fall in the amount of retained austenite.

For the lower transformation temperatures the model seems to overestimate the maximum volume fraction of retained austenite. One reason for this might be the discrepancy between the T_0 curve and the measured carbon concentrations illustrated in Fig. 6.4. Thomson *et al.* [110] have in their models used an empirical factor to correct the T_0 value in order to obtain better agreement with certain kinetic data. In our case this empirical factor needed to fit x_{T_0} to the measured carbon concentration would be 1.35. However, it is emphasised that this should be regarded as an upper limit to the uncertainty since as pointed out earlier, X-ray measurements tend to overestimate the carbon concentration of austenite in bainitic microstructures. Fig. 6.8 is therefore a comparison of measured data against a shaded region defined by calculations using the unadjusted T_0 curve and

one with the empirical adjustment. It appears therefore that the major reason for any discrepancy between theory and experiment is the inhomogeneous distribution of carbon in the residual austenite.

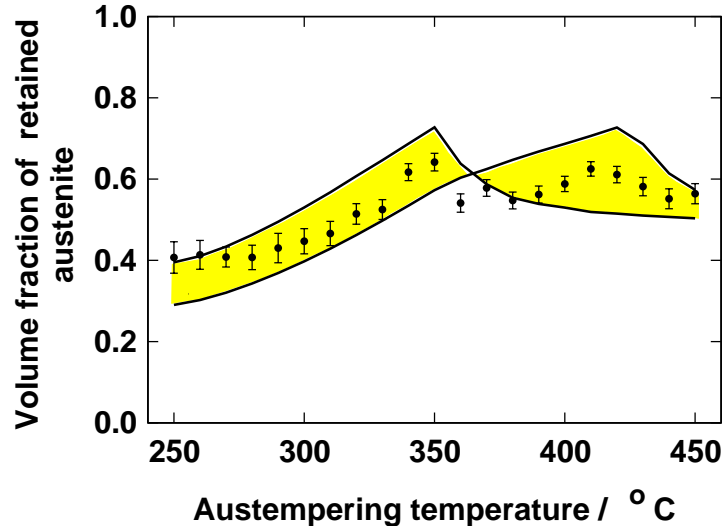


Figure 6.8: Comparison between measure data and predicted retained austenite using the present model (unadjusted T_0), and a model with an empirical adjustment of 1.35 times x_{T_0} .

6.6 Summary

There are many results in the literature [53, 62, 55], and new ones have been obtained in the present work, which show that the maximum content of retained austenite that can be obtained in austempered ductile cast iron peaks as a function of the isothermal transformation temperature.

It has been demonstrated that this behaviour can be understood in terms of two competing effects. The first is that the formation of bainite enriches the residual austenite so that more austenite is retained on cooling to ambient temperature. The second effect dominates at the lower transformation temperatures because the very formation of bainite leaves less austenite available for retention.

Consistent with the observation of lower bainite, it has been necessary to assume that the amount of carbon that is trapped within bainitic ferrite, as carbides and in solution, increases as the transformation temperature is reduced below 350 °C.

Chapter 7

Physical Model of Carbide Precipitation

7.1 Introduction

Prolonged austempering induces the precipitation of carbides from retained austenite. This precipitation is detected using microscopy, but there is no method to predict the kinetics of the process in ADI. The work presented here is an attempt to create a model using the theory of overall transformation kinetics.

7.2 Nucleation and Growth Transformation

The precipitation of carbides is a nucleation and growth process. The driving force for precipitation increases with undercooling below the equilibrium temperature, whereas the diffusion coefficient decreases exponentially as the temperature is reduced. It follows that the overall rate of reaction which combines nucleation, growth and impingement between different particles, will show a ‘C’ curve dependence (Fig. 7.1). This is because the driving force is minimal close to the equilibrium temperature whereas the diffusion coefficient is small at low temperatures. The rate of reaction is therefore rapid at an intermediate temperature where there is sufficient driving force and atomic mobility to sustain nucleation and growth. Hence the ‘C’ curve on an isothermal transformation diagram.

7.3 Classical Theory of Nucleation in Solids

Carbides have to nucleate during precipitation from austenite. Consider the precipitation of the carbide phase θ from the matrix γ which is supersaturated in solute X . For nucleation to occur there must be simultaneous fluctuation of composition and crystal structure, the new phase being separated from the old by an interface. The interface is a defect and the associated energy opposes the formation of the nucleus. If there is a shape

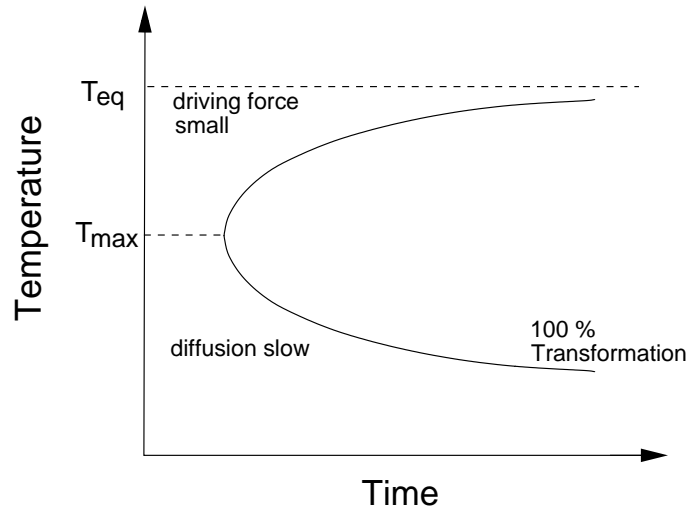


Figure 7.1: A schematic illustration of the C-curve kinetics, typical of nucleation and growth transformations. T_{eq} is the thermodynamic transformation temperature. T_{max} is the temperature at which the growth and nucleation rates are such that the transformation kinetics are most rapid.

change associated with nucleation there will be a corresponding strain energy contribution. Strain energy is excluded as an explicit term in the analysis which follows, partly because it has the effect of reducing the chemical free energy change and hence may vanish in empirical fitting, but also because there is no knowledge about the shape or size of the nucleus, knowledge which is necessary to estimate strain energy. The net change in free energy in forming a spherical embryo of radius r is

$$\Delta G = 4\pi r^2 \sigma + \frac{4}{3}\pi r^3 \Delta G_v \quad (7.1)$$

where σ is the γ/θ interfacial energy per unit area and $\Delta G_v = G_\theta - G_\gamma$ the chemical driving force for the transformation. The superposition of these two terms gives an overall free energy change which varies with the radius of the embryo as shown in Fig. 7.2.

The nucleus will be viable (*i.e.* will tend to grow rather than to dissolve) when an increase in its size leads to a reduction in the free energy (when $\frac{dG}{dr}$ is negative). As can be seen from Fig. 7.2 this occurs when the radius exceeds a critical value r^* by overcoming the activation barrier G^*

$$G^* = \frac{16\pi\sigma^3}{3(\Delta G_v)^2} \quad (7.2)$$

The embryos attempt to overcome the activation barrier with a frequency ν , the probability of success being $\exp(\frac{-G^*}{kT})$. There is a further barrier to consider, that for the transfer of atoms across the γ/θ interface, defined by the activation energy Q . Therefore, the nucleation rate per unit volume is given by

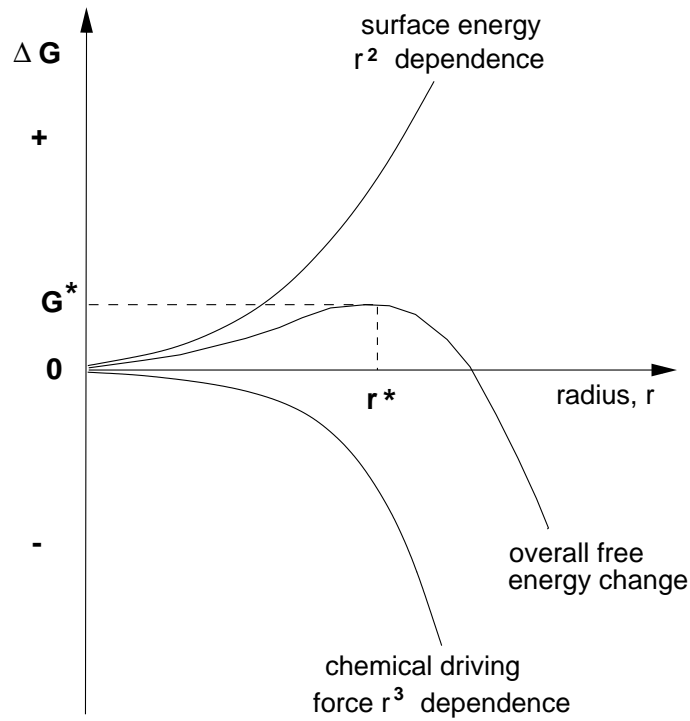


Figure 7.2: The free energy change associated with the formation of a nucleus as a function of radius r .

$$I = N_0 \nu \exp \left(-\frac{G^* + Q}{kT} \right) \quad (7.3)$$

The attempt frequency, ν , may be written as kT/h from classical theory so that

$$I = N_0 \frac{kT}{h} \exp \left(-\frac{G^* + Q}{kT} \right) \quad (7.4)$$

Q is temperature independent, while G^* is strongly temperature dependent (Eq. 7.2).

7.4 Free energy change during nucleation

Fig. 7.3a shows schematic free energy curves for the case where θ precipitates from a supersaturated matrix of γ . The overall driving force for the transformation, given by the familiar common tangent construction, is ΔG_0 . This, however, is not the driving force for the nucleation of θ , since the formation of minute nuclei cannot significantly alter the composition of γ . To find the correct driving force, the nucleation of θ may be considered in the following way

1. A small amount of material with the nucleus composition is removed from the γ phase. This material has a free energy given by the point P in Fig. 7.3a.
2. The atoms in this material are then rearranged from the γ to the θ structure.

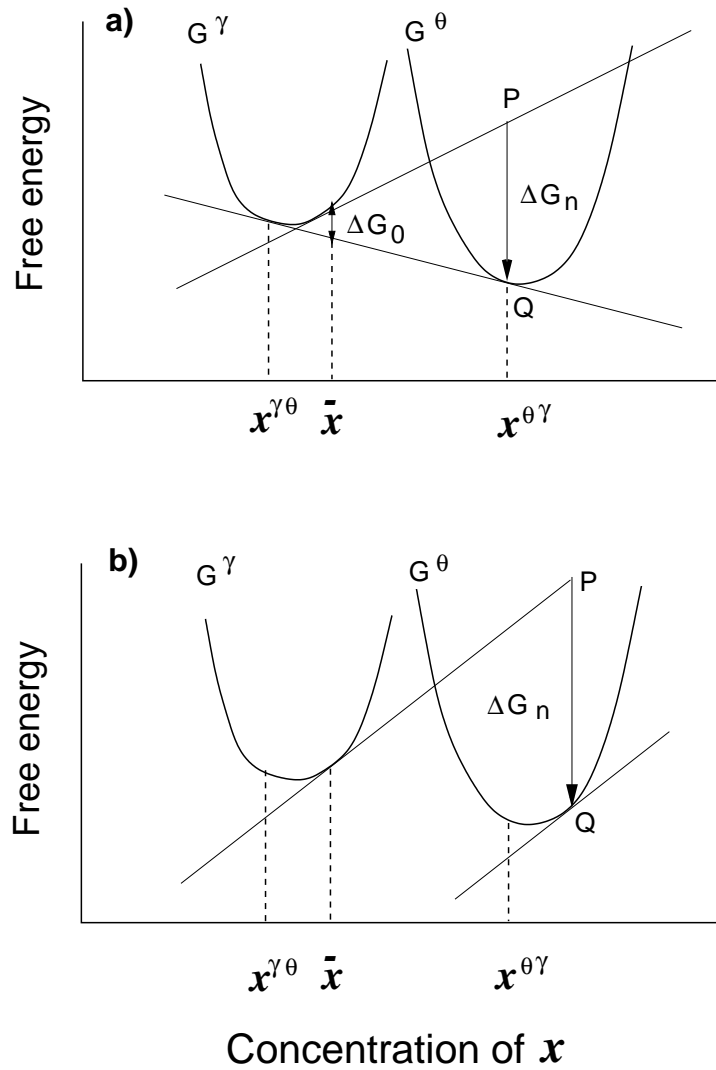


Figure 7.3: Construction for finding the driving force for nucleation (a) The tangent construction, assuming that θ nucleates with its equilibrium composition, (b) The parallel tangent construction which gives the maximum driving force.

3. The θ material is now replaced. The net decrease in free energy P-Q, is the driving force for nucleation per mole of θ .

The driving force for nucleation per mole, ΔG_n , may be converted into a driving force per volume of nucleus by dividing by the molar volume of θ , V_m^θ

$$\Delta G_v = \frac{\Delta G_n}{V_m^\theta} \quad (7.5)$$

In drawing Fig. 7.3a the composition of the θ nucleus was assumed to be equal to the equilibrium composition of the θ phase according to the common tangent construction. The free energy reduction on forming a nucleus could be increased, however, by forming a θ nucleus at a composition displaced from equilibrium, leading to the *parallel tangent construction* shown in Fig. 7.3b. In many cases, however, the compo-

sitions and driving forces predicted by both constructions are similar, and in such cases it is simpler to use the common tangent approximation.

7.4.1 Heterogeneous Nucleation

In the theory as described above it has been assumed implicitly that nucleation can occur with equal probability throughout the assembly. This state of *homogeneous* nucleation is rare. The presence of defects will enable nuclei to form with a much lower activation energy at specific sites in the matrix. This *heterogeneous* nucleation is common at grain boundaries, impurity particles and dislocations. This is because, at such sites, the creation of a nucleus will either relax lattice strain or destroy a defect, both of which liberate free energy, reducing the net free energy required to form a nucleus. The theory for homogeneous nucleation may be adapted for heterogeneous nucleation by using the values for site density and critical free energy appropriate to the site in question.

7.5 Overall Transformation Kinetics

Overall transformation incorporates nucleation and growth rates, but an estimation of the volume fraction requires impingement between particles to be taken into account [42]. There are basically two kinds of impingement [84]. Hard impingement is when particles growing from different sites touch each other. Soft impingement is when the particles interact via their diffusion fields. In this section, hard impingement will be introduced via the concept of extended volume [111]. Suppose that two particles exist at time t (Fig. 7.4); a small interval δt later, new regions marked a, b, c & d are formed assuming that they are able to grow unrestricted in extended space whether or not the region into which they grow is already transformed. However, only those components of a, b, c & d which lie in previously untransformed matrix can contribute to a change in the real volume of the product phase (θ). Assuming random nucleation, the possibility that new transformation occurs in untransformed parent phase should be $(1 - \frac{V^\theta}{V})$ where V^θ is the real volume of θ and the total volume is V . During the interval between t and Δt , the relationship between real volume fraction increase and extended volume fraction increase is therefore:

$$dV^\theta = \left(1 - \frac{V^\theta}{V}\right) dV_e^\theta \quad (7.6)$$

where dV^θ and dV_e^θ are changes of real volume and extended volume of θ during the time increment dt . Since a random distribution of precipitated particles is assumed.

Multiplying the change in extended volume by the probability of finding untransformed regions has the effect of excluding regions such as b , which clearly cannot contribute to the real change in volume of the product. For a random distribution of precipitated particles, this equation can easily be integrated to obtain the real volume fraction,

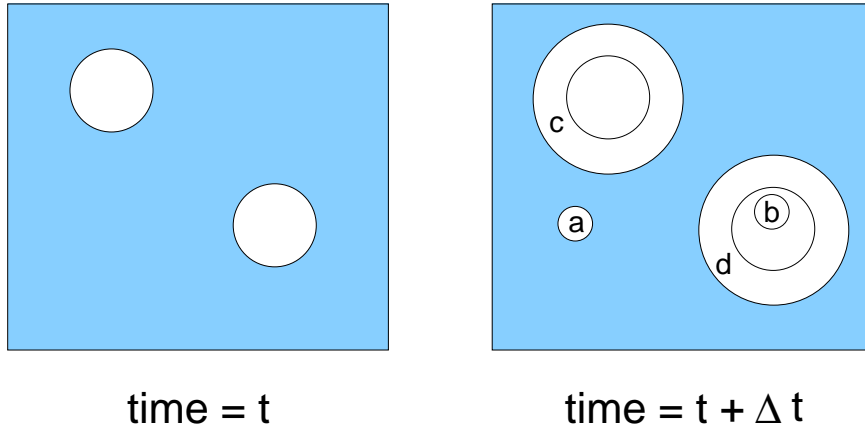


Figure 7.4: An illustration of the concept of extended volume. Two precipitate particles have nucleated together and grown to a finite size in the time t . New regions c and d are formed as the original particles grow, but a and b are new particles, of which b has formed in a region which is already transformed.

$$\frac{V^\theta}{V} = 1 - \exp \left\{ -\frac{V_e^\theta}{V} \right\} \quad (7.7)$$

The extended volume V_e^θ is straightforward to calculate using nucleation and growth models and neglecting completely any impingement effects. Consider a simple case where the θ grows isotropically at a constant rate χ and where the nucleation rate per unit volume is I . The volume of a particle nucleated at time τ is given by

$$v_\tau = \frac{4}{3} \pi \chi^3 (t - \tau)^3 \quad (7.8)$$

In the whole assembly the number of new θ regions nucleated in the time interval between $t = \tau$ and $t = \tau + d\tau$ is $IV^\gamma d\tau$ where V^γ is the instantaneous volume of the γ phase. If interactions between neighboring growing regions are neglected then the increase in the volume of θ particles nucleated in this very small time increment $d\tau$ is given by

$$dV_e^\theta = IV \left(\frac{4\pi}{3} \right) \chi^3 (t - \tau)^3 d\tau \quad (7.9)$$

where V is the total volume of the system.

On substitution into equation 7.4 and writing $\xi = V^\theta / V$, we get

$$dV^\theta = \left(1 - \frac{V^\theta}{V} \right) \frac{4}{3} \pi \chi^3 (t - \tau)^3 I d\tau \quad (7.10)$$

so that

$$-\ln\{1 - \xi\} = \frac{4}{3} \pi \chi^3 I \int_0^t (t - \tau)^3 d\tau \quad (7.11)$$

and

$$\xi = 1 - \exp\{-\pi \chi^3 I t^4/3\} \quad (7.12)$$

This equation has been derived for the specific assumptions of random nucleation, a constant nucleation rate and a constant growth rate. There are different possibilities but they often reduce to the general form:

$$\xi = 1 - \exp\{-k_A t^n\} \quad (7.13)$$

Where k_A and n are constants whose values depend on the nucleation and growth conditions. This equation is often used in the interpretation of experimental results since it is found that in many types of phase transformations the volume fraction of the product phase varies with time according to this type of relationship. The application of the Avrami method is now applied to model the kinetics of carbide precipitation from carbon-enriched austenite in ADI.

Carbide precipitation in austempered ductile iron is essentially identical to that in steels. It is possible therefore to draw on all the knowledge accumulated on steels. The precipitation process of concern here is from the carbon-enriched austenite associated with bainite. It is known [112] that this cementite sometimes decomposes into transition carbides (and α) rather than cementite. However, it is assumed for simplicity that cementite is the only carbide that forms. There are no adequate thermodynamic data available on the transition carbides.

Carbides which form during the bainite reaction or indeed during the tempering of martensite seem to grow by a displacive mechanism [42]. Such a mechanism must naturally involve the diffusion of carbon, but not substitutional solutes or iron atoms. The Fe:X ratio thus remains constant everywhere and subject to that constraint, carbon achieves equality of chemical potential. The cementite is then said to grow by *paraequilibrium* transformation. Babu *et al.* [113] using the atom probe technique have shown that the cementite obtained by tempering martensite is forced to inherit the silicon concentration of martensite. They did not find any redistribution of substitutional solutes even on the finest conceivable scale; the atom-probe technique has single atom resolution for both chemical and spatial analysis (Fig.7.5). These results establish the *paraequilibrium* mode of cementite precipitation.

7.6 The Model

7.6.1 Nucleation of cementite

The simplest way of incorporating nucleation into the model is to assume that cementite precipitates with a constant nucleation rate. The nucleation rate is given from the classical

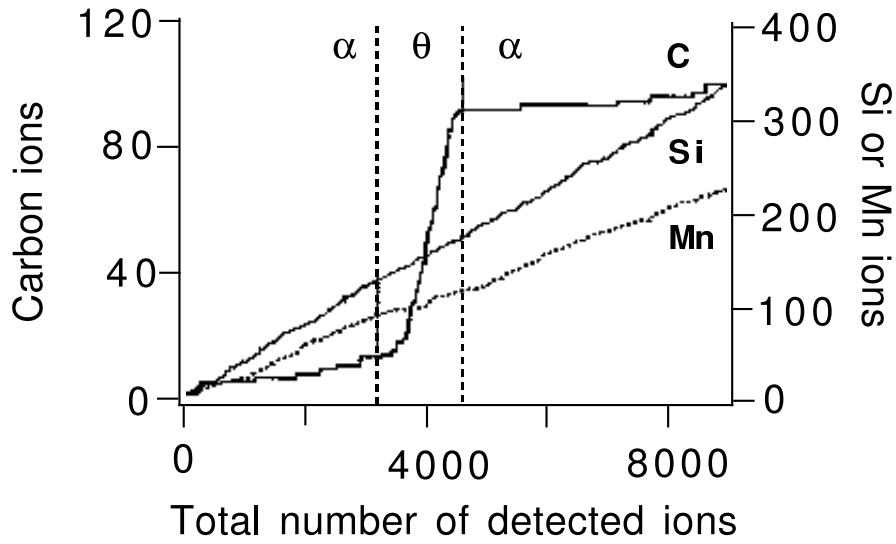


Figure 7.5: The results of an atomic resolution chemical analysis experiment across a pair of ferrite/cementite (α/θ) interfaces. Any changes in composition are represented by a change in the slope. It is shown that there is no partitioning of silicon or manganese when cementite precipitates from martensite. The alloy used has the chemical composition Fe-1.84C-3.84Si-2.95Mn at%, and was tempered at 350°C for 30 min [113].

nucleation theory (section 7.3) as

$$I = N_0 \frac{kT}{h} \exp \left(-\frac{G^* + Q}{kT} \right) \quad (7.14)$$

Where the activation energy barrier to nucleation G^* is given by

$$G^* = \frac{16\pi\sigma^3}{3(\Delta G_v)^2} \quad (7.15)$$

To evaluate the nucleation rate, values for the number density of nucleation sites N_0 , the driving force for nucleation ΔG_v , and the interfacial energy per unit area σ , are necessary.

The volume fraction of cementite must depend on the carbon content. It has been assumed [114, 115] that the number density of cementite particles N_0 in power plant steels is given by an empirical equation:

$$N_0 = 2.23 \times 10^{22} w_C - 10^{21} \text{ m}^{-3} \quad (7.16)$$

where w_C is the carbon concentration in wt%.

The activation energy Q was assumed to be that for self-diffusion of iron in austenite, at 286,000 J mol⁻¹ [116]. This is the activation energy for transfer of atoms across a coherent nucleus/matrix boundary.

MTDATA [34] has been used to calculate the driving force for nucleation of cementite from retained austenite. MTDATA is capable of calculating paraequilibrium for multi-component systems where many phases may coexist. It works by combining experimentally

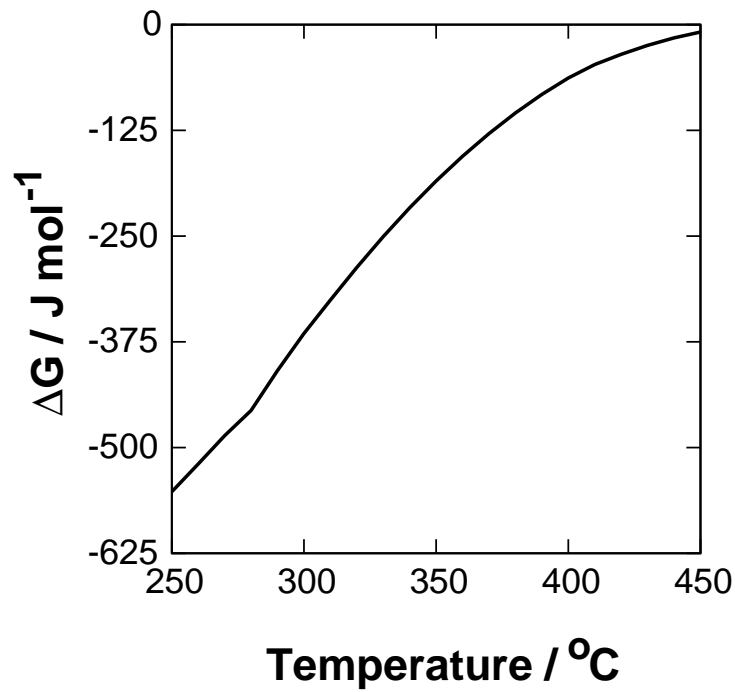


Figure 7.6: The free energy change for the precipitation of cementite in retained austenite with temperature for an Fe-3.5-2.4Si-0.1Mn-0.2Mo wt% ductile iron calculated using MTDATA [34].

determined data from the appropriate unary, binary and perhaps ternary sub-systems using thermodynamic theory to estimate what happen in larger systems. For any given system, MTDATA calculates the equilibrium composition and volume fractions of the phases present by minimising the Gibbs energy, along with the requirement for conservation of mass. It is possible to suppress the formation of any phase and recalculate the phase equilibria without that phase present. Although it can be used to predict what is possible thermodynamically, it cannot predict the time dependence of the microstructure which clearly requires kinetic modelling. Nevertheless, much useful information can be generated on the basis of thermodynamic calculations.

The following procedure was used in order to calculate the driving force for cementite precipitation. It is assumed that the decomposition of the austenite begins with the precipitation of cementite (θ).

The database *MIKE2* which allows silicon in cementite, and *PLUS* which is a database for the solutions, were utilised in MTDATA calculations. ΔG is for the change in free energy from γ to $\gamma' + \theta$, where γ' refers to austenite which is in paraequilibrium with cementite. The Gibbs energy of carbon-enriched austenite was first calculated at the austempering temperature allowing austenite as the only phase present (G_1); then the Gibbs energy of both austenite along with cementite ($\gamma' + \theta$) was calculated (G_2). θ was considered to grow with paraequilibrium. $\Delta G = G_2 - G_1 < 0$ is shown in Fig.7.6.

When the driving force ΔG is large as it is in this case, the value of G^* is small in

comparison with Q in Eq. 7.14, therefore, G^* can be neglected.

In addition, there is no information about sigma values for cementite growing in paraequilibrium. Previous work [114, 115] on precipitation of carbides in steels for power plants shows values of σ in the range of 0.2 to 0.29 J m⁻². However, experiments are necessary to find adequate values for the case of ADI.

7.6.2 Overall Transformation Kinetics

It is assumed that cementite grow as spherical particles, each of radius r . A particle that nucleated in the interval τ to $\tau + \delta\tau$ has a radius r_τ given by

$$r_\tau = \chi(t - \tau)^{\frac{1}{2}} \quad (7.17)$$

where χ is the three-dimensional parabolic growth constant. Since the volume of the particle is

$$v_\tau = \frac{4}{3} \pi r_\tau^3 \quad (7.18)$$

It follows that

$$v_\tau = \frac{4}{3} \pi \chi^3 (t - \tau)^{\frac{3}{2}} \quad (7.19)$$

From Eq. 7.11

$$-\ln\{1 - \xi\} = \frac{4}{3} \pi \chi^3 I \int_0^t (t - \tau)^{\frac{3}{2}} d\tau \quad (7.20)$$

which gives

$$\xi = 1 - \exp\left\{-\frac{4}{3} \pi \chi^3 I \frac{2}{5} t^{\frac{5}{2}}\right\} \quad (7.21)$$

The value of χ has been assumed to be the Zener [117] approximation for low supersaturation in terms of the composition of austenite (γ) and cementite (θ) which were also calculated using MTDATA [34].

$$\chi \simeq \sqrt{2D} \frac{(\bar{x} - x^{\gamma\theta})^{\frac{1}{2}}}{(x^{\theta\gamma} - \bar{x})^{\frac{1}{2}}} \quad (7.22)$$

where

D is the carbon diffusion coefficient in γ

\bar{x} is the mean carbon concentration of γ given by x_{T_0} calculated as in reference [91].

$x^{\gamma\theta}$ is the concentration of carbon in γ in equilibrium with θ

$x^{\theta\gamma}$ is the concentration of carbon in θ in equilibrium with γ

Thus, the final equation for the overall transformation kinetics of cementite precipitating by a paraequilibrium mechanism from enriched austenite is:

$$\xi = 1 - \exp \left\{ -\frac{4}{3} \pi D^{\frac{3}{2}} 2^{\frac{3}{2}} \frac{(\bar{x} - x^{\gamma\theta})^{\frac{3}{2}}}{(x^{\theta\gamma} - \bar{x})^{\frac{3}{2}}} I \left(\frac{2}{5} \right) t^{\frac{5}{2}} \right\} \quad (7.23)$$

It is important to make clear that the volume fraction of cementite calculated using Eq. 7.23 considers precipitation only from the retained austenite. Therefore, in order to find the real volume fraction of cementite in the whole ADI, the volume fraction of cementite needs to be multiplied by the volume fraction of retained austenite contained in it.

Table 7.1 indicates the values of the constants used to estimate the nucleation rate of cementite growing from austenite (I).

The parameters	The values used in calculations
Boltzmann constant, k	$1.380 \times 10^{-23} \text{ J mol}^{-1} \text{ K}^{-1}$
Plank's constant h	$6.6234 \times 10^{-34} \text{ J s}$
Gas constant, R	$8.314 \text{ J mol}^{-1} \text{ K}^{-1}$
Absolute temperature, T	Austempering temperature °K
Density of nucleation sites, N_0	$2.23 \times 10^{22} \text{ m}^{-3}$
Activation energy, Q	$286 \times 10^3 \text{ J mol}^{-1}$

Table 7.1: The parameters used in the calculation of the nucleation rate for cementite

The subroutines DIFFUS and MUCG46 used to calculate the diffusion coefficient of carbon in γ , and the value of x_{T_0} respectively, were included in a FORTRAN program. These subroutines are available on Materials Algorithms Library (MAP) [118]. The FORTRAN program was linked to MTDATA in the slave mode to enable kinetic calculations of cementite precipitation for any chemical composition of cast iron at any austenitisation and austempering temperature.

7.7 Predictions

The model was used to make predictions on a ductile iron of chemical composition Fe-3.5C-2.4Si-0.1Mn-0.2Mo wt% at different austempering temperatures; 300, 350 and 400°C. Fig. 7.7a shows these predictions as obtained from the model. It is observed that the volume fraction of cementite decreases with austempering temperature because the retained austenite at higher temperature contains less carbon. It also observed that at lower austempering temperature the precipitation process takes longer time. Fig. 7.7b is the same as in (a) but taking into account the volume fraction of retained austenite present

under particular austempering conditions. The volume fraction of retained austenite was obtained using the model described in chapter 5. The error bars of these calculations are not shown on the graphs for the sake of clarity, however, the values are indicated in Table 7.2.

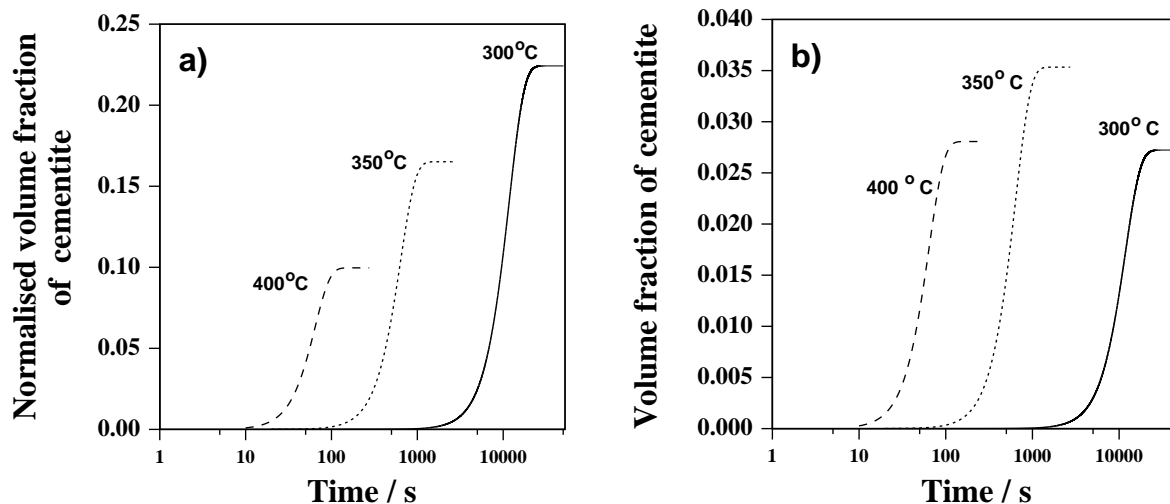


Figure 7.7: Predictions of cementite transformation in a ductile iron Fe-3.5C-2.4Si-0.1Mn-0.2Mo wt%. Austempered at 400, 350, 300°C. (a) Kinetics and normalised volume fraction of cementite as obtained from the model. (b) Kinetics and volume fraction of cementite taking into account the volume fraction of retained austenite present in the ADI at specific conditions.

7.7.1 Effect of Manganese

Manganese is expected to indirectly delay cementite precipitation because it retards the bainite transformation. Therefore, the enrichment of carbon in austenite and its subsequent decomposition to ferrite and cementite are also delayed. This is shown clearly in Fig. 7.8a, which shows volume fraction and kinetics of cementite without consideration of the volume fraction of retained austenite. Fig. 7.8b shows also the retardation effect of manganese, however, in this case the volume fraction of cementite precipitation is affected by the volume fraction of retained austenite calculated with the model of chapter 5.

7.7.2 Effect of Silicon

It is known that silicon retards the onset of cementite precipitation because its solubility in this carbide is very poor. Predictions changing the silicon content of an ADI were performed to see the effect of this element. Fig. 7.9a shows that the model qualitatively reproduces the expected effect of silicon. According to the model described in chapter 5, silicon increases the volume fraction of retained austenite. This is observed in Fig. 7.9b.

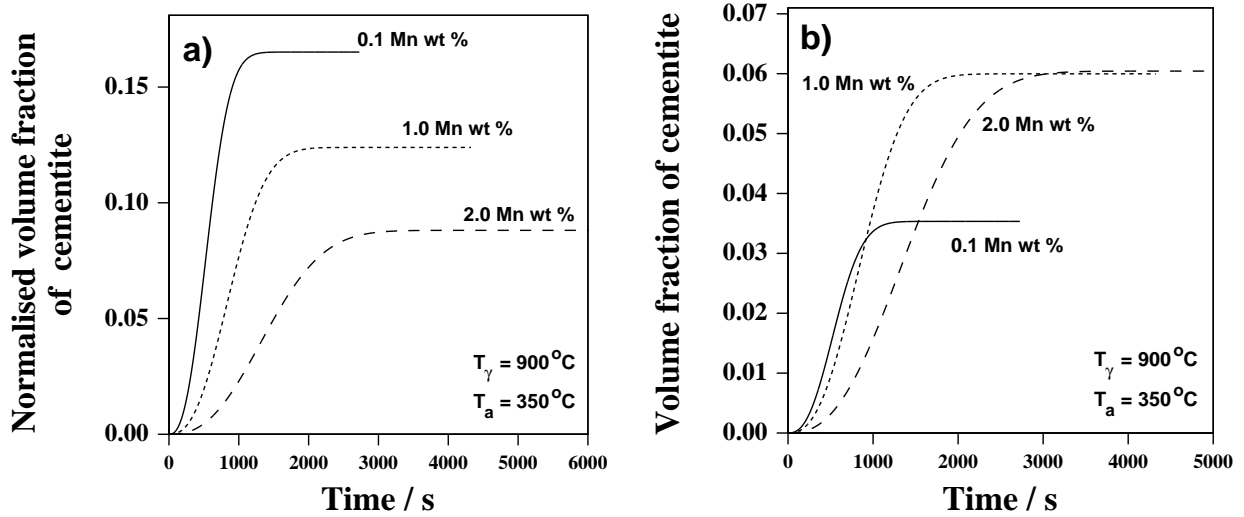


Figure 7.8: Predictions of cementite transformation in a ductile iron Fe-3.5C-2.4Si-Mn-0.2Mo wt%. Austempered 350°C with different manganese contents. (a) Kinetics and normalised volume fraction of cementite as obtained from the model. (b) Kinetics and volume fraction of cementite taking into account the volume fraction of retained austenite calculated using the model of chapter5.

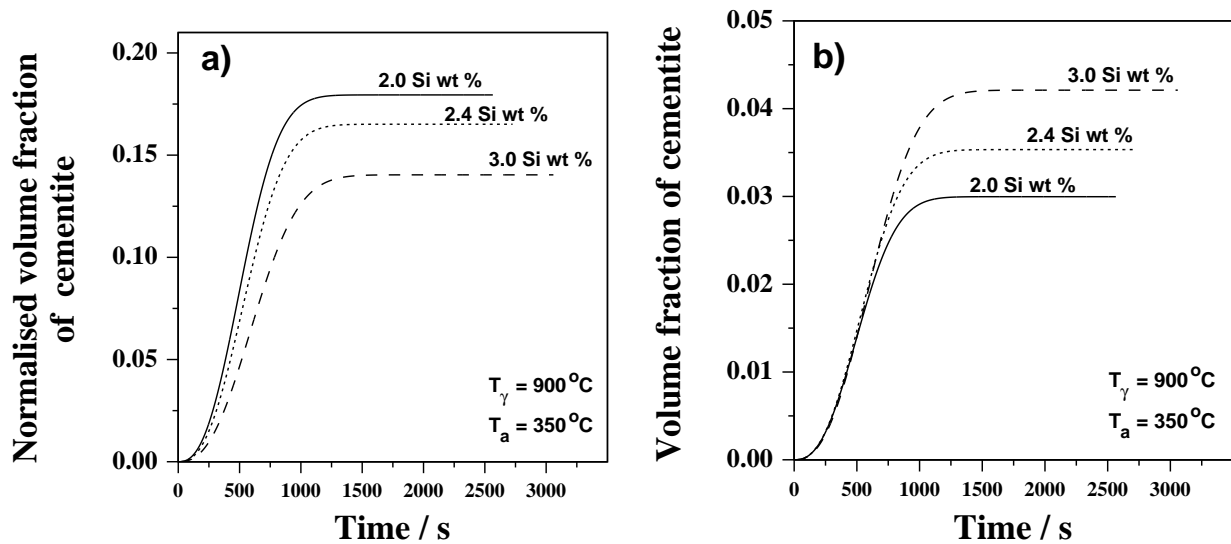


Figure 7.9: Predictions of cementite transformation in a ductile iron Fe-3.5C-Si-0.1Mn-0.2Mo wt%. Austempered 350°C with different silicon contents. (a) Kinetics and normalised volume fraction of cementite as obtained from the model. (b) Kinetics and volume fraction of cementite taking into account the volume fraction of retained austenite calculated using the model of chapter5.

It is found that the model behaves properly according to expected trends of metallurgical phenomena. This means that the effect of temperature, manganese and silicon is well described by the model.

It should be indicated that this model is applicable only to the beginning of cementite precipitation since the ferrite transformation which simultaneously occur as cementite is forming was not taken into account in this model. Nevertheless, this is a first attempt to model the precipitation of cementite in ADI.

Chemical composition wt %	T_A °C	max fraction of γ	lower error bar	upper error bar
Fe-3.5C-2.4-0.1Mn-0.2Mo	300	0.12	0.05	0.04
Fe-3.5C-2.4-0.1Mn-0.2Mo	350	0.21	0.05	0.05
Fe-3.5C-2.4-0.1Mn-0.2Mo	400	0.28	0.06	0.06
Fe-3.5C-2.4-1.0Mn-0.2Mo	350	0.48	0.07	0.08
Fe-3.5C-2.4-2.0Mn-0.2Mo	350	0.68	0.26	0.41
Fe-3.5C-2.0-0.1Mn-0.2Mo	350	0.17	0.08	0.06
Fe-3.5C-3.0-0.1Mn-0.2Mo	350	0.3	0.07	0.07

Table 7.2: Maximum volume fraction of retained austenite for a ductile iron with different composition and austempering temperature. Austenitisation temperature of 900°C for 60 min, as calculated using the neural network model of chapter 5.

7.8 Summary

A model for the kinetics of the precipitation of cementite from retained austenite has been developed. It includes the concept of the extended volume and the mechanism of para-equilibrium growth for new particles of cementite growing from austenite. Although this model does not take into account the simultaneous formation of ferrite when decomposition of retained austenite takes place, it describes the kinetics of cementite precipitation as expected from the metallurgical point of view.

Chapter 8

Neural Network Models for Mechanical Properties

8.1 Introduction

The mechanical properties of austempered ductile irons depend on the microstructure which is basically determined by the casting, the chemical composition and the heat treatment. In this chapter, neural networks are used to model important mechanical properties; Vickers hardness, ultimate tensile strength, yield strength, % of elongation, and the Charpy impact toughness, all of them as a function of the chemical composition, austenitisation temperature and time, and austempering temperature and time.

8.2 Vickers Hardness Model

Hardness, is easily measured and widely reported. It is frequently used as a quality control parameter to ensure that the processes and materials used are behaving in a reproducible manner.

Since the hardness correlates with the microstructure, it can also be used to optimise the production process. For example, it is known that during austempering, the microstructure is very sensitive to the time at the isothermal transformation temperature [52]. Thus, a short time leads to a final microstructure which is predominantly martensitic, and hence very hard. As the transformation time is increased, the formation of bainitic ferrite and the consequent carbon enrichment of the residual austenite leads to a softer microstructure. Prolonged austempering causes the decomposition of austenite into carbides and ferrite, which leads to a small increase in hardness. The precipitation of carbides is detrimental to properties, so the hardness can be used as a simple way of optimising the austempering time in the development process.

8.2.1 The variables

Analysis is based on published data. Fortunately, hardness is a value which is easily measured and hence is frequently reported. Hardness is strictly a function of the microstructure and solid solution strengthening. Both of the latter depend on the chemical composition and heat treatment. Therefore, the inputs to the model included the detailed chemical composition in wt%, the austenitisation temperature in °C and time in minutes (T_γ and t_γ respectively), and the austempering temperature and time (T_A and t_A respectively), Table 8.1. This should be all that is necessary to define the hardness. Chromium and vanadium were not included since these elements are not common alloying elements in ADI, and indeed, there are few data available. A total of 1822 experimental data were collected from the published literature [13,20,21,25,27,53,63,68,124-174] and digitised; elementary checks on the data included an assessment of the minimum and maximum values for each variable.

Input element	Minimum	Maximum	Mean	Standard Deviation
Carbon / wt%	2.3	4.05	3.56	0.181
Silicon / wt%	2.0	3.58	2.56	0.244
Manganese / wt%	0.01	1.52	0.33	0.229
Molybdenum / wt%	0.0	0.74	0.13	0.138
Nickel / wt%	0.0	4.83	0.37	0.598
Copper / wt%	0.0	2.00	0.29	0.348
Austenitising temperature / °C	800	1050	905	31.5
Austenitising time / min	15	480	79	38.3
Austempering temperature / °C	220	550	357	49.2
Austempering time / min	0.33	60000	1419	8022
Austempering time $\log\{t_A/s\}$	1.296	6.556	3.60	0.886
Vickers hardness / HV	194	693	391.9	93.11

Table 8.1: The variables used to develop the neural network model. Molybdenum, nickel and copper were frequently not reported in publications since they were not deliberate additions, in which case their concentrations were set to zero.

As has been shown previously (chapter 5), the austempering time is better expressed in logarithmic form as $\log\{t_A\}$ rather than t_A . In the same way, it is conceivable that there might be some unknown process which varies directly with t_A so both the logarithmic time and the time were included as input variables. This has the advantage of avoiding bias in the inputs; the method used here has automatic relevance determination [50] and hence sets the weights associated with an irrelevant input to small or zero values should that be justified. A visual impression of the whole hardness database is shown in Fig. 8.1.

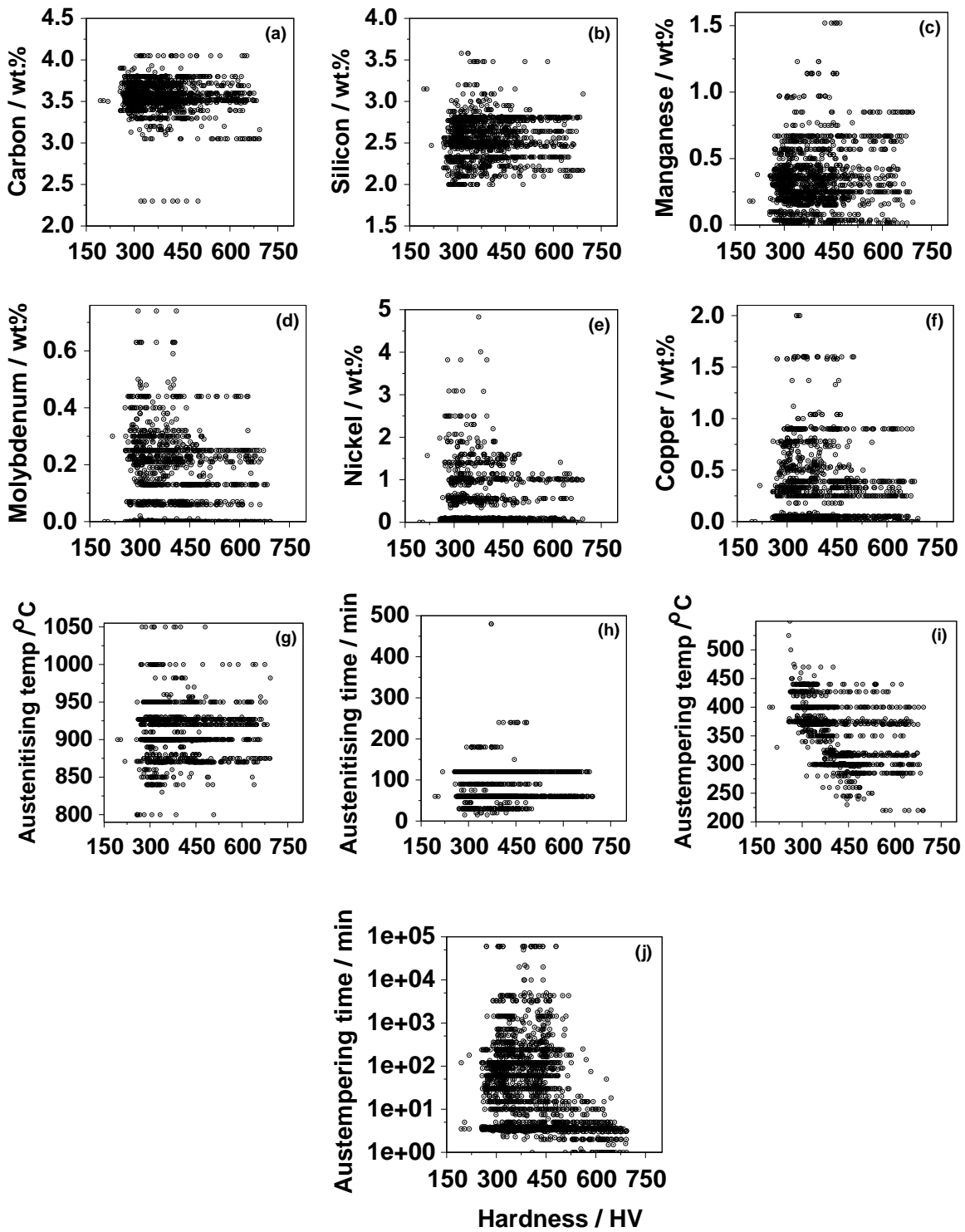


Figure 8.1: The database values of each variable versus the Vickers hardness in HV

8.2.2 Characteristics of the model

Since the complexity of the model is controlled by the number of hidden nodes, and the values of the regularisation constants [50], the inferred noise level σ_ν is expected to decrease as the number of hidden units increase. This is shown in Fig. 8.2a. The test error

also tends to go through a minimum at an optimum complexity (Fig. 8.2b). A selected committee with ten models was found to have an optimum membership with the smallest test error (Fig. 8.2c).

Figs. 8.2d,e show normalised predicted values versus experimental values for the best model in the training and test datasets. The predictions made using the optimum committee of models are illustrated in Fig. 8.2f.

Fig. 8.3 illustrates the significance of each of the input variables, as perceived by the neural network, in influencing the hardness of ADI. The magnitude of the significance is a measure of the extent to which a particular input explains the variation in hardness. log of austempering time has the largest significance.

8.2.3 Application of the model

The model can be used in extrapolation given that it indicates appropriately large uncertainties when knowledge is sparse.

Fig. 8.4a, is a classical plot showing clearly the change in hardness as a function of the austempering time due to the evolution of microstructure during the austempering process. The minimum value of hardness in this curve corresponds to the maximum volume fraction of retained austenite and to the minimum volume fraction of martensite. Fig. 8.4b is a contour plot which illustrates the interaction of two major variables in hardness predictions. First it shows that at low austempering time (t_A), the hardness increases as austempering temperature (T_A) increases. This is because the total amount of bainite that can form decreases as T_A increases, since the fraction of bainite is limited by the T_0 curve of the phase diagram (defined in chapter 6).

A second interesting point from the contour plot is that it shows that at low T_A , the hardness is maintained at a very high value even for large values of t_A . This is because even though V_{α_b} is large, the microstructure is very fine [175].

Fig. 8.5a shows that hardness increases slightly as the carbon concentration of the cast iron (\bar{x}) is increased from 3.1 to 3.6 wt%. This behaviour is not obvious since in an ideal pure iron–carbon binary cast iron, there should be no change in the equilibrium carbon concentration of the austenite (x_γ) as the average concentration \bar{x} is increased. However, the cast iron studied is not a binary alloy but contains many other elements which may be interacting in a more complex way.

Fig. 8.5b shows that for a fixed austempering time of 60 min, manganese systematically increases the hardness. This is because it retards the transformation by increasing the hardenability. The fraction of martensite in the microstructure therefore increases, causing a corresponding increase in hardness. There is of course, a small substitutional hardness effect as well. The effect of nickel illustrated in Fig. 8.5d can be similarly ex-

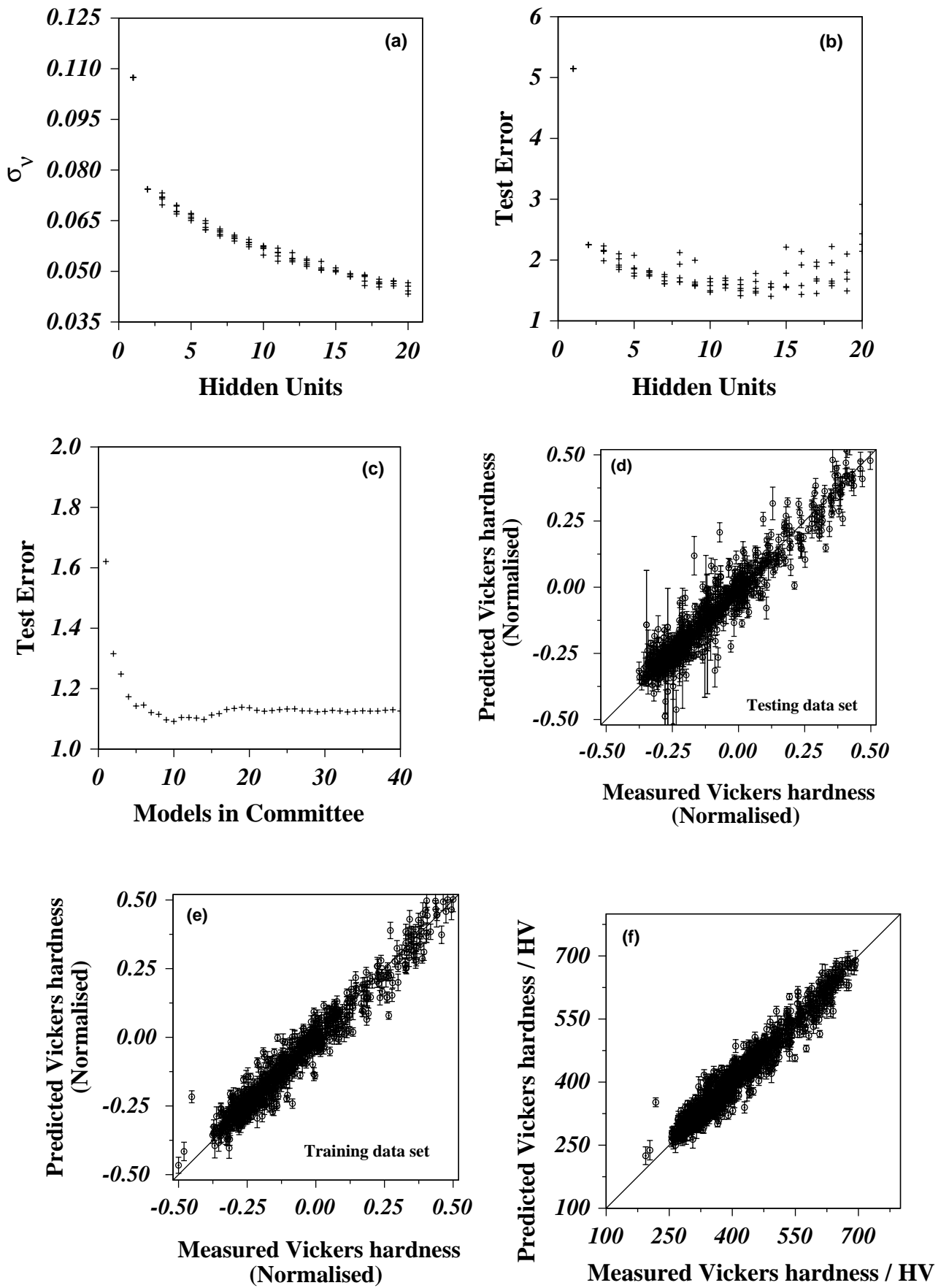


Figure 8.2: Characteristics of the Vickers hardness model. σ_ν is the model perceived level of noise in hardness. (d) and (e) represent the behaviour of the best single model, whereas (f) shows the performance of the optimum committee model on the entire dataset.

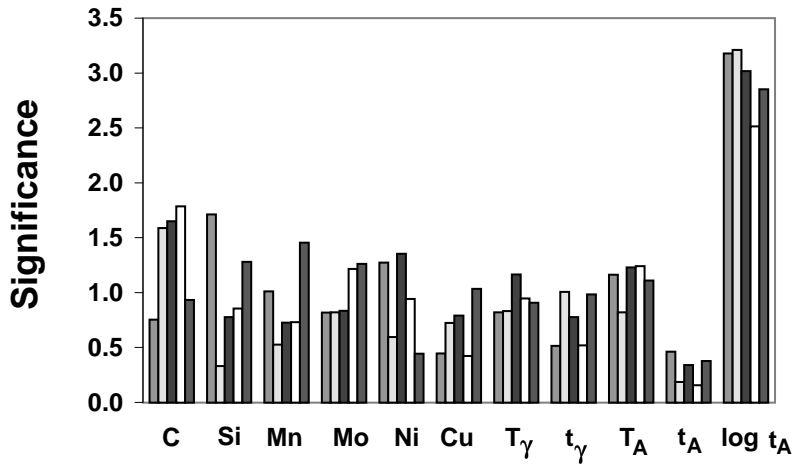


Figure 8.3: Model perceived significance of input parameters in the best five models from the committee trained on the Vickers hardness. σ_w values are presented for each variable.

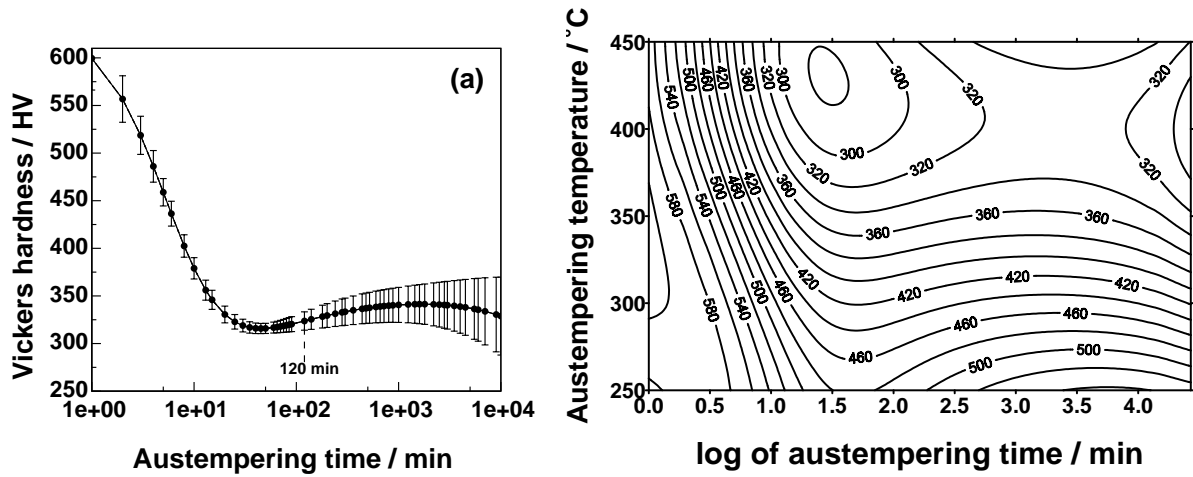


Figure 8.4: Predictions using the Vickers hardness model. (a) As a function of austempering time. (b) Contour plot of hardness as a function of austempering time and temperature. The error bars associated with these predictions have been omitted for the sake of clarity. Cast iron: Fe-3.5C-2.5Si-0.25Mn-0.25Mo-0.5Ni-0.5Cu wt% austenitised at 900°C, for 60 min.

plained, although the uncertainty is greater because nickel is not usually added in large concentrations.

Fig. 8.5c shows an increase in hardness when molybdenum is increased from 0.0 to 0.1 wt%, however, over this value there is a sharp decrease in hardness. Although molybdenum does not have a marked influence on the amount of retained austenite [176], its influence in hardness seems to be significant. The decrease in hardness as manganese increase has been indicated to be due to non-uniform transformation response caused by negative segregation

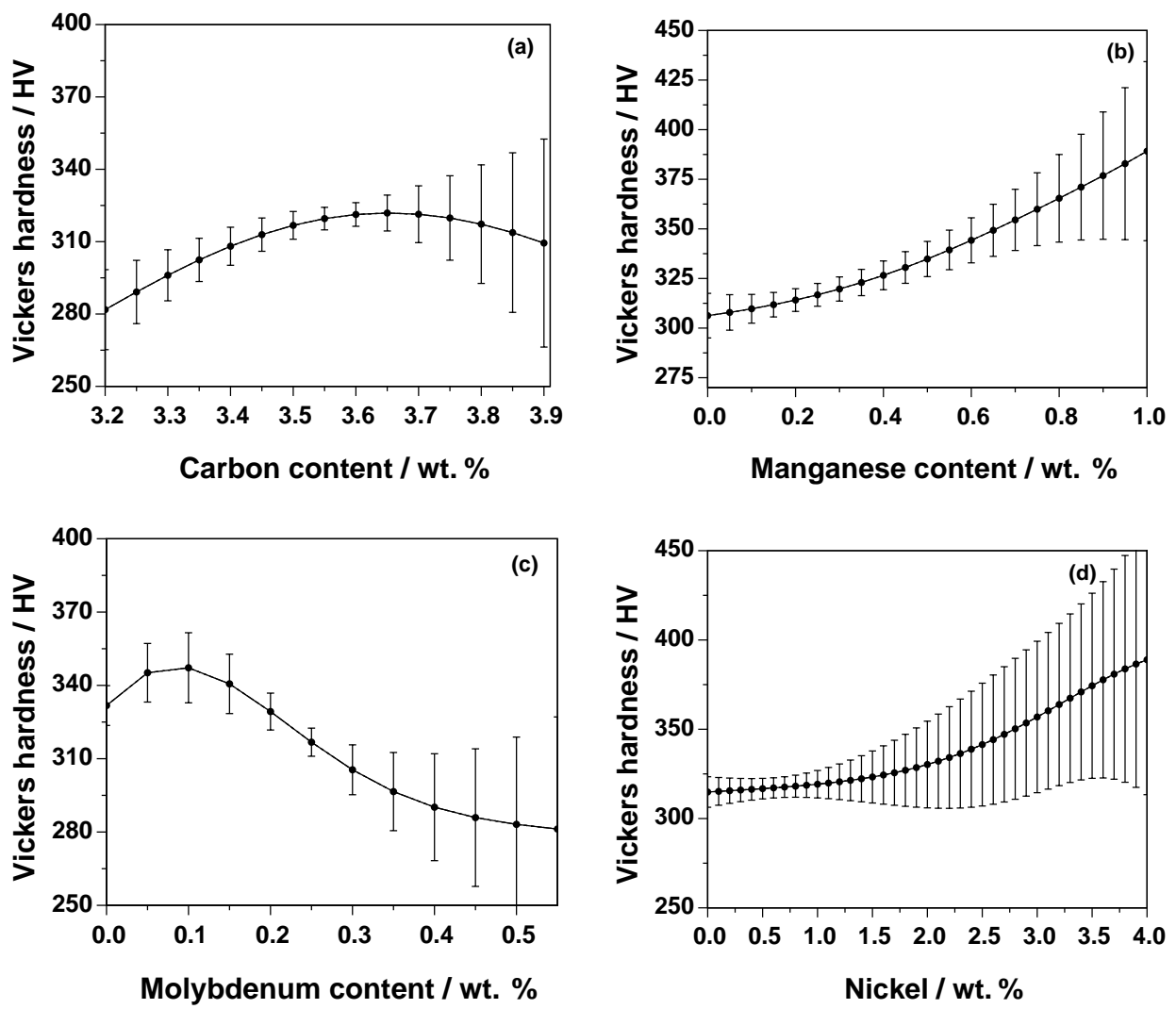


Figure 8.5: Predictions of Vickers hardness as a function of chemical composition (Basic cast iron: Fe-3.5C-2.8Si-0.25Mn-0.25Mo-0.5Ni-0.5Cu wt%). Austenitised at 900°C for 60 min, and austempered at 370°C for 60 min.

tendency of molybdenum [177]. Dorazil *et al.* [178] indicated that this behaviour is due to the segregation of molybdenum during solidification, resulting in the formation of stable intercellular carbides and also the local formation of martensite in the segregation regions.

8.3 Ultimate Tensile Strength, Yield Strength and Elongation Models

There is considerable scope for engineers to use austempered ductile irons because the austempering treatment provides a versatile combination of mechanical properties with a corresponding wide range of applications. There is then a need to find a better way to predict optimum mechanical properties for specific applications.

During tensile testing usually the ultimate tensile strength, yield strength and elongation are determined, and most researchers report these properties when assessing the effect of variables such as chemical composition, heat treatment conditions, segregation or section size. The data-bases for the three properties were almost identical.

A total of 1856 experimental data were collected from the published literature [12-14,20,21,25,27,54,63,68,87,119-174,179-246] and digitised. The input variables were the same as those for the Vickers hardness model.

For the ultimate strength model, 7 trained models were selected for the committee. 6 for the yield strength model, and 12 for the elongation model. Predictions made using these optimum committees are shown in Fig. 8.6.

8.3.1 Predictions using the model

Fig. 8.7a shows the change in ultimate tensile strength as a function of austempering time. The lowest values of tensile strength occur at low austempering time because the large amount of martensite in the microstructure. This martensite is very hard and the cast iron therefore does not have ductility and hence fails prematurely without significant plasticity. This is revealed by the model which shows zero elongation at the beginning of the austempering process (Fig. 8.9a). It follows that fracture is brittle.

As the austempering time increases, the volume fraction of martensite decreases and the austempered cast iron exhibits more plasticity and the ultimate tensile strength increases. The maximum in tensile strength arrives when the volume fraction of retained austenite and bainite are also maximum. The onset of carbide precipitation leads to a smooth decrease in tensile strength but apparently it is reversed at longer austempering times due to the coarsening of carbides (Fig. 8.7a).

Fig. 8.7b shows the effect of austempering temperature on tensile strength. The strength decreases because less bainitic ferrite is formed at high temperature (the T_0 effect) and there is an increase in the amount of soft retained austenite. As expected, the same trend is observed in Fig. 8.8b for yield strength and opposite trend in elongation (Fig. 8.9b). The peak in elongation occurs presumably because of the increase in the amount of martensite at the highest Austempering temperature.

The effect of increasing the manganese concentration is in principle identical to in-

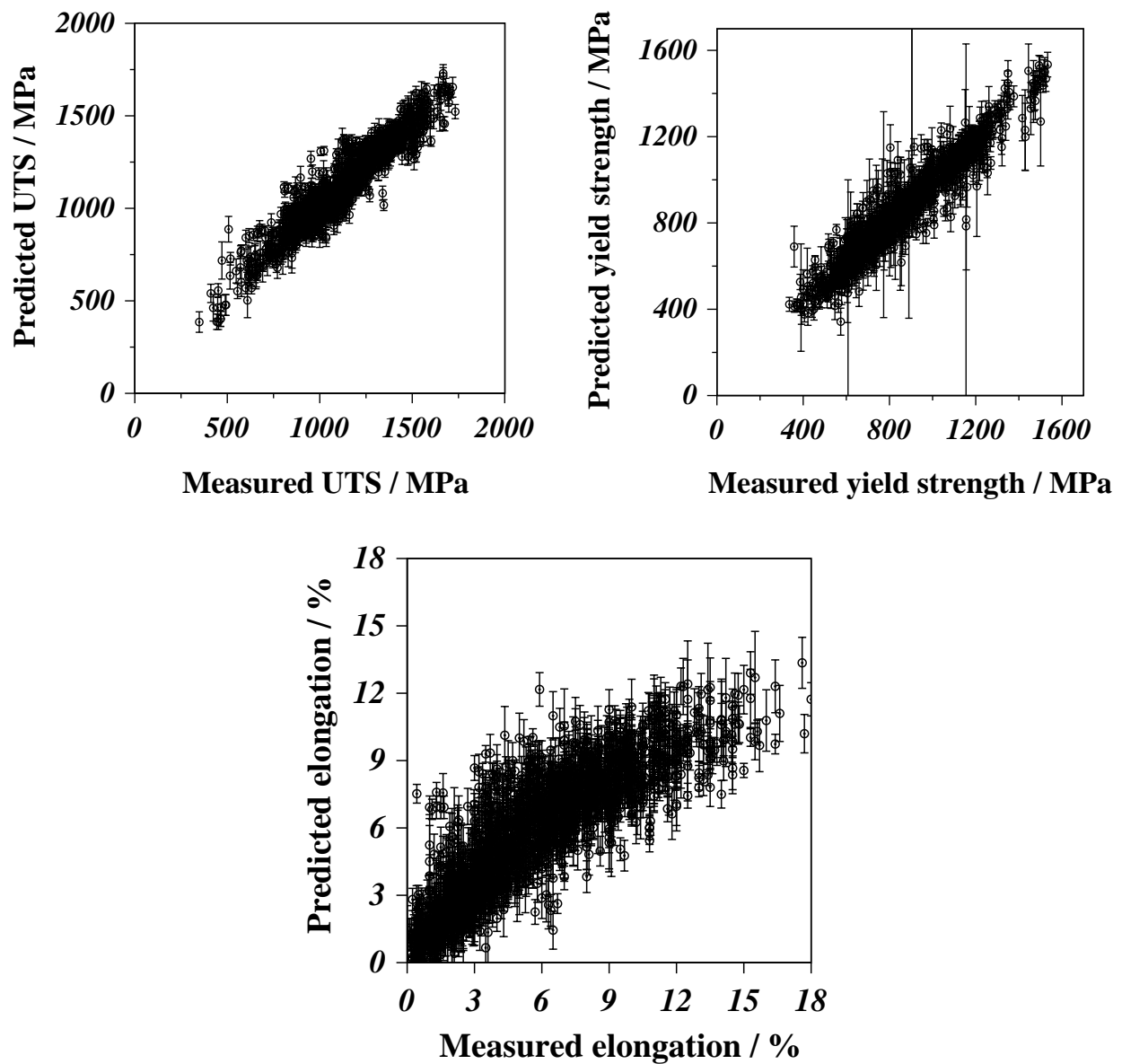


Figure 8.6: Predictions versus measured values of optimum committees for (a) ultimate tensile strength model (b) yield strength model and (c) elongation model.

creasing the austempering temperature (T_A) since manganese reduces the driving force of transformation. Therefore, all the tensile properties vary with Mn essentially as they do for T_A (Fig. 8.7c). The same applies to the effect of molybdenum and nickel.

It has been reported by Gagne [87] that silicon lowers the tensile strength but improves the yield strength whereas the elongation increases to an optimum value. After this, silicon causes a deterioration of all tensile properties. Predictions, however, show that silicon increases the three tensile properties. On the other hand, as Gagne indicated, predictions show that there is an optimum value of silicon after which tensile properties drop (Fig. 8.7e, Fig. 8.8e, and Fig. 8.9e). This is due to the formation of free-ferrite [87].

It should be borne in mind that all predictions described before were made for a particular chemical composition and/or fixed heat treatment conditions. This means that

trends may vary should the conditions change. A somewhat better picture of variable interactions is obtained by creating contour plots including two variables at the same time.

8.3.2 Contour plots

Contour plots are effective in visualising the interaction of two variables. Fig. 8.10 shows the combination of manganese concentration with austempering time to predict ultimate tensile and yield strength, and tensile elongation. The plots show immediately that a combination of high strength and ductility can, for the cast iron considered, be optimum at $t_A = 10^{2.5}$ min and 0.5 wt% Mn. This conclusion, which is obvious from the contour plots, would be difficult to perceive from a simple examination of experimental data.

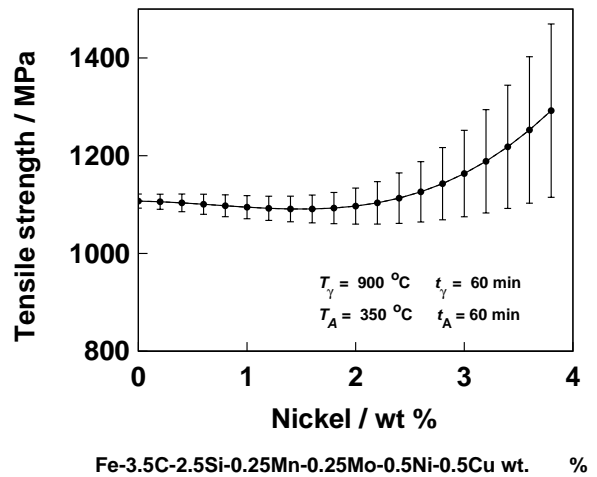
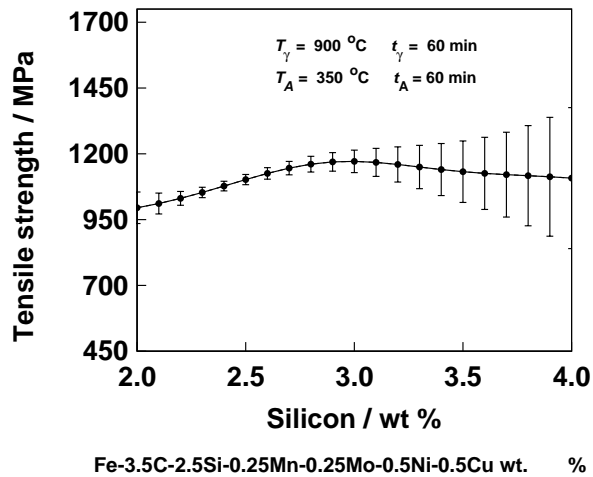
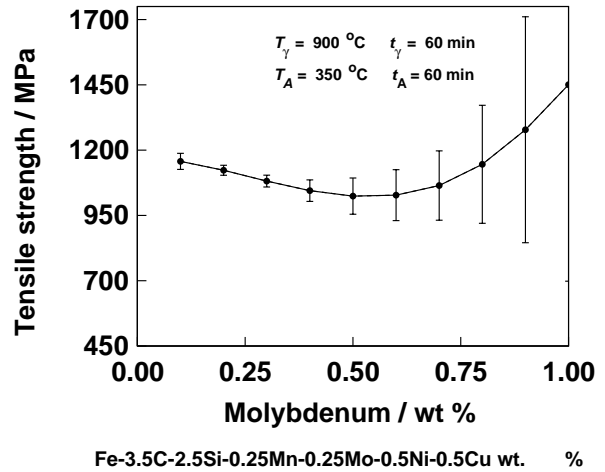
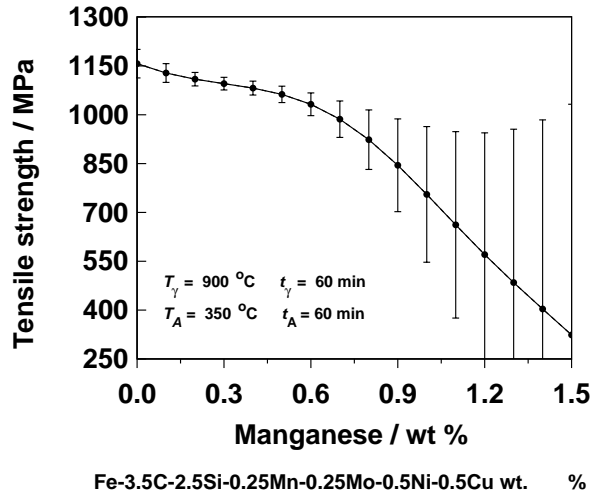
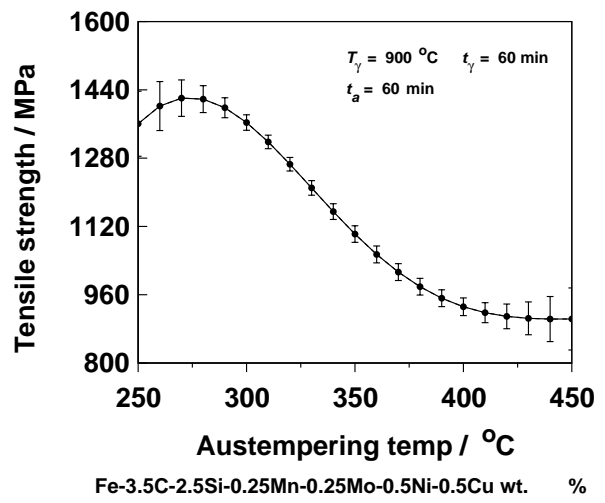
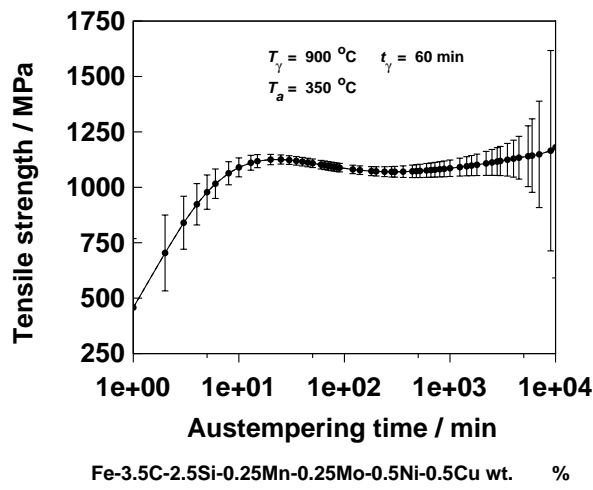


Figure 8.7: Predictions of ultimate tensile strength as a function of chemical composition (basic cast iron: Fe-3.5C-2.8Si-0.25Mn-0.25Mo-0.5Ni-0.5Cu wt%). Austenitised at 900 $^{\circ}\text{C}$ for 60 min, and austempered at 350 $^{\circ}\text{C}$ for 60 min.

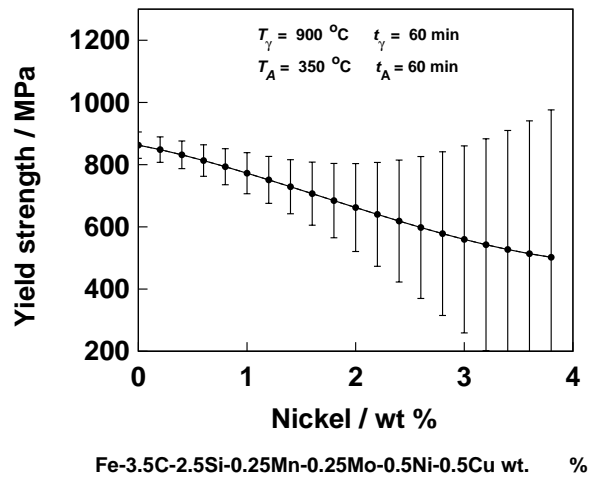
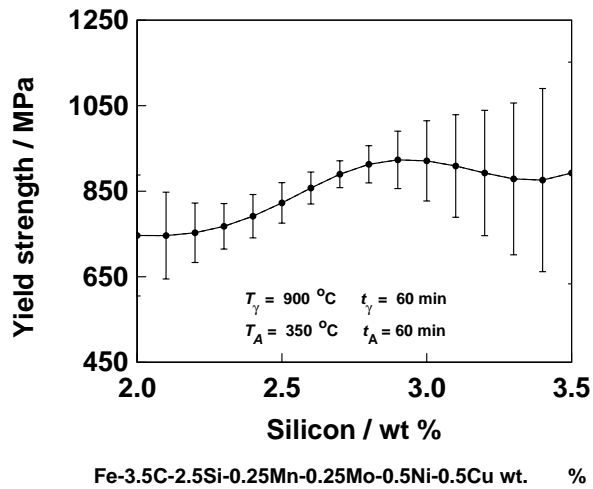
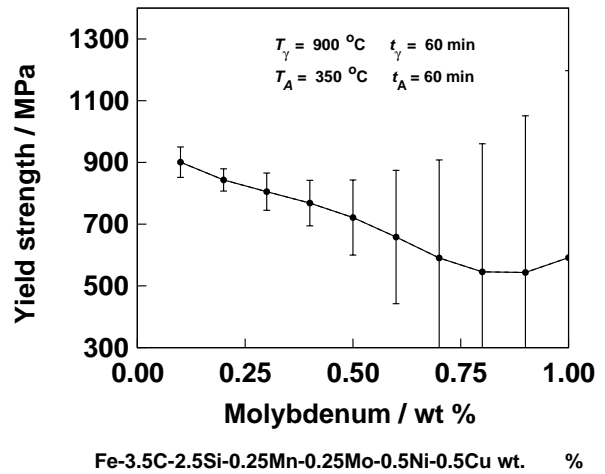
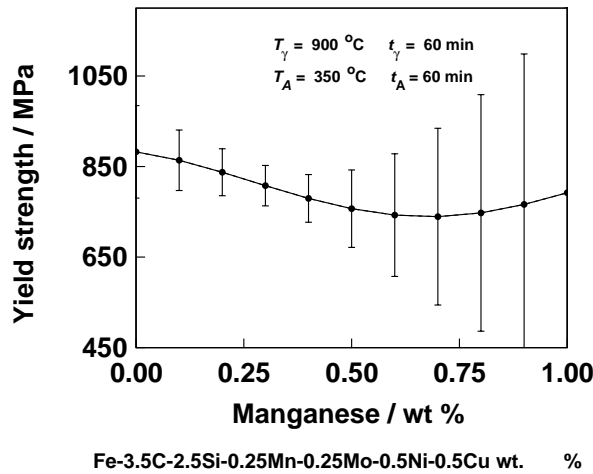
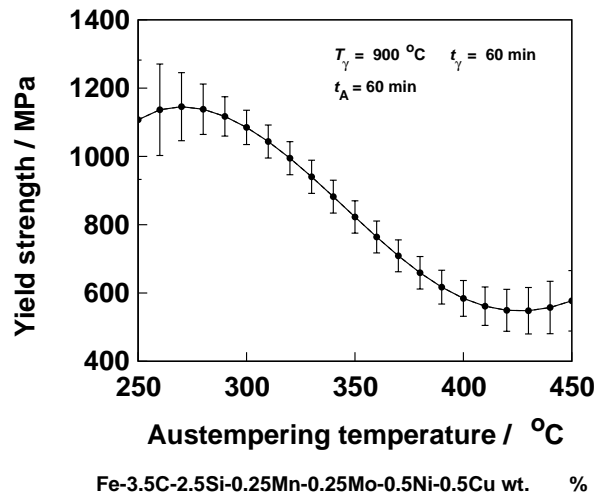
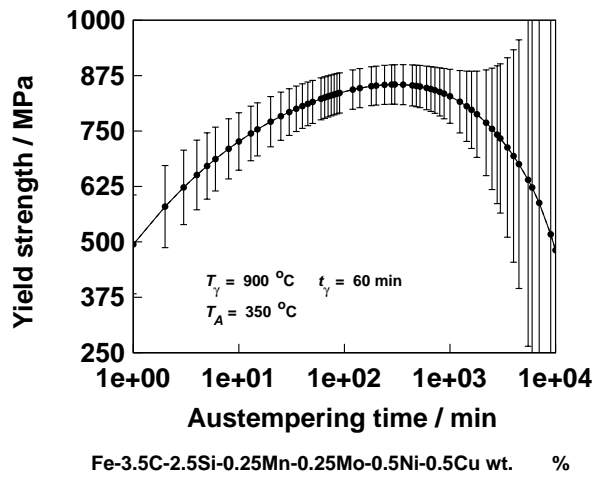


Figure 8.8: Predictions of yield strength as a function of chemical composition (basic cast iron: Fe-3.5C-2.5Si-0.25Mn-0.25Mo-0.5Ni-0.5Cu wt%). Austenitised at 900°C for 60 min, and austempered at 350°C for 60 min.

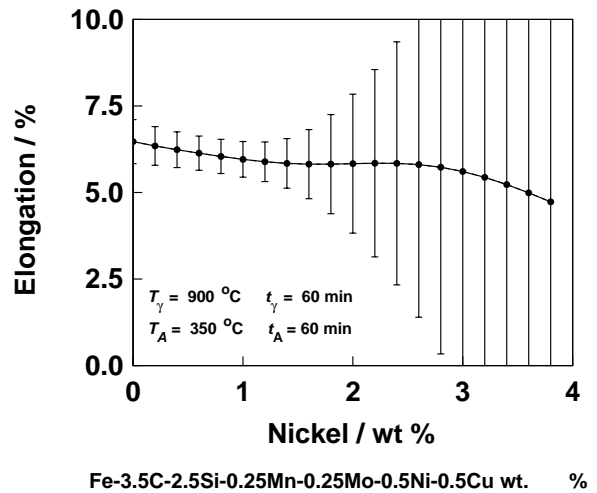
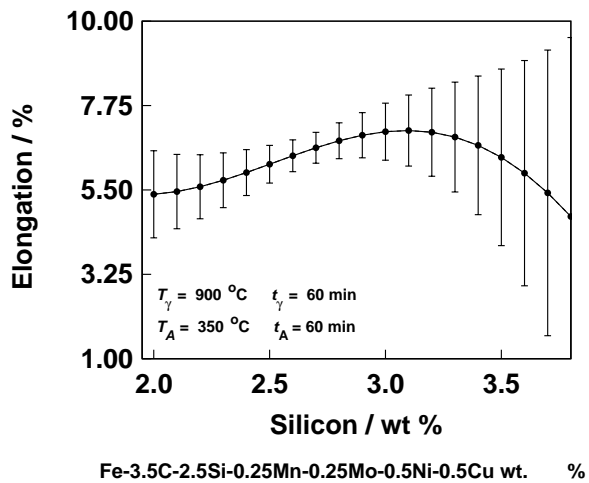
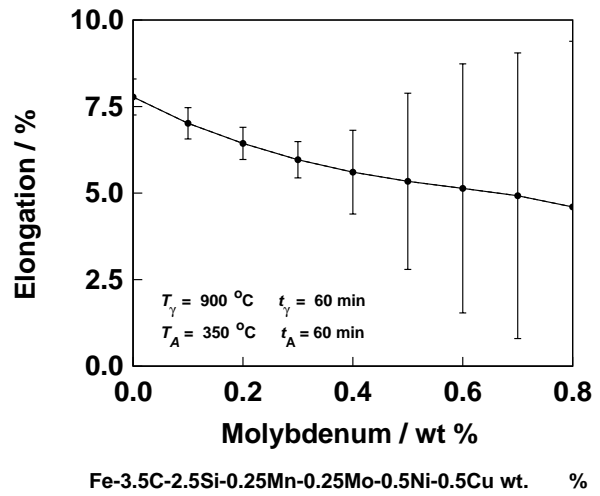
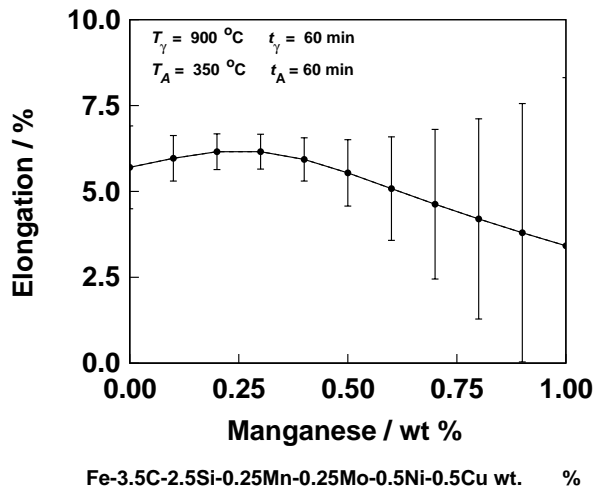
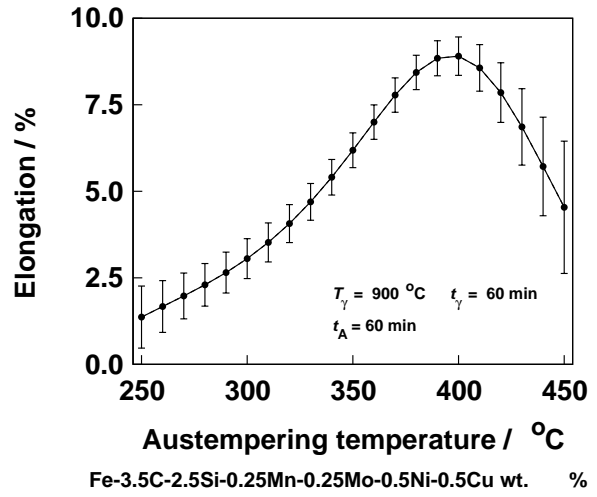
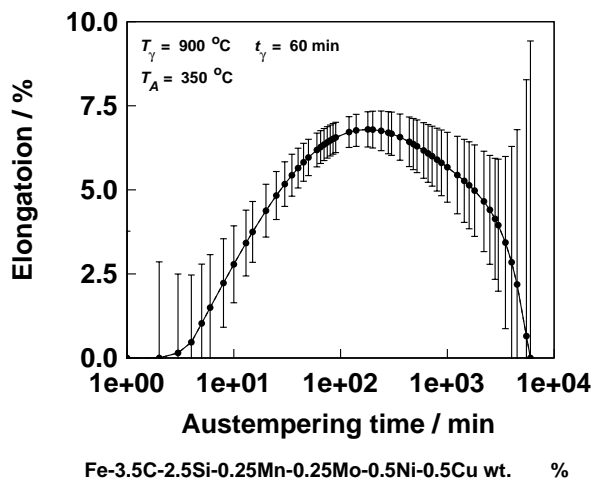


Figure 8.9: Predictions of elongation as a function of chemical composition (basic cast iron: Fe-3.5C-2.5Si-0.25Mn-0.25Mo-0.5Ni-0.5Cu wt%). Austenitised at 900°C for 60 min, and austempered at 350°C for 60 min.

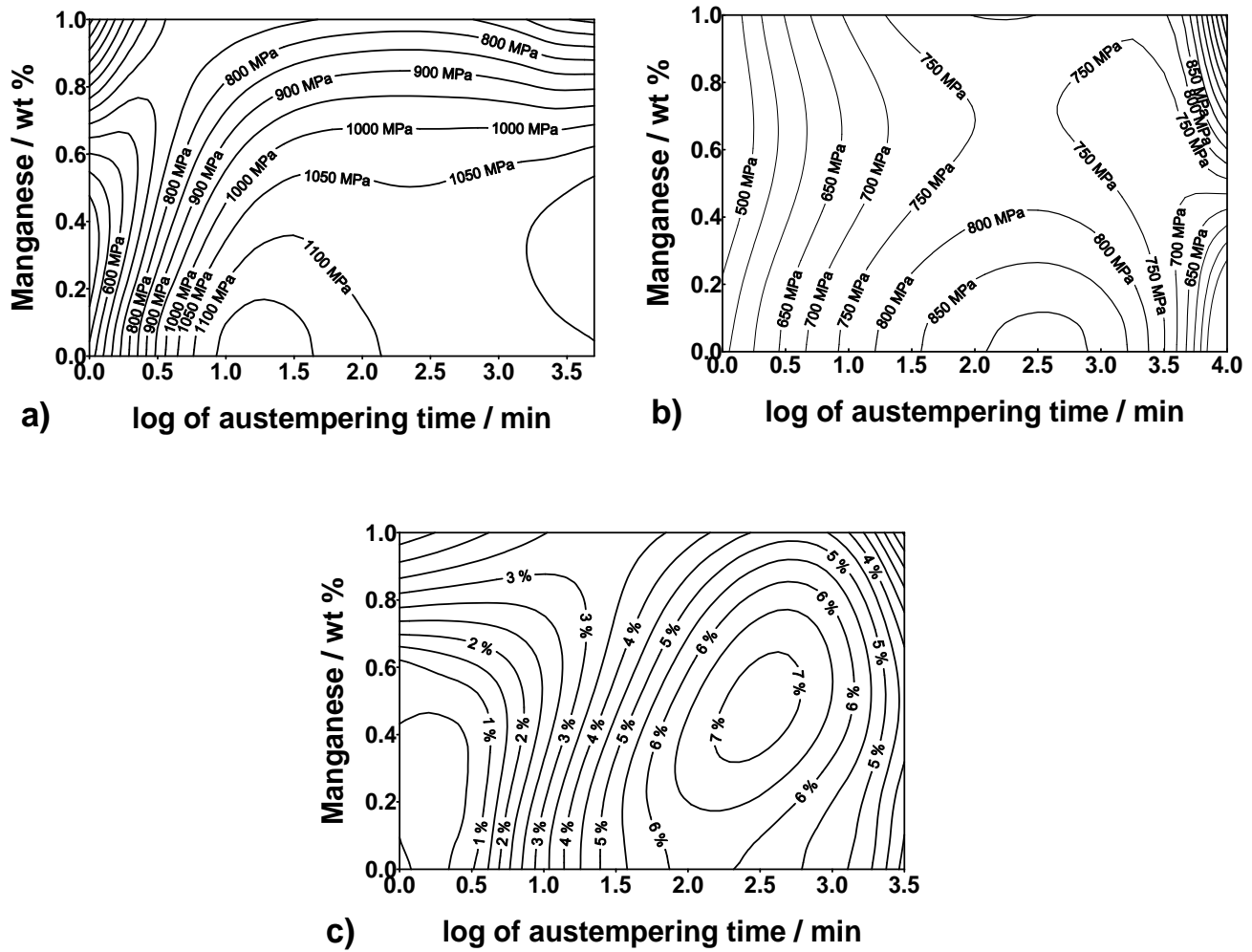


Figure 8.10: Contour plots combining two variables; manganese concentration and austempering time to predict tensile properties in an Fe-3.5C-2.5Si-Mn-0.25Mo-0.5Ni-0.5Cu wt% austenitised at 900°C for 60 min and austempered at 350°C. (a) ultimate tensile strength, (b) yield strength and (c) tensile elongation. The error bars have been removed for the sake of clarity.

8.4 Charpy Toughness Model

The toughness of a material is its ability to absorb energy by plastic deformation. The ability to withstand occasional stresses above the yield stress without fracturing is important. This toughness to a large extent determines the applicability of ADI in engineering components. ADI has a good combination of strength and toughness but this is in general lower than in steels. After all, there are graphite nodules in the microstructure which in turn reflects the effects of solidification-induced segregation. This leads to the majority of researchers to use unnotched Charpy type specimens when empirically measuring toughness. The Charpy specimen has a square cross section (10×10 mm). Most of data available for Charpy toughness experiments are of this kind, and the tests are usually performed at room temperature. It is worth mentioning, however, that few researchers have used notched samples and others have performed the tests at 0°C but those limited-data were not included in the data-base created for neural network analysis.

Thus, 1330 data were collected from published literature¹ and digitised in the usual way. The input variables used to create the model were the same as those used in previous models; chemical composition and heat treatment conditions.

Since the data-base contains fewer experimental results, and was created using different sources than those used for the tensile test models, it is interesting to illustrate the database (Fig. 8.11).

A committee with seven models was found to have the optimum membership with the smallest test error. Predictions made using this committee are illustrated in Fig. 8.12.

Fig. 8.13 illustrates the effect of some variables on the calculated value of Charpy toughness for the same chemical composition and heat treatment conditions as used in previous models. A remarkable observation is that in all cases, the Charpy data follow essentially the same trends as the elongation data illustrated in Fig. 8.9. A correlation like this is not obtained in wrought materials or in weld metals [253]. Fig. 8.14a shows that when plotting experimental values of elongation and Charpy of the same chemical composition and heat treatment from the literature, a correlation is found. It has long been accepted that measurements of ductility in the tensile test, such as elongation or reduction in area, are not suitable for predicting the material's resistance to fast crack propagation in service [254]. However, the "Charpy" test which has been used without notch in ADI is not recommended for such purpose either, because it does not fulfill its aim. It is probable that the strong correlation between the elongation and "Charpy" values (Fig. 8.14) in ADI is because the samples are not notched and hence do not reflect properly the constraints introduced by the presence of a blunt notch. Even though the impact test involves a large rate of deformation, the un-notched Charpy test is essentially

¹[119-120,129,132,142,144,146,150-151,153-154,183-187,189,191,193-194,200,212,219,223,225,227,233,239,242,245,247-252]

a bend test and hence might be expected to correlate with ductility. Furthermore, the tests are all conducted at room temperature where the fracture mode in the un-notched Charpy probably is by a ductile mechanism.

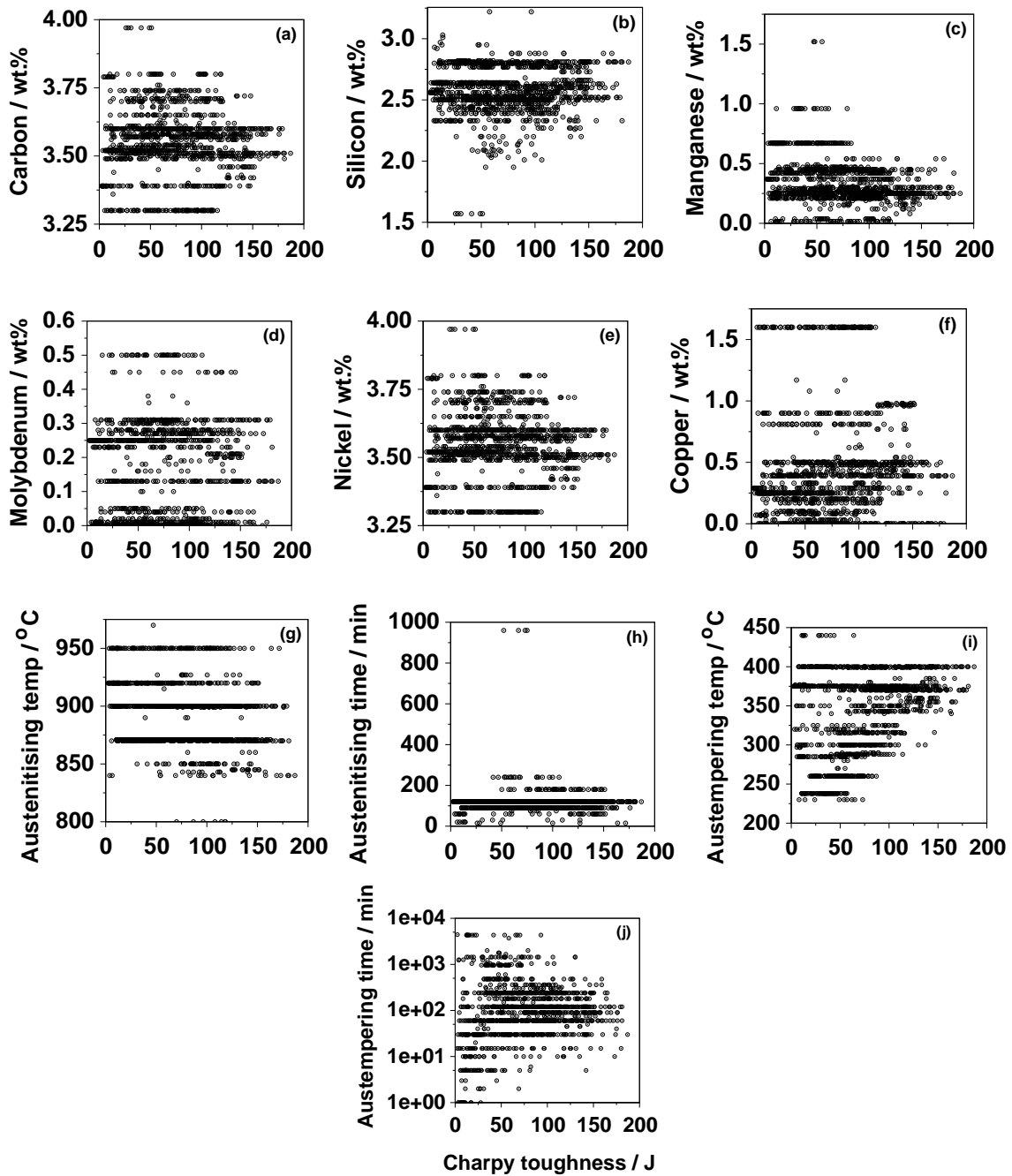


Figure 8.11: The database values of each variable versus the “Charpy” toughness in J

Fig. 8.15 shows some contour plots, which enable the selection of conditions for the optimisation of the Charpy toughness by visual inspection. One example is the combination of low austenitising temperature with austempering temperature. This is remarkable

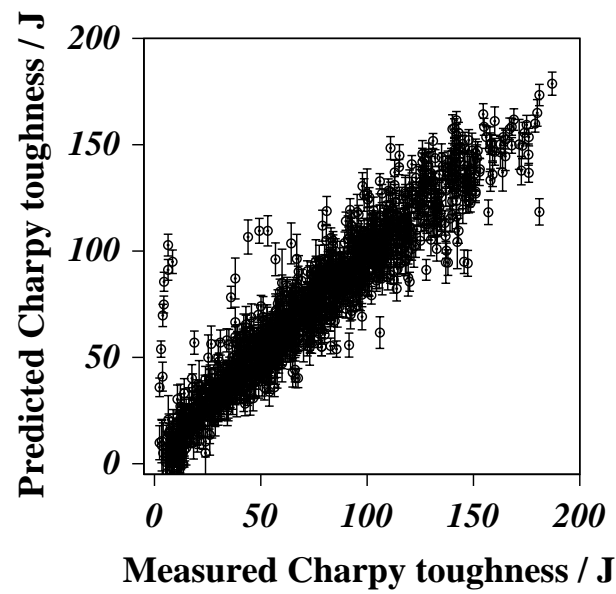


Figure 8.12: Charpy toughness model optimum committee model results

since it reinforces what has been reported by Darawish *et al.* [191]. They have claimed that at high austempering temperatures and low austenitising temperatures, there is an improvement in the mechanical properties.

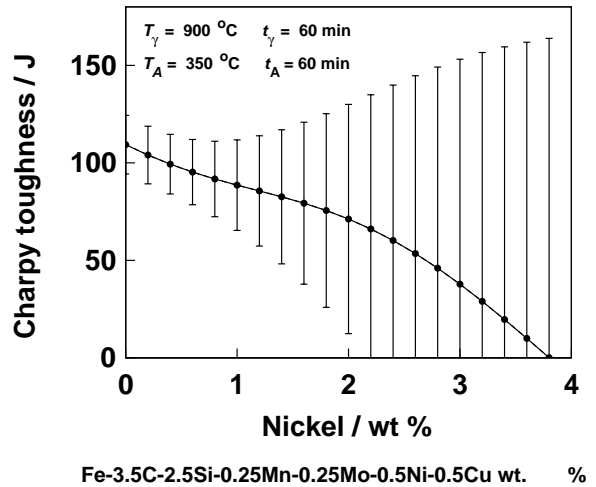
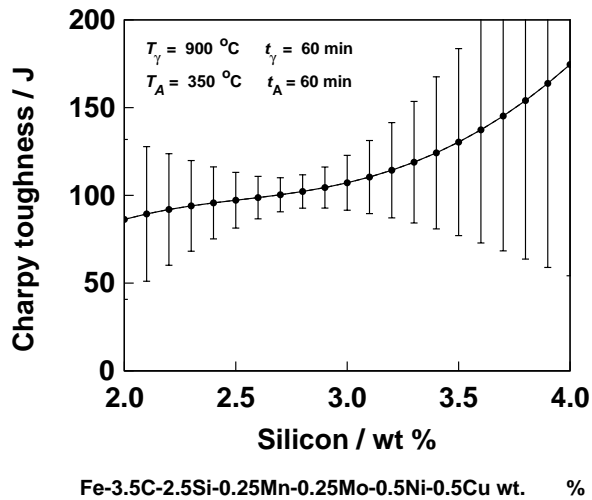
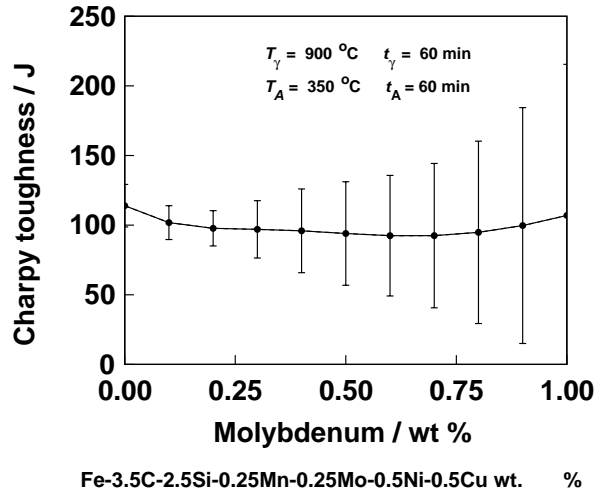
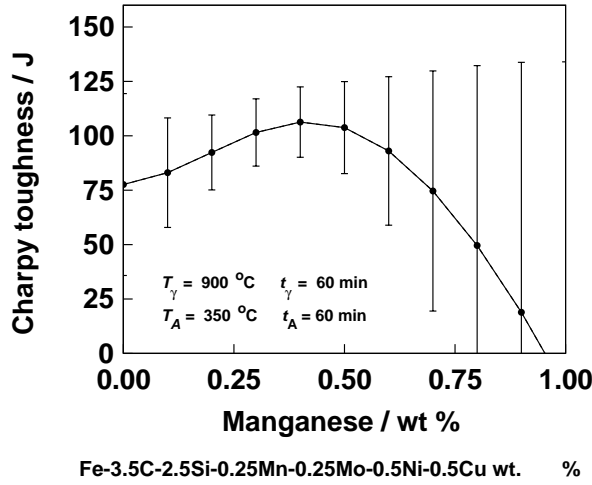
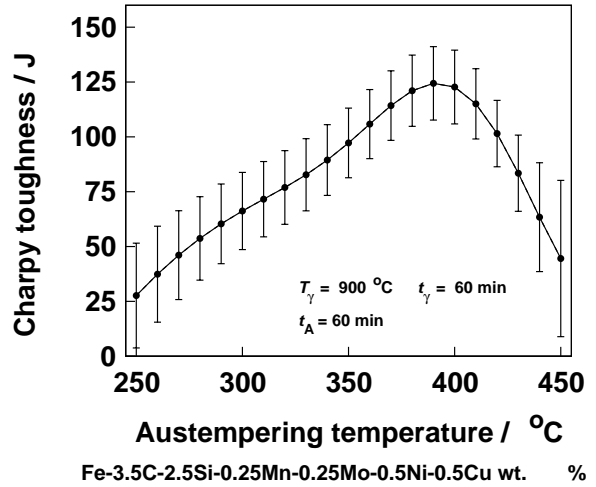
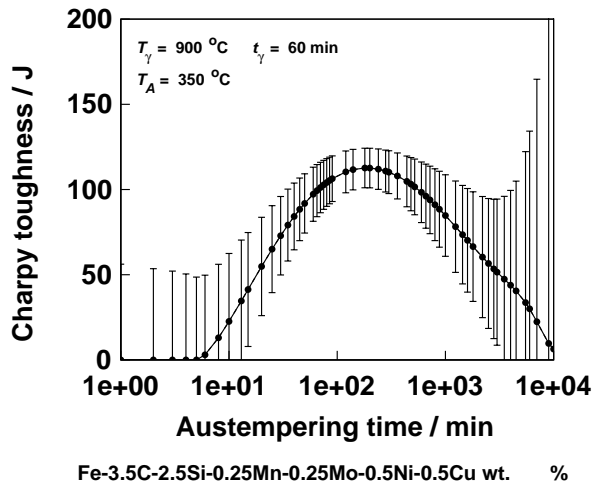


Figure 8.13: Predictions of Charpy toughness as a function of chemical composition (Basic cast iron: Fe-3.5C-2.5Si-0.25Mn-0.25Mo-0.5Ni-0.5Cu wt%). Austenitised at 900 $^\circ\text{C}$ for 60 min, and austempered at 350 $^\circ\text{C}$ for 60 min.

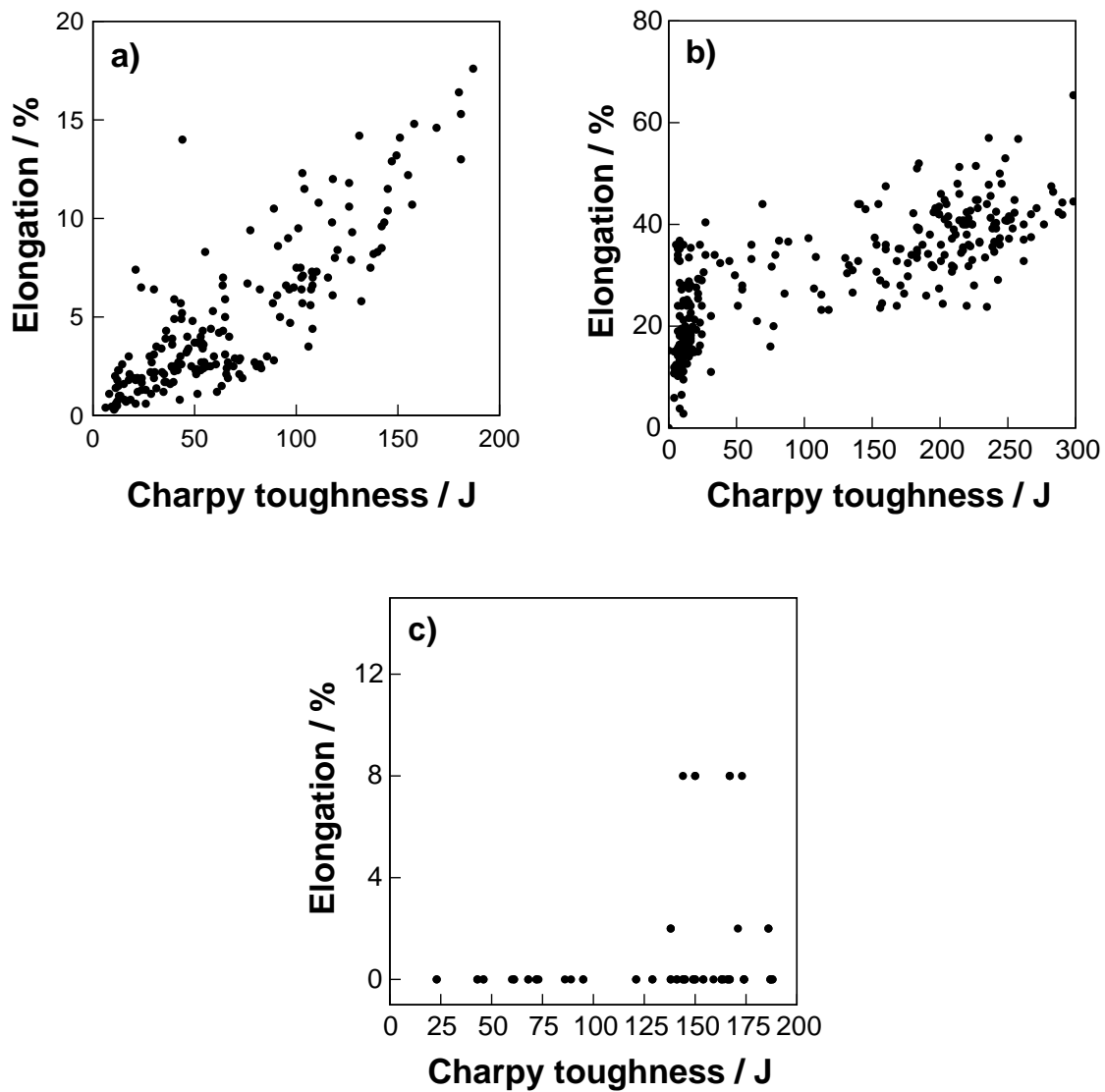


Figure 8.14: “Charpy” versus elongation experimental results. (a) ADI at room temperature [150, 154, 189, 191, 193, 200] correlation coefficient 0.72. (b) Steel at room temperature [255], correlation coefficient 0.67. (c) Steel at 0 °C [256], no correlation between elongation and Charpy toughness.

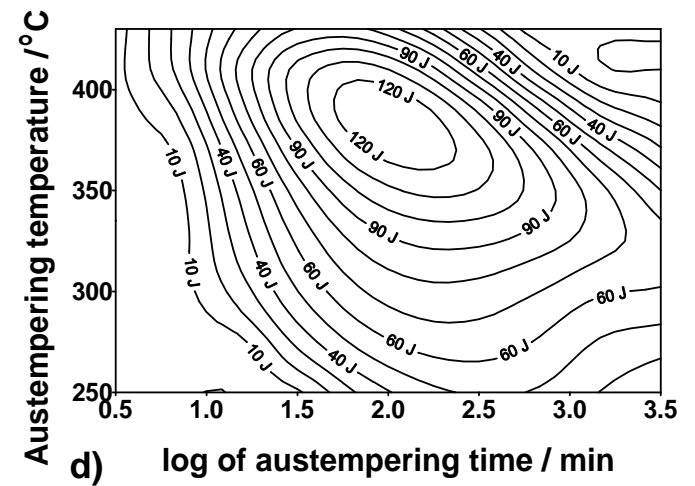
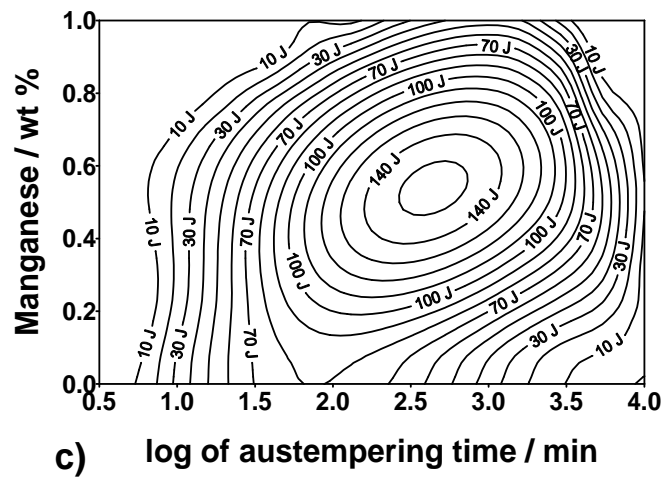
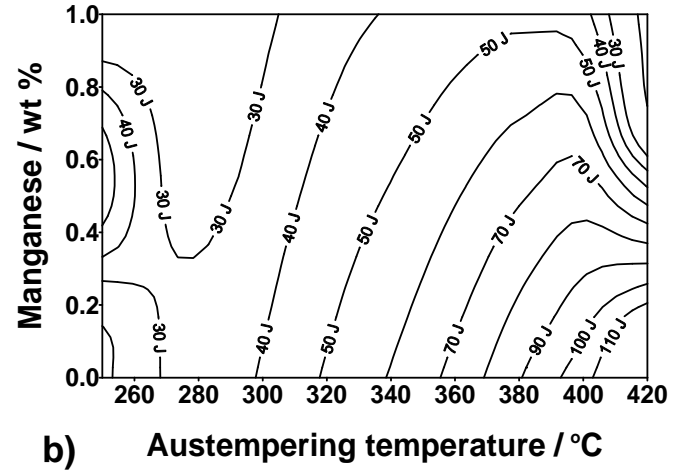
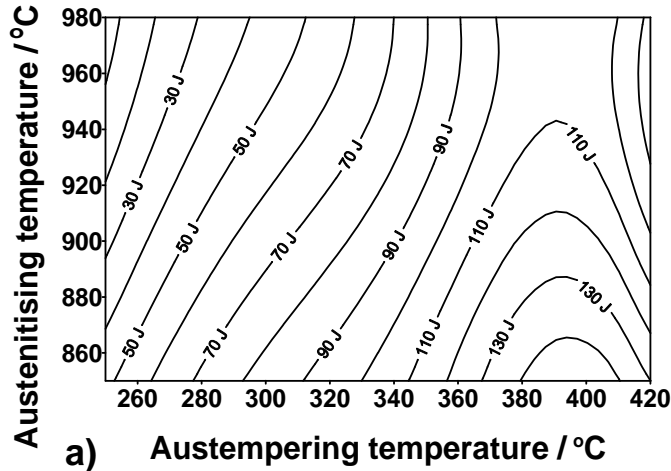


Figure 8.15: Contour plots of Charpy toughness as a function of chemical composition and heat treatment conditions (Basic cast iron: Fe-3.5C-2.5Si-0.25Mn-0.25Mo-0.5Ni-0.5Cu wt%). Austenitised at 900°C for 60 min, and austempered at 350°C for 60 min.

8.5 The processing window

The main concern of a heat-treater is to estimate the austempering time required to achieve the specified mechanical properties for the selected austenitising and austempering temperatures. Two criteria have been used to define the time interval for the processing window [25]. The first is the optimum mechanical property criterion. The procedure is to select a range of austempering temperatures and to measure the specified mechanical properties as a function of austempering time. Darawish *et al.* [25] claim that a disadvantage of this criterion is that it is not related directly to microstructural features that control the mechanical properties and the transformation kinetics associated with their formation. Furthermore, it is not clear when properties are achieved the optimum at the specified austempering temperature. For example, it may be the case that by changing the austenitising temperature the mechanical properties may be improved. In this respect the neural network models enable a more comprehensive investigation of the input space without exhaustive experimentation and time can be cut down.

The second is a microstructural criterion that uses transformation kinetics to define t_1 , the time corresponding to the end of stage I, and the time t_2 corresponding to the start of stage II. Since martensite is the most detrimental microstructural feature in stage I, it has been used to define t_1 [25]. A value of 1% of martensite has been considered to be measurable and also to correspond to a structure containing non-continuous martensite [25, 52].

The changes of microstructure accompanying the stage II reaction cannot be observed easily because of the fine scale. As a result, the time t_2 has been defined using the decrease in the volume fraction of austenite V_{γ_r} as an indication of the formation of carbide from austenite. The time t_2 in Fig. 8.16 thus represents a maximum time beyond which significant carbide formation can be expected. A horizontal line is constructed at a value of 10 % below the maximum value of V_{γ_r} , intersecting the curve at times t_{min} and t_{max} . The value of t_2 is then defined by

$$\ln\{t_2\} = \frac{\ln\{t_{min}\} + \ln\{t_{max}\}}{2} \quad (8.1)$$

$$\equiv \sqrt{t_{min} t_{max}} \quad (8.2)$$

If t_1 exceeds t_2 as it may happen, then the processing window is closed and the optimum mechanical properties will not be achieved. The neural network models can be used to estimate the processing window, and a combination of microstructure and mechanical properties criteria can be used to assess the heat-treatment procedure.

Fig. 8.17 shows retained austenite and mechanical property variations as a function of the austempering time. Fig. 8.17a shows the time t_2 which is the time for the end of

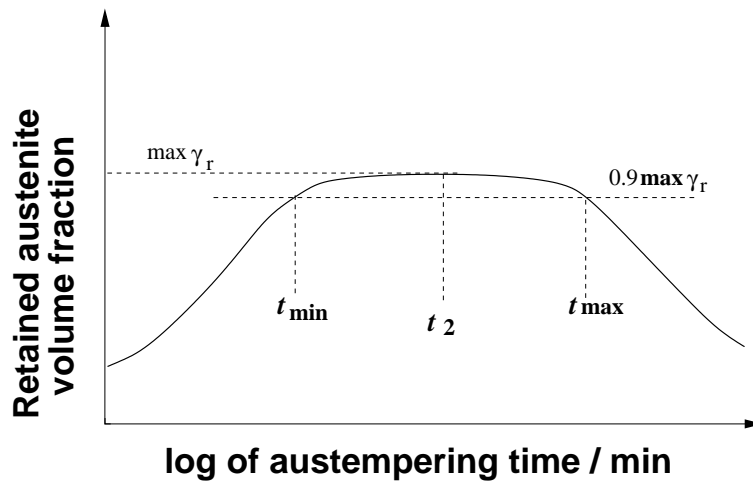


Figure 8.16: Schematic representation of calculation of time t_2 .

the processing window calculated using the microstructure criterion is 39 min. According to the microstructural criterion the processing window is closed at this time. This does not correspond to the optimum mechanical properties. It is after the processing window when the best mechanical properties are found. Furthermore, it is found that it is after the processing window where the grade 950/6 of the British Standards and even the grade 2 of the ASTM standard are satisfied.

It has been said [25] that the processing window defined from the microstructural observations is not coincident with the optimum mechanical properties; this is confirmed here. Darawish *et al.* have claimed that the microstructure criteria should be modified to make the measured window coincident with the optimum mechanical properties; They suggested that the $V_{\alpha'} = 1\%$ requirement for defining the beginning of the processing window should be more stringent, whereas the requirement for the beginning of the stage II reaction should be relaxed, *i.e.* more carbide formation could be tolerated.

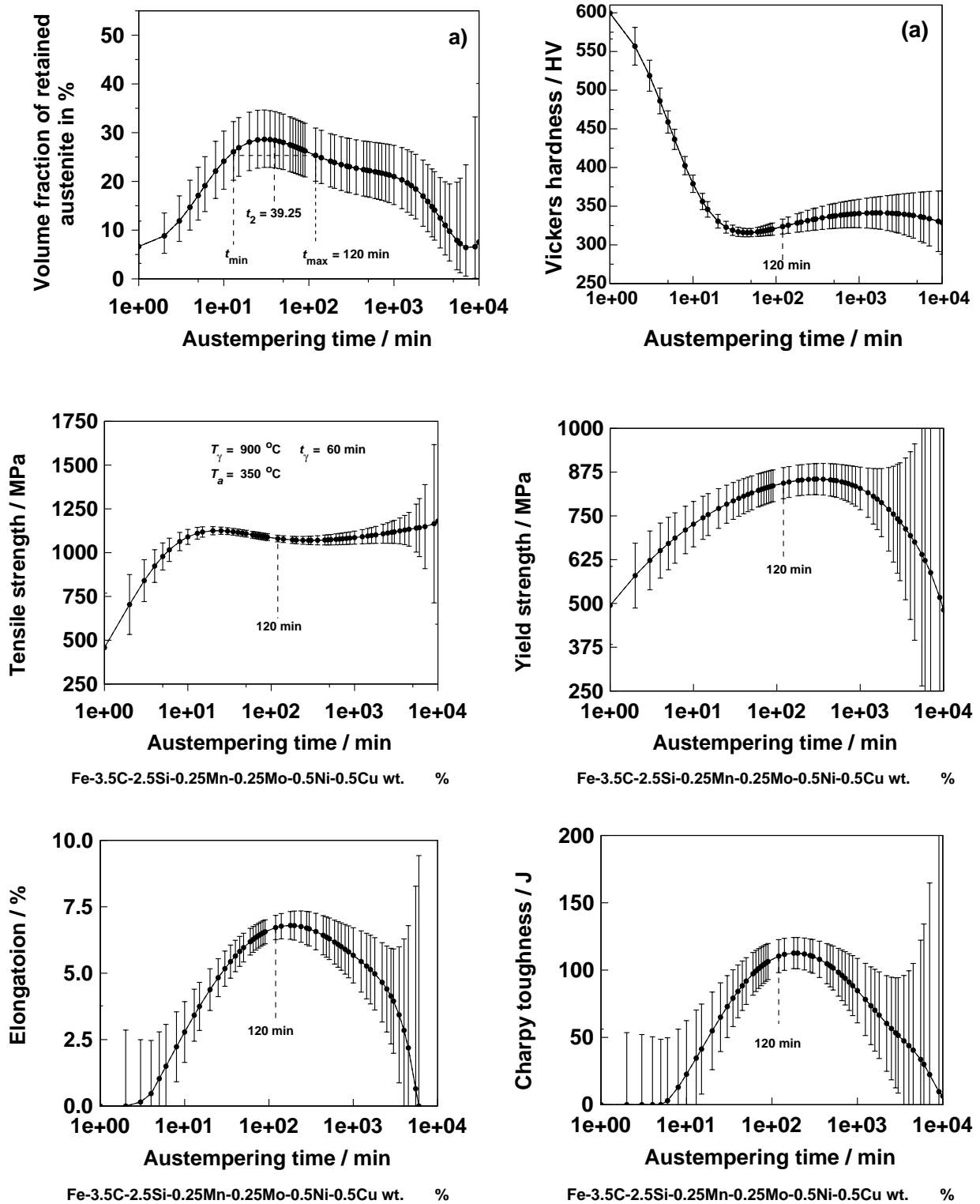


Figure 8.17: Predictions of microstructure and mechanical properties versus austempering time to compare the microstructure with the mechanical properties criteria to find the processing window (basic cast iron: Fe-3.5C-2.5Si-0.25Mn-0.25Mo-0.5Ni-0.5Cu wt%). Austenitised at 900°C for 60 min, and austempered at 350°C .

8.6 Summary

The development of the models presented here allows the selection of appropriate chemical composition and optimum procedure for the austempering heat treatment of ductile irons. This is helpful to meet required level of mechanical properties for specific applications.

Interesting results were found when comparing predictions with the Charpy and elongation models. That is, a correlation between these properties is found. This is in general not common in wrought metals or weld metal. This suggests that performing Charpy tests without notch to measure toughness in ADI may not be the best way since it may be that the Charpy test in ADI is giving a measure of ductility rather than a measure of toughness.

It should be emphasised that the trends of mechanical properties as a function of austempering time predicted with the models are the same as those shown by Elliot [4] (Compare Fig. 8.17 with Fig. 8.18).

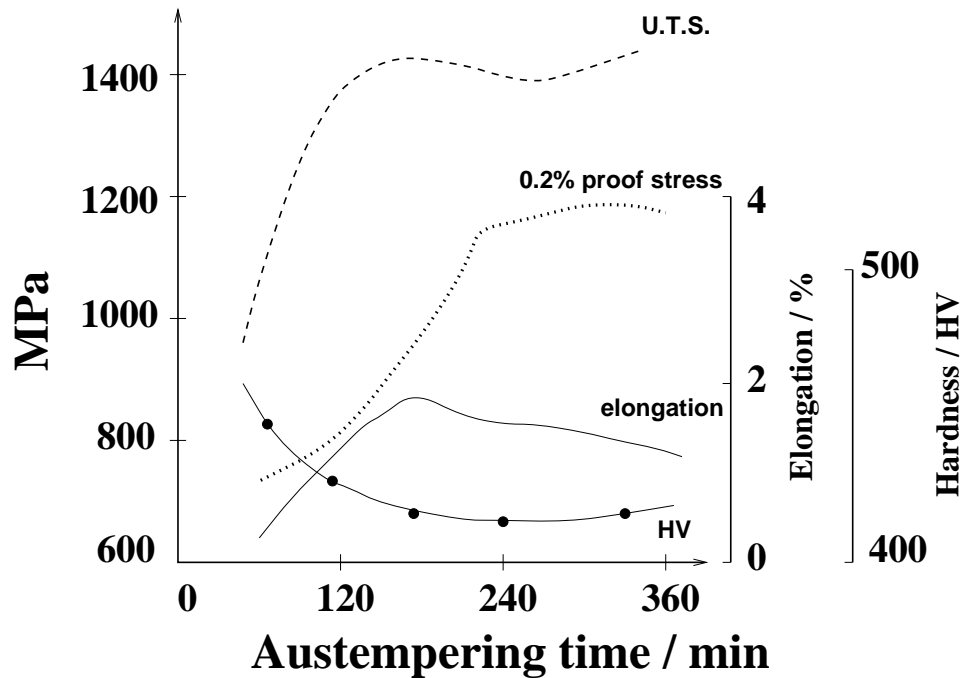


Figure 8.18: The effect of austempering time at 245°C on mechanical properties in an iron of composition Fe-3.5C-2.7Si-0.15Mn-1.0Ni-0.5Cu-0.16Mo wt % [4].

Chapter 9

Ultra Low Temperature ADI

9.1 Introduction

A large variety of austempered ductile irons can be obtained by changing the austenitising and austempering conditions, and the chemical composition. Thus, the tensile strength can range from 800 to about 1700 MPa with elongations of 11 to 1% respectively. Recently, the theory of phase transformations has been applied to the design of novel high-strength steels [175]. These steels contain high-carbon, silicon and manganese, and are isothermally heat-treated at a very low temperature to achieve a tensile strength of about 2.5 GPa [175]. Although there are differences between ductile iron and steels, it is striking that the matrix of ductile iron is similar in composition to these steels. It may therefore be possible to widen even more the range of properties of ADI's family. This chapter describes a series of austempering experiments performed at very low temperatures and following the same philosophy used for steels.

9.2 Previous work

Many features of bainitic microstructures in silicon-rich steels and ductile irons can be calculated theoretically. These include the maximum volume fractions of bainitic ferrite and austenite as a function of alloy composition, transformation temperature and the chemical composition of the austenite and bainitic ferrite. There are two essential morphologies of retained austenite in silicon steels and ADI. There are films of austenite between the individual platelets (subunits) of bainitic ferrite, and coarser more equiaxed blocks of austenite between non-parallel shaves of bainite. Both of them have already been described (Chapter 3). As discussed in chapter 6, a smaller fraction of bainitic ferrite is obtained at high austempering temperatures (until the fraction becomes zero at B_S); the blocks of austenite therefore become larger at high isothermal transformation temperatures. A finer microstructure with bainitic ferrite plates separated by thin films of retained austenite is promoted by low transformation temperatures. Such a microstructure is in many respects ideal from the point of view of mechanical properties [257]. Caballero *et*

al. [258] reported novel high-strength bainitic steels designed to minimise the amount of blocky austenite. They reported an ultimate tensile strength of 1790 MPa in a steel of composition Fe-0.32C-1.5Si-2Mn-1.26Cr-0.26Mo-0.1V wt % [258].

Two methods of increasing the maximum permitted degree of transformation to bainitic ferrite have been suggested [91, 259]. The first is by reducing the overall carbon content \bar{x} of the alloy concerned, so that the critical concentration in the austenite at which displacive transformation becomes impossible is reached at a later stage in the transformation and hence a higher volume fraction of bainite is obtained. This is only useful if the reduction of the overall carbon content of the alloy does not at the same time lead to a decrease in the strength of the microstructure. The second method is by modifying the substitutional alloying elements such that the T_0 curve is shifted to higher austenite carbon concentrations.

In a more recent work Caballero *et al.* [175] reported that extremely fine bainitic ferrite can be obtained when transforming a high-carbon steel at temperatures as low as 125 °C during prolonged periods of time. However, optimum mechanical properties were found when the isothermal heat-treatment was performed at 190 °C for two weeks. The volume fraction of bainitic ferrite obtained was close to 0.87, and the tensile strength was over 2.5 GPa. The chemical composition of their steel is Fe-0.8C-1.6Si-1.94Mn-1.33Cr-0.3Mo-0.11V wt %, which is similar to the chemical composition of the austenite in ductile irons.

9.3 Experiments

The chemical composition of the ductile cast iron used is Fe-3.5C-2.51Si-0.55Mn-0.15Mo-0.31Cu wt %. Six cylindrical-specimens of 8 mm diameter and 12 mm length were machined from a keel block for heat treatment. These samples were sealed in quartz tubes under a partial pressure of argon to prevent oxidation during austenitisation. An austenitisation temperature of 960 °C was chosen to get about 1.0 carbon wt % in the matrix in all samples. This temperature was found by making thermodynamic calculations with MTDATA [34]. The phases allowed to exist at 960 °C for the purposes of calculations were austenite and graphite. The data base used was *PLUS* which is for solutions.

After austenitisation, five samples were austempered at 190 °C for different periods of time: 10, 20, 60, 120 and 240 days. Sample six was austempered at 400°C for 50 min. After austenitisation the sample was quenched in boiling water until its temperature was close to 400 °C, in order to avoid pearlite formation, and then placed into a furnace at 400°C. Finally, sample seven was austempered in two stages, first at 400°C for 50 min, and then at 190 °C for 10 days. Fig. 9.1 shows the cycles for all heat treatments. Table 9.1 shows also the conditions for the austempering and the identification given to each sample for easy reference.

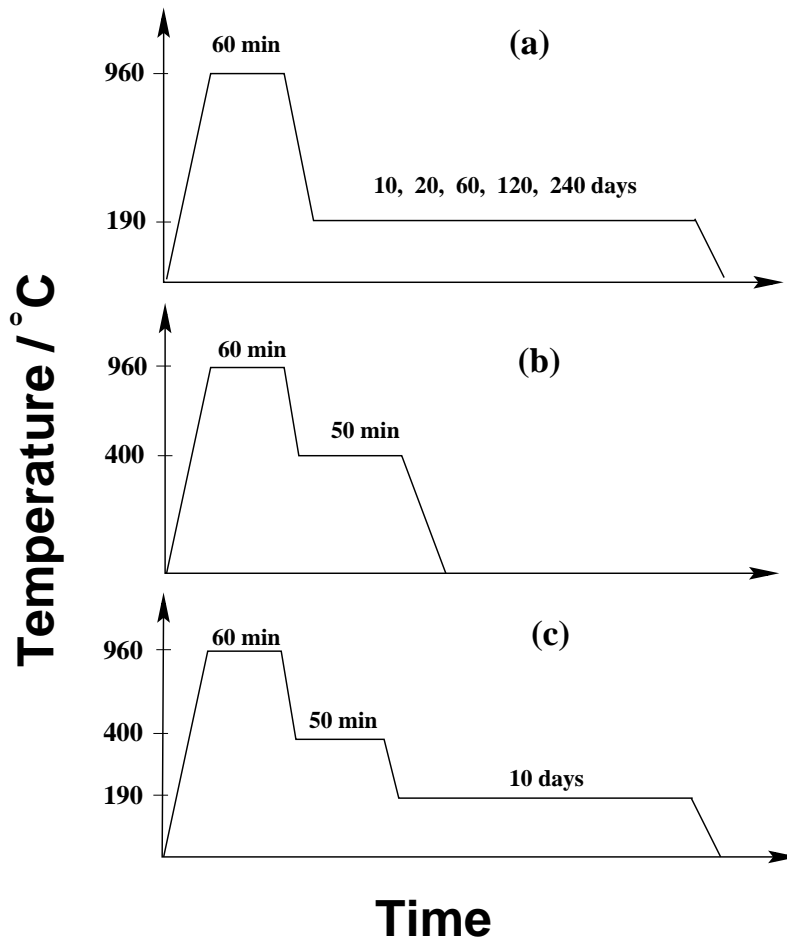


Figure 9.1: Heat treatment conditions for samples studied.

Sample name	T_γ °C	t_γ °C	T_A °C	t_A
<i>A</i>	960	60	190	10 days
<i>B</i>	960	60	190	20 days
<i>C</i>	960	60	190	60 days
<i>D</i>	960	60	190	120 days
<i>E</i>	960	60	190	240 days
<i>F</i>	960	60	400	50 min
<i>G</i>	960	60	400/190	50 min/10 days

Table 9.1: Samples studied.

9.4 Vickers hardness

The Vickers hardness method described in chapter 2 was used for the seven samples studied. Table 9.2 shows the averaged values obtained for each condition. It can be seen that samples *A* to *E* have very high hardness. From condition *A* to condition *B*

there is a small increase in hardness, however, after 20 days of austempering there is an apparent small decrease in this property. The hardness of sample *G*, which has the double austempering heat treatment, is higher than that of *F* with a single austempering at 400 °C.

Sample	Vickers hardness	Standard deviation
<i>A</i>	574	9
<i>B</i>	579	13
<i>C</i>	576	18
<i>D</i>	570	31
<i>E</i>	549	33
<i>F</i>	310	8
<i>G</i>	363	5

Table 9.2: Vickers hardness of samples studied in this chapter

9.5 Microscopy

All samples were prepared for microscopy using the procedure described in chapter 2. The microstructure of sample *A* consists of very fine bainitic ferrite and small areas of retained austenite close to the cell boundaries. Carbides were also found at the cell boundaries (Fig. 9.2a). Sample *B* shows a microstructure similar to *A*, but it seems to have more bainite transformation at the cell boundaries (Fig. 9.2b). The microstructure obtained in samples *C* to *E* were found to be similar to that of *B*.

Micrographs were taken also from samples *F* and *G*. Fig. 9.3a shows retained austenite, upper bainitic ferrite and martensite at the centre of blocky areas of austenite. This microstructure corresponds to the sample with single austempering at 400 °C for 50 min. This austempering time was calculated using the neural network model described in chapter 5 to achieve a maximum volume fraction of retained austenite. Since the austempering temperature is high, the volume fraction of bainitic ferrite is low and the carbon enrichment of austenite is poor; therefore, some areas transform to martensite. On the other hand, the sample austempered at 400 °C for the same time, and then austempered at low temperature (190 °C) for 10 days, shows very fine bainitic ferrite. This bainitic ferrite is observed where martensite would form otherwise (Fig. 9.3b). This fine bainitic ferrite is of the same kind as that observed in samples *A* to *E*. The increase in hardness from 310 in sample *F* to 363 HV of sample *G* is due to the formation of the fine bainite ferrite at low temperature.

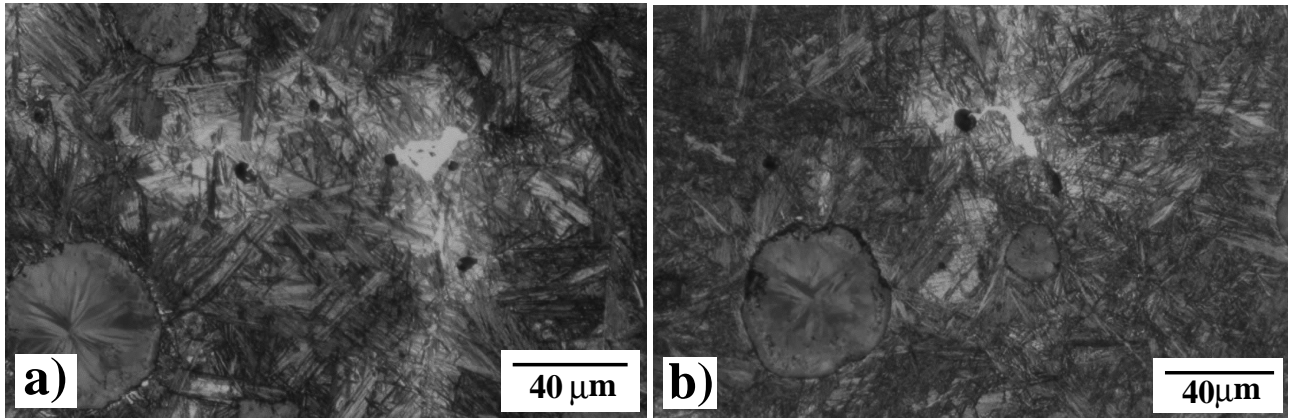


Figure 9.2: Microstructure samples austenitised at 960 °C for one hour and quenched to austempering temperature (190 °C for 10 (sample *A*) and 20 (sample *B*) days. (a) *A* Fine bainitic ferrite (dark sheaves), some retained retained austenite at intercellular areas (light phase), and carbides (white particles). (b) The same microstructure as (a) but with apparently more bainitic ferrite in the matrix.

9.6 X-ray diffraction

X-ray diffraction showed that high volume fractions of bainite were obtained after long heat treatments at very low temperature. These levels of bainite transformation are consistent with the T_0 concept which indicates that larger volume fractions are expected at lower temperatures. Table 9.3 shows that the sample austempered for 10 days at 190 °C (*A*) contains less bainite than that austempered for 20 days. Samples austempered for longer times (*C, D, E*) have similar bainite volume fractions to sample *B*. This may imply that bainitic transformation is very close to completion at 10 days

Sample	Volume fraction of austenite	error	Volume fraction of bainite	error
<i>A</i>	0.22	0.05	0.78	0.04
<i>B</i>	0.18	0.05	0.82	0.04
<i>C</i>	0.19	0.05	0.80	0.04
<i>D</i>	0.17	0.06	0.83	0.04
<i>E</i>	0.20	0.06	0.81	0.04
<i>F</i>	0.53	0.02	0.47	0.03
<i>G</i>	0.45	0.03	0.55	0.03

Table 9.3: X-ray diffraction results

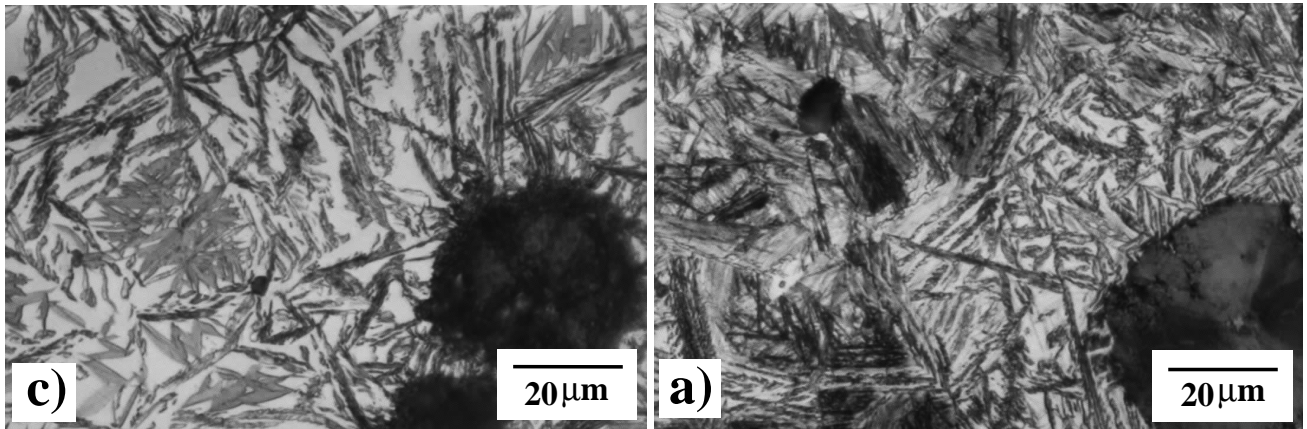


Figure 9.3: Microstructure of samples *F* and *G* austenitised at 960 °C for one hour and quenched to austempering temperature. (a) Sample *F* austempered at 400 °C for 50 minutes. The microstructure shows a mixture of upper bainitic ferrite, retained austenite and some martensite at the centre of blocky areas of retained austenite. (b) Sample austempered at two different temperatures; 400 °C for 50 min, and 190 for 10 days. The microstructure is a mixture of upper bainitic ferrite, retained austenite and extremely fine bainitic ferrite at the centre of blocky areas of retained austenite.

9.7 TEM

Thin-foil samples were prepared from specimen *C* for transmission electron microscopy. Bright field images are useful to reveal the fine features of bainitic ferrite obtained with the very low austempering temperature (Fig. 9.4).

There are two essential morphologies of austenite in ADI. The films of austenite between individual platelets (subunits) of bainitic ferrite, and the coarser more equiaxed blocks of austenite between non-parallel shaves of bainite. The former, is extremely fine when obtained at very low temperatures and can only be resolved using TEM (Fig. 9.4a). The coarser, at this low temperature of heat treatment may be observed at the cell boundaries, as shown in Fig. 9.2.

9.8 Tensile test

Two tensile specimens with 5 mm diameter cross-section, as shown in Fig. 9.5a, were tested on a 100 kN hydraulic *INSTRON 8501* universal testing machine with a crosshead rate of 0.01 mm/min. Samples were machined before heat-treatment and the tests were conducted following recommendations of the ASTM standard E8-91. The samples were sealed in quartz tubes under a partial pressure of argon to prevent oxidation when austenitising at 960 °C for 60 min. After austenitisation, the quartz tubes were broken and the samples placed into a furnace at 190 °C for 20 days; *B*. The furnace employed (*CARBOLITE*) was equipped with a low-temperature control to enable temperature stability.

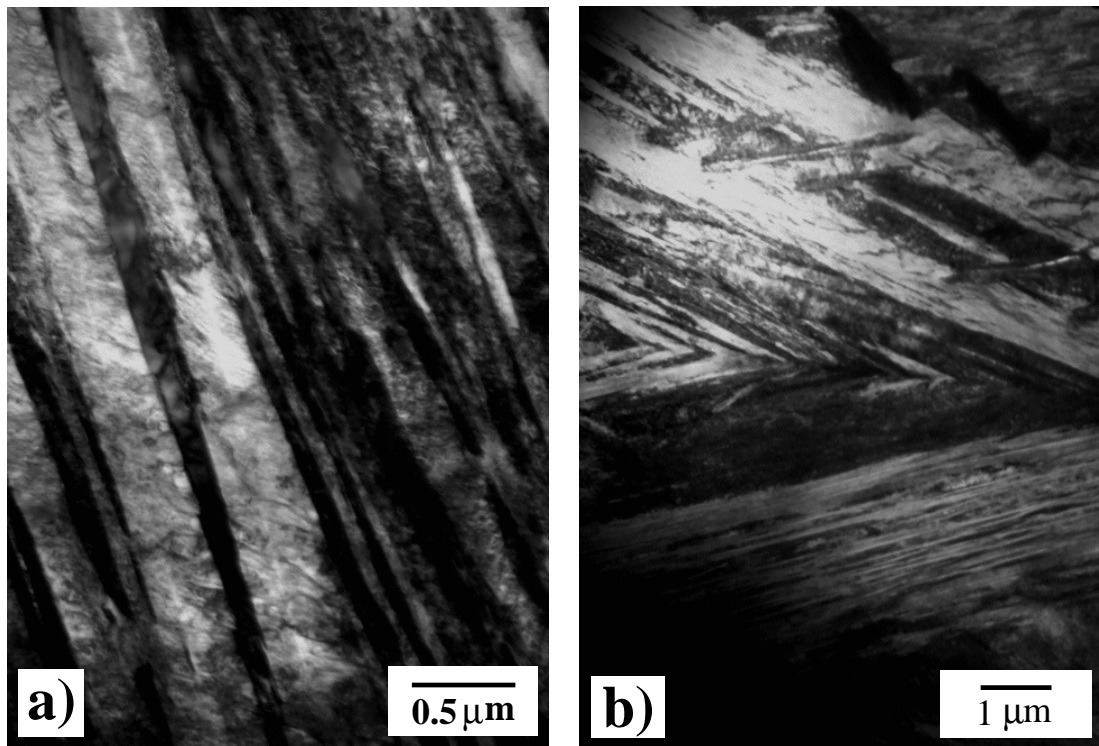


Figure 9.4: TEM bright field images obtained from sample *C*. (a) Sub-units of bainitic ferrite (light microstructure) and films of retained austenite in a sheaf of bainite. (b) Two sheaves of bainite.

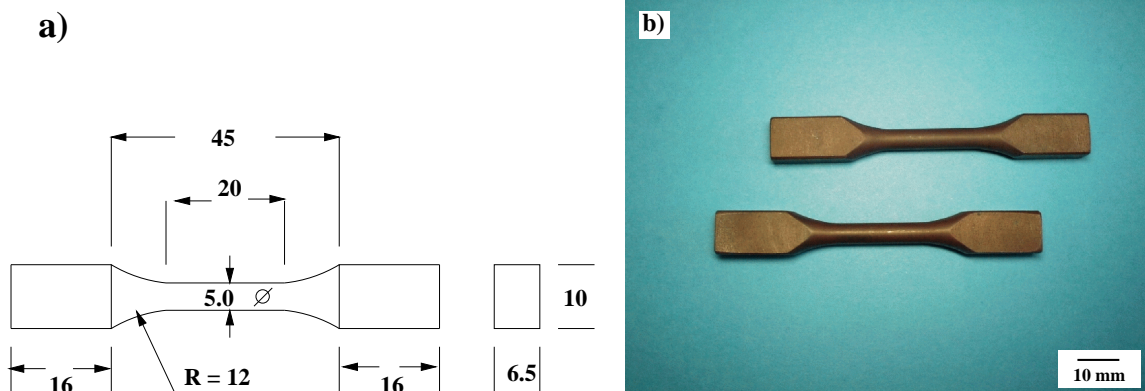


Figure 9.5: Tensile specimen (a) Dimensions in mm, (b) photograph of actual samples as heat treated. Austenitised at 960 °C for 60 min, and austempered at 190 °C for 20 days (condition *B*).

The ultimate tensile strength was 972 MPa for the first and 1109 MPa for the second sample, and both of them broke in a similar way. Fig. 9.6 shows the engineering stress-strain curve of the second tensile specimen. It can be seen that samples broke with

no apparent plastic deformation. Fig. 9.7 shows no detectable reduction in area at the fracture zone. Despite this apparent lack of plastic deformation, fractography analysis revealed some dimple rupture due to microvoid coalescence (Fig. 9.8).

Additional X-ray diffraction analyses were performed on a broken tensile sample. The purpose of these tests was to assess any change in the volume fraction of retained austenite due to the tensile test. Two longitudinal sections were evaluated, one close to the fracture site and the other on a section far from the fracture. The results 0.124 ± 0.04 and 0.123 ± 0.04 volume fraction at the fracture section, and for the area far from the fracture (grips section) respectively, show that no change in the volume fraction occurred. This means that retained austenite did not transform into martensite indicating its high stability.

The microstructure obtained on the low temperature ADI is similar to that observed on steels reported by Caballero *et al.* [175]. This is, a very fine mixture of bainitic ferrite and high carbon content retained austenite. Thus, the theory of phase transformations is confirmed, specially the T_0 concept which indicates that at lower temperature the volume fraction of bainite formation is increased.

The strength of this ADI was not as high as expected (and inconsistent with the high hardness) according to what has been reported for steels (2.5 GPa). It may be that carbides at the cell boundaries are causing a decrease in strength. Less manganese and higher nodule count would reduce carbide volume fraction and segregation effects. This should be taken into account to improve the mechanical properties of ADI. The literature shows that other researchers have reported a maximum U.T.S of 1.733 GPa with 1.1% of elongation [219], The chemical composition of this ADI is Fe-3.58C-2.63Si-0.22Mn-0.51Cu wt%, austenitised at 871 °C for 90 min and austempered at 260 °C for 90 min.

The ultimate tensile strength obtained in the present work is inconsistent with the measure of hardness. This is because according to the widely known approximation of Eq. 9.1 [260] which relates the yield strength from the hardness value, the yield strength would be 1893 MPa.

$$HV \equiv 3Y \quad (9.1)$$

where HV is the Vickers hardness number, and Y the 0.2 percent offset yield strength, kgf mm^{-2} ($= 9.81 \text{ MPa}$). However, the tensile sample failed prematurely (Fig. 9.6).

The fracture surfaces in Figs. 9.8 and 9.9 show that cleavage precedes ductile fracture, which is confined to regions around graphite nodules where plane stress conditions may occur locally.

The cleavage process is sensitive to the presence of heterogeneities such as large carbides or graphite. In detailed fractographic work on cleavage fractures in steels Gibson [261]

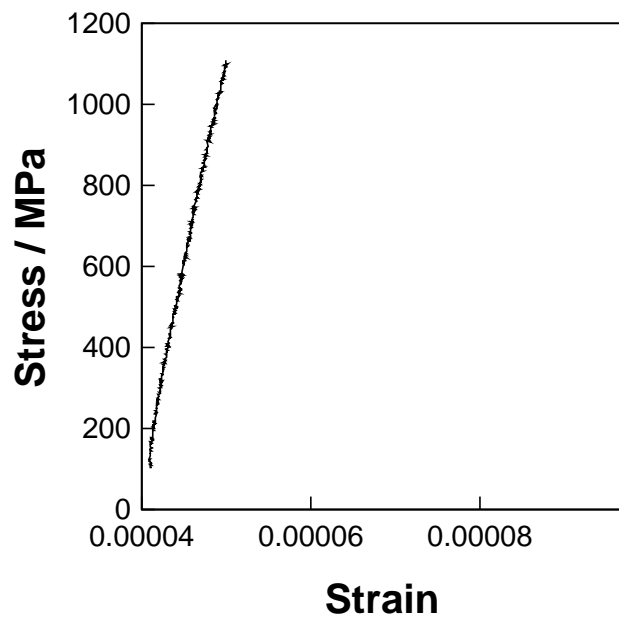


Figure 9.6: The engineering stress-strain curve of one of the tensile samples. Notice that only elastic strain was recorded.



Figure 9.7: The tensile samples after testing. Notice the fracture of both at the gauge length

found that cleavage fracture was initiated by the cracking of brittle second phase particles, namely iron carbides. Evidence of this phenomenon is observed in Fig. 9.10. It is possible therefore that the measured tensile strength is really a cleavage fracture stress. This is confirmed with the compression test, since the results show that only 0.5% of deformation occurred under 2.52 GPa of stress without fracture. The Vickers hardness at the centre of the sample, where deformation is maximum, increased from 579 to 605 HV.

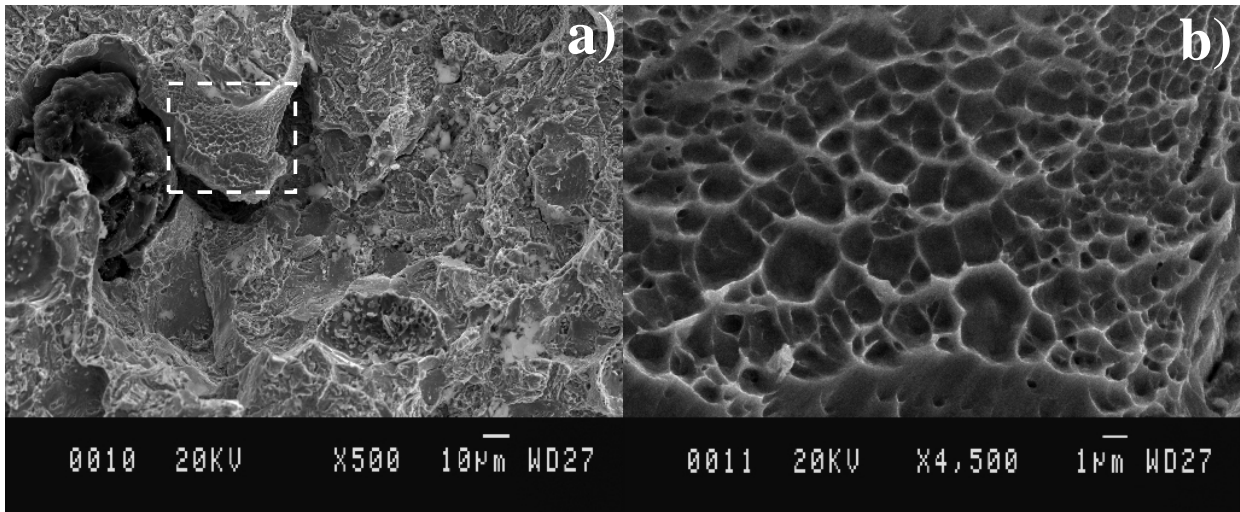


Figure 9.8: SEM micrographs showing the features of the fracture surface. (a) Lower magnification of the broken surface, (b) Enlarged image of an area with microvoid coalescence. This corresponds to the marked area in image (a).

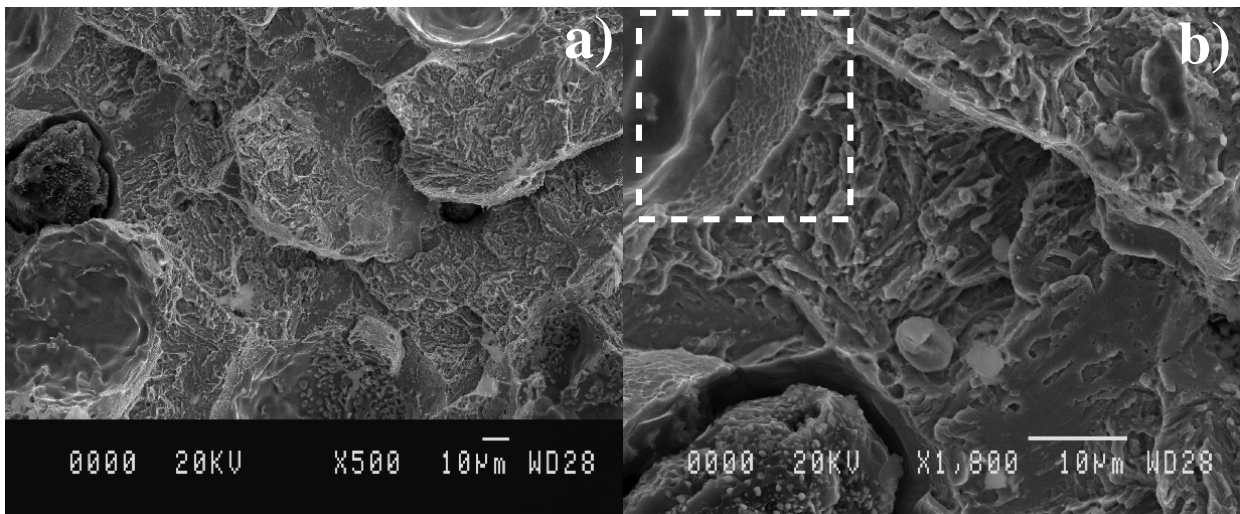


Figure 9.9: SEM micrographs showing brittle and ductile areas. (a) Low magnification of fracture surface in tensile sample identified as 1st. (a) The area indicated by the square seems to be another ductile area.

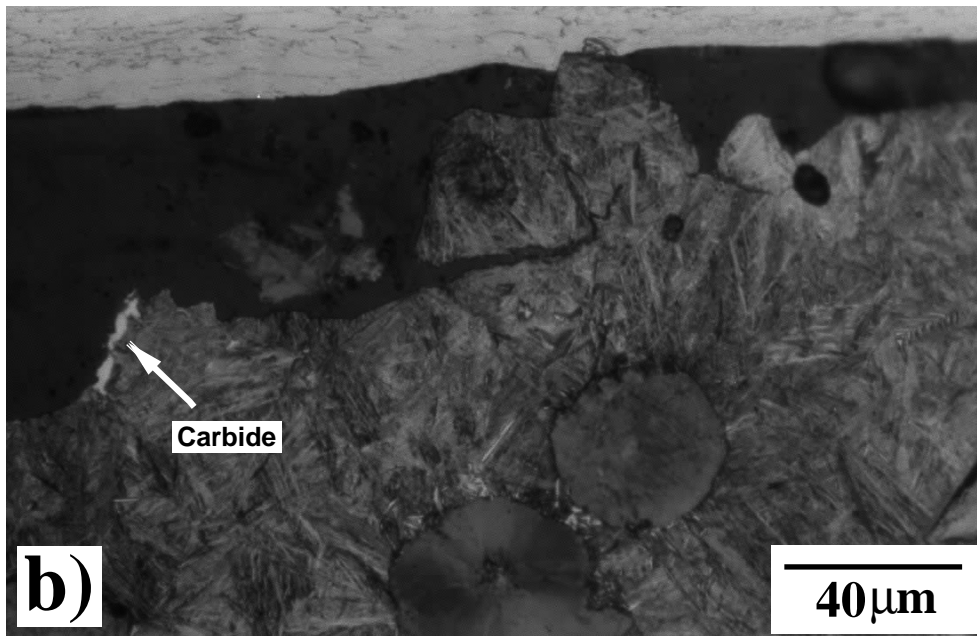
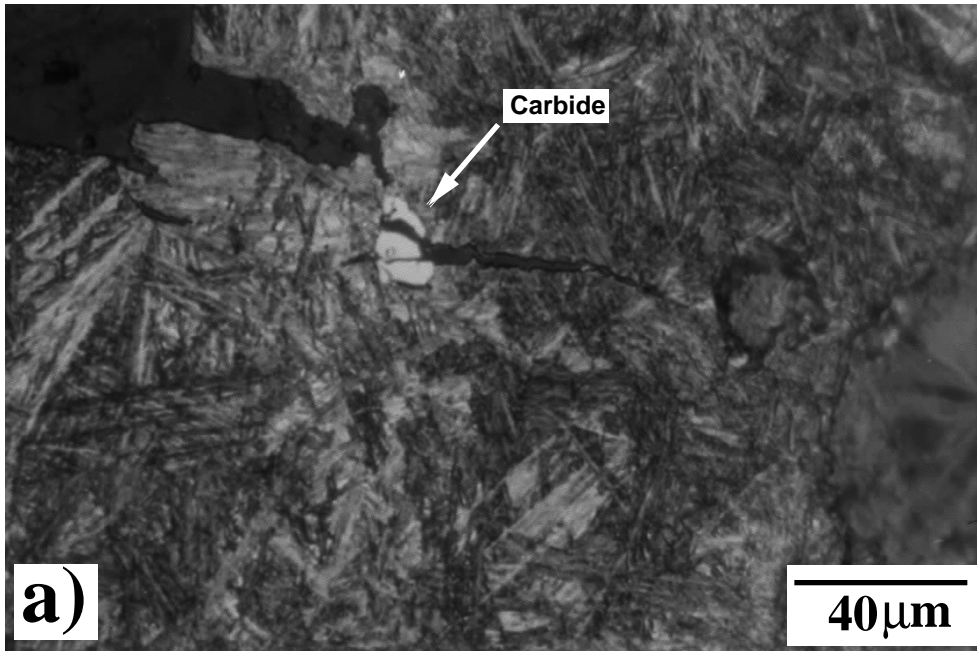


Figure 9.10: Longitudinal view of the fracture surface of one of the tensile samples. (a) Shows the fracture of a manganese carbide which might be the cause of cleavage fracture initiation of this ADI. (b) Shows also the fracture surface and carbides at the edge of the fracture. Notice, however, that the fracture surface reveals ductile areas.

9.9 Summary

According to results, it was found that the theory of phase transformations applied to the design of ultra-high strength steels, can also be applied to austempered ductile irons. This is because the microstructure obtained at very low austempering temperature is identical to that found in steels, which have proved to have tensile strength over 2.5 GPa. However, ductile irons contains nodules of graphite, and they are cast. This leads to a natural segregation of chemical elements with negative effects. Manganese for example, forms carbides at the cell boundaries. These hard carbides are presumably to be blamed for the premature failure on tensile testing.

If the presence of brittle manganese carbides is diminished, initiation of cleavage fracture may be eliminated and tensile strength improved. This would widen the range of ADI's mechanical properties.

Chapter 10

Summary and Future Work

It can be said with certainty that austempered ductile cast irons are complex materials with heterogeneous microstructures. They are, nevertheless, versatile materials whose mechanical properties can be varied over wide ranges by altering the chemical composition or processing conditions.

The work presented in this thesis has contributed to understanding the factors which control the development of microstructure. One of the important microstructural constituents is the fraction of austenite that is retained on cooling the cast-iron from the austempering temperature to ambient temperature. It is known that the fraction of austenite is maximised by transformation to bainite at a temperature somewhere between the bainite-start and martensite-start temperatures. It was possible to quantitatively reproduce this observation using a neural network model in which the inputs consisted of the detailed chemical composition and the austenitising and austempering heat-treatments.

The model for retained austenite was created using a large quantity of experimental data collected from the published literature. It is interesting that the choice of inputs made a crucial difference to the accuracy of the model. Thus, the use of time alone as an input is ill-advised because the real dependence of microstructural evolution is on the logarithm of time, and the network is found not to be sufficiently powerful to capture this vital detail.

The neural network model is particularly useful in two respects: (i) it reveals complex interactions between the variables controlling the retained austenite content; (ii) it serves as an assessment of the experimental data by providing estimates of uncertainty.

Thus, the neural network model was used in a unique way to provide “experimental data” for the validation of a physical model for retained austenite. This latter model was based on the bainite transformation mechanism. Very little bainite can form at high transformation temperatures, thus limiting the amount of carbon that partitions into the residual austenite, which then remains unstable to martensitic transformation on cooling. On the other hand, transformation at high undercoolings below the bainite-start temperature leaves little austenite available for retention on cooling to ambient temperature.

The model was therefore able to explain the experimental observations, without using any adjustable parameters; remaining discrepancies between the model and experimental data could reasonable and qualitatively be explained in terms of an inhomogeneous distribution of carbon.

One of the most exciting outcomes of all the work is that a suite of models has been created (Fig. 10.1) which represents the most complete set to date, necessary for the design of austempered ductile cast iron. The suite includes thermodynamic, kinetic and mechanical property models, which together can be used in design.

There are a number of interesting outcomes from even just the cursory use of the models. Thus, it has been demonstrated that the use of un-notched Charpy impact samples for ambient temperature tests is essentially redundant because the test correlates directly with tensile ductility.

It would be useful to continue to develop the mathematical models. The attempt to describe the kinetics of cementite precipitation from austenite has many unjustified approximations. For example, it is unlikely that the initial carbide is cementite; thermodynamic data are needed to deal with any transition carbides. A useful model would allow all carbides to precipitate at the same time albeit at different rates, so that the sequence or parallel development of the microstructure could be modelled. The transition from upper to lower bainite also needs to be expressed quantitatively. Models like these rely on thermodynamic data which are not yet available, together with a knowledge of interfacial energies and the number densities of nucleation sites. Validation would require quite detailed microstructural analysis.

Recent work [175] has shown that incredibly strong steels can be obtained by transforming to bainite at very low temperatures. Promising preliminary work has been done in this context by austempering ADI at very low temperatures. The indications are that a strength greater than 2300 MPa is possible, but the cast irons contain large inclusions which prevent this from being achieved in a tensile test. Further work could be carried out on thoroughly homogenised samples.

Modelling the Microstructure and Mechanical Properties of ADI

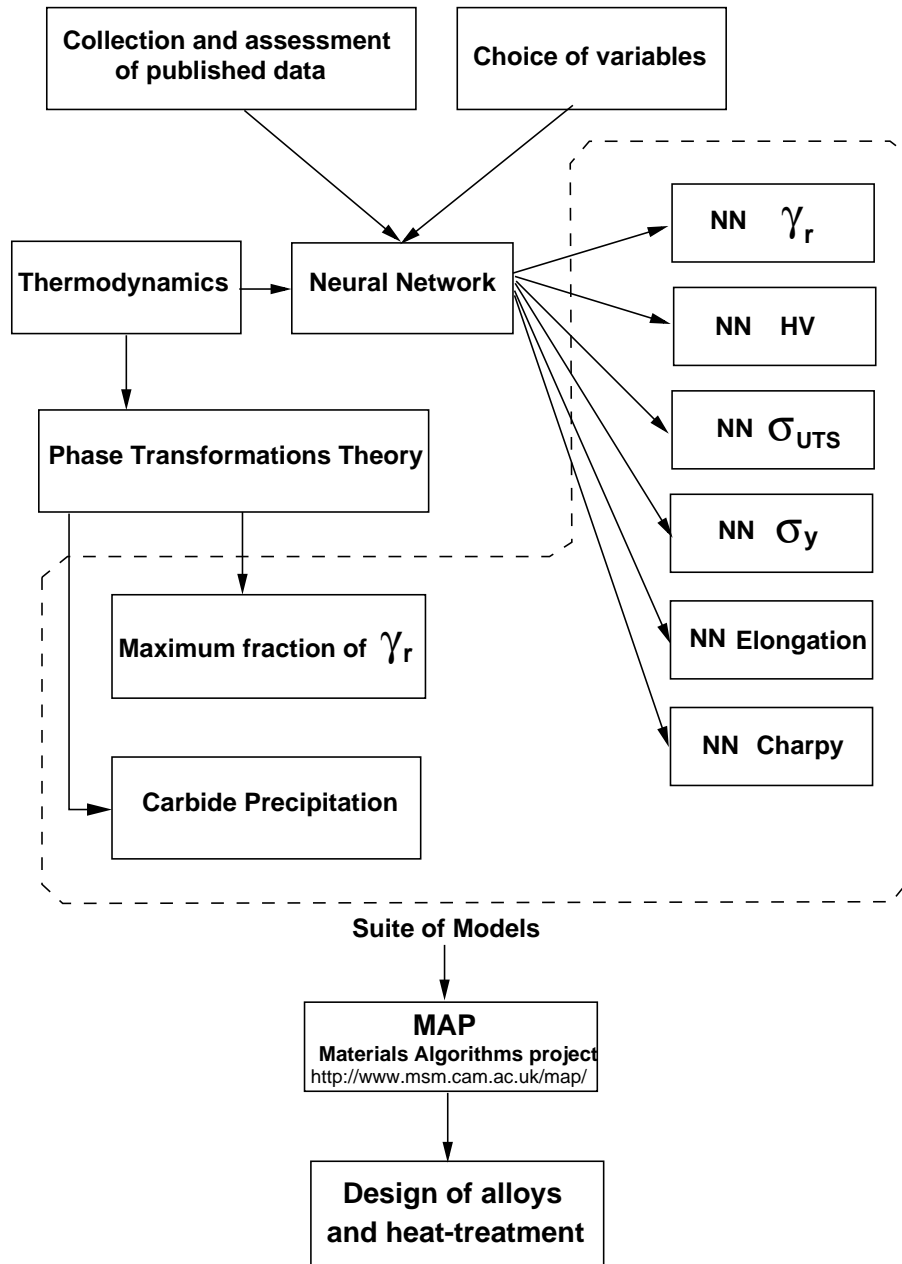


Figure 10.1: Flow chart of models created to design ADI alloys and find optimum austempering heat-treatment for the best mechanical properties according to specific needs

APPENDIX ONE

MAP_NEURAL_ADL_RETAINED-AUSTENITE

This appendix presents the model described in chapter 5 and associated documentation following the MAP format, <http://www.msm.cam.ac.uk/map/mapmain.html>.

1. Provenance of Source Code

Miguel Angel Yescas-Gonzalez,
Phase Transformation & Complex Properties Research Group,
Department of Materials Science and Metallurgy,
University of Cambridge,
Cambridge, CB2 3QZ, U. K.

The neural network program was produced by:

David MacKay,
Cavendish Laboratory,
University of Cambridge,
Madingley Road,
Cambridge, CB3 0HE, U. K.

Added to MAP: August 2000

2. Purpose

Estimation of the amount of retained austenite in austempered ductile irons (ADI) as a function of chemical composition and heat treatment conditions (austenitising temperature, austenitising time, austempering temperature, and austempering time).

3. Specification

Language: FORTRAN / C
Product form: Source code/ Executable files
Operating System: Linux, Solaris 5.5.1 & DOS

4. Description

MAP_NEURAL_ADL_RETAINED-AUSTENITE contains the programs which enable the user to estimate the amount in percent of retained austenite for any austempered ductile iron (ADI) as a function of chemical composition and heat treatment conditions. It makes use of a neural network program called *generate44*, which was developed by David MacKay and is part of the *bigback5* program. The network was trained using a large database of experimental results [1]. 16 different models are provided, which differ from each other by

the number of hidden units and by the value of the seed used when training the network. It was found that a more accurate result could be obtained by averaging the results from all models [1]. The programs calculate the results of each model and then combines them, by averaging, to produce a *committee result* and error estimate, as described by MacKay [2].

Programs are available which run on a Solaris 5.5.1 UNIX operating system, Linux, and on a PC under Windows 95/98. A set of programs and data files are provided for the model. The files for UNIX and Linux are included in a directory called ADI. This directory contains the following files and subdirectories.

README

A text file containing step-by-step instructions for running the program, including a list of input variables.

MINMAX

A text file containing the minimum and maximum limits of each input and output variable. This file is used to normalise and unnormalise the input and output data.

test.dat

An input file containing the input variables used for predictions.

model.gen

This is a UNIX shell file containing the command steps required to run the module. It can be executed by typing 'csh model.gen' at the command prompt. This shell file compiles and runs all the programs necessary for normalising the input data, executing the network for each model, unnormalising the output data and combining the results of each model to produce the final *committee* result.

RET_AUST.exe

This executable program for the PC corresponds to the UNIX command file *model.gen*

no_of_lines.ex

This executable file reads the information of number of data from the keyboard input and creates *rows.dat* file. This file is used by *spec.ex* to create *spec.t1*.

spec.ex

This executable file reads the information in *no_of_rows.dat* and creates a file called *spec.t1*

spec.t1

A dynamic file, created by executable **spec.ex**, which contains information about the module and the number of data items being supplied. It is read by the program *generate44/generate55.exe*

norm_test.in

This is text file which contains the normalised input variables. It is generated by the program *normtest.for* in subdirectory *s* .

generate44/generate55.exe

This is executable file for the neural network program. *generate44* runs on UNIX system and *generate55* on the PC. It reads the normalised input data file *norm_test.in*, and uses the weight files in subdirectory c. The results are written in the temporary output file_out.

_ot, _out, _res, _sen

These files are created by *generate44* and can be deleted. **Results**

Contains the final un-normalised committee results for the predicted percentage of retained austenite.

SUBDIRECTORY s

no_of_lines.c

The source code for the program *no_of_lines.ex*.

spec.c

The source code for the program *spec.ex*

normtest.for Program to normalise the data in *test.dat* and produce the normalised input file *norm_test.in*. It makes use of information read in from *no_of_rows.dat*

gencom.for

this program uses the information in *committee.dat* and combines the predictions from the individual models, in the subdirectory *outprdt*, to obtain an averaged value (*committee prediction*). The output (in normalised form) is written to *com.dat*.

treatout.for

Program to un-normalise the committee results in *com.dat* and write the output predictions to *unnorm_com*. This file is then renamed *Results*.

committee.dat

A text file containing the number of models to be used to form the committee results and the number of input variables. It is read by *gencom.for*, *normtest.for* and *treatout.for*

SUBDIRECTORY c

_w*f

The weights files of the different models.

***.lu**

Files containing information for calculating the size of the error bars for the different models.

_c*

Files containing information about the perceived significance value [1] for each model.

_R*

Files containing values of the noise, test error and log predictive error [1] for each model.

SUBDIRECTORY d

outran.x

A normalised output file which was created during the building of the model. It is accessed by *generate44* via *spec.tl*

SUBDIRECTORY outprdt

out1, out2, etc.

The normalised output files for each model.

com.dat The normalised output file containing the committee results. It is generated by gencom.for

5. References

1. Miguel Angel Yescas, H. K. D. H. Bhadeshia and D. J. C. MacKay, *Estimation of the amount of retained austenite in austempered ductile irons* Materials Science and Engineering A311, (2001) 162-173.
2. D. J. C. MacKay, *Mathematical modelling of weld phenomena 3*, eds. H. Cerjak and H. K. D. H. Bhadeshia, Institute of Materials, London, (1997) 359.
3. D. J. C. MacKay's website at <http://wol.ra.phy.cam.ac.uk/mackay/README.html>

6. Input parameters

The input variables for the model are listed in the README or README.DOC files in the corresponding directory. The maximum and minimum values for each variable are given in the file MINMAX.

7. Output parameters

This program gives the amount of retained austenite value in %. The output is written in the file Result or Result.dat.

Prediction	Upper-limit	Lower-limit
(%)	(%)	(%)

Accuracy

A full calculation of the error bars is presented in reference 1.

Program data

See sample data file: test.dat

Program results

See sample output file: Result or Result.dat

Keywords

Neural network, retained austenite, ADI, Austempered ductile iron, bainite.

Download

The model for the calculation of the volume fraction of retained austenite of ADI for UNIX, Linux, and PC version can be downloaded from: <http://www.msm.cam.ac.uk/map/mapmain.html>.

APPENDIX TWO

MAP_NEURAL_ADLHV

This appendix presents the model described in chapter 8 which estimates the Vickers hardness of austempered ductile irons, and associated documentation following the MAP format, <http://www.msm.cam.ac.uk/map/mapmain.html>.

1. Provenance of Source Code

Miguel Angel Yescas-Gonzalez,
Phase Transformation & Complex Properties Research Group,
Department of Materials Science and Metallurgy,
University of Cambridge,
Cambridge, CB2 3QZ, U. K.

The neural network program was produced by:

David MacKay,
Cavendish Laboratory,
University of Cambridge,
Madingley Road,
Cambridge, CB3 0HE, U. K.

Added to MAP: August 2000

2. Purpose

Estimation of hardness in ADI as a function of chemical composition and heat treatment conditions (austenitising temperature, austenitising time, austempering temperature, and austempering time).

3. Specification Language: FORTRAN / C

Product form: Source code/ Executable files

Operating System: Linux, Solaris 5.5.1 & DOS

4. Description

MAP_NEURAL_ADLHV contains the programs which enable the user to estimate the hardness in HV for any austempered ductile iron (ADI) as a function of chemical composition and heat treatment conditions. It makes use of a neural network program called *generate44*, which was developed by David MacKay and is part of the *bigback5* program. The network was trained using a large database of experimental results [1]. 10 different models are provided, which differ from each other by the number of hidden units and by the value of the seed used when training the network. It was found that a more accu-

rate result could be obtained by averaging the results from all models [1]. The programs calculate the results of each model and then combines them, by averaging, to produce a *committee result* and error estimate, as described by MacKay [2].

Programs are available which run on a Solaris 5.5.1 UNIX operating system, Linux, and on a PC under Windows 95/98. A set of programs and data files are provided for the model. The files for UNIX and Linux are included in a directory called ADI. This directory contains the following files and subdirectories.

README

A text file containing step-by-step instructions for running the program, including a list of input variables.

MINMAX

A text file containing the minimum and maximum limits of each input and output variable. This file is used to normalise and unnormalise the input and output data.

test.dat

An input file containing the input variables used for predictions.

model.gen

This is a UNIX shell file containing the command steps required to run the module. It can be executed by typing 'csh model.gen' at the command prompt. This shell file compiles and runs all the programs necessary for normalising the input data, executing the network for each model, unnormalising the output data and combining the results of each model to produce the final *committee* result.

MODEL.exe

This executable program for the PC corresponds to the UNIX command file *model.gen*

no_of_lines.ex

This executable file reads the information of number of data from the keyboard input and creates *rows.dat* file. This file is used by *spec.ex* to create *spec.t1*.

spec.ex

This executable file reads the information in *no_of_rows.dat* and creates a file called *spec.t1*

spec.t1

A dynamic file, created by executable **spec.ex**, which contains information about the module and the number of data items being supplied. It is read by the program *generate44/generate55.exe*

norm_test.in

This is text file which contains the normalised input variables. It is generated by the program *normtest.for* in subdirectory *s* .

generate44/generate55.exe

This is executable file for the neural network program. *generate44* runs on UNIX system and *generate55* on the PC. It reads the normalised input data file *norm_test.in*, and uses

the weight files in subdirectory c. The results are written in the temporary output file_out.

_ot, _out, _res, _sen

These files are created by *generate44* and can be deleted. **Results**

Contains the final un-normalised committee results for the predicted percentage of retained austenite.

SUBDIRECTORY s

no_of_lines.c

The source code for the program *no_of_lines.ex*.

spec.c

The source code for the program *spec.ex*

normtest.for Program to normalise the data in *test.dat* and produce the normalised input file *norm_test.in*. It makes use of information read in from *no_of_rows.dat*

gencom.for

this program uses the information in *committee.dat* and combines the predictions from the individual models, in the subdirectory *outprdt*, to obtain an averaged value (*committee prediction*). The output (in normalised form) is written to *com.dat*.

treatout.for

Program to un-normalise the committee results in *com.dat* and write the output predictions to *unnorm_com*. This file is then renamed *Results*.

committee.dat

A text file containing the number of models to be used to form the committee results and the number of input variables. It is read by *gencom.for*, *normtest.for* and *treatout.for*

SUBDIRECTORY c

_w*f

The weights files of the different models.

***.lu**

Files containing information for calculating the size of the error bars for the different models.

_c*

Files containing information about the perceived significance value [1] for each model.

_R*

Files containing values of the noise, test error and log predictive error [1] for each model.

SUBDIRECTORY d

outran.x

A normalised output file which was created during the building of the model. It is accessed by *generate44* via *spec.t1*

SUBDIRECTORY outprdt

out1, out2, etc.

The normalised output files for each model.

com.dat The normalised output file containing the committee results. It is generated by gencom.for

5. References

1. Miguel Angel Yescas, *Prediction of the Vickers hardness in austempered ductile irons using neural networks*, International Journal of Cast Metals Research, in press.
2. D. J. C. MacKay, *Mathematical modelling of weld phenomena 3*, eds. H. Cerjak and H. K. D. H. Bhadeshia, Institute of Materials, London, (1997) 359.
3. D. J. C. MacKay's website at <http://wol.ra.phy.cam.ac.uk/mackay/README.html>

6. Input parameters

The input variables for the model are listed in the README or README.DOC files in the corresponding directory. The maximum and minimum values for each variable are given in the file MINMAX.

7. Output parameters

This program gives the value of hardness in Vickers units. The output is written in the file Result or Result.dat.

Prediction Error bar Upper-limit Lower-limit

Accuracy

A full calculation of the error bars is presented in reference 1.

Program data

See sample data file: test.dat

Program results

See sample output file: Result or Result.dat

Keywords

Neural network, Vickers hardness, ADI, Austempered ductile iron.

Download

The model for the calculation of the Vickers hardness of ADI for UNIX, Linux, and PC versions can be downloaded from: <http://www.msm.cam.ac.uk/map/mapmain.html>.

APPENDIX THREE

MAP_NEURAL_ADI_UTS

This appendix presents the model described in chapter 8 which estimates the ultimate tensile strength (UTS) of austempered ductile irons, and associated documentation following the MAP format, <http://www.msm.cam.ac.uk/map/mapmain.html>.

1. Provenance of Source Code

Miguel Angel Yescas-Gonzalez,
Phase Transformation & Complex Properties Research Group,
Department of Materials Science and Metallurgy,
University of Cambridge,
Cambridge, CB2 3QZ, U. K.

The neural network program was produced by:

David MacKay,
Cavendish Laboratory,
University of Cambridge,
Madingley Road,
Cambridge, CB3 0HE, U. K.

Added to MAP: November 2000

2. Purpose

Estimation of the ultimate tensile strength of ADI as a function of chemical composition and heat treatment conditions (austenitising temperature, austenitising time, austempering temperature, and austempering time).

3. Specification

Language: FORTRAN / C
Product form: Source code/ Executable files
Operating System: Linux, Solaris 5.5.1 & DOS

4. Description

MAP_NEURAL_ADI_UTS contains the programs which enable the user to estimate the ultimate tensile strength in MPa for any austempered ductile iron (ADI) as a function of chemical composition and heat treatment conditions. It makes use of a neural network program called *generate44*, which was developed by David MacKay and is part of the *bigback5* program. The network was trained using a large database of experimental results [1]. 7 different models are provided, which differ from each other by the number of hidden

units and by the value of the seed used when training the network. It was found that a more accurate result could be obtained by averaging the results from all models [1]. The programs calculate the results of each model and then combines them, by averaging, to produce a *committee result* and error estimate, as described by MacKay [2].

Programs are available which run on a Solaris 5.5.1 UNIX operating system, Linux, and on a PC under Windows 95/98. A set of programs and data files are provided for the model. The files for UNIX and Linux are included in a directory called ADI. This directory contains the following files and subdirectories.

README

A text file containing step-by-step instructions for running the program, including a list of input variables.

MINMAX

A text file containing the minimum and maximum limits of each input and output variable. This file is used to normalise and unnormalise the input and output data.

test.dat

An input file containing the input variables used for predictions.

model.gen

This is a UNIX shell file containing the command steps required to run the module. It can be executed by typing 'csh model.gen' at the command prompt. This shell file compiles and runs all the programs necessary for normalising the input data, executing the network for each model, unnormalising the output data and combining the results of each model to produce the final *committee* result.

MODEL.exe

This executable program for the PC corresponds to the UNIX command file *model.gen*

no_of_lines.ex

This executable file reads the information of number of data from the keyboard input and creates *rows.dat* file. This file is used by *spec.ex* to create *spec.t1*.

spec.ex

This executable file reads the information in *no_of_rows.dat* and creates a file called *spec.t1*

spec.t1

A dynamic file, created by executable **spec.ex**, which contains information about the module and the number of data items being supplied. It is read by the program *generate44/generate55.exe*

norm_test.in

This is text file which contains the normalised input variables. It is generated by the program *normtest.for* in subdirectory *s* .

generate44/generate55.exe

This is executable file for the neural network program. *generate44* runs on UNIX system

and *generate55* on the PC. It reads the normalised input data file *norm_test.in*, and uses the weight files in subdirectory *c*. The results are written in the temporary output file *_out*.

_ot, _out, _res, _sen

These files are created by *generate44* and can be deleted. **Results**

Contains the final un-normalised committee results for the predicted percentage of retained austenite.

SUBDIRECTORY s

no_of_lines.c

The source code for the program *no_of_lines.ex*.

spec.c

The source code for the program *spec.ex*

normtest.for Program to normalise the data in *test.dat* and produce the normalised input file *norm_test.in*. It makes use of information read in from *no_of_rows.dat*

gencom.for

this program uses the information in *committee.dat* and combines the predictions from the individual models, in the subdirectory *outprdt*, to obtain an averaged value (*committee prediction*). The output (in normalised form) is written to *com.dat*.

treatout.for

Program to un-normalise the committee results in *com.dat* and write the output predictions to *unnorm_com*. This file is then renamed *Results*.

committee.dat

A text file containing the number of models to be used to form the committee results and the number of input variables. It is read by *gencom.for*, *normtest.for* and *treatout.for*

SUBDIRECTORY c

_w*f

The weights files of the different models.

***.lu**

Files containing information for calculating the size of the error bars for the different models.

_c*

Files containing information about the perceived significance value [1] for each model.

_R*

Files containing values of the noise, test error and log predictive error [1] for each model.

SUBDIRECTORY d

outran.x

A normalised output file which was created during the building of the model. It is accessed by *generate44* via *spec.tl*

SUBDIRECTORY outprdt

out1, out2, etc.

The normalised output files for each model.

com.dat The normalised output file containing the committee results. It is generated by gencom.for

5. References

1. Chapters 4 and 8.
2. D. J. C. MacKay, *Mathematical modelling of weld phenomena 3*, eds. H. Cerjak and H. K. D. H. Bhadeshia, Institute of Materials, London, (1997) 359.
3. D. J. C. MacKay's website at <http://wol.ra.phy.cam.ac.uk/mackay/README.html>

6. Input parameters

The input variables for the model are listed in the README or README.DOC files in the corresponding directory. The maximum and minimum values for each variable are given in the file MINMAX.

7. Output parameters

These program gives the value of ultimate tensile strength in MPa. The output is written in th file Result or Result.dat.

Prediction Error bar Upper-limit Lower-limit

Accuracy

A full calculation of the error bars is presented in reference 1.

Program data

See sample data file: test.dat

Program results

See sample output file: Result or Result.dat

Keywords

Neural network, ultimate tensile strength, ADI, Austempered ductile iron, mechanical properties.

Download

The model for the calculation of the ultimate tensile strength of ADI for UNIX, Linux, and PC versions can be downloaded from: <http://www.msm.cam.ac.uk/map/mapmain.html>.

APPENDIX FOUR

MAP_NEURAL_ADI_YS

This appendix presents the model described in chapter 8 which estimates the yield strength (YS) of austempered ductile irons, and associated documentation following the MAP format, <http://www.msm.cam.ac.uk/map/mapmain.html>.

1. Provenance of Source Code

Miguel Angel Yescas-Gonzalez,
Phase Transformation & Complex Properties Research Group,
Department of Materials Science and Metallurgy,
University of Cambridge,
Cambridge, CB2 3QZ, U. K.

The neural network program was produced by:

David MacKay,
Cavendish Laboratory,
University of Cambridge,
Madingley Road,
Cambridge, CB3 0HE, U. K.

Added to MAP: November 2000

2. Purpose

Estimation of the yield strength of ADI as a function of chemical composition and heat treatment conditions (austenitising temperature, austenitising time, austempering temperature, and austempering time).

3. Specification Language: FORTRAN / C

Product form: Source code/ Executable files

Operating System: Linux, Solaris 5.5.1 & DOS

4. Description

MAP_NEURAL_ADI_YS contains the programs which enable the user to estimate the yield strength in MPa for any austempered ductile iron (ADI) as a function of chemical composition and heat treatment conditions. It makes use of a neural network program called *generate44*, which was developed by David MacKay and is part of the *bigback5* program. The network was trained using a large database of experimental results [1]. 6 different models are provided, which differ from each other by the number of hidden

units and by the value of the seed used when training the network. It was found that a more accurate result could be obtained by averaging the results from all models [1]. The programs calculate the results of each model and then combines them, by averaging, to produce a *committee result* and error estimate, as described by MacKay [2].

Programs are available which run on a Solaris 5.5.1 UNIX operating system, Linux, and on a PC under Windows 95/98. A set of programs and data files are provided for the model. The files for UNIX and Linux are included in a directory called ADI. This directory contains the following files and subdirectories.

README

A text file containing step-by-step instructions for running the program, including a list of input variables.

MINMAX

A text file containing the minimum and maximum limits of each input and output variable. This file is used to normalise and unnormalise the input and output data.

test.dat

An input file containing the input variables used for predictions.

model.gen

This is a UNIX shell file containing the command steps required to run the module. It can be executed by typing 'csh model.gen' at the command prompt. This shell file compiles and runs all the programs necessary for normalising the input data, executing the network for each model, unnormalising the output data and combining the results of each model to produce the final *committee* result.

MODEL.exe

This executable program for the PC corresponds to the UNIX command file *model.gen*

no_of_lines.ex

This executable file reads the information of number of data from the keyboard input and creates *rows.dat* file. This file is used by *spec.ex* to create *spec.t1*.

spec.ex

This executable file reads the information in *no_of_rows.dat* and creates a file called *spec.t1*

spec.t1

A dynamic file, created by executable **spec.ex**, which contains information about the module and the number of data items being supplied. It is read by the program *generate44/generate55.exe*

norm_test.in

This is text file which contains the normalised input variables. It is generated by the program *normtest.for* in subdirectory *s* .

generate44/generate55.exe

This is executable file for the neural network program. *generate44* runs on UNIX system

and *generate55* on the PC. It reads the normalised input data file *norm_test.in*, and uses the weight files in subdirectory *c*. The results are written in the temporary output file *_out*.

_ot, _out, _res, _sen

These files are created by *generate44* and can be deleted. **Results**

Contains the final un-normalised committee results for the predicted percentage of retained austenite.

SUBDIRECTORY s

no_of_lines.c

The source code for the program *no_of_lines.ex*.

spec.c

The source code for the program *spec.ex*

normtest.for Program to normalise the data in *test.dat* and produce the normalised input file *norm_test.in*. It makes use of information read in from *no_of_rows.dat*

gencom.for

this program uses the information in *committee.dat* and combines the predictions from the individual models, in the subdirectory *outprdt*, to obtain an averaged value (*committee prediction*). The output (in normalised form) is written to *com.dat*.

treatout.for

Program to un-normalise the committee results in *com.dat* and write the output predictions to *unnorm_com*. This file is then renamed *Results*.

committee.dat

A text file containing the number of models to be used to form the committee results and the number of input variables. It is read by *gencom.for*, *normtest.for* and *treatout.for*

SUBDIRECTORY c

_w*f

The weights files of the different models.

***.lu**

Files containing information for calculating the size of the error bars for the different models.

_c*

Files containing information about the perceived significance value [1] for each model.

_R*

Files containing values of the noise, test error and log predictive error [1] for each model.

SUBDIRECTORY d

outran.x

A normalised output file which was created during the building of the model. It is accessed by *generate44* via *spec.tl*

SUBDIRECTORY outprdt

out1, out2, etc.

The normalised output files for each model.

com.dat The normalised output file containing the committee results. It is generated by gencom.for

5. References

1. Chapters 4 and 8.
2. D. J. C. MacKay, *Mathematical modelling of weld phenomena 3*, eds. H. Cerjak and H. K. D. H. Bhadeshia, Institute of Materials, London, (1997) 359.
3. D. J. C. MacKay's website at <http://wol.ra.phy.cam.ac.uk/mackay/README.html>

6. Input parameters

The input variables for the model are listed in the README or README.DOC files in the corresponding directory. The maximum and minimum values for each variable are given in the file MINMAX.

7. Output parameters

This program gives the value of yield strength in MPa. The output is written in the file Result or Result.dat.

Prediction	Error bar	Upper-limit	Lower-limit
------------	-----------	-------------	-------------

Accuracy

A full calculation of the error bars is presented in reference 1.

Program data

See sample data file: test.dat

Program results

See sample output file: Result or Result.dat

Keywords

Neural network, yield strength, ADI, Austempered ductile iron, mechanical properties.

Download

The model for the calculation of the yield strength of ADI for UNIX, Linux, and PC versions can be downloaded from: <http://www.msm.cam.ac.uk/map/mapmain.html>.

APPENDIX FIVE

MAP_NEURAL_ADI_ELONGATION

This appendix presents the model described in chapter 8 which estimates the tensile elongation of austempered ductile irons, and associated documentation following the MAP format, <http://www.msm.cam.ac.uk/map/mapmain.html>.

1. Provenance of Source Code

Miguel Angel Yescas-Gonzalez,
Phase Transformation & Complex Properties Research Group,
Department of Materials Science and Metallurgy,
University of Cambridge,
Cambridge, CB2 3QZ, U. K.

The neural network program was produced by:

David MacKay,
Cavendish Laboratory,
University of Cambridge,
Madingley Road,
Cambridge, CB3 0HE, U. K.

Added to MAP: November 2000

2. Purpose

Estimation of the tensile elongation in % of ADI as a function of chemical composition and heat treatment conditions (austenitising temperature, austenitising time, austempering temperature, and austempering time).

3. Specification Language: FORTRAN / C

Product form: Source code/ Executable files

Operating System: Linux, Solaris 5.5.1 & DOS

4. Description

MAP_NEURAL_ADI_ELONGATION contains the programs which enable the user to estimate the tensile elongation in % for any austempered ductile iron (ADI) as a function of chemical composition and heat treatment conditions. It makes use of a neural network program called *generate44*, which was developed by David MacKay and is part of the *bigback5* program. The network was trained using a large database of experimental results [1]. 12 different models are provided, which differ from each other by the number of hidden units and by the value of the seed used when training the network. It was found that a

more accurate result could be obtained by averaging the results from all models [1]. The programs calculate the results of each model and then combines them, by averaging, to produce a *committee result* and error estimate, as described by MacKay [2].

Programs are available which run on a Solaris 5.5.1 UNIX operating system, Linux, and on a PC under Windows 95/98. A set of programs and data files are provided for the model. The files for UNIX and Linux are included in a directory called ADI. This directory contains the following files and subdirectories.

README

A text file containing step-by-step instructions for running the program, including a list of input variables.

MINMAX

A text file containing the minimum and maximum limits of each input and output variable. This file is used to normalise and unnormalise the input and output data.

test.dat

An input file containing the input variables used for predictions.

model.gen

This is a UNIX shell file containing the command steps required to run the module. It can be executed by typing 'csh model.gen' at the command prompt. This shell file compiles and runs all the programs necessary for normalising the input data, executing the network for each model, unnormalising the output data and combining the results of each model to produce the final *committee* result.

MODEL.exe

This executable program for the PC corresponds to the UNIX command file *model.gen*

no_of_lines.ex

This executable file reads the information of number of data from the keyboard input and creates *rows.dat* file. This file is used by *spec.ex* to create *spec.t1*.

spec.ex

This executable file reads the information in *no_of_rows.dat* and creates a file called *spec.t1*

spec.t1

A dynamic file, created by executable **spec.ex**, which contains information about the module and the number of data items being supplied. It is read by the program *generate44/generate55.exe*

norm_test.in

This is text file which contains the normalised input variables. It is generated by the program *normtest.for* in subdirectory *s* .

generate44/generate55.exe

This is executable file for the neural network program. *generate44* runs on UNIX system and *generate55* on the PC. It reads the normalised input data file *norm_test.in*, and uses

the weight files in subdirectory c. The results are written in the temporary output file_out.

_ot, _out, _res, _sen

These files are created by *generate44* and can be deleted. **Results**

Contains the final un-normalised committee results for the predicted percentage of retained austenite.

SUBDIRECTORY s

no_of_lines.c

The source code for the program *no_of_lines.ex*.

spec.c

The source code for the program *spec.ex*

normtest.for Program to normalise the data in *test.dat* and produce the normalised input file *norm_test.in*. It makes use of information read in from *no_of_rows.dat*

gencom.for

this program uses the information in *committee.dat* and combines the predictions from the individual models, in the subdirectory *outprdt*, to obtain an averaged value (*committee prediction*). The output (in normalised form) is written to *com.dat*.

treatout.for

Program to un-normalise the committee results in *com.dat* and write the output predictions to *unnorm_com*. This file is then renamed *Results*.

committee.dat

A text file containing the number of models to be used to form the committee results and the number of input variables. It is read by *gencom.for*, *normtest.for* and *treatout.for*

SUBDIRECTORY c

_w*f

The weights files of the different models.

***.lu**

Files containing information for calculating the size of the error bars for the different models.

_c*

Files containing information about the perceived significance value [1] for each model.

_R*

Files containing values of the noise, test error and log predictive error [1] for each model.

SUBDIRECTORY d

outran.x

A normalised output file which was created during the building of the model. It is accessed by *generate44* via *spec.t1*

SUBDIRECTORY outprdt

out1, out2, etc.

The normalised output files for each model.

com.dat The normalised output file containing the committee results. It is generated by gencom.for

5. References

1. Chapters 4 and 8.
2. D. J. C. MacKay, *Mathematical modelling of weld phenomena 3*, eds. H. Cerjak and H. K. D. H. Bhadeshia, Institute of Materials, London, (1997) 359.
3. D. J. C. MacKay's website at <http://wol.ra.phy.cam.ac.uk/mackay/README.html>

6. Input parameters

The input variables for the model are listed in the README or README.DOC files in the corresponding directory. The maximum and minimum values for each variable are given in the file MINMAX.

7. Output parameters

These program gives the value of tensile elongation in %. The output is written in th file Result or Result.dat.

Prediction	Error bar	Upper-limit	Lower-limit
%	%	%	%

Accuracy

A full calculation of the error bars is presented in reference 1.

Program data

See sample data file: test.dat

Program results

See sample output file: Result or Result.dat

Keywords

Neural network, tensile elongation, ADI, Austempered ductile iron, mechanical properties.

Download

The model for the calculation of the tensile elongation of ADI for UNIX, Linux, and PC versions can be downloaded from: <http://www.msm.cam.ac.uk/map/mapmain.html>.

APPENDIX SIX

MAP_NEURAL_ADI_CHARPY

This appendix presents the model described in chapter 8 which estimates the tensile elongation of austempered ductile irons, and associated documentation following the MAP format, <http://www.msm.cam.ac.uk/map/mapmain.html>.

1. Provenance of Source Code

Miguel Angel Yescas-Gonzalez,
Phase Transformation & Complex Properties Research Group,
Department of Materials Science and Metallurgy,
University of Cambridge,
Cambridge, CB2 3QZ, U. K.

The neural network program was produced by:

David MacKay,
Cavendish Laboratory,
University of Cambridge,
Madingley Road,
Cambridge, CB3 0HE, U. K.

Added to MAP: November 2000

2. Purpose

Estimation of the Charpy toughness in Joules of ADI as a function of chemical composition and heat treatment conditions (austenitising temperature, austenitising time, austempering temperature, and austempering time).

3. Specification Language: FORTRAN / C

Product form: Source code/ Executable files

Operating System: Linux, Solaris 5.5.1 & DOS

4. Description

MAP_NEURAL_ADI_CHARPY contains the programs which enable the user to estimate the Charpy toughness in Joules for any austempered ductile iron (ADI) as a function of chemical composition and heat treatment conditions. It makes use of a neural network program called *generate44*, which was developed by David MacKay and is part of the *bigback5* program. The network was trained using a large database of experimental results [1]. 7 different models are provided, which differ from each other by the number of hidden units and by the value of the seed used when training the network. It was found that a

more accurate result could be obtained by averaging the results from all models [1]. The programs calculate the results of each model and then combines them, by averaging, to produce a *committee result* and error estimate, as described by MacKay [2].

Programs are available which run on a Solaris 5.5.1 UNIX operating system, Linux, and on a PC under Windows 95/98. A set of programs and data files are provided for the model. The files for UNIX and Linux are included in a directory called ADI. This directory contains the following files and subdirectories.

README

A text file containing step-by-step instructions for running the program, including a list of input variables.

MINMAX

A text file containing the minimum and maximum limits of each input and output variable. This file is used to normalise and unnormalise the input and output data.

test.dat

An input file containing the input variables used for predictions.

model.gen

This is a UNIX shell file containing the command steps required to run the module. It can be executed by typing 'csh model.gen' at the command prompt. This shell file compiles and runs all the programs necessary for normalising the input data, executing the network for each model, unnormalising the output data and combining the results of each model to produce the final *committee* result.

MODEL.exe

This executable program for the PC corresponds to the UNIX command file *model.gen*

no_of_lines.ex

This executable file reads the information of number of data from the keyboard input and creates *rows.dat* file. This file is used by *spec.ex* to create *spec.t1*.

spec.ex

This executable file reads the information in *no_of_rows.dat* and creates a file called *spec.t1*

spec.t1

A dynamic file, created by executable **spec.ex**, which contains information about the module and the number of data items being supplied. It is read by the program *generate44/generate55.exe*

norm_test.in

This is text file which contains the normalised input variables. It is generated by the program *normtest.for* in subdirectory *s* .

generate44/generate55.exe

This is executable file for the neural network program. *generate44* runs on UNIX system and *generate55* on the PC. It reads the normalised input data file *norm_test.in*, and uses

the weight files in subdirectory c. The results are written in the temporary output file_out.

_ot, _out, _res, _sen

These files are created by *generate44* and can be deleted. **Results**

Contains the final un-normalised committee results for the predicted percentage of retained austenite.

SUBDIRECTORY s

no_of_lines.c

The source code for the program *no_of_lines.ex*.

spec.c

The source code for the program *spec.ex*

normtest.for Program to normalise the data in *test.dat* and produce the normalised input file *norm_test.in*. It makes use of information read in from *no_of_rows.dat*

gencom.for

this program uses the information in *committee.dat* and combines the predictions from the individual models, in the subdirectory *outprdt*, to obtain an averaged value (*committee prediction*). The output (in normalised form) is written to *com.dat*.

treatout.for

Program to un-normalise the committee results in *com.dat* and write the output predictions to *unnorm_com*. This file is then renamed *Results*.

committee.dat

A text file containing the number of models to be used to form the committee results and the number of input variables. It is read by *gencom.for*, *normtest.for* and *treatout.for*

SUBDIRECTORY c

_w*f

The weights files of the different models.

***.lu**

Files containing information for calculating the size of the error bars for the different models.

_c*

Files containing information about the perceived significance value [1] for each model.

_R*

Files containing values of the noise, test error and log predictive error [1] for each model.

SUBDIRECTORY d

outran.x

A normalised output file which was created during the building of the model. It is accessed by *generate44* via *spec.t1*

SUBDIRECTORY outprdt

out1, out2, etc.

The normalised output files for each model.

com.dat The normalised output file containing the committee results. It is generated by gencom.for

5. References

1. Chapters 4 and 8.
2. D. J. C. MacKay, *Mathematical modelling of weld phenomena 3*, eds. H. Cerjak and H. K. D. H. Bhadeshia, Institute of Materials, London, (1997) 359.
3. D. J. C. MacKay's website at <http://wol.ra.phy.cam.ac.uk/mackay/README.html>

6. Input parameters

The input variables for the model are listed in the README or README.DOC files in the corresponding directory. The maximum and minimum values for each variable are given in the file MINMAX.

7. Output parameters

This program gives the value of Charpy toughness in Joules. The output is written in the file Result or Result.dat.

Prediction	Error bar	Upper-limit	Lower-limit
J	J	J	J

Accuracy

A full calculation of the error bars is presented in reference 1.

Program data

See sample data file: test.dat

Program results

See sample output file: Result or Result.dat

Keywords

Neural network, Charpy toughness, ADI, Austempered ductile iron, mechanical properties.

Download

The model for the calculation of the Charpy toughness of ADI for UNIX, Linux, and PC versions can be downloaded from: <http://www.msm.cam.ac.uk/map/mapmain.html>.

APPENDIX SEVEN

MAP_NEURAL_ADI_MAX-RETAINED-AUSTENITE

This appendix presents the model described in chapter 6 and associated documentation following the MAP format, <http://www.msm.cam.ac.uk/map/mapmain.html>.

1. Provenance of Source Code

Miguel Angel Yescas-Gonzalez,
Phase Transformation & Complex Properties Research Group,
Department of Materials Science and Metallurgy,
University of Cambridge,
Cambridge, CB2 3QZ, U. K.

Added to MAP: November 2000

2. Purpose

Estimation of the maximum amount of retained austenite in austempered ductile irons (ADI) as a function of chemical composition and heat treatment conditions (austenitising temperature, austenitising time, austempering temperature, and austempering time).

3. Specification

Language: FORTRAN Product form: Source file/ Executable files

Operating System: Solaris 5.5.1

4. Description

MAP_NEURAL_ADI_MAX-RETAINED-AUSTENITE contains the program which enable the user to estimate the maximum volume fraction of retained austenite for any austempered ductile iron (ADI) as a function of chemical composition, austenitising temperature and austempering temperature. The model is based on the T_0 concept [1]. The FORTRAN program has been created using application interface programming under the master mode to link it with MTDATA [2]. MTDATA calculations are necessary to find the equilibrium carbon concentration of carbon at austenitising temperature, and to calculate free energies of austenite and ferrite to obtain the M_S temperature according to MAP_STEEL_MS.

The program is available and should be compiled on Solaris 5.5.1 UNIX operating system. In order to compile the program, a script file is needed. The name of this file is *compile*, it is also available and should be in the same folder as the main program. The command to compile the program is: *./compile program-name executable-name*

5. References

1. Miguel Angel Yescas, and H. K. D. H. Bhadeshia. *Model for the maximum fraction of retained austenite in austempered ductile cast iron* Materials Science and Engineering, (2001) in press.
2. *MTDATA*, Metallurgical Thermochemistry and Thermodynamic Database, National Physical Laboratory, Teddington, U. K. 1996.

6. Input parameters

The input variables for the model are the chemical composition of the ductile iron, austenitising temperature, and austempering time. These input variables should be contained in a data file named *Input.data* as a single row. This file can have up to 10 rows. The chemical components used in these model are *C, Si, Mn, Mo, Ni, Cu*. *Fe* does not need to be typed in. Elements are in weight %. Austenitising temperature should be in °C.

An example of the *Input.data* file for only one alloy (one row):

```
3.5 2.5 0.4 0.25 0.5 0.5 900 350
```

An **.mpi* file is another input file which was necessary to create with *MTDATA* (version 4.70) using the *ACCESS* module. This file which contains thermodynamical calculations of the system is necessary to run the program. Three phases that were allowed to exist are graphite, austenite, and ferrite. The **.mpi* file should be located at the *MTDATA* home space (*/home4/users/guest/*). The file *adi1.mpi* is also available.

Input Data file name : *Input.data*

No. of Components in INPUT DATA FILE: 9

No. of lines in INPUT DATA FILE: n

OUTPUT DATA File Name FOR VOL. FRACTION Calculations: file name

OUTPUT RESULT File Name : *aus.out*

Input File Name (**.mpi*) : *adi1*

Output File Name For Austenite : any name.

7. Output parameters

The program gives the maximum volume fraction of retained austenite in an ADI at a given austempering temperature. The output is written in th file *aus.out* but more information is printed on the screen. An example of these information as follow:

Temp °C	Ret austenite Vol.fraction	Carbon in γ wt %	M_S °C	Carbon in α mol fraction	Bainite Vol.fraction	Martensite. Vol.fraction.
250.	0.2299	1.820	-142.1	0.0210	0.7701	0.0000
260.	0.2425	1.805	-141.9	0.0203	0.7575	0.0000
270.	0.2589	1.786	-141.5	0.0192	0.7411	0.0000
280.	0.2780	1.769	-141.1	0.0180	0.7220	0.0000
290.	0.3067	1.721	-139.6	0.0164	0.6933	0.0000

300.	0.3387	1.672	-137.1	0.0146	0.6613	0.0000
310.	0.3727	1.629	-132.9	0.0126	0.6273	0.0000
320.	0.4099	1.582	-126.8	0.0103	0.5901	0.0000
330.	0.4492	1.535	-118.7	0.0077	0.5508	0.0000
340.	0.4900	1.488	-104.5	0.0049	0.5100	0.0000
350.	0.5317	1.442	-74.4	0.0019	0.4683	0.0000
360.	0.5635	1.396	5.6	0.0000	0.4365	0.0000
370.	0.4717	1.350	54.8	0.0000	0.4174	0.1109
380.	0.4270	1.304	82.3	0.0000	0.3970	0.1760
390.	0.4013	1.259	101.8	0.0000	0.3752	0.2234
400.	0.3790	1.213	117.3	0.0000	0.3519	0.2691
410.	0.3749	1.182	126.4	0.0000	0.3346	0.2905
420.	0.3721	1.150	134.5	0.0000	0.3162	0.3117
430.	0.3689	1.118	142.8	0.0000	0.2966	0.3344
440.	0.3621	1.086	151.2	0.0000	0.2758	0.3621
450.	0.3617	1.053	159.8	0.0000	0.2535	0.3848

8. Auxiliary subroutines required

The subroutines required are contained in the main program.

9. Accuracy

See reference 1.

11. Any additional information

“DIRUSRAP.FOR” (which should be in the local directory) is a header file for definitions of all variables used in the FORTRAN module to interface with MTDATA. The following line is written at the top of the main program. “DIRUSRAP.FOR” comes with the auxiliary files of MTDATA.

```
INCLUDE 'DIRUSRAP.FOR'
```

The compiled program should be run inside MTDATA software.

The last version of MTDATA used to run the program was 4.72.

Program data

See sample data file: INPUT.dat

Program results

See sample output file: aus.out

Keywords

Retained austenite, bainite, ADI, Austempered ductile iron, bainite.

Download

The source program (model.f), ad11.mpi file and script file to compile the program used to calculate the maximum volume fraction of retained austenite in ADI can be downloaded from: <http://www.msm.cam.ac.uk/map/mapmain.html>.

APPENDIX EIGHT

MAP_NEURAL_ADI_CARBIDE

This appendix presents the model described in chapter 7 and associated documentation following the MAP format, <http://www.msm.cam.ac.uk/map/mapmain.html>.

1. Provenance of Source Code

Miguel Angel Yescas-Gonzalez,
Phase Transformation & Complex Properties Research Group,
Department of Materials Science and Metallurgy,
University of Cambridge,
Cambridge, CB2 3QZ, U. K.

Added to MAP: November 2000

2. Purpose

Estimation of the kinetics and volume fraction of carbide precipitation in austempered ductile irons (ADI) from carbon-enriched austenite as a function of chemical composition and heat treatment conditions (austenitising temperature, austempering temperature).

3. Specification

Language: FORTRAN Product form: Source file/ Executable files

Operating System: Solaris 5.5.1

4. Description

MAP_NEURAL_ADI_CARBIDE contains the program which enable the user to estimate the kinetics and volume fraction of carbide which precipitate from carbon-enriched austenite which is associated with bainitic ferrite in the stage II of the austempering process [1] of any austempered ductile iron (ADI) as a function of chemical composition, austenitising temperature and austempering temperature. The model is based on the theory of overall transformation kinetics, and assumes that cementite grows by paraequilibrium transformation [1]. The FORTRAN program has been created using application interface programming under the master mode to link it with MTDATA [2]. MTDATA calculations are necessary to find the equilibrium carbon concentration of carbon at austenitising temperature, and to calculate the driving force for nucleation of cementite from retained austenite.

The program is available and should be compiled on Solaris 5.5.1 UNIX operating system. In order to compile the program, a script file is needed. The name of this file is *compile*, it is also available and should be in the same folder as the main program. The command

to compile the program is: `./compile program-name executable-name`

5. References

1. Miguel Angel Yescas, Modelling the Microstructure and Mechanical Properties of Austempered ductile Iron, Ph.D. Thesis, University of Cambridge, 2001.
2. *MTDATA*, Metallurgical Thermochemistry and Thermodynamic Database, National Physical Laboratory, Teddington, U. K. 1996.

6. Input parameters

The input variables for the model are the chemical composition of the ductile iron, austenitising temperature, and austempering time. These input variables should be contained in a data file named *Input.data* as a single row. This file can have up to 10 rows. The chemical components used in these model are *C, Si, Mn, Mo, Ni, Cu*. *Fe* does not need to be typed in. Elements are in weight %. Austenitising temperature should be in °C.

An example of the *Input.data* file for only one alloy (one row):

```
3.5 2.5 0.4 0.25 0.5 0.5 900 350
```

An **.mpi* file is another input file which was necessary to create with *MTDATA* (version 4.70) using the *ACCESS* module. This file which contains thermodynamical calculations of the system is necessary to run the program. Three phases that were allowed to exist are graphite, austenite, and ferrite. The **.mpi* file should be located at the *MTDATA* home space (`/home4/users/guest/`). The file *adi6.mpi* is also available.

Input Data file name : *Input.data*

No. of Components in INPUT DATA FILE: 9

No. of lines in INPUT DATA FILE: n

OUTPUT DATA File Name FOR VOL. FRACTION Calculations: *output file*

OUTPUT RESULT File Name : *out*

Input File Name (**.mpi*) : *adi1*

Output File Name For Austenite : *any name.*

7. Output parameters

The program gives the time and volume fraction of cementite found in an ADI at a given austempering temperature. The output is written in the output file as follow:

```
DATA LINE : 1
Time (s)           Volume fraction of cementite
1 .1234098041D-03  0.000000000000000D+00
2 .3354626279D-03  0.000000000000000D+00
3 .9118819656D-03  0.000000000000000D+00
4 .2478752177D-02  0.000000000000000D+00
5 .6737946999D-02  0.000000000000000D+00
6 .1831563889D-01  0.000000000000000D+00
```

7	.4978706837D-01	0.000000000000000D+00
8	.1353352832D+00	0.000000000000000D+00
9	.3678794412D+00	0.000000000000000D+00
10	.1000000000D+01	0.000000000000000D+00
11	.2718281828D+01	0.000000000000000D+00
12	.7389056099D+01	0.000000000000000D+00
13	.2008553692D+02	0.000000000000000D+00
14	.5459815003D+02	0.000000000000000D+00
15	.1484131591D+03	0.000000000000000D+00
16	.4034287935D+03	0.000000000000000D+00
17	.1096633158D+04	0.000000000000000D+00
18	.2980957987D+04	0.000000000000000D+00
19	.8103083928D+04	0.000000000000000D+00
20	.2202646579D+05	0.000000000000000D+00
21	.5987414172D+05	0.000000000000000D+00
22	.1627547914D+06	0.000000000000000D+00
23	.4424133920D+06	0.000000000000000D+00
24	.1202604284D+07	0.000000000000000D+00
25	.3269017372D+07	0.000000000000000D+00
26	.8886110521D+07	0.000000000000000D+00
27	.2415495275D+08	0.155828644524069D-16
28	.6565996914D+08	0.155828644524069D-15
29	.1784823010D+09	0.190110946319364D-14
30	.4851651954D+09	0.230938051184670D-13
31	.1318815734D+10	0.281270703365944D-12
32	.3584912846D+10	0.342650048157529D-11
33	.9744803446D+10	0.417432837979208D-10
34	.2648912213D+11	0.508537384937033D-09
35	.7200489934D+11	0.619525339695976D-08
36	.1957296094D+12	0.754736184222270D-07
37	.5320482406D+12	0.919454136213752D-06
38	.1446257064D+13	0.112008342024751D-04
39	.3931334297D+13	0.136393226760762D-03
40	.1068647458D+14	0.165261133305894D-02
41	.2904884967D+14	0.188590843333103D-01
42	.7896296018D+14	0.116157501417006D+00

More information is given on the screen after running the program such as the temperature in Kelvin, the Gibbs energy of austenite, and of ferrite, etc.

8. Auxiliary subroutines required

The subroutines required are contained in the main program.

9. Accuracy

See reference 1. Since the program does not consider the formation of ferrite when retained austenite decomposes during the stage II [1], the model is only applicable for the beginning of carbide precipitation.

11. Any additional information

“DIRUSRAP.FOR” (which should be in the local directory) is a header file for definitions of all variables used in the FORTRAN module to interface with MTDATA. The following line is written at the top of the main program. “DIRUSRAP.FOR” comes with the auxiliary files of MTDATA.

```
INCLUDE 'DIRUSRAP.FOR'
```

The compiled program should be run inside MTDATA software.

The last version of MTDATA used to run the program was 4.72.

Program data

See sample data file: INPUT.dat

Program results

See sample output file

Keywords

Carbide, cementite, retained austenite, ADI, Austempered ductile iron, bainite.

Download

The source program (cementite.f), adi6.mpi file and script file to compile the program used to calculate the time and volume fraction of cementite in ADI can be downloaded from: <http://www.msm.cam.ac.uk/map/mapmain.html>.

References

- [1] Rimmer A. *Materials World*, 5:252–255, 1997.
- [2] Owen W. S. *Transactions of the ASM*, 46:812–829, 1954.
- [3] Voigt R. C. *Cast Metals*, 2:72–93, 1989.
- [4] Elliott R. *Cast Iron Technology*. Butterworths & Co.(publishers) Ltd, 1988.
- [5] Rollason E. C. *Metallurgy for Engineers*. Edward Arnold Ltd, 4th edition edition, 1973.
- [6] Guy A. G. *Elements of Physical Metallurgy*. Addison-Wesley Publishing Company, Inc., 2nd edition edition, 1960.
- [7] Angus H. T. *Cast iron: Physical and engineering properties*. Butterworths & Co. (publishers) Ltd, 2nd edition edition, 1976.
- [8] A Modern casting Staff Report. 34th annual census of world casting production-1999. *Modern casting*, 2000.
- [9] Bedolla-Jacuinde A. *International Journal of Cast Metals Reseach*, 13:343–361, 2001.
- [10] Flinn R. A. and Kraft R.W. *Transactions ASM*, 44:282–306, 1952.
- [11] Petty E. R. *Physical Metallurgy of Engineering Materials*. George Allen and Unwin Ltd, 1970.
- [12] Rundman K. B., Moore D. J., Hayrynen K. L., Dubensky W. J., and Rouns T. N. *Journal of Heat Treating*, 5:79–95, 1988.
- [13] Singh I. and Putatunda S. K. *Transactions of the Indian Institute of Metals*, 47:317–325, 1994.
- [14] Dorazil E. *High Strength Austempered Ductile Cast Iron*. Series Editor: E.G. West, Obe. Horwood Series in Metals and Associated Materials, 1991.

- [15] Harding R. A. In *Proceedings, 2nd International Conference on Austempered Ductile Iron*, pages 39–54, Ann Arbor, MI, USA, March 17-19 1986.
- [16] Rouns T. N. and Rundman K. B. *AFS Transactions*, 95:851–874, 1987.
- [17] Trudel A. and Gagne M. *Canadian, Metallurgical, Quarterly*, 36:289–298, 1998.
- [18] Morgan H. L. *The British Foundryman*, Feb/Mar:98–108, 1987.
- [19] Bhadeshia H. K. D. H. *Bainite in Steels*. The Institute of Materials, 1992.
- [20] Dubensky W. J. and Rundman K. B. *AFS Transactions*, 93:389–394, 1985.
- [21] Harris D. A. Tech B. and R.J. Maitland. *Iron and Steel*, pages 53–60, 1970.
- [22] Rundman K. B. and Klug R. C. *AFS Transactions*, 90:499–508, 1982.
- [23] Schissler J. M., Arnould J., and Metauer G. *Mmoires Scientifiques Revue Mtallurgie*, 6:779–793, 1975.
- [24] Moore D. J., Rouns T. N., and Rundman K. B. *AFS Transactions*, 94:255–264, 1986.
- [25] Darawish N. and Elliott R. *Materials Science and Technology*, 9:572–585, 1993.
- [26] Schissler J. S., Chabaut J., Bak C., and Gouvenel D. In *2nd International Conference on Austempered Ductile Iro*, pages 149–155, Ann Arbor, MI, USA, March 17-19 1986.
- [27] Bayati H. and Elliott R. *Materials Science and Technology*, 11:118–129, 1995.
- [28] Varahraam N. and Yanagisawa O. *Cast Metals*, 3:129–139, 1990.
- [29] Gundlach R. B. and Janowak J. *Metal Progress*, pages 19–26, 1985.
- [30] Lin. C. K. and Hung T.P. *International Journal of Fatigue*, 18:309–320, 1995.
- [31] Rossi F. S. and Gupta B. K. *Metal Progress*, pages 25–31, 1981.
- [32] Salonen P. In *International Conference on Engineering Design ICED 97*, pages 637–640, Tampere, August 1997.
- [33] Internal Report. Selected case studies of austempered ductile iron components. Technical report, British Cast Iron Reseach Asociation (BCIRA).
- [34] MTDATA. Metallurgical and thermochemical databank. Technical report, National Physical Laboratory, Teddington, U. K., 1989.
- [35] Kovacs B. V. *Modern Casting*, 4:34–35, 1987.

- [36] Brandon D. G. *Modern Techniques in Metallography*. Butterworths & Co. (publishers) Ltd, 1966.
- [37] Ahmadabadi M. N. *Cast Metals*, 4:182–188, 1994.
- [38] Williams D. B. and Carter C. B. *Transmission Electron Microscopy II: Diffraction*. Plenum Press, New York, 1996.
- [39] Barret C. S. and Massalski T. B. *Structure of Metals and Alloys*. McGraw-hill, New York, 1968.
- [40] Cullity B. D. *Elements of X-ray diffraction*. Reading, MA, Addison-Wesley, 1978.
- [41] Dyson D. J. and Holmes B. *Journal of the Iron and Steel Institute*, pages 469–474, 1970.
- [42] Bhadeshia H. K. D. H. *Bainite in Steels*. The Institute of Materials, 2001.
- [43] Oblak J. M., Goodenow R. H., and Hehemann R.F. *Transactions AIME*, 230:258–259, 1964.
- [44] Bayati H. and Elliott R. *Materials Science and Technology*, 11:118–129, 1995.
- [45] Ahmadabadi M. N. *Metallurgical and Materials Transactions A*, 29A:2297–2306, 1998.
- [46] Bhadeshia H. K. D. H., Vitek D. S. A., and Reed. R.W. *Materials Science and Technology*, 7:686–698, 1991.
- [47] Bhadeshia H. K. D. H. *Acta Metallurgica*, 25:1103–1114, 1980.
- [48] Sandvik B. P. J. *Metallurgical Transactions A*, 13A:777–787, 1982.
- [49] Reisdorf B. G. *TMS-AIME*, 227:1334, 1963.
- [50] D. J. C. MacKay. In *Mathematical Modelling of Weld Phenomena-3*, editor, *H. Cerjak and H. K. D. H Bhadeshia*, pages 359–389, London, U.K., 1997. The Institute of Materials.
- [51] Fujii H. and Bhadeshia H. K. D. H. *ISIJ International*, 39:965–979, 1999.
- [52] Moore D. J., Rouns T. N., and Rundman K. B. *AFS Transactions*, 94:255–264, 1986.
- [53] Stenfors J., Storesun R., and Sandstrom R. In *2nd International Conference on Austempered Ductile Iron*, pages 227–236, Ann Arbor, Michigan, University of Michigan, March 1986.

- [54] Grech J. *Cast Metals*, 3:98–103, 1990.
- [55] Zhou W. S., Zhou Q. D., and Meng S. K. *Cast Metals*, 6:69–75, 1993.
- [56] Ahmadabadi M. N. *Cast Metals*, 5:62–72, 1992.
- [57] Prado J. M., Pujol A., Cullerell J., and Tartera J. *Materials Science and Technology*, 11:294–298, 1995.
- [58] Cox G. J. *British Foundryman*, 79:215–219, 1986.
- [59] Takahashi T., Abe T., and Tada S. *Metallurgical and Materials Transactions*, 27A:1589–1598, 1996.
- [60] Darawish N. and Elliott R. *Materials Science and Technology*, 9:586–602, 1993.
- [61] Aranzabal J., Gutierrez I., , and Urcola J.J. *Materials Science and Technology*, 10:728–737, 1994.
- [62] Shea M. M. and Ryntz E. F. *AFS Transactions*, 94:683–688, 1986.
- [63] Rouns T. N. and Rundman K. B. *Transactions ASM*, 46:812–829, 1954.
- [64] Dorazil E., Podrabsky T., and Svejcar J. *AFS Transactions*, 98:765–774, 1990.
- [65] Grech M. and Young J. M. *AFS Transactions*, 98:345–353, 1990.
- [66] Nadkarni G., Behravesi A. H., Warda R. D., Davis K. G., and Sahoo M. *AFS Transactions*, 103:93–101, 1995.
- [67] Yazadani S. and Elliott R. *Materials Science and Technology*, 15:531–540, 1999.
- [68] Bayati H., Elliott R., and Lorimer G. W. *Materials Science and Technology*, 11:776–786, 1995.
- [69] Boschen R., Vettters H., Mayr P., and Ryder P. L. *Practical Metallography*, 15:524–531, 1988.
- [70] Chen C. T. and Lei T. S. *Cast Metals Reseach*, 10:117–123, 1997.
- [71] Gagne M. and Fallon P. A. *Canadian, Metallurgical, Quarterly*, 25:79–90, 1986.
- [72] Hamid A. S. and Elliott R. *Materials Science and Technology*, 12:1021–1031, 1996.
- [73] Kazerooni R., Nazarboland A., and Elliott R. *Materials Science and Technology*, 13:1007–1015, 1997.
- [74] Kobayashi T. and Yamamoto H. *Metallurgical Transactions A*, 19A:319–327, 1988.

- [75] Lin C. K. and Wei J. Y. *Materials transactions JIM*, 38:682–691, 1997.
- [76] Owhadi A., Hedjazi J., and Davami P. *Materials Science and Technology*, 14:245–250, 1998.
- [77] Putatunda S. K. and Gadicherla P. K. *Materials Science and Engineering A*, 286:15–31, 1999.
- [78] Prasad P. and Putatunda S. K. *Metallurgical and Materials Transactions A*, 28A:1457–1470, 1997.
- [79] Prasad P. and Putatunda S. K. *Metallurgical and Materials Transactions A*, 29A:3005–3016, 1998.
- [80] Schmid I. and Schuchert A. *Metallkde*, 78:871–875, 1987.
- [81] Shah S. M. and Verhoeven J. D. *Wear*, 113:267–278, 1986.
- [82] Shanmugam P., Prasad P., Rajendra K. U., and Venkataraman N. *Journal of Materials Science*, 29:4933–4940, 1994.
- [83] Shih T. S. and Yang Z. C. *Int. J. Cast Metals Res*, 10:335–344, 1998.
- [84] W. Christian J. *Theory of Transformations in Metals and alloys part 1*. Pergamon Press, Oxford, 2nd edition edition, 1975.
- [85] Ueda Y. and Takita M. In *2nd International Conference on Austempered Ductile Iron*, pages 141–147, Ann Arbor, Michigan, University of Michigan, March 1986.
- [86] Lee Y. H. and Voigt R. C. *AFS Transactions*, 97:915–938, 1989.
- [87] Gagne M. *AFS Transactions*, 93:801–812, 1985.
- [88] Kovacs B. V. In *2nd International Conference on Austempered Ductile Iron*, pages 291–296, Ann Arbor, Michigan, University of Michigan, March 1986.
- [89] Mi Y. *Materials Science and Technology*, 9:1313–1317, 1995.
- [90] Hehemann R. F. In *V. F. Zackay, H. I. Aaronson (Eds), Phase Transformations*, page 397, ASM Metals Park, OH, 1970.
- [91] Bhadeshia H. K. D. H. and Edmonds D. V. *Acta Metallurgica*, 28:1265–1273, 1980.
- [92] Bhadeshia H. K. D. H. and Edmonds D. V. *Acta Metallurgica*, 28:1103–1114, 1980.
- [93] Bhadeshia H. K. D. H. and Edmonds D. V. *Acta Metallurgica*, 10A:895–907, 1979.

- [94] Honeycombe R. W. K. and Bhadeshia H. K. D. H. *Steels Microstructure and Properties*. Edward Arnold, London, U. K., 1995.
- [95] Khan S. A. and Bhadeshia H. K. D. H. *Materials Science and Engineering A*, 129:257–272, 1990.
- [96] Koistinen D. P. and Marburger R. E. *Acta Metallurgica*, 7:59–60, 1959.
- [97] Bhadeshia H. K. D. H. and Waugh A. R. *Acta Metallurgica*, 30:775–784, 1982.
- [98] Nieswaag H. and Nijhof J. W. *In: Proceedings of The International Symposium on Physical Metallurgy of Cast Iron*, 34:411–422, 1985.
- [99] Ahmadabadi M. N. *Metallurgical and Materials Transactions A*, 28A:2159–394, 1997.
- [100] Chang L. C. *Scripta Materialia*, 39:35–38, 1998.
- [101] Houillier R. L., Begin G., and Dube A. *Metallurgical Transactions*, 2:2645–2652, 1971.
- [102] Matas S. J. and Heheman R. F. *Transactions of the Metallurgical society of AIME*, 221:179–185, 1961.
- [103] Pickering F. B. *In: Transformatio and Hardenabilitu in Steels, Ann Aebor MI*, pages 109–132, 1967.
- [104] Huang D. and Thomas G. *Metallurgical Transactions A*, 8A:1661–1674, 1977.
- [105] Sandvik B. P. J.
- [106] Ahmadabadi M. N. *Metallurgical and Materials Transactions A*, 29A:2297–2306, 1998.
- [107] Roberts C. S., Averbach B. L., and Cohen M. *Transactions ASM*, 45:576, 1957.
- [108] Kang M. K., Sun J. L., and Yang Q. M. *Metallurgical Transactions A*, 21A:853–858, 1990.
- [109] Cool T. *Design of Steel Weld Deposits*. PhD thesis, University of Cambridge, 1996.
- [110] Thomson R. C., James J. S., and Putman D. C. *Materials Science and Technology*, 16:1412–1419, 2000.
- [111] Avrami M. *Journal Chem. Phys*, 8:212, 1940.
- [112] Gutierrez I., Aranzabal J., Castro F., and Urcola J. J. *Metallurgical and Materials Transactions A*, 26A:1045–1060, 1995.

- [113] Babu S. S., Hono K., and Sakuri T. *Applied Surface Science*, 67:321–327, 1993.
- [114] Fujita N. and Bhadeshia H. K. D. H. *Materials Science and Technology*, 15:627–634, 1999.
- [115] Robson J. D. and Bhadeshia H. K. D. H. *Materials Science and Technology*, 13:631–644, 1997.
- [116] Fridberg J., Torndahl L-E., and Hillert M. Diffusion in iron. *Jernkontorets Ann.*, 153:263–276, 1969.
- [117] Zener C. *Journal of Applied Physics*, 20:950, 1949.
- [118] <http://.msm.cam.ac.uk/map/mapmain.html>.
- [119] Aoyama M. and Kobayashi T. *Cast Metals*, 3:122–128, 1990.
- [120] Grech M. and Young M. J. *Cast Metals*, pages 98–103, 1988.
- [121] Prado J. M., Pujol A., Cullerell J., and Tartera J. *Materials Science and Technology*, 11:294–298, 1995.
- [122] Cox G. J. *The British Foundryman*, June:215–219, 1986.
- [123] Voigt R. C.. *AFS Transactions*, 92:253–262, 1983.
- [124] Dorazil E., Podrabsky T., and Svejcar J. *AFS Transactions*, 98:765–774, 1990.
- [125] Velez J. M., Garboggini A., and Tschiptchin A. P. *Materials Science and Technology*, 12:329–337, 1996.
- [126] Grech M. and Young M. J. *AFS Transactions*, 98:345–353, 1990.
- [127] Viau R., Gagne M., and Thibau R. *AFS Transactions*, 95:171–178, 1987.
- [128] Ahmadabadi M. N., Nategh S., and Davami P. *Cast Metals*, 4:188–194, 1992.
- [129] Lin C. K. and Wei J. Y. *Materials Transactions JIM*, 38:682–691, 1997.
- [130] Hayrynen K.L., Faubert G.P., Moore D.J., and Rundman K.B. *AFS Transactions*, 97:747–756, 1989.
- [131] Korichi S. and Priestner R. *Materials Science and Technology*, 11:901–907, 1995.
- [132] Kazerooni R., Nazarboland A., and Elliott R. *Materials Science and Technology*, 13:1007–1015, 1997.
- [133] Hamid A. S. and Elliott R.

- [134] Ahmadabadi M. N. *Cast Metals*, 5:62–72, 1992.
- [135] Sidjanin L., Smallman R. E., and Young J.M. *Acta Metallurgica et Materialia*, 42:3149–3156, 1994.
- [136] Zhou W. S., Zhou Q. D., and Meng S. K. *Cast Metals*, 6:69–75, 1993.
- [137] Lin B. Y., Chen E. T., and Lei T.S. *Scripta Metallurgica et Materialia*, 32:1363–1367, 1995.
- [138] Shih T. S. and Yang Z. C. *International Journal of Cast Metals Research*, 10:335–344, 1998.
- [139] Schmid I. and Schuchert A. *Z. Metallkde*, 78:871–875, 1987.
- [140] Shanmugam P., Prasad P., Rajendra K. U., and Venkataraman N. *Materials Science*, 29:4933–4940, 1994.
- [141] Putatunda S. K. and Gadicherla P. K. *Materials Science and Engineering*, A286:15–31, 1999.
- [142] Owhadi A., Hedjazi J., and Davami P. *Materials Science and Technology*, 14:245–250, 1998.
- [143] Schissler J. S., Chabaut J., Bak C., and Gouvenel D. In *2nd International Conference on Austempered Ductile Iron*, pages 149–155, Ann Arbor, Michigan, University of Michigan, March 1986.
- [144] Shea M. M. and Ryntz E. F. *AFS Transactions*, 94:683–688, 1986.
- [145] Robinson L., Spear W. M., and Tuffnell G. W. In *1st International Conference on Austempered Ductile Iron*, pages 39–43, Chicago, Illinois, 2-4 April 1984.
- [146] Shiokawa T. In *1st International Conference on Austempered Ductile Iron*, pages 107–115, Chicago, Illinois, 2-4 April 1984.
- [147] Yoshino S. In *2nd International Conference on Austempered Ductile Iron*, pages 337–348, Ann Arbor, Michigan, University of Michigan, March 1986.
- [148] Ford L. In *2nd International Conference on Austempered Ductile Iron*, pages 17–19, Ann Arbor, Michigan, University of Michigan, March 1986.
- [149] Shiokawa T. In *2nd International Conference on Austempered Ductile Iron*, pages 397–420, Ann Arbor, Michigan, University of Michigan, March 1986.
- [150] Yazadani S. and Elliott R.. *Materials Science and Technology*, 15:885–894, 1999.

- [151] Chen C. T. and Lei T. S. *Materials Transactions JIM*, 40:82–85, 1999.
- [152] Bartosiewicz L., Krause A. R., Alberts F. A., Singh I., and Putatunda K. *Materials Characterization*, 30:221–234, 1993.
- [153] Yazadani S. and Elliott R.. *Materials Science and Technology*, 15:531–540., 1999.
- [154] Yazadani S. and Elliott R.. *Materials Science and Technology*, 15:541–546, 1999.
- [155] Hasegawa N., Sasajima S., Endo H., and Marui E. *Zairyo*, 48:301–307, 1999.
- [156] Tsukahara S. and Yamada S. *Chuzo Kogaku*, 70:241–246, 1998.
- [157] Era H. and Kishitake K. *Chuzo Kogaku*, 69:911–916, 1997.
- [158] Ikenaga A., Nitta Y., and Kawamoto M.
- [159] Nagai K. and Era H. and Kishitake K. *Imono*, 66:827–832, 1994.
- [160] Shimizu K. and Naguchi T. *Imono*, 66:489–494, 1994.
- [161] Takahashi T., Tada S., and Abe T. *Imono*, 65:615–620, 1993.
- [162] Hori K. and Kobayashi T.
- [163] Kage H. and Tanaka Y.
- [164] Kovayashi T., Hori K., and Yamada S. *Imono*, 65:197–203, 1993.
- [165] Tanaka Y., Shimizu A., and Yokouchi H. *Imono*, 65:93–98, 1993.
- [166] Sunada H. *Zairyo*, 40:669–674, 1991.
- [167] Fujita T., Ogi K., and Suenaga M. *Imono*, 63:775–780, 1991.
- [168] Yamamoto H., Ji Y., and Kovayashi T. *Imono*, 62:810–815, 1990.
- [169] Yoshida T., Komatsu K., and Okada S. *Imono*, 65:221–226, 1993.
- [170] Feng H. P., Lee S. C., Hsu C. H., and Ho J. M. *Materials Chemistry and physics*, 59:154–161, 1999.
- [171] Ahmadabadi M. N. Ghasemi H. M. and Osia M. *Wear*, 231:293–300, 1999.
- [172] Lin C. K. and Lee W. J. *International Journal of Fatigue*, 20:301–307, 1997.
- [173] Wen D. C. and Lei T. S. *ISIJ International*, 39:493–500, 1999.
- [174] Dommarco R. C., Bastias P. C., Dall’O H. A., Hahn G. T., and Rubin C. A. *Wear*, 221:69–74, 1998.

- [175] Caballero F. G., Bhadeshia H. K. D. H., Mawella K. J. A., Jones D. G., and Brown P. *In press, Materials Science and Technology.*
- [176] Yescas M. A., Bhadeshia H. K. D. H., and MacKay D. J. C. *Materials Science and Engineering A*, 311:162–173, 2001.
- [177] Voigt R. C. and Loper C.R. *Journal of Heat Treating*, 3:291–309, 1984.
- [178] Dorazil E., Barta B., Munsterova E., Stransky L., and Huvar A. *Cast Metals Journal*, pages 52–62, 1982.
- [179] Blackmore P. A. and Harding R. A. *Journal of Heat Treating*, 3:310–325, 1984.
- [180] Shi J., Zou S., and Too J. J. M. *Cast Metals*, 5:103–108, 1992.
- [181] Luyendijk T. and Niesawaag H. In *50th International Foundry Congress Cairo*, pages 1–11, Cairo, 6-11 November 1983.
- [182] Klug R.C., Hintz M.B., and Rundman K.B. *Metallurgical Transactions A*, 16A:797–805, 1985.
- [183] BahmaniM., Elliott R., and Varahram N. *Journal of Materials Science*, 32:4783–4791, 1997.
- [184] Hamid A. S. and Elliott R. *Materials Science and Technology*, 12:780–787, 1996.
- [185] Hamid A. S. and Elliott R. *Materials Science and Technology*, 13:24–30, 1996.
- [186] Ahmadabadi M. N. *AFS Transactions*, 102:269–278, 1994.
- [187] Hamid A. S., Uzlov K. I., Darawish N., and Elliott R. *Materials Science and Technology*, 10:35–40, 1994.
- [188] Mallia J. and Grech M. *Materials Science and Technology*, 13:408–414, 1997.
- [189] Bayati H., Elliott R., and Lorimer G. W. *Materials Science and Technology*, 11:908–913, 1995.
- [190] Moore D. J., Rouns T. N., and Rundman K. B. *AFS Transactions*, 93:705–718, 1985.
- [191] Darawish N. and Elliott R. *Materials Science and Technology*, 9:882–889, 1993.
- [192] Shah S. M. and Verhoeven J. D. *Wear*, 113:267–278, 1986.
- [193] Gagne M. and Fallon P. A. *Canadian Metallurgical Quarterly*, 25:79–90, 1986.

- [194] Teng-Shih S. and Zang-Chou Y. *International Journal of Cast Metals Research*, 10:335–344, 1998.
- [195] Prasad P. and Putatunda S. K. *Metallurgical and Materials Transactions A*, 28A:1457–1470, 1997.
- [196] Prasad P. and Putatunda S. K. *Materials Science and Technology*, 14:1257–1265, 1998.
- [197] Sharma V. K. In *1st International Conference on Austempered Ductile Iron*, pages 53–62, Chicago, Illinois, 2-4 April 1984.
- [198] Voigt R. C. and Loper C. R. In *1st International Conference on Austempered Ductile Iron*, pages 83–106, Chicago, Illinois, 2-4 April 1984.
- [199] Corlu B., Venugoplalan D., and Alagarsamy A. In *1st International Conference on Austempered Ductile Iron*, pages 187–193, Chicago, Illinois, 2-4 April 1984.
- [200] Yazadani S. and Elliott R.. *Materials Science and Technology*, 15:896–902, 1999.
- [201] Aoyama M., Takatu M., and Takagi H. *Chuzo kogaku*, 70:556–562, 1998.
- [202] Fujita T., Ogi K., and Sawamoto A. *Chuzo kogaku*, 70:260–265, 1998.
- [203] Shibutani S. and Tanaka Y. *Chuzo kogaku*, 70:115–120, 1998.
- [204] Tanaka Y. and Osafune Y. *Imono*, 64:325–331, 1992.
- [205] Tsukahara S. and Yamada S. *Chuzo Kogaku*, 71:523–528, 1999.
- [206] Sugiyama Y., Asami K., and Tabata S. *Imono*, 66:833–839, 1994.
- [207] Saito K., Ichimura T., Kawano Y., and Mita Y. *Imono*, 65:36–40, 1993.
- [208] Sugiyama Y., Asami K., and Kuroiwa H. *Zairyo*, 40:65–71, 1991.
- [209] Sugiyama Y., Asami K., and Tabata S. *Imono*, 67:190–196, 1995.
- [210] Shimizu K. and Naguchi T. *Wear*, 176:255–260, 1994.
- [211] Pashby I. R., Wallbank J., and Boud F. *Wear*, 162-164:22–33, 1993.
- [212] Lin C. K., Lai P. K., and Shih T. S. *International Journal of Fatigue*, 18:297–307, 1996.
- [213] Lin C. K. and Pai Y. L. *International Journal of Fatigue*, 21:45–54, 1999.
- [214] Fordyce E. P. and Allen C. *Wear*, 135:265–278, 1990.

- [215] Yamamoto S., Nakajima H., and Miyaji H. *Imono*, 81:19–24, 1995.
- [216] Hwang J. R., Perng C. C., and Shan Y. S. *International Journal of Fatigue*, 12:481–488, 1990.
- [217] Putatunda S. K. and Singh I. *Journal of Testing and Evaluation*, 23:325–332, 1995.
- [218] Prasad P. and Padmaprabha. *Fatigue and Fracture of Engineering Materials and Structures Ltd.*, 18:693–697, 1995.
- [219] Kovacs B.V., Keough J.R., , and Pramstaller D.M. Austempered ductile iron (adi) process. Technical report, Gas Research Institute, 1988.
- [220] Palmer K. B. *BCIRA internal report 1760*, pages 80–86, 1989.
- [221] Burke C. M., Moore D. J., and Rundman K. B. *AFS Transactions*, 106:91–97, 1998.
- [222] Gilbert G. N. J. *BCIRA internal report 1666*, pages 258–266, 1986.
- [223] Janowak J. F. and Morton P. A. *AFS Transactions*, 92:489–498, 1984.
- [224] Cooper R. G. *BCIRA internal report 1703*, pages 277–287, 1987.
- [225] Shih T. S., Lin C. K., and Twan H. Z. *AFS Transactions*, 105:367–376, 1997.
- [226] Srinivasan M. N. and Komatsu S. *Journal of Testing and Evaluation*, 27:100–105, 1999.
- [227] Palmer K. B. *BCIRA internal report 1776*, pages 238–246, 1989.
- [228] Blackmore P. A. *BCIRA internal report 1610*, pages 41–49, 1984.
- [229] Mills K. A. A. *BCIRA internal report CT.46*, pages 1–18, 1987.
- [230] Cushway A. A. *BCIRA internal report 1764*, pages 106–114, 1989.
- [231] Rivera G., Boeri R., and Sikora J. *International Journal of Cast Metals Research*, 11:533–538, 1999.
- [232] Frier M. J. D. *BCIRA internal report 1820*, pages 1–4, 1991.
- [233] Cooper R. G. *BCIRA internal report 1801*, pages 127–130, 1990.
- [234] Cooper R. G. *BCIRA internal report 1787*, pages 381–392, 1990.
- [235] Matharu I. S., Frier M. J. D., and Selby K. *BCIRA internal report 1813*, pages 223–231, 1990.
- [236] Blackmore P. A. *BCIRA internal report 1596*, pages 386–392, 1984.

- [237] Blackmore P. A. *BCIRA internal report 1615*, pages 77–83, 1985.
- [238] Cooper R. G. *BCIRA internal report 1735*, pages 173–180, 1988.
- [239] Martinez R. A., Boeri R. E., and Sikora J. A. *AFS Transactions*, 105:27–30, 1998.
- [240] Greno G. L. *AFS Transactions*, 106:31–37, 1998.
- [241] Faucher B., Wang K. C., and Gagne M. *AFS Transactions*, 95:127–132, 1987.
- [242] Park Y. J., Morton P. A., Gagne M., and Goller R. *AFS Transactions*, 92:395–400, 1984.
- [243] Debanshu B. and Rastogi P. K. In *International Congress and Exposition*, pages 1–6, Detroit, Michigan, February 25-March 1 1991.
- [244] Palmer K. B. *BCIRA internal report 1782*, pages 312–317, 1989.
- [245] Huh Y. J., Arroyo M. H., Rimmer A. L., and Elliott R. *International Journal of Cast Metals Research*, 11:237–245, 1999.
- [246] Moncada O. J. *AFS Transactions*, 106:39–45, 1998.
- [247] Bayati H. and Elliott R. *Materials Science and Technology*, 11:284–298, 1995.
- [248] Takahashi T., Abe T., and Tada S. *Metallurgical and Materials Transactions A*, 27A:1589–1598, 1996.
- [249] Gilbert G. N. J. *BCIRA internal report 1683*, pages 32–45, 1989.
- [250] Nazarboland A. and Elliott R. *Materials Science and Technology*, 13:223–232, 1997.
- [251] Bahmani M. and Elliott R. *Materials Science and Technology*, 10:1068–1072, 1994.
- [252] Ratto P. J. J., Ansaldi A. F., Fierro V. E., Aguera F. R., Alvarez H. N., and Sikora J. A. *ISIJ International*, 41:372–380, 2001.
- [253] Lalam S. H., Bhadeshia H. K. D. H., and MacKay D. J. C. *Science and Technology of Welding and Joining*, 5:149–160, 2000.
- [254] Knott J. F. *Fundamentals of Fracture Mechanics*. Butterworths, U.K., 1973.
- [255] Buttler S. A. *British Steel BS-STC internal reports*, 2000.
- [256] Lalam S. H. *Modeling of Mechanical Properties of Ferritic Weld Metals*. PhD thesis, University of Cambridge, 2000.
- [257] Young C. H. and Bhadeshia H. K. D. H. *Materials Science and Technology*, 10:209–214, 1994.

- [258] Caballero F. G., Bhadeshia H. K. D. H., Mawella K. J. A., Jones D. G., and Brown P. *Materials Science and Technology*, 17:517–522, 2001.
- [259] Bhadeshia H. K. D. H. *Acta Metallurgica*, 29:1117–1130, 1981.
- [260] Cottrell A. *An introduction to Metallurgy*. The Institute of Materials, London U. K., 2nd edition edition, 1995.
- [261] Gibson G. P. Review of cleavage fracture mechanisms in ferritic steels. Technical report, UKAEA Report R13227, Harwell, Oxon, 1988.